UNIVERSIDAD NACIONAL AUTÓNOMA DE MÉXICO
PROGRAMA DE POSGRADO EN ASTROFÍSICA

INSTITUTO DE RADIOASTRONOMÍA Y ASTROFÍSICA

IRAS 16293–2422 FROM CENTIMETER TO FAR INFRARED WAVELENGTHS AND THE DETERMINATION OF ITS THREE-DIMENSIONAL STRUCTURE

TESIS
QUE PARA OPTAR POR EL GRADO DE
DOCTOR EN CIENCIAS (ASTROFÍSICA)

PRESENTA
ANTONIO HERNÁNDEZ GÓMEZ

TUTORES
DR. LAURENT LOINARD
DR. EMMANUEL CAUX

MORELIA, MICHOACÁN, ENERO DE 2019

THÈSE

En vue de l'obtention du

DOCTORAT DE L'UNIVERSITÉ DE TOULOUSE

Délivré par l'Université Toulouse 3 - Paul Sabatier

Cotutelle internationale : Universidad Nacional Autonoma de Mexico

Présentée et soutenue par

Antonio HERNANDEZ GOMEZ

Le 22 janvier 2019

IRAS 16293-2422 : des longueurs d'onde centimétriques à l'infrarouge lointain et détermination de sa structure tridimensionnelle

Ecole doctorale : **SDU2E - Sciences de l'Univers, de l'Environnement et de l'Espace**

Spécialité : **Astrophysique, Sciences de l'Espace, Planétologie**

Unité de recherche :
IRAP - Institut de Recherche en Astrophysique et Planetologie

Thèse dirigée par
Emmanuel CAUX et Laurent LOINARD

Jury

M. René PLUME, Rapporteur
M. Mauricio TAPIA, Rapporteur
Mme Aina PALAU, Examinateur
M. Arturo GOMEZ, Examinateur
Mme Karine DEMYK, Examinateur
Mme Cécile GRY, Examinateur
M. Emmanuel CAUX, Directeur de thèse
M. Laurent LOINARD, Co-directeur de thèse

Resumen para el público en general

La teoría que explica la formación de estrellas como nuestro Sol es ampliamente aceptada hoy en día. Sin embargo, las observaciones hechas con telescopios han mostrado que la gran mayoría de estas estrellas se forman en grupos o sistemas múltiples. Aún hay muchas preguntas abiertas acerca de la formación y evolución de tales sistemas. Para responder a estas preguntas, debemos estudiar las propiedades de sistemas estelares en formación con el fin de conocer las condiciones físicas y químicas iniciales en las que nacen. En esta tesis, presentamos un estudio de las propiedades de IRAS 16293-2422, un sistema múltiple muy joven que formará un pequeño grupo de estrellas como nuestro Sol. Para esto hemos utilizado observaciones realizadas con telescopios en longitudes de onda de radio e infrarrojas para estudiar y modelar las condiciones físicas y químicas en IRAS 16293-2422.

Résumé grand public

La théorie qui explique la formation des étoiles comme notre Soleil est aujourd'hui largement acceptée. Cependant, des observations avec des télescopes ont montré que la plupart de ces étoiles se forment dans des groupes de plusieurs étoiles. De nombreuses questions sur la formation et l'évolution des étoiles dans de tels systèmes restes encore ouvertes. Pour répondre à ces questions, nous devons étudier les propriétés des systèmes stellaires en formation afin d'en savoir plus sur les conditions physiques et chimiques régnants dans les nuages où ils sont nés. Dans cette thèse, nous présentons une étude des propriétés d'IRAS16293-2422, un très jeune système multiple qui formera dans l'avenir un petit groupe d'étoiles comme notre Soleil. Nous avons notamment utilisé des observations effectuées à l'aide de télescopes à des longueurs d'onde radiométriques et infrarouges pour étudier et modéliser les conditions physiques et chimiques d'IRAS16293-2422.

General summary

The theory that explains how the stars like our Sun are formed is nowadays widely accepted. However, observations with telescopes have shown that most of these stars form in groups or multiple systems. There are many open questions regarding how stars form and evolve in such systems. To answer these questions, we need to study the properties of young stellar systems to know more about the initial physical and chemical conditions in which they are born. In this thesis, we present a study of the properties of IRAS 16293-2422, a very young multiple stellar system that will form a small group of stars like our Sun in the future. In particular, we used observations performed with telescopes at radio and infrared wavelengths to study and model the physical and chemical conditions in IRAS 16293-2422.

RESUMEN

En esta Tesis presentamos un estudio observacional multi-frecuecia de las propiedades de IRAS 16293-2422, un sistema estelar múltiple de tipo solar de baja masa muy bien estudiado, y que se encuentra localizado en la nube oscura L 1689 N dentro del complejo de Ofiuco. Dado que IRAS 16293–2422 es la fuente prototípica para estudios de la astroquímica debido a su riqueza de líneas moleculares, proporciona un laboratorio ideal para estudiar no sólo la formación estelar en grupos, sino también la química en etapas tempranas de este proceso. En este trabajo, pondremos especial énfasis en moléculas nitrogenadas presentes en IRAS 16293–2422, dado que estas especies son herramientas muy útiles para derivar propiedades químicas, cinemáticas y dinámicas en regiones de formación estelar en un amplio rango de condiciones.

La primera parte de esta tesis esta basada en el análisis de las componentes individuales de IRAS 16293–2422 a partir de observaciones en el continuo en longitudes de onda centimétricas y milimétricas. Dado que la correcta interpretación de las observaciones y su modelación correspondiente dependen fuertemente de la medición precisa de su distancia, hemos medido el paralaje a su emisión maser de H_2O a 22.2 GHz a partir de observaciones obtenidas del archivo del Very Large Baseline Array (VLBA). Hemos obtenido una estimación más precisa de la distancia hacia IRAS 16293–2422 de 141^{+30}_{-21} pc. A partir de observaciones de alta resolución angular con el Very Large Array (VLA) y el Atacama Large Millimeter/submillimeter Array (ALMA), seguimos la astrometría de los objetos individuales del sistema por casi 30 años. Hemos visto que las propiedades de la fuente B son notables porque su emisión se encuentra dominada por radiación térmica de polvo. Presentamos un modelo completo de transferencia radiativa para la estructura de esta fuente. Los perfiles de densidad y temperature necesarios para explicar las propiedades observacionales de la fuente B son muy parecidos a los esperados para un primer núcleo hidrostático. Estos hechos, combinados con la ausencia de emisión centimétrica libre-libre, podrían indicar que la fuente B apenas está alcanzando la fase protoestelar.

En la segunda parte de la tesis nos enfocamos en la química de IRAS 16293–2422 a partir de observaciones de moléculas nitrogenadas con telescopios de un solo plato con los radiotelescopios IRAM-30m, APEX, JCMT y el instrumento HIFI a bordo del Observatorio Espacial Herschel en un rango amplio de frecuencias desde 80 GHz a 1 THz. Hemos extraído las transiciones rotacionales de la molécula ácido isocianuro (HNCO) de estos datos y hemos usado un modelo de transferencia radiativa fuera de Equilibrio Termodinámico Local (ETL) para reproducir los perfiles de línea observados de HNCO. Concluimos que IRAS 16293–2422 puede ser modelada considerando tres regiones: una componente densa, compacta y caliente asociada con el núcleo caliente, una componente tibia y extendida asociada con la parte interna de la envolvente y una capa más extendida y fría asociada con la parte más externa de la envolvente. Es importante enfatizar que la emisión producida por cada una de estas regiones interactúa con las otras regiones. Como consecuencia, nuestro análisis no sólo constriñe las propiedades de las diferentes regiones, sino que también establece sus posiciones relativas a lo largo de la línea de visión. Calculamos un perfil radial de abundancia de HNCO para la

envolvente de IRAS 16293–2422 con el código químico Nautilus, el cual es completamente consistente con las abundancias calculadas con nuestro modelo de transferencia radiativa. Por otra parte, los perfiles de línea de cianuro (CN) en IRAS 16293–2422 son mucho más complejos que los perfiles de HNCO dado que presentan absorciones profundas. Dado que detectamos las transiciones rotacionales de CN correspondientes a los niveles $J = 1 - 0$ hasta $J = 5 - 4$, hemos utilizado un modelo en LTE dentro de CASSIS y definimos un modelo por separado para cada transición. Para poder reproducir los perfiles de línea correctamente, es necesario considerar una componente extendida más grande que la misma envolvente de IRAS 16293–2422 definida previamente en la literatura. Derivamos los cocientes para los isótopos de CN a partir de ^{13}CN y $C^{15}N$. El conjunto de resultados presentados en este trabajo permitió constreñir la estructura de IRAS 16293–2422 desde la escala de sus protoestrellas individuales (~ 10 AU), hasta la escala de su envolvente extendida ($\sim 10{,}000$ AU).

RÉSUMÉ

Dans cette thèse, nous présentons une étude observationnelle et multifréquence des propriétés d'IRAS 16293-2422, un système d'étoiles multiples de faible masse et de type solaire bien étudié, qui se trouve dans le nuage sombre L1689 N dans le complexe d'Ophiuchus. IRAS 16293-2422 est la source prototype pour les études d'astrochimie en raison de sa richesse en raies moléculaires, elle constitue un laboratoire idéal pour étudier non seulement la formation de systèmes stellaires, mais également la chimie pendant les premiers stades de la formation des étoiles. Dans ce travail, nous mettrons particulièrement l'accent sur les molécules azotée présentes dans IRAS 16293-2422, car ces espèces sont des outils puissants pour mesurer les propriétés chimiques, cinématiques et dynamiques des régions de formation d'étoiles dans un large éventail de conditions physiques.

La première partie de cette thèse est basée sur l'analyse des composants individuels d'IRAS 16293-2422 à partir d'observations dans le continuum aux longueurs d'onde centimétriques et millimétriques. Étant donné que l'interprétation correcte des observations et leur modélisation dépendent fortement de la mesure précise de la distance, nous avons mesuré l'émission maser à 22 GHz obtenues avec l'interféromètre de très longue ligne de base (VLBA) et obtenu une estimation plus précise de la distance d'IRAS 16293-2422, 141^{+30}_{-21} pc. À partir d'observations à haute résolution angulaire avec le VLA et ALMA, nous avons suivi l'astrométrie des objets individuels du système pendant près de 30 ans. En effet, son spectre indique que son émission est dominée par l'émission thermique des poussières. Nous présentons ici un modèle complet de transfert radiatif de la structure de cette source. Les profils de densité et de température nécessaires pour expliquer les propriétés de la source B sont très similaires à ceux attendus pour un premier coeur hydrostatique. Ce fait, combiné à l'absence d'émission centimétrique libre-libre, pourrait indiquer que la source B vient tout juste d'atteindre la phase protostellaire.

Dans la deuxième partie de la thèse, nous nous intéressons à la chimie d'IRAS 16293-2422 à partir d'observations des molécules azotées avec les radiotélescopes IRAM-30m, APEX, JCMT et l'instrument HIFI à bord de l'observatoire spatial Herschel dans une large gamme de fréquences allant de 80 GHz à 1 THz. Nous avons extrait les transitions de rotation de l'acide isocyanurique (HNCO) à partir de ces données et nous avons utilisé un modèle de transfert radiatif hors de l'équilibre thermodynamique local (ETL) pour reproduire les profils observés des raies. À partir de ce modèle, nous concluons qu'IRAS 16293-2422 est formée de trois régions d'émission: un composant dense, compact et chaud associé au hot corino, un composant chaud et étendu associé à la partie interne de l'enveloppe et une couche plus étendue et froide associée à la partie la plus extérieure de l'enveloppe. Il est important de souligner que l'émission produite par chacune de ces régions interagit avec les autres. En conséquence, notre analyse ne contraint pas seulement les propriétés des différentes régions, mais établit également leurs positions relatives le long de la ligne de visée. Nous avons calculé le profil d'abondance de HNCO pour l'enveloppe d'IRAS 16293-2422 avec le code chimique Nautilus, qui est tout à fait compatible avec les abondances déterminées par notre modèle de transfert radiatif. D'autre part, les profils de raie de cyanure (CN) dans IRAS

16293-2422 sont beaucoup plus complexes que les profils de HNCO, car ils présentent une absorption profonde. Dans la mesure où nous détectons les transitions de rotation du CN correspondant aux niveaux $J = 1 - 0$ à $J = 5 - 4$, nous avons utilisé ces profils pour tester la distribution de cette molécule à différentes échelles spatiales. Nous avons utilisé un modèle LTE dans CASSIS et défini un modèle distinct pour chaque transition. Afin de reproduire correctement les profils de raie, il est nécessaire de prendre en compte un composant étendu plus étendu que l'enveloppe d'IRAS 16293-2422 définie précédemment dans la littérature. Finalement, nous dérivons les rapports d'abondance entre CN et ses isotopes ^{13}CN et C^{15}N. Dans leur ensemble, les données presentées dans cette thèse nous ont permis de contraindre la structure d'IRAS 16293-2422 depuis les échelles qui correspondent à ses proto-étoiles individuelles (~ 10 AU) jusqu'à l'échelle de son enveloppe étendue ($\geq 10,000$ AU).

SUMMARY

In this thesis we present a multi-frequency observational study of the properties of IRAS 16293–2422, a very-well studied low-mass solar-type multiple stellar system located within the Ophiuchus complex. Because IRAS 16293–2422 is the prototype source for astrochemistry due to its wealth of molecular lines, it provides a suitable laboratory to study not only the physics of clustered star-formation but also the chemistry in early stages of this process. In this thesis, we will place special emphasis on nitrogen-bearing molecules present in IRAS 16293–2422 since these species are known to be powerful tools to derive chemical, kinematic and dynamic properties of star-forming regions over a wide range of conditions.

The first part of this work is based on the analysis of the individual components of IRAS 16293–2422 from interferometric centimeter -and millimeter- wavelength continuum observations. Since the correct interpretation of the observations and their corresponding modelling strongly depend on the accurate measurement of its distance, we have measured the parallax to its H_2O maser emission at 22.2 GHz based on archival Very Large Baseline Array (VLBA) observations, obtaining a precise estimation of the distance of 141^{+30}_{-21} pc. From high angular resolution observations with the Very Large Array (VLA) and the Atacama Large Millimeter/submillimeter Array (ALMA), we followed the astrometry of the individual objects in the system for almost 30 years. We have seen that the properties of source B are remarkable because its spectrum indicates that its emission is dominated by thermal dust radiation. We present a full radiative transfer modelling of the structure of this source. The density and temperature profiles needed to explain the observational properties of source B resemble those expected for first hydrostatic cores. This fact, combined with the lack of free-free centimeter emission, might indicate that source B is just entering the protostellar phase.

In the second part of the thesis we focus on the chemistry of IRAS 16293–2422 based on single-dish observations of nitrogen-bearing molecules obtained with the radiotelescopes IRAM-30m, APEX, JCMT and the HIFI instrument on-board the Herschel Space Observatory over a wide frequency range from 80 GHz to 1 THz. We have extracted the rotational transitions of isocyanic acid (HNCO) from the observations and used a radiative transfer model out of Local Thermodynamical Equilibrium (non-LTE) to reproduce the observed line profiles. We conclude that IRAS 16293–2422 can be modelled considering three regions: a dense, compact and warm component related with the hot corino, a warm and extended component associated with the innermost part of the envelope and a more extended and cold layer associated with the outermost part of the envelope. It is important to emphasize that the emission produced by these regions interacts one with another. As a consequence, our analysis not only constraints the properties of the different regions, but also establishes their relative positions along the line of sight. An HNCO abundance profile for the envelope of IRAS 16293–2422 computed with the chemical code Nautilus shows a good agreement with the abundances derived from our radiative transfer model. On the other hand, the lines of cyanide (CN) have much more complex profiles since they show hyperfine structure and present deep absorptions. Indeed, since we detect the CN rotational transitions from $J = 1 - 0$ to $J = 5 - 4$ level, we have used an LTE model in CASSIS and defined a separate model for each transi-

tion. We noted that an extended emission larger than the envelope of IRAS 16293–2422 is needed to correctly model the line profiles. We also derived the abundance ratio between CN and its isotopes ^{13}CN and C^{15}N.

Taken together, the results presented here enabled us to constrain the structure of IRAS 16293–2422 from the scale of its individual protostars ($\sim$ 10 AU) up to the scale of its extended envelope ($\sim$ 10,000 AU).

A mis padres

Agradecimientos

Primero que nada quisiera agradecer de manera muy especial a mis directores de Tesis. A Laurent Loinard y su familia por ofrecerme su apoyo incondicional en todo momento. Su continua motivación y confianza en mi para llevar a cabo el trabajo de Tesis hicieron que disfrutara mucho de esta gran experiencia. A Emmanuel Caux por ser también un excelente asesor y por toda su paciencia y consejos, además de su trato siempre amigable y cordial. He aprendido tanto de ambos y les debo mucho por guiarme durante todo el camino. He sido muy afortunado de estar bajo su tutela y siempre les estaré muy agradecido.

A mis papás, Elizabeth y Antonio, y a mi hermano David porque es gracias a ellos que he podido llegar hasta esta etapa. Su apoyo para superarme y lograr cumplir mis sueños es lo que me ha permitido alcanzar mis metas.

A ti Carolina, por haberme brindado siempre tu amor, comprensión y apoyo constante e incansable. Gracias por haber sido fundamental para que lograra alcanzar esta meta. Lo logramos juntos porque formamos el mejor ecuipo.

A mi amigo Poncho López, por sus buenos consejos para seguir siempre adelante y por brindarme su apoyo en todo momento.

A todos mis primos y tíos que me han apoyado siempre. En especial a mi tía Chayito y a su familia que siempre han estado conmigo.

En el IRyA, tengo que agradecerle a muchas personas: a Stan Kurtz y Luis Zapata quienes fueron mis guías desde el principio. A mis amigos/roomies/compañeros/cuates: Mariana, Tere, Gisela, Jairo, Luis Angel, Diana, Sergio, Karin.

De igual manera, les debo mucho a tantas personas en el IRAP: a David Quénard, por su sincera amistad y por apoyarme tanto desde que comencé el doctorado. A los miembros de mi comité e investigadores que siempre estuvieron al pendiente de mis avances: Sandrine Bottinelli, Peter von Ballmoos, Isabelle Ristorcelli, y Frédéric Boone. A mis compañeros y amigos en Toulouse: Sarah, Agnes, Paolo, Martha, Olivier y Abraham.

A todos mis sinodales por sus valiosos comentarios y sugerencias: Mauricio Tapia, René Plume, Karine Demik, Aina Palau, Arturo Gómez y Cécile Gry.

Publications

This thesis consists of a collection of papers that were written during the period towards the PhD degree.

I. A revised distance to IRAS 16293-2422 from VLBA astrometry of associated water masers
S. A. Dzib, G. N. Ortiz-León, **A. Hernández-Gómez**, L. Loinard, A. J. Mioduzewski, M. Claussen, K. M. Menten, E. Caux and A. Sanna, 2018, A&A, 614, 20.

II. On the nature of the compact sources in IRAS 16293-2422 seen at centimeter to submillimeter wavelengths
Antonio Hernández-Gómez, Laurent Loinard, Claire Chandler, Luis F. Rodríguez, Luis A. Zapata, David J. Wilner, Paul T.P. Ho, Emmanuel Caux, David Quénard, Sandrine Bottinelli, Crystal L. Brogan, Lee Hartmann and Karl M. Menten (submitted to the Astrophysical Journal).

III. IRAS 16293-2422 B: an overlooked first hydrostatic core?
David Quénard, **Antonio Hernández-Gómez**, Laurent Loinard, Emmanuel Caux, Sandrine Bottinelli, Karl M. Menten et al. (to be submitted to the Astrophysical Journal).

IV. Modelling the abundance structure of isocyanic acid (HNCO) toward the low-mass solar type protostar IRAS 16293-2422
Antonio Hernández-Gómez, Emna Sahnoun, Emmanuel Caux, Laurent Wiesenfeld, Laurent Loinard, Sandrine Bottinelli, Kamel Hammami and Karl M. Menten, 2019, MNRAS, 483, 2014

V. Probing the structure of IRAS 16293-2422 from the emission and absorption of cyanide (CN)
Antonio Hernández-Gómez, Emmanuel Caux, Laurent Loinard, Sandrine Bottinelli and Karl M. Menten (submitted to the Monthly Notices of the Royal Astronomical Society).

Contents

Chapter 1

Introduction

1.1 A general picture of the single low-mass star formation process

The theory of the formation of single low-mass stars has been widely studied and is very well-described by Shu et al. (1987). This process begins with the fragmentation of large molecular clouds (with typical sizes of $\sim$ 10 pc) into cold condensations (T $\sim$ 10 K). These condensations collapse gravitationally to form a pressure-supported compact object in equilibrium, called first hydrostatic core (FHC, Larson 1969). The lifetime of a FHC is expected to be about $1 \times 10^3 - 3 \times 10^4$ yr, while the radius of these objects is only a few AU and they have temperatures of $\sim$ 100 K. Since most of the emission from the FHC is absorbed and re-radiated by its colder envelope, its spectrum is very similar to that of a starless core. The FHC increases its temperature adiabatically until it reaches about 2000 K, when the dissociation of H_2 begins to occur. Since this process is exothermic, it allows the core to continue with the gravitational collapse until the internal pressure stops again the collapse, and a second equilibrium phase (known as a protostar) is reached. The protostellar stage is commonly divided in five classifications: Class 0, Class I, Flat spectrum, Class II and Class III protostars. These different stages are characterized observationally by their spectral energy distributions (SED; André et al. 1993; Greene et al. 1994). More specifically, the class is defined by the behaviour of the SED through the so-called infrared spectral index:

$$\alpha_{IR} = d \log (\lambda F_\lambda)/d \log \lambda \qquad (1.1)$$

where λ is the observed wavelength (between [2.2, 10-25] μm) and F_λ is the flux at the given wavelength. This quantity is directly related with the amount of dust in the disk and the envelope. The properties of the protostellar stages are described below:

Class 0 protostars. The term Class 0 protostar was first introduced by André et al. (1993) to describe a young stellar object that has accreted less than half of its final mass and is still deeply embedded in its surrounding envelope. In this stage, the protostar accretes material from its envelope via an accretion disk. Because of the conservation of angular momentum,

part of the material is ejected in the form of powerful bipolar outflows. Given that Class 0 are embedded in their parental cloud, they emit only at millimeter, sub-millimeter and far infrared wavelengths. Although the continuum spectrum of the envelope probe the cold gas, the central object contains a region of warm gas. This stage lasts about $10^4 - 10^5$ yr.

Class I protostars. As the protostar evolves, the bipolar outflows interacts with the dense envelope, pushing away the material. When the mass of the protostar is higher than the mass of the envelope, the protostar becomes a Class I object. The outflow in this stage is less powerful and the accretion rate decreases since the envelope becomes less massive. Observationally, their SED is characterized by a spectral index $\alpha_{IR} > 0$. Since the disk dominates the emission at infrared (IR) wavelengths, an IR excess in the SED is expected.

Flat spectrum protostars. These objects show a spectral index close to 0. Some of them are visible at optical wavelengths and show strong emission lines and large veilings. Their SED can be modelled as in infalling circumstellar envelope with large polar cavities or holes.

Class II protostars. During this stage the outflow has interacted enough with the envelope to clean it (see Figure 1.1). Once the protostar has completely lost all its surrounding envelope and becomes visible at optical wavelengths, it is called a Class II object or T Tauri star. This is because T Tauri was the first identified member of this class. The main feature of this stage is the presence of a protoplanetary disk around the protostar. The spectral index is between $-1.5 < \alpha_{IR} < 0$.
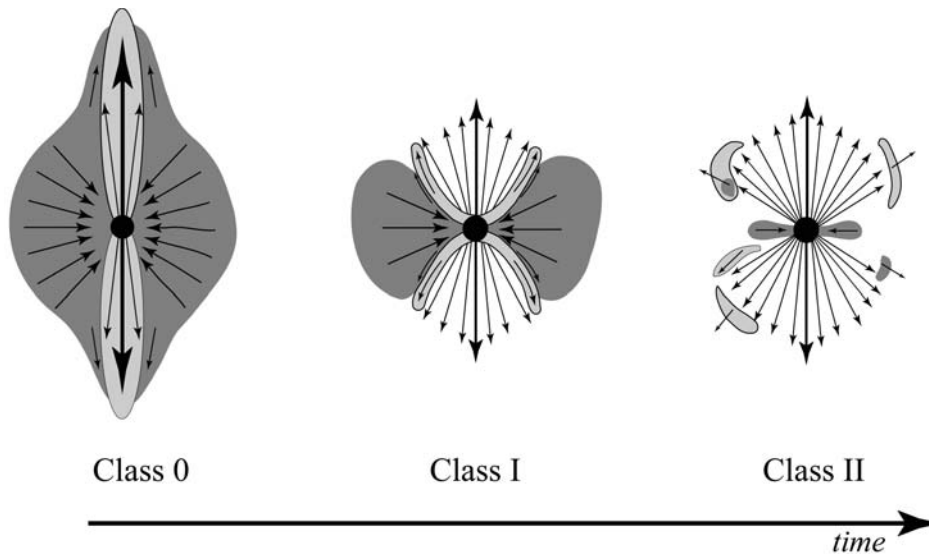
Figure 1.1. Scheme of the evolutionary interaction of a molecular outflow and the envelope in a protostar. Figure taken from Arce and Sargent (2006).

Class III protostars. The protoplanetary disk will evolve further to form planetesimals, becoming a debris disk. In this stage, the IR emission from the disk will decrease considerably and the central compact object will dominate the SED. An object in this stage is called Class III protostar or weak-line T Tauri star. The spectral index is $\alpha_{IR} < -1.5$.

In Figure 1.2 we show a picture of the SED of the protostars according to their evolutionary states.
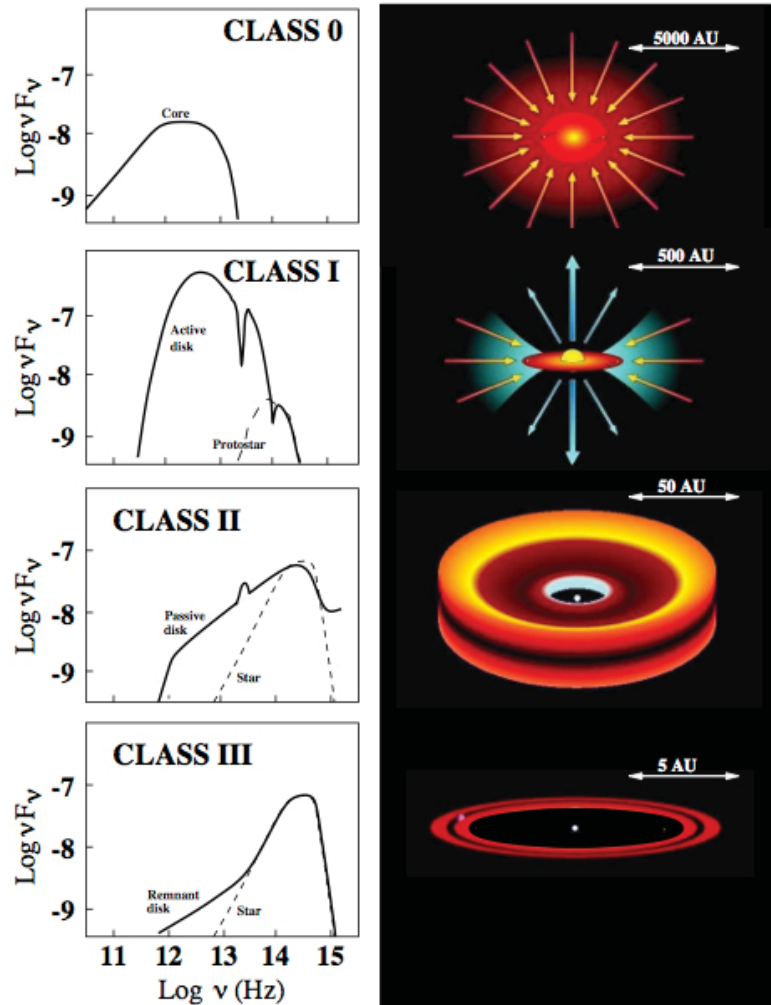
Figure 1.2. Classification of the protostars according to their spectral energy distribution. Figure taken from Andrea Isella PhD thesis (2006).

The end of the protostellar stage is reached when the central object evolves toward the main sequence stage. The formation of a planetary system like ours is expected. In Figure 1.3 a schematic view of the scenario described above is shown.
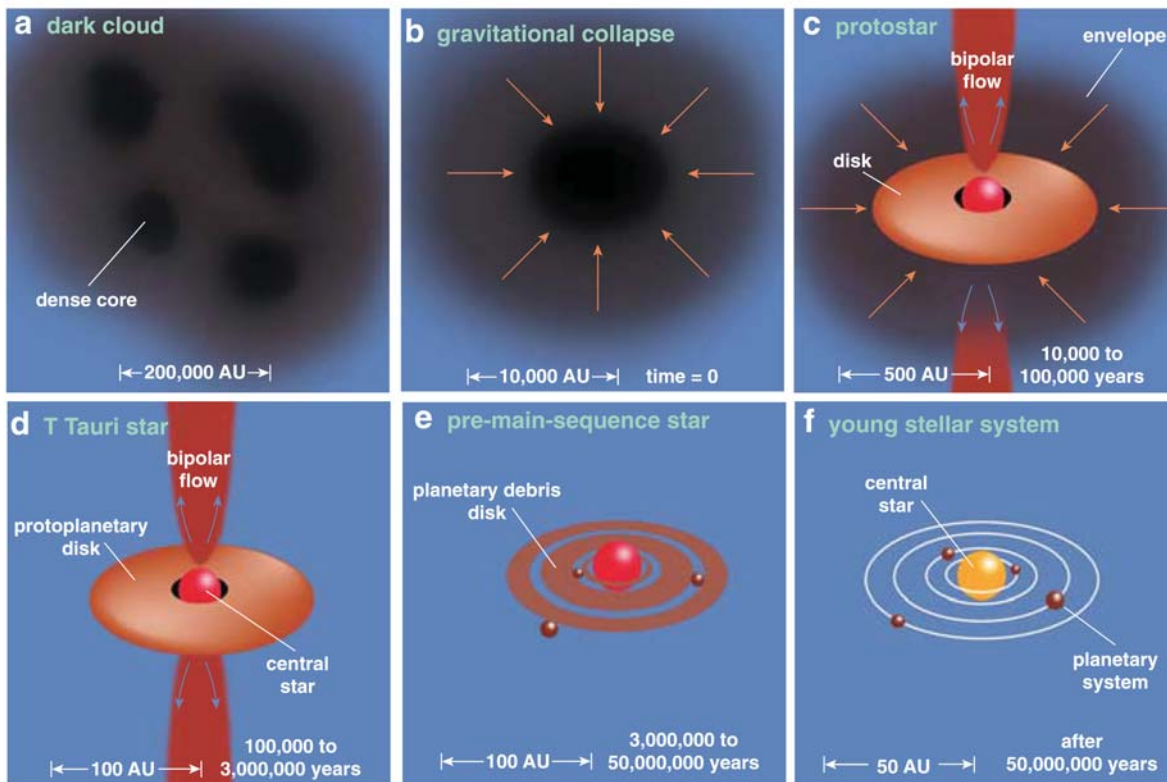
Figure 1.3. Single low-mass star formation scheme. Figure taken from Greene (2001).

1.1.1 Stellar formation in multiple systems

The process described in the previous section is valid for stars born in isolation. However, observational studies from optical to centimeter wavelengths have revealed that the formation of stars occurs often in binary or multiple systems. Characterizing the multiplicity of proto-stars during their earliest stages of evolution provides a useful approach to understanding the formation mechanism of multiple systems. Since the youngest protostars are still deeply embedded in their environments, radio and submillimeter interferometric observations are needed to probe their multiplicity. Several studies have been devoted to address this problem. For instance, Haisch et al. (2004) performed a survey of 76 Class I protostars and found a companion star fraction of $18\% \pm 4\%$ with a separation range of $\sim 300 - 2000$ AU. A similar study from Duchêne et al. (2004) reported a companion fraction of $27\% \pm 6\%$ with a separation $\sim 110 - 1400$ AU. Later, Duchêne et al. (2007) found a companion fraction of $47\% \pm 8$ in a survey of 45 protostars with separations $\sim 14 - 1400$ AU. Chen et al. (2013) made a survey of 33 Class 0 objects with the SMA at 1.3 mm and found that at least 20 of the objects in their sample had a companion with separations between $\sim 50 - 5000$ AU. In Figure 1.4, the multiplicity frequency as function of evolutionary stage found by Chen et al. (2013) is shown. The diminution in multiplicity with the evolutionary state found by Chen et al. (2013) might suggest that multiple systems evolve dynamically, being disrupted with time as result of dynamical interactions. Because the multiplicity found by Chen et al. (2013) and

other authors are only lower estimates due to the instrumental limitations, one could argue that virtually all stars are born in binary or multiple systems (as Larson 1972 suggested).
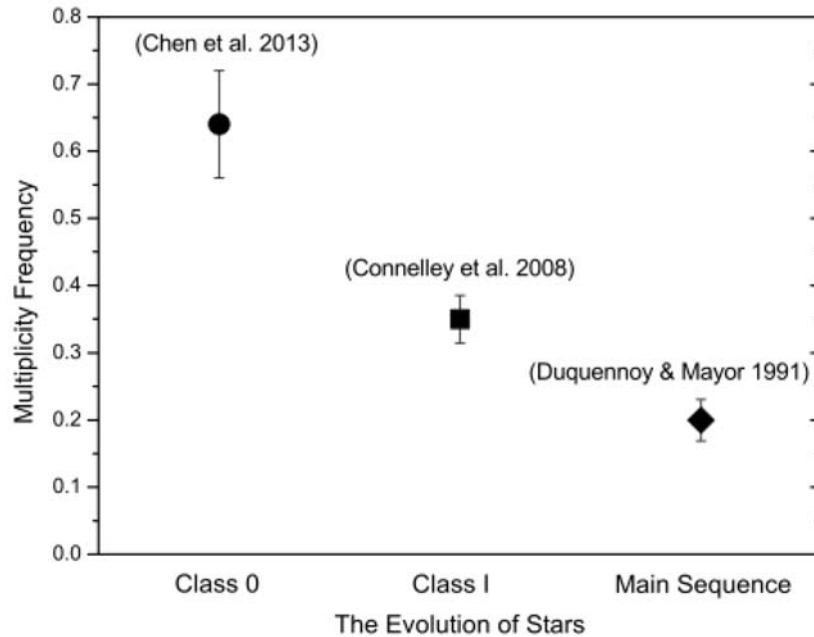
Figure 1.4. Multiplicity frequency decreasing with protostellar age due to the breakup of multiple systems. Credit: Chen et al. (2013).

One of the most accepted scenarios to explain the formation of binary and multiple systems is the collapse and fragmentation of cloud molecular cores (Boss and Bodenheimer 1979). In this process, the large-scale fragmentation of turbulent gas cores or filaments is expected to form wide binary systems. However, a disk fragmentation due to a rotational instability mechanism has been also proposed to explain the formation of a tight multiple system (Adams et al. 1989).

Multiplicity can affect early stellar evolution. For instance, tidal mechanisms could affect the accretion and time evolution of each of the members of a multiple system. Very young Class 0 systems are particularly interesting in this context because they probe the initial conditions of multiple stellar evolution.

1.1.2 Chemistry in low-mass star-forming regions

Chemical processes play a fundamental role in the formation of stars. Molecules provide us a unique tool to study the kinematics of star-forming regions from the analysis of their line profiles. The presence (or absence) of certain species might give us a clue of the physical conditions ongoing in stellar forming regions that favour the creation or destruction of such species. Moreover, comparisons between observed chemical abundances and the predictions

from chemical models allow us to estimate evolutionary timescales. In this section we present briefly the two paths leading to the formation and destruction of molecules in star-forming regions.

1.1.3 Gas phase chemistry

Gas phase reactions can occur over a wide range of density and temperature conditions. Some important chemical processes are:

Ion-molecule reactions:

$$A^+ + B \rightarrow C^+ + D. \tag{1.2}$$

Dissociative recombination:

$$AB^+ + e \rightarrow A + B. \tag{1.3}$$

Radiative association:

$$A + B \rightarrow AB + h\nu. \tag{1.4}$$

Neutral-neutral reactions:

$$A + B \rightarrow C + D. \tag{1.5}$$

Photodissociation:

$$AB + h\nu \rightarrow A + B. \tag{1.6}$$

Charge-transfer:

$$A^+ + B \rightarrow A + B^+. \tag{1.7}$$

These reactions can be more or less frequent depending of the environment. For instance, in dark molecular clouds, ion-molecule reactions are particularly important since the production of ions begins with the interaction of cosmic rays with H_2 to form H_2^+, which reacts with H_2 to form H_3^+. This is a very important molecular ion since it can easily transfer a proton, and therefore helps to increase the molecular complexity.

1.1.4 Surface chemistry

Surface chemistry is fundamental for the formation of a number of molecules since dust grains can play the role of catalysers to form molecules (such as H_2) that cannot form in the gas phase. Surface chemistry is very important to explain the abundance enhancement of certain species in molecular outflows. It also is at play near star-forming regions where the complexity of molecular species is found to be large. There are three main mechanism for

grain surface reactions: Langmuir-Hinshelwood, Eley-Rideal and the hot atom mechanism. These processes are illustrated in Figure 1.5 that represent a regular grain surface with a periodic potential.
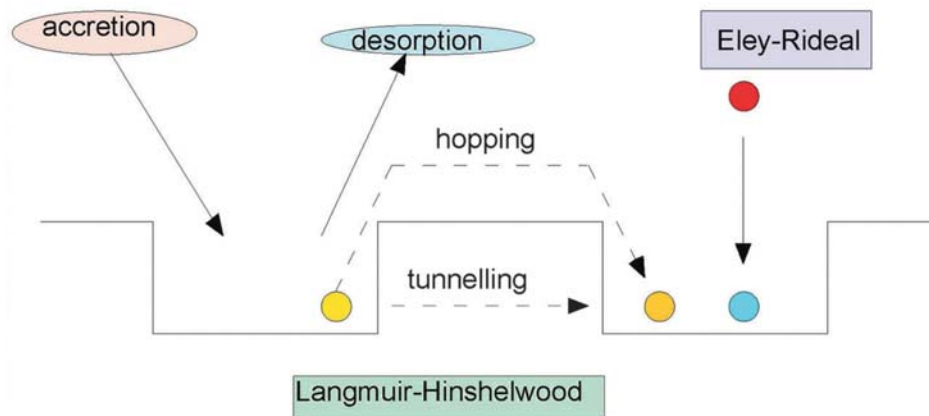
Figure 1.5. Main surface chemistry processes. Credit: Bromley et al. (2014).

Accretion can occur in the binding sites that correspond to potential minima. Also, desorption can occur by thermal evaporation (sublimation) for light species or by non-thermal processes. The Langmuir-Hinshelwood mechanism consists in the tunnelling or thermal hopping over the barrier between binding sites. In the hot atom mechanism, a gas phase species lands on a surface and moves considerably before thermalization. On the other hand, the Eley-Rideal mechanism allow reactive adsorbates such as atoms and radicals to react by sticking together when they lie in the same potential minimum, letting the grain absorb the energy excess.

1.1.5   Hot core chemistry and hot corinos

High-mass protostars have been found to have warm regions with high abundances of complex organic molecules (COMs), called hot cores. These regions are small ($\sim$ 0.1 pc), dense ($n_H > 2 \times 10^7$ cm^{-3}) and reach temperatures above 100 K where water-ice grain mantles evaporate, giving place to rich chemistry (e.g. see Kurtz et al. 2000). At the same time, the relative high densities and temperatures are favourable for the excitation of several molecular transitions. The molecules are originally in the surface of dust grains coming from the cold dense cloud where the protostar is formed. Once they evaporate in the hot core, gas phase chemical reactions occur, giving place to the creation and destruction of new molecules (see e.g. Garrod and Herbst 2006; Herbst and van Dishoeck 2009). Low-mass protostars have been found also to have such regions, called hot corinos. The use of the term hot corino for low-mass solar-type protostars was first made by Ceccarelli (2004) alluding to the similarities with hot cores of high mass protostars, including their molecular complexity. These objects have typical sizes of a few tens of AU. In fact, Ceccarelli et al. (1996) defined the first model for a thermal structure of a low-mass protostellar envelope. This model assumes

that a protostar with 1 $M_\odot$ accreting mass in a period of 10^5 yr could have a region of a size of a few hundred AUs where the dust reaches temperatures higher than 100 K, enough to evaporate water ice grain mantles. One of the main differences between hot cores and hot corinos is their size, which translates to different infall time scales that could affect the chemical compositions.

Understanding the chemistry of hot corinos associated with low-mass stars as our Sun is of vital importance to understand the history of the material from which the planetary systems are formed.

1.1.6 Nitrogen chemistry

Nitrogen, the 6th most abundant element in the Universe (after H, He, O, C, Ne) is a compound essential for life as we know it. Of the ~ 200 molecules that have been detected in the interstellar medium or circumstellar shells, 75 of them contain nitrogen (see Table 1.1).

						Number of atoms						
2	3	4	5	6	7	8	9	10	11	12	>12
CN	HCN	C_3N	H_2CCN	CH_3CN	CH_2CHCN	CH_3C_3N	CH_3CH_2CN	CH_3C_5N	HC_9N	$n\text{-}C_3H_7CN$	$c\text{-}C_6H_5CN$
NH	HNC	NH_3	HC_3N	CH_3NC	HC_5N	CH_2CCHCN	HC_7N			$i\text{-}C_3H_7CN$	
NO	HNO	HCCN	HC_2NC	HC_3NH^+	CH_3NH_2	H_2NCH_2CN	$CH_3C(O)NH_2$				
NS	MgCN	$HCNH^+$	H_2CNH	NH_2CHO	CH_3NCO	CH_3CHNH	$CH_3NHCHO?$				
PN	MgNC	HNCO	H_2NCN	C_5N							
SiN	N_2H^+	HNCS	HNC_3	$l\text{-}HC_4N$							
CN^-	N_2O	H_2CN	HC(O)CN	$H_2CCNH?(?)$							
N_2	NaCN	C_3N^-	HNCNH	$C_5N^?$							
$NO^+?$	NH_2	HCNO	NH_4^+	HNCHCN							
NS^+	SiCN	HOCN	H_2NCO^+	SiH_3CN							
	AlNC	HSCN	$NCCNH^+$								
	SiNC	HMgNC									
	KCN										
	FeCN										
	C_2N										
	NCO										

Table 1.1. Nitrogen-bearing molecules detected in the ISM or circumstellar shells (as of 05/2018). Adapted from The Cologne Database for Molecular Spectroscopy (CDMS). Tentative detections are indicated by "?". Some detections that have been reported as secure ones are indicated by "(?)" because overlap of lines cannot be ruled out at the moment.

A number of molecular species containing nitrogen have been found to be good tracers of the kinematics and the physical conditions in star-forming regions. For instance, the N_2H^+ molecule (diazenylium) is known to be a good tracer of dense gas (e.g. Pagani et al. 2007), while NH_3 (ammonia) is good probe of temperature in molecular clouds (e.g. Maret et al. 2009).

The major reservoir of interstellar nitrogen is believed to be in the form of atomic and molecular nitrogen. However, N_2 is not easy to observe since it has no permanent dipole moment. In general, the chemistry of nitrogen is still poorly understood. This is because observing key molecules in chemical reactions related to nitrogen chemistry is difficult due to observational constraints. However, a chemical network for the formation of some of the simplest molecules in the gas phase has been proposed. For instance, some of the main chem-

ical reactions occurring in the gas phase for dark clouds are shown in Figure 1.6. From this Figure we observe that neutral radical-radical reactions play a key role in nitrogen chemistry.
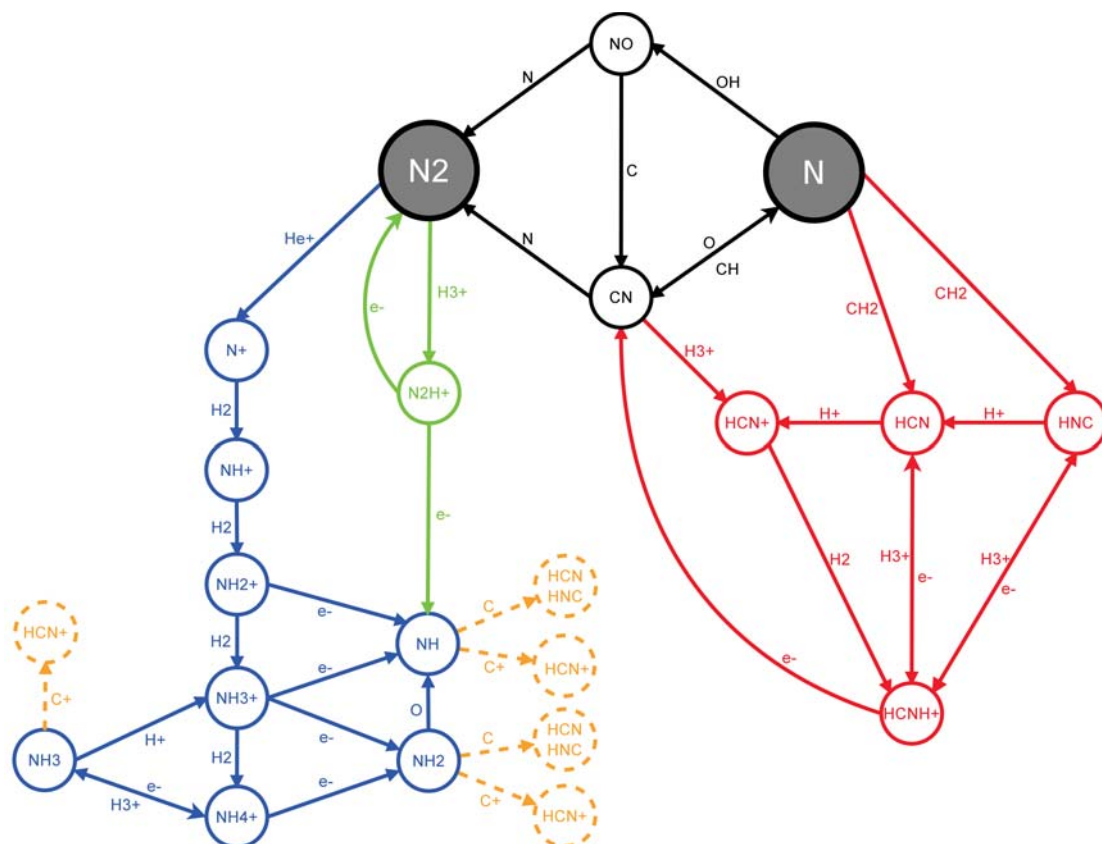
Figure 1.6. Main gas phase chemical reactions involving nitrogen in dark clouds. In blue, the reactions for hydrides are shown, while the reactions for nitriles are shown in red. The green colour indicate the main formation path for NH. The orange-dashed reactions indicate the routes for the conversion from hydrides to nitriles which depend on the C/O ratio. Figure taken from Le Gal et al. (2014).

Nitrogen hydrides (such as NH) are believed to originate from N_2, while nitriles (such as HNC) are thought to derive from atomic nitrogen. This means that since N_2 has to be synthesized first to form hydrides, they follow a slower formation path than nitriles. The formation of N_2 is though to have origin in the chemical reactions

$$N + OH \rightarrow NO + H, \tag{1.8}$$
$$NO + N \rightarrow N_2 + O. \tag{1.9}$$

Molecular nitrogen can also be formed from

$$N + CH \rightarrow CN + H, \tag{1.10}$$

$$CN + N \rightarrow N_2 + C. \tag{1.11}$$

Also, NO can be destroyed to form CN:

$$NO + C \rightarrow CN + O. \tag{1.12}$$

Thus, the C/O ratio is directly related to the abundance of both CN and NO, and ultimately, to the dominant formation path of N_2. Although the abundances predicted by these chemical reactions have been compared with observations in several environments, detailed chemical models and deeper observations are needed to constrain the chemistry of nitrogen in the ISM.

1.2 Observational techniques

Theoretical models have been developed to explain the physical and chemical processes regarding the formation of the stars. These models need to be contrasted with the observations of stars in different environments and at different evolutionary states to probe their validity. In addition, adequate computational analysis is needed to interpret and model the observations. In this section we briefly review the basics regarding the observations used in this thesis, the instruments used to obtain them and the theory for their analysis.

1.2.1 Singe-dish telescopes

Telescopes are built and designed to work in a given range of wavelengths. A fundamental quantity defining the capabilities of a telescope is the angular resolution it can achieve. The angular resolution of a telescope with a diameter D is given by the diffraction limit:

$$\theta = 1.22\frac{\lambda}{D} \tag{1.13}$$

where λ is the observing wavelength. Two objects in the sky can be resolved if one of them is spatially located outside the first minimum of the Airy disk from the other defined by equation (1.13). In other words, to distinguish between two objects in the sky separated by a given angular distance, the angular resolution needs to be better (smaller) than this separation. To have high angular resolution observations with a telescope, we need to have an instrument with a diameter as large as possible. A physical limitation appears when building large size telescopes since their structures can be very heavy. These structures need to be moved to point toward the target source in the sky and follow it with an enormous precision while compensating the rotation of the Earth. The design, building and maintaining of large telescopes is therefore a difficult task.

1.2.2 Heterodyne receivers

Heterodyne receivers are instruments that work at radio wavelengths and use the frequency mixing method to convert a signal to a fixed intermediate frequency (IF) while preserving the phase information (i.e. the receivers are coherent). This IF can then be treated in a more convenient way instead of processing the original signal. In astronomy, these receivers are commonly used since they provide a suitable way to process the signal received from objects in the sky. Indeed, most modern radio receivers use these instruments (e.g. communication satellites, radars, telephonic systems and tv devices).

The heterodyne receivers work as follows: first, the radio signal is received by an antenna; since the input signal from the antenna might be weak (a few microvolts), it may be amplified in a so-called radio frequency (RF) by an amplifier. This signal is shifted to lower frequencies by adding a signal called local oscillator (LO) and passing the resulting sum through a non-linear device, whose output contains the difference frequency. Although a non-linear device is involved, the conversion from input to output is linear for the small signal. This process is called mixing and the output will be the IF.

1.2.3 Observations with heterodyne instruments

Nowadays, most of the telescopes working at radio and far infrared wavelengths use broadband continuum receivers and heterodyne detection spectral line receivers. Because a multiwavelength study is the best way to investigate the properties of IRAS 16293-2422, we have based our work on the analysis of continuum and heterodyne line observations obtained with the IRAM, APEX and JCMT radiotelescopes. We have also used observations performed with the Heterodyne Instrument for the Far Infrared (HIFI) on-board the Herschel Space Observatory.

The IRAM radiotelescope

The IRAM (Institut de radioastronomie millimétrique) telescope is located near Pico Veleta in Granada, Spain (see Figure 1.7). Placed at an altitude of ~ 3000 m, IRAM has a diameter of 30 m and works at frequencies between 80 and 300 GHz ($\sim 0.8 - 3$ mm). IRAM has 8 superheterodyne (SIS) receivers that work in the following frequencies: 83–117 GHz (EMIR90); 124–184 GHz (EMIR150); 202–274 GHz (EMIR230) and 277–350 GHz (EMIR330) (all with both polarizations). IRAM also has 3 bolometers MAMBO1 and MAMBO2, and NIKA-2. It is also equipped with an heterodyne receiver called HERA working at a central frequency of 230 GHz.

The Atacama PathFinder EXperiment (APEX) telescope

At an altitude of ~ 5100 m above the sea level, the APEX telescope is located in the Chajnantor desert in Chile (see Figure 1.8). It has a diameter of 12 m and works mainly in the submillimeter regime from 0.2 to 1.5 mm. APEX is equipped with two bolometer cameras

Figure 1.7. The IRAM-30m telescope located in Granada, Spain.

(LABOCA and SABOCA). It is also equipped with a versatile heterodyne receiver called First Light APEX Submillimeter Heterodyne (FLASH), a dual-frequency receiver with a tuning range between 0.34–0.38 mm (780–880 GHz) and between 0.60–0.71 mm (420–500 GHz) and intermediate frequency bandwidths of 2 and 4 GHz, respectively.

Figure 1.8. The APEX 12m telescope.

The Heterodyne Instrument for Far Infrared (HIFI)

The Herschel Space Observatory was active from 2013 to 2019 and was built by the European Space Agency (ESA) (see Figure 1.9). This observatory contained a mirror of 3.5 m in diameter and several instruments working at wavelengths from 55 to 672 μm (from infrared to submillimeter). These instruments included two cameras/spectrometers (called PACS and SPIRE) and an heterodyne receiver called HIFI.
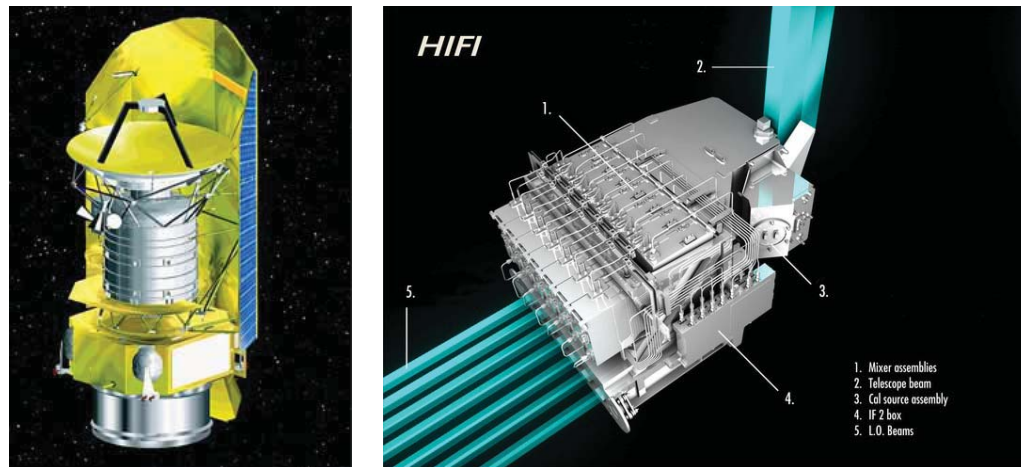
Figure 1.9. Left: A sketch of the Herschel Space Observatory. Right: The HIFI instrument.

The James Clerck Maxwell Telescope (JCMT)

The JCMT is a 15 m diameter radiotelescope located 4092 m above the sea level in Mauna Kea, Hawaii (see Figure 1.10) that works at submillimeter wavelengths (between 0.4 and 1.4 mm). It has both broadband continuum receivers and heterodyne detection spectral line receivers. The JCMT is equipped with the Submillimetre Common-User Bolometer Array (SCUBA) and SCUBA-2 bolometers that work at 450 and 850 μm. It is also equipped with three heterodyne receivers for spectral line observations. Finally, it also has the HARP heterodyne array receiver that works at 350 GHz and that can be used also with the ACSIS spectrometer.

1.2.4   Interferometers

Single-dish telescopes are particularly sensitive to detect extended sources in the sky, but, given their limited diameter, they have relatively low spatial resolution. However, since IRAS 16293–2422 is (at least) a binary source, high angular resolution observations are needed to study the properties of the individual compact components in this protostar. Interferometers are formed by a group or array of antennas that simulate a single-dish with a

Figure 1.10. The JCMT telescope at the center of the image.

diameter equivalent to the maximum distance between two elements of the array. The angular resolution obtained by an interferometer is given by

$$\theta = 1.22\frac{\lambda}{B}, \tag{1.14}$$

where B is la largest distance between two antennas in the interferometer (commonly called baseline). The basic equations used in interferometry are shown in the following subsection.

1.2.5 Basic equations of interferometry

Let us consider the simplest interferometer array with only two antennas as the one shown in Figure 1.11. The power received on each antenna is given by

$$P = I(\vec{s_0}, \nu)A(\vec{s_0}, \nu)d\nu d\Omega, \tag{1.15}$$

where $I(\vec{s_0}, \nu)$ is the intensity in the direction of $\vec{s_0}$, $A(\vec{s_0}, \nu)$ is the effective area of the antenna and Ω is the solid angle. The radiation (seen as a planar wavefront) coming from the source is first received by antenna 1, and then by antenna 2 with a delay in time. This delay is known as the geometric delay and is given by

$$\tau_g = \frac{\vec{B} \cdot \vec{s_0}}{c}, \tag{1.16}$$
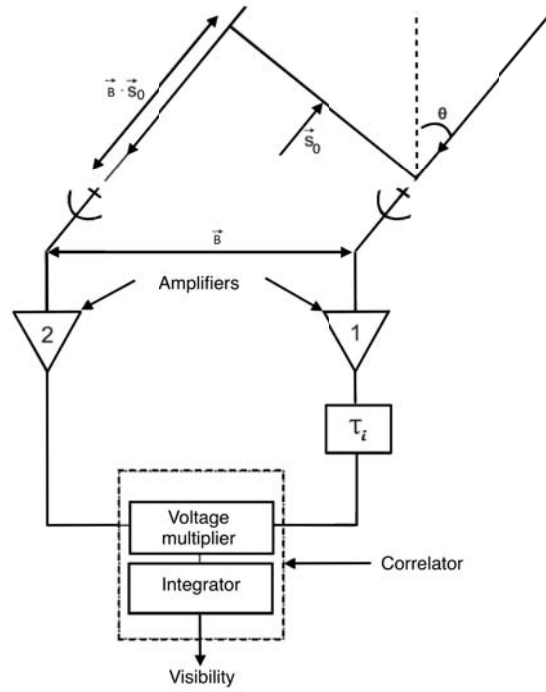
Figure 1.11. Sketch of a two elements interferometer.

where $\vec{B}$ is the vector of the baseline and c is the speed of light. Both antennas receive the signal coming from the source, generating a voltage detected by the instruments installed on them. These voltages are amplified and are given by

$$V'_1(t) = V_0 \cos[2\pi\nu t], \tag{1.17}$$
$$V'_2(t) = V_0 \cos[2\pi\nu(t - \tau_g)], \tag{1.18}$$

where V_0 is the amplitude of the voltage. After, the signal from one of the antennas is delayed electronically by $\pi/2$ to create a sinusoidal pattern. The voltages are then

$$V_1(t) = V_0 \exp[i\, 2\pi\nu t], \tag{1.19}$$
$$V_2(t) = V_0 \exp[i\, 2\pi\nu(t - \tau_g)]. \tag{1.20}$$

On the other hand, to compensate for the geometric delay on antenna 2, an instrumental delay is introduced in the signal received by antenna 1. The voltages will be

$$V_1(t) = V_0 \exp[i\, 2\pi\nu(t - \tau_i)], \tag{1.21}$$
$$V_2(t) = V_0 \exp[i\, 2\pi\nu(t - \tau_g)]. \tag{1.22}$$

Both signals are processed inside the correlator where they are multiplied and averaged in time, giving

$$V''(\tau_g, \tau_i) = I(\vec{s_0}, \nu)A(\vec{s_0}, \nu)\exp[i2\pi\nu(\tau_g - \tau_i)]d\nu d\Omega, \tag{1.23}$$

where V_0^2 has been replaced by the power $I(\vec{s_0}, \nu)$. This equation can be written as

$$V''(\vec{B}, \vec{s_0}, \tau_i) = I(\vec{s_0}, \nu)A(\vec{s_0}, \nu)\exp\left[i2\pi\nu\left(\frac{\vec{B} \cdot \vec{s_0}}{c} - \tau_i\right)\right]d\nu d\Omega. \tag{1.24}$$

For an arbitrary direction $\vec{s} = \vec{s_0} + d\vec{s}$ we have

$$V''(\vec{B}, \vec{s_0}, d\vec{s}, \tau_i) = I(\vec{s}, \nu)A(\vec{s}, \nu)\exp\left[i2\pi\nu\left(\frac{\vec{B} \cdot \vec{s_0}}{c} + \frac{\vec{B} \cdot d\vec{s}}{c} - \tau_i\right)\right]d\nu d\Omega. \tag{1.25}$$

The point in the source in the direction of $\vec{s_0}$ is called phase reference point of the map. It is useful to compensate for the geometric delay from the phase reference introducing the instrumental delay as

$$\tau_i = \vec{B} \cdot \frac{\vec{s_0}}{c} + \tau_i'. \tag{1.26}$$

Substituting we get

$$V''(\vec{B}, \vec{s_0}, d\vec{s}, \tau_i') = I(\vec{s}, \nu)A(\vec{s}, \nu)\exp\left[i2\pi\nu\left(\frac{\vec{B} \cdot d\vec{s}}{c} - \tau_i'\right)\right]d\nu d\Omega. \tag{1.27}$$

To obtain the contribution from the full source over the full bandwidth, we must integrate

$$V'(\vec{B}, \vec{s_0}, \tau_i') = \int_\Omega \int_{-\infty}^{\infty} I(\vec{s}, \nu)A(\vec{s}, \nu)\exp\left[i2\pi\nu\left(\frac{\vec{B} \cdot d\vec{s}}{c} - \tau_i'\right)\right]d\nu d\Omega. \tag{1.28}$$

By calculating the Fourier transform of V' with respect to τ_i' we obtain

$$V(\vec{B}, \vec{s_0}) = \int_\Omega I(\vec{s}, \nu)A(\vec{s}, \nu)\exp\left[i2\pi\nu\left(\frac{\vec{B} \cdot d\vec{s}}{c}\right)\right]d\Omega. \tag{1.29}$$

We can assume I and A to be constant over a small bandwidth $\Delta\nu$:

$$V(\vec{B}, \vec{s_0}) = \int_\Omega I(\vec{s})A(\vec{s})\exp\left[i2\pi\nu\left(\frac{\vec{B} \cdot d\vec{s}}{c}\right)\right]d\Omega. \tag{1.30}$$

$V(\vec{B}, \vec{s_0})$ is the complex visibility of the source with intensity $I(\vec{s})$. It is useful to define this quantity in terms of the plane of the projected baselines in the plane of the sky

$$d\vec{s} = (x, y). \tag{1.31}$$

We can write then

16

$$v_0 \vec{B} \cdot (x, y)/c = \left(\frac{v_0 B_x}{c}, \frac{v_0 B_y}{c} \right) \cdot (x, y). \tag{1.32}$$

In terms of wavelength we have

$$\left(\frac{B_x}{\lambda_0}, \frac{B_y}{\lambda_0} \right) \cdot (x, y) = (u, v) \cdot (x, y), \tag{1.33}$$

where (u, v) are the projections of the baselines over the coordinates (x, y). The visibility can be written then as

$$V(u, v) = \int_{-\infty}^{\infty} \int_{-\infty}^{\infty} I(x, y) A(x, y) \exp[i2\pi(ux + vy)] dx dy. \tag{1.34}$$

This is the basic equation in interferometry. When an inteferometer makes a measurement, it produces a visibility point in the (u, v) plane. As the source moves in the sky, the projection $\vec{B}$ changes and we measure visibilities at different (u, v) points. Also, if the number of antennas of the interferometers is larger, the number of measured visibilities will be larger as well. If we could fill the (u, v) plane, we could recover the intensity of the source by computing the Fourier transform of the visibilities as

$$A(x, y) I(x, y) = \int_{-\infty}^{\infty} \int_{-\infty}^{\infty} V(u, v) \exp[-i2\pi(ux + vy)] du dv. \tag{1.35}$$

Since $A(x, y)$ is known a priori, we can recover $I(x, y)$. These concepts are used by the ALMA, VLA and VLBA interferometers used in this thesis.

The Atacama Large Millimeter/submillimeter Array (ALMA)

ALMA is an interferometer located at the Llano de Chajnantor in Chile at an altitude of about 5000 m over the sea level (see Figure 1.12). ALMA has a total of 66 antennas. The main array contains 50 antennas of 12 m, having a total of 1225 baselines. The ALMA Compact Array (ACA) is a smaller array in ALMA containing 4 antennas of 12 m and 12 antennas of 7 m. Because interferometers filter extended emission, the ACA can recover part of the observed extended emission. The maximun baseline of ALMA is 16 km and is designed to work in a range of frequencies between 30–900 GHz.

The Very Large Array (VLA)

The VLA is an array composed by 27 antennas of 25 m each located in the plains of San Agustin near Socorro in New Mexico (see Figure 1.13). These antennas are placed on tracks that allow them to move and change the distance between them. The most extended configuration of the array has an extension of about 36 km. This instrument can reach angular resolutions up to 0.04″. The VLA works in the centimeter and millimeter range of the electromagnetic spectrum (from 1 to 50 GHz).

Figure 1.12. The ALMA interferometer.

Figure 1.13. The VLA interferometer.

The Very Large Baseline Array (VLBA)

Among the three interfometers used in this thesis, the VLBA has the longest baseline, which corresponds to a distance between the stations of 8611 km. This interferometer is composed by 10 antennas of 25 m diameter each distributed in the United States (see Figure 1.14) and forms the longest system in the world that uses very long baseline interferometry (VLBI). The VLBA can observe in a frequency range between 0.3–96 GHz (3 mm to 90 cm) and it can reach angular resolutions smaller than 0.2 mas.

As conclusion of this section, we must mention that single-dish telescopes do not reach angular resolutions as high as the interferometer do, but since they have filled apertures they can achieve higher sensitivities. Therefore, both single-dish and interferometric observations are needed to characterize IRAS 16293–2422 at several spatial scales from a multi-frequency
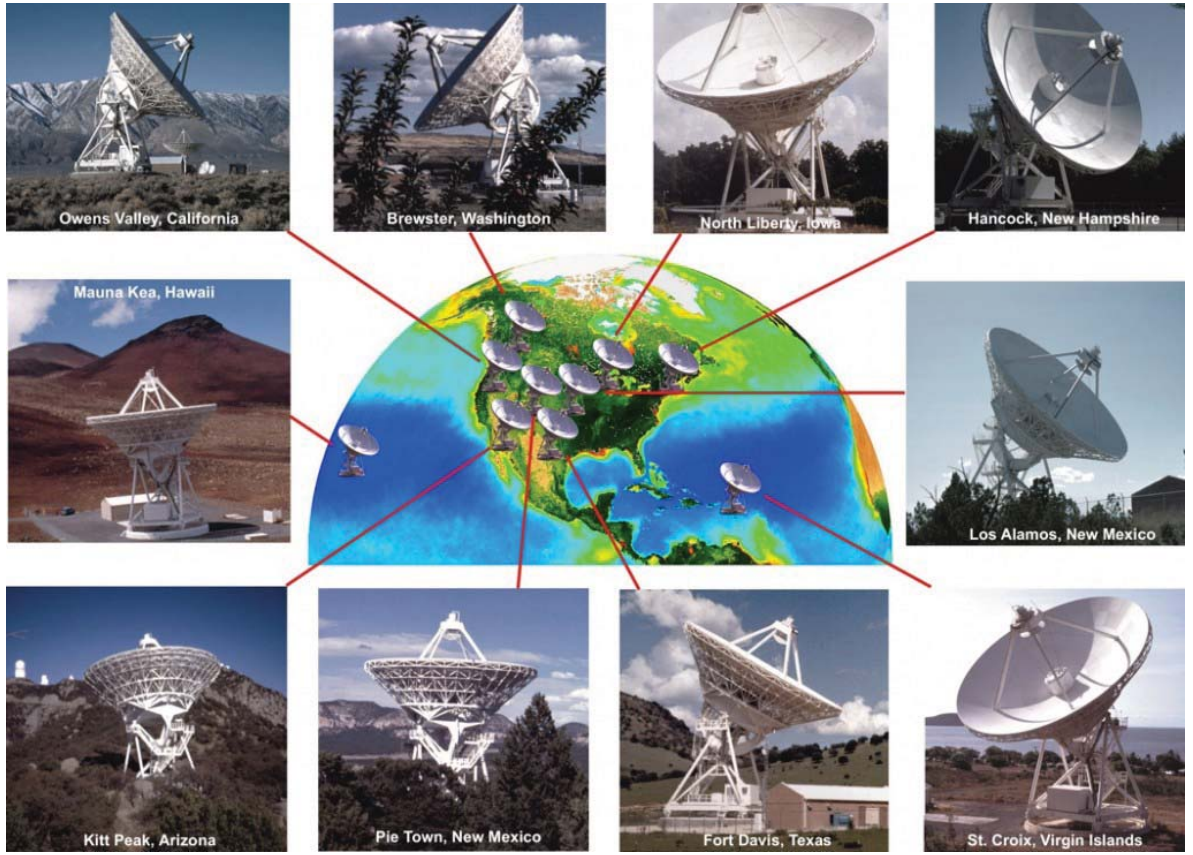
Figure 1.14. The VLBA interferometer. The location of each station in the array is indicated.

point of view.

1.3 Basic concepts of radiative transfer

Radiative transfer models provide us a useful formalism to describe how radiation is absorbed or emitted when it interacts with the interstellar medium. Because in this thesis we will make use of radiative transfer models extensively, I will introduce very briefly some of the basic concepts.

Let us consider an astronomical source emitting radiation with intensity I_ν which interacts with the interstellar medium between the source and the observer. The change in the intensity I_ν at a given frequency can be described by the radiative transfer equation

$$\frac{dI_\nu}{ds} = -\alpha_\nu I_\nu + j_\nu, \tag{1.36}$$

where ds indicate the thickness of the material (or cloud) along the line of sight and α_ν and j_ν are the absorption and emissivity coefficients respectively. Let us consider a gas containing atoms with discrete energy levels E_u and E_l, where u and l refers to the upper and lower

level, respectively. According to the quantum theory (Einstein), the excited state E_u can spontaneously return to the lower energy state E_l with a given probability A_{ul}. The absorption and emissivity coefficients can be written in terms of the Einstein coefficients as

$$\alpha_\nu = \frac{h\nu}{c}(n_l B_{lu} - n_u B_{ul})\Phi(\nu), \tag{1.37}$$

$$j_\nu = \frac{h\nu}{4\pi} n_u A_{ul}\Phi(\nu), \tag{1.38}$$

where n is the density of the state (such that $n_u A_{ul}$ is the number of spontaneous transitions per second in a unit volume), $\nu = (E_u - E_l)/h$, B is the coefficient of absorption and $\Phi(\nu)$ is a line profile function such that the absorption line is peaked and normalized:

$$\int_0^\infty \Phi(\nu)d\nu = 1. \tag{1.39}$$

If the intensity of the radiation field is I_ν, we can define an average intensity as

$$I = \int_0^\infty I_\nu \Phi(\nu)d\nu. \tag{1.40}$$

In the case of a system in stationary state, the number of absorbed and emitted photons must be equal:

$$n_u A_{ul} + n_u B_{ul}U = n_l B_{lu}U. \tag{1.41}$$

where U is the average energy density of the radiation field such that

$$U = \frac{4\pi I}{c}. \tag{1.42}$$

We can divide equation 1.36 by α_ν to write

$$\frac{dI_\nu}{d\tau_\nu} = S_\nu - I_\nu, \tag{1.43}$$

where $d\tau_\nu = \alpha_\nu ds$ is the opacity and $S_\nu = \frac{j_\nu}{\alpha_\nu}$ is the source function. If we consider blackbody thermodynamic radiation, this is, radiation emitted by matter under thermal equilibrium, we have from the Kirchhoff law that

$$S_\nu = B_\nu, \tag{1.44}$$

where B_ν is the Planck function. Therefore, we will have blackbody radiation when $I_\nu = B_\nu$ and thermal radiation when $S_\nu = B_\nu$. In other words, thermal emission becomes blackbody radiation in the case of an optically thick medium ($\tau \gg 1$). Solving equation 1.43 we have

$$\frac{dI_\nu}{d\tau_\nu} = S_\nu - I_\nu, \tag{1.45}$$

$$\frac{dI_\nu}{d\tau_\nu}e^\tau + I_\nu e^\tau = S_\nu e^\tau, \tag{1.46}$$

$$\frac{d}{d\tau_\nu}(I_\nu e^\tau) = S_\nu e^\tau. \tag{1.47}$$

Integrating we obtain

$$\int_0^{\tau_\nu} \frac{d}{d\tau_\nu}(I_\nu e^\tau)d\tau_\nu = \int_0^{\tau_\nu} S_\nu e^\tau d\tau_\nu. \tag{1.48}$$

In the source function is constant we have

$$I_\nu = S_\nu + e^{-\tau_\nu}(I_{\nu_0} - S_\nu), \tag{1.49}$$

or

$$I_\nu = S_\nu + e^{-\tau_\nu}(I_\nu(CMB) - S_\nu), \tag{1.50}$$

where I_{ν_0} represents the cosmic microwave background (CMB) at 2.73 K. The emitted intensity is coupled with the CMB. To compare the observed intensity with the original intensity of the emitting source in the absence of ISM ($I_\nu(0)$) we get

$$I_{\nu\text{obs}}(s) = I_\nu(s) - I_\nu(0) = (S_\nu(T) - I_\nu(0))(1 - e^{-\tau_\nu}). \tag{1.51}$$

Here we assume that the source function does not vary as function of the opacity. The source function can be written as

$$S_\nu(T) = \frac{2h\nu^3}{c^2}\frac{1}{e^{h\nu/kT} - 1}. \tag{1.52}$$

The population level can be described by a excitation temperature T_{ex} such that

$$\frac{n_u}{n_l} = \frac{g_u}{g_l}e^{-\frac{h\nu}{kT_{ex}}}. \tag{1.53}$$

In other words

$$S_\nu(T) = \frac{A_{ul}c}{4\pi}\frac{1}{\frac{g_l}{g_u}e^{E_{ul}/kT_{ex}}B_{lu} - B_{ul}}. \tag{1.54}$$

In local thermodynamical equilibrium (LTE) we have

$$S_\nu(T) = \frac{2h\nu^3}{c^2}\frac{1}{e^{h\nu/kT} - 1}, \tag{1.55}$$

$$I_\nu(T) = \frac{2h\nu^3}{c^2}\frac{1}{e^{h\nu/2.73k} - 1}. \tag{1.56}$$

The intensity of radiation at frequency ν observed by a telescope is given by

$$I_{obs} = (I(T_{ex}) - I(T_{CMB}))(1 - e^{-\tau}), \tag{1.57}$$

where T_{ex} is the excitation temperature of the cloud and T_{CMB} is the cosmic microwave background at 2.73 K. In radioastronomy it is useful to define the brightness temperature. This is obtained when considering the Rayleigh-Jeans approximation in which $h\nu/kT \ll 1$, then

$$I_\nu = 2kT/\lambda^2 \tag{1.58}$$

or

$$T_b = I_\nu c^2/2k\nu^2. \tag{1.59}$$

From equation 1.57, the brightness temperature can be written as

$$T_b = \frac{h\nu}{k}\left(\frac{1}{e^{\frac{h\nu}{kT_{ex}}}} - \frac{1}{e^{\frac{h\nu}{k(2.73)}}}\right)(1 - e^{-\tau}). \tag{1.60}$$

In the case where a background continuum source (T_{dust}, τ_{dust}) is coupled to the molecular atomic cloud (T_{ex}, τ) along the line of sight, the brightness temperature in an off-on observation is given by

$$T_b = J_\nu(CMB)e^{-\tau_{dust}}e^{-\tau} + \Omega_{dust}J_\nu(T_{dust})(1 - e^{-\tau_{dust}})e^{-\tau} + \Omega J_\nu(T_{ex})(1 - e^{-\tau}) - J_\nu(CMB), \tag{1.61}$$

where $J_\nu = (h\nu/k)/(1 - e^{h\nu/kT})$ and Ω is the dilution factor. In the case of $\tau_{dust} = 0$ and $\Omega = 1$:

$$T_b = J_\nu(T_{ex}) - J_\nu(CMB))(1 - e^{-\tau}). \tag{1.62}$$

In the particular case where $\Omega = \Omega_{dust} = 1$ we have

$$T_b = J_\nu(CMB)e^{-\tau_{dust}}e^{-\tau} + J_\nu(T_{dust})(1 - e^{-\tau_{dust}})e^{-\tau} + J_\nu(T_{ex})(1 - e^{-\tau}) - J_\nu(CMB). \tag{1.63}$$

Towards the continuum source, the continuum in on-off observation is defined by

$$T_C = J_\nu(CMB)e^{-\tau_{dust}} + J_\nu(T_{dust})(1 - e^{-\tau_{dust}}) - J_\nu(CMB). \tag{1.64}$$

Finally, combining 1.63 and 1.64

$$T_b = T_C e^{-\tau} + (1 - e^{-\tau})(J_\nu(T_{ex}) - J_\nu(CMB)). \tag{1.65}$$

The line opacity (with a gaussian shape) can be expressed in function of the column density of the lower state N_u as

$$\tau_0 = \frac{c^2 A_{ul} N_u}{8\pi\nu^2 \Delta\nu \sqrt{\pi}/2 \sqrt{\ln 2}}(e^{h\nu/kT_{ex}} - 1). \tag{1.66}$$

1.3.1 Radiative transfer out of LTE

There are some cases where LTE conditions are not satisfied. In this more general case, a non-LTE analysis can be implemented. Let us consider a transition level i that goes to a transition j caused by the process k. The change of number density of the state i is given by

$$\frac{dn_i}{dt} = -n_i \sum_j \sum_k P_{ij}^k + \sum_j n_j \sum_k P_{ji}^k, \tag{1.67}$$

where P_{ij}^k is the transition probability for the transition from i to j caused by the process k. In a stationary case, we have $\frac{dn_i}{dt} = 0$. If we consider only a system with two levels we have

$$n_u(A_{ul} + B_{ul}U + C_{ul}) = n_l(B_{lu}U + C_{lu}), \tag{1.68}$$

where the U is the average radiation field intensity and C_{ij} are the collision rates per second per molecule of the species of interest (which depend on the temperature). These collisional coefficients depend on the density of the collision partner $n_{collision}$ (such as H_2, He, etc.) given by

$$C_{ij} = n_{collision} \times \gamma_{ij}, \tag{1.69}$$

where γ_{ij} is the velocity integrated collision cross section in cm^3 s^{-1}. In the case where the collisions dominate ($C_{ul} \gg A_{ul}$) we have

$$\frac{C_{lu}}{C_{ul}} = \frac{n_u}{n_l} = \frac{g_u}{g_l} e^{-h\nu/kT_k} \tag{1.70}$$

where T_k is the kinetic temperature. By combining the equations we can write

$$\frac{n_u g_l}{n_l g_u} = e^{-h\nu/kT_{ex}} = \frac{A_{ul} + C_{ul}e^{-h\nu/kT_k}(e^{h\nu/kT_{bg}} - 1)}{A_{ul}e^{h\nu/kT_{bg}} + C_{ul}(e^{h\nu/kT_{bg}} - 1)}. \tag{1.71}$$

Neglecting the T_{bg} such that $h\nu \gg kT_{bg}$ we have

$$T_{ex} = \frac{h\nu/k}{h\nu/kT_k + ln(1 + A_{ul}/C_{ul})}. \tag{1.72}$$

In the case of LTE, all excitation temperatures are the same. For non-LTE excitation, a different excitation temperature may characterize the population of each level relative to any other level.

In the next section we present one of the most used methods use to solve the radiative transfer under non-LTE conditions.

1.3.2 The large velocity gradient method

This method was first introduced by Sobolev (1960) and is one of the most widely used radiative transfer methods. The large velocity gradient (LVG) approximation considers the transport of a photon when the lines are optically thick. Let us consider the probability that

a photon emitted in a transition at a radius r will escape from a cloud. Assuming that these photons only interact with the closest molecules where they are produced, the local mean radiation can be written as

$$J_\nu^{loc} = (1 - \beta(\tau))S_\nu + \beta(\tau)J_\nu(T_{bg}) \qquad (1.73)$$

where $\beta(\tau)$ correspond to the probability that a photon produced at the optical depth τ can escape and S is the source function and depends on the molecular level population

$$S_\nu = \frac{A_{ul}}{B_{ul}} \frac{1}{\frac{n_l g_u}{n_u g_l} - 1}. \qquad (1.74)$$

If $\beta(\tau) = 0$, J_ν^{loc} becomes the blackbody radiation field intensity (LTE case). This method is valid if the conditions of the gas does not change over the Sobolev length defined as

$$L_S = \frac{v_{th}}{dv/dr}, \qquad (1.75)$$

where v_{th} is the thermal broadening and dv/dr is the velocity gradient. The $\beta(\tau)$ factor can be written as a function of the opacity as

$$\beta(\tau) = \frac{1 - e^{-\tau}}{\tau}, \qquad (1.76)$$

for a radially expanding sphere. If the geometry is replaced by an homogeneous slab we have

$$\beta(\tau) = \frac{1 - e^{-3\tau}}{3\tau}. \qquad (1.77)$$

From equation 1.67, a two level state system, the statistical equilibrium equations can be written as

$$\frac{dn_1}{dt} = -n_1 C_{12} + n_2 C_{21} + \beta(\tau)n_2 A_{21}, \qquad (1.78)$$

$$\frac{dn_2}{dt} = +n_1 C_{12} - n_2 C_{21} - \beta(\tau)n_2 A_{21}. \qquad (1.79)$$

The excitation temperature can be written as

$$T_{ex} = \frac{h\nu/k}{h\nu/kT_k + ln(1 + A_{ul}\beta(\tau)/C_{ul})}. \qquad (1.80)$$

1.3.3 CASSIS

In this thesis, we have used CASSIS (Centre d'Analyse Scientifique de Spectres Instrumentaux et Synthétiques, Vastel et al. 2015), a software developed at IRAP (Institut de Recherche en Astrophysique et Planétologie, Toulouse, France) and designed to handle molecular line spectra. This software contains the following functionalities:

- Line identification tool. CASSIS has a spectroscopic database (presently CDMS (The Cologne Database for Molecular Spectroscopy) + JPL (Jet Propulsion Laboratory) + NIST (National Institute of Standards and Technology)) + some molecules for which an ortho-para and A-E separation has been made, and that can be regularly updated.

- Prediction of spectra. Radiative transfer models in LTE and non-LTE are used to compute the spectra. CASSIS uses RADEX (van der Tak et al. 2007), a one-dimensional non-LTE radiative transfer code that uses the escape probability formulation. RADEX is comparable to the LVG method described above and allow us to put constraints on physical conditions such as density and temperature based on the analysis observational data.

- Comparison between radiative transfer models and observations. This can be done directly in CASSIS when the radiative transfer model has been computed and the resulting synthetic spectrum is compared directly with the observed one.

- Rotational diagrams. CASSIS can also implement the rotational diagram method to compute the rotational temperature and column density a a given molecule from the analysis of a spectrum.

For more details on the capabilities of this software, we refer to the reader to the CASSIS[1] webpage.

The analysis of the molecular lines present in IRAS 16293–2422 and the modelling (both LTE and non-LTE) of its spectra as seen by several telescopes has been made in this work made with CASSIS-RADEX.

1.3.4   LIME

LIME (Line Modelling Engine, Brinch and Hogerheijde 2010) is a 3D non-LTE radiative transfer code based in the 1D radiative transfer RATRAN (Hogerheijde and van der Tak 2000), a non-LTE radiative transfer code. RATRAN takes the point of view of cells to account for local and external contributions of the radiation field. Indeed, the incoming rays into the cell are traced back to the origin at the edge of the cloud and are used to compute the radiation field. RATRAN uses the Monte Carlo method to randomly chose the origin of the photons from the edge of the model and uses a method called Accelerated Lambda Iteration (ALI) which allows to separate efficiently the local and global radiation contribution. Once the population level densities are computed, the distribution of emission for transitions are calculated with a method called ray-tracing. Although LIME derives from RATRAN and they share part of the code and solution method, they use a different photon propagation method.

---

[1]http://cassis.irap.omp.eu/

1.3.5 GASS

GASS (Generator of Astrophysical Sources Structures, Quénard et al. 2017) is an interface developed to define the physical structure of a star-forming region such as spherical sources, disks and outflows. Indeed, these structures can be mixed to have a region adapted to the needs of the user. GASS creates input models for radiative transfer models. In particular, we have used GASS combined with LIME to model the 3D structure of source B in IRAS 16293–2422 and compare the resulting continuum images with the maps those obtained with the VLA (see Chapter 4).

1.4 A full overview of IRAS 16293–2422

The Lynds 1689 N dark cloud within the Ophiuchus cloud complex harbours the low-mass Solar type protostar IRAS 16293-2422, one of the best studied Class 0 objects in the literature (see Figure 1.15). IRAS 16293–2422 was identified for the first time by the Infrared Astronomical Satellite (IRAS) (Lada and Wilking 1984) and was first catalogued as a Class 0 protostar by André et al. (1993).
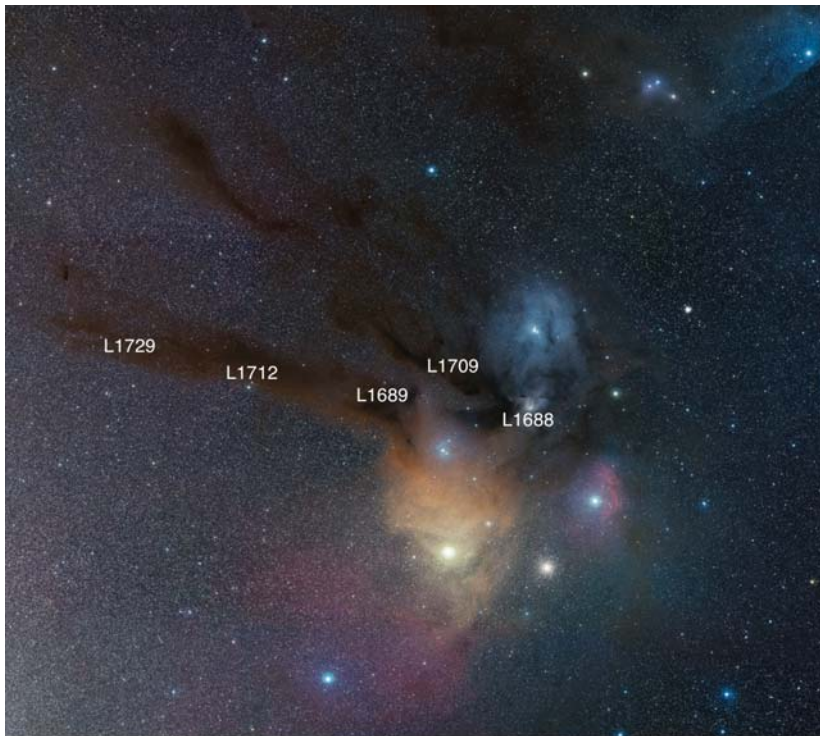
Figure 1.15. Optical image of the Ophiuchus cloud complex. The group of stars to the northern part of the blue reflection nebula are the quadruple star system ρ Oph from which the cloud derives its name. Labeled are the main dark clouds and streamer trails in Ophiuchus. IRAS 16293–2422 is located in the L 1689 N dark cloud.

IRAS 16293–2422 drew early attention because its energy spectral distribution (SED) revealed that it was the coldest protostar known (André and Montmerle 1994). IRAS 16293–2422 is undetectable at wavelengths shorter than 10 μm and has a luminosity $L = 21 \pm 5$ $L_\odot$ (Jørgensen et al. 2016). The first studies on this source were focused in distinguishing whether the circumstellar material was dominated by infall toward the protostar or by rotation in a disk-like structure. Indeed, evidence for large-scale infall was found from single-dish observations (e.g. Walker et al. 1986; Narayanan et al. 1998; Ceccarelli et al. 2000).

Interferometric centimeter (cm) and millimeter (mm) observations made with the VLA and OVRO (Owens Valley Radio Observatory Millimeter Wavelength Interferometer) revealed that IRAS 16293–2422 is composed by two compact sources called A and B (Wootten 1989; Mundy et al. 1992) separated by $\sim5\rlap{.}''5$. Source A itself was found to split into two subcomponents at cm wavelengths, called A1 and A2 and separated by $0\rlap{.}''3$ (Wootten 1989). Chandler et al. (2005) detected two other sources from submillimeter observations called Aa and Ab. The source Aa is located between A1 and A2, while Ab is located about $0\rlap{.}''64$ to the NE of the A1/A2 pair (see Figure 1.16).
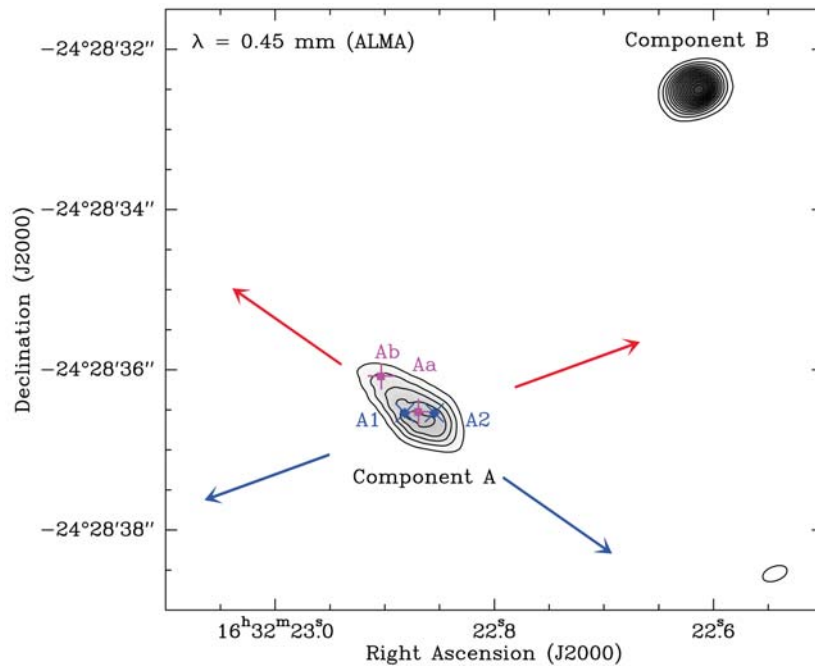
Figure 1.16. ALMA submillimeter continuum image of IRAS 16293–2422 . The two main components A and B are labelled, including the subcomponents A1 and A2 associated with source A and the submillimeter peaks Aa and Ab. The arrows indicate the direction of the two outflows driven from source A identified from Mizuno et al. (1990). Figure taken from Loinard et al. (2013).

Chandler et al. (2005) argued that the nature of these sources Aa and Ab might be protostellar, leading source A to be at least a triple system. However, since source A seems to be elongated at mm wavelengths, Aa and Ab might not necessarily be discrete objects. On the

other hand, the lack of a counterpart at 7 cm from VLA observations (Loinard et al. 2007) suggest that these sources could be starless clumps.

1.4.1   The structure of IRAS 16293–2422 at large scale

Large scale continuum maps have shown that IRAS 16293–2422 is close to a pre-stellar core called IRAS16293E at an angular distance of 1.′5 to the east (e.g. Stark et al. 2004; see Figure 1.17).
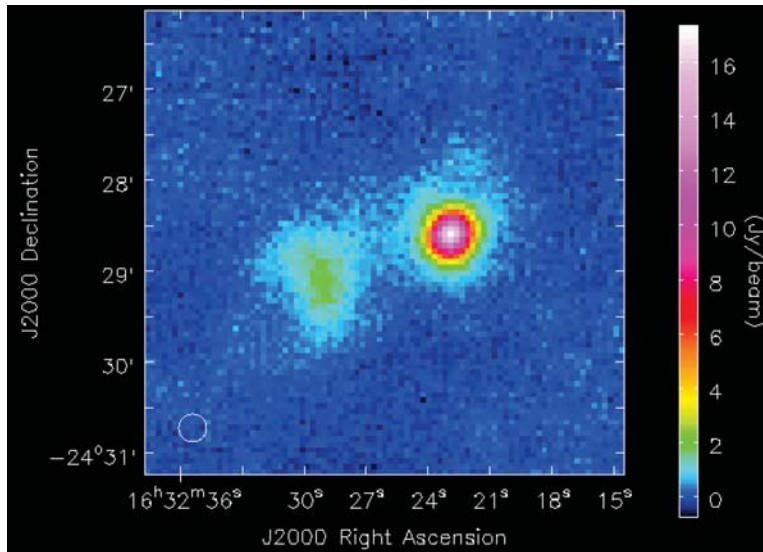
Figure 1.17. Image of IRAS 16293–2422 at 345 GHz obtained with the LABOCA camera on the APEX telescope. The weak extension toward the east traces a pre-stellar core called IRAS 16293E. Figure taken from Siringo et al. (2009).

The Figure 1.18 represents a large scale sketch of IRAS 16293–2422, including its extended envelope, the hot core comprising sources A and B and the position of the pre-stellar core IRAS 16293E. Several studies have shown outflow activity in IRAS 16293–2422 (see next section) and apparently one of the outflows could be interacting with the prestellar core as indicated in the sketch.

Several studies have been performed on IRAS 16293–2422 to reconstruct its physical structure from both interferometric and single-dish observations. Ceccarelli et al. (2000) used water and oxygen molecular transitions observed with the Infrared Space observatory (ISO) to derive the gas and dust density and temperature profiles. Also, Schöier et al. (2002) used dust continuum observations to constrain the physical structure. These studies concluded that the envelope of IRAS 16293–2422 has a density distribution which is in agreement with the inside-out collapse picture (Shu 1977). They also concluded that there was a region of about 300 AU diameter where the dust mantles sublimate. Later, Schöier et al. (2004) and Jørgensen et al. (2005) from OVRO and Spitzer observations respectively, deduced the presence of a cavity of 800 to 1200 AU in the envelope. However, from single-dish and
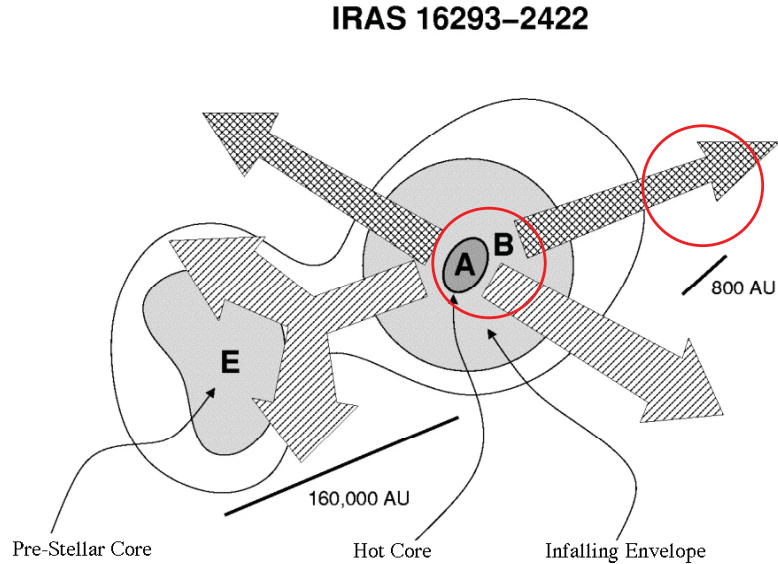
IRAS 16293–2422

Figure 1.18. Sketch of IRAS 16293–2422 at large scale. The prestellar core IRAS16293E is at 1′5 to the east. The sources A and B and the direction of observed outflows in IRAS 16293-2422 are indicated. Figure taken from Stark et al. (2004).

interferometric observations Crimier et al. (2010) obtained the radial density and temperature profiles from about 20 to ∼ 6000 AU without the necessity of having such cavity. Crimier et al. (2010) concluded that the envelope follows a density power law of $r^{-3/2}$ at radius smaller than 1300 AU, while it follows a r^{-2} power law at larger radii, consistent with a Shu-like density distribution. For this envelope they also obtained a mass of 2 $M_\odot$ and a luminosity of 22 $L_\odot$ (assuming a distance of 120 pc). In their model, the grain mantles are predicted to sublimate at a distance of 75 AU, where the density is 2×10^8 cm^{-3}. The border of the envelope has a dust temperature of about 13 K and a density of about 10^5 cm^{-3}. More recently Jacobsen et al. (2018) modelled the 3D structure of IRAS 16293–2422 from ALMA observations of dust continuum and CO isotopologues considering an envelope of ∼ 8000 AU radius, two disk around the protostars and a dust filament between the protostars. Such dust filament bridge between A and B sources has been recently observed with ALMA by Jørgensen et al. (2016) (see Figure 1.19).

1.4.2   Outflow activity in IRAS 16293–2422

The presence of molecular outflows is recognized as a clear evidence of early star-formation processes. IRAS 16293–2422 is known to drive a multi-lobe outflow system (Walker et al. 1988; Mizuno et al. 1990). Source A was confirmed to power two outflows at scales of ∼ 0.1 pc in the E-W (P.A. = 110°) and NE-SW (P.A. = 60°) directions (e.g. Castets et al. 2001; Hirano et al. 2001). The E-W outflow was confirmed to arise from source A from SMA observations of CO (3–2) and CO (2–1) transitions by Yeh et al. (2008), although due to the
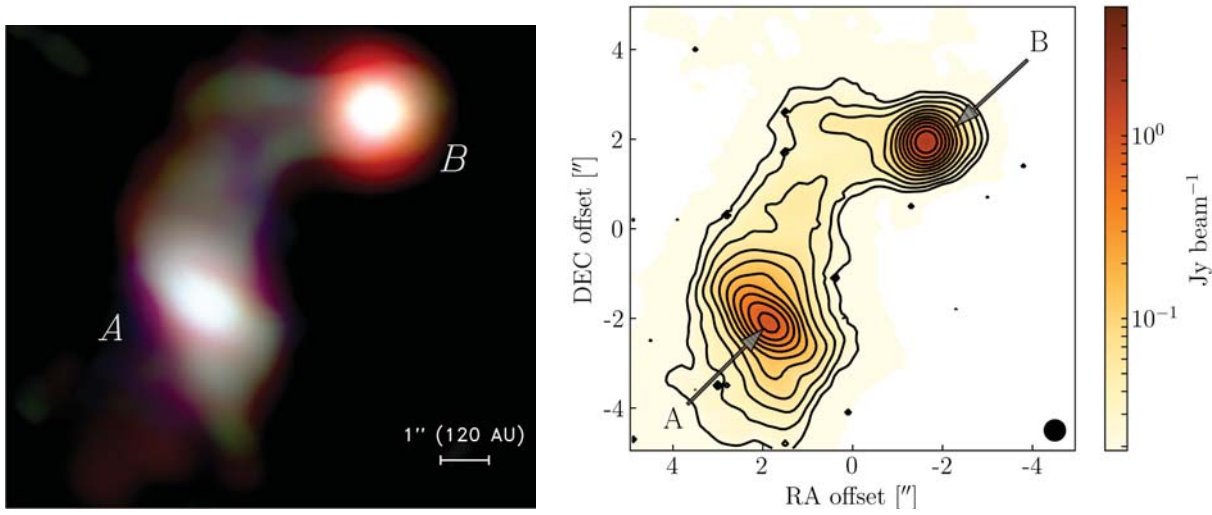
Figure 1.19. Left panel: ALMA three color image of the continuum at 3, 1.3 and 0.87 mm (Jørgensen et al. 2016). Right panel: Dust continuum at 868 μm in log-scale. Figure taken from Jacobsen et al. 2018.

low spatial resolution they could not distinguish which source within A drives this outflow. On the other hand, the outflow in the NE-SW direction was confirmed to originate from source A2 (Loinard et al. 2007; Pech et al. 2010).

Very strong blue-shifted CO emission to the south of source B was reported by Yeh et al. (2008) and Rao et al. (2009) from SMA observations. There is some debate, however, about whether this outflow is part of a compact outflow from source B or an extension from a third outflow driven by source A in the NW-SE direction (P.A. $\sim$ 145°). Loinard et al. (2013) reported that a monopolar blue shifted bubble-like outflow was arising from source B based on CO (6–5) ALMA observations. They argued that the short dynamical time scale ($\sim$ 200 yr), low velocity and moderate collimation of this outflow supported the idea that source B is the youngest protostar of the system. Later, Girart et al. (2014) performed observations of the CO (3–2) and SiO (7–6) transitions and found that while the two outflows associated with source A showed moderate velocities, the third and more compact outflow from A pointed toward source B. This led Girart et al. (2014) to suggest that the monopolar outflow reported by Loinard et al. (2013) was in fact part of this outflow (see Figure 1.20). They also found that the SiO emission presented a jet-like morphology in the redshifted southern part of this outflow, while it traced a well-defined arc on the border of source B in the blueshifted northern lobe. This was interpreted as an impact of the NW-SE outflow arising from source A on source B.

1.4.3   Recent ejection activity in IRAS 16293–2422A and its binarity

IRAS 16293–2422 presents intense molecular outflow activity. This phenomenon appears to be especially important in source A. Very recent cm observations revealed that IRAS 16293–
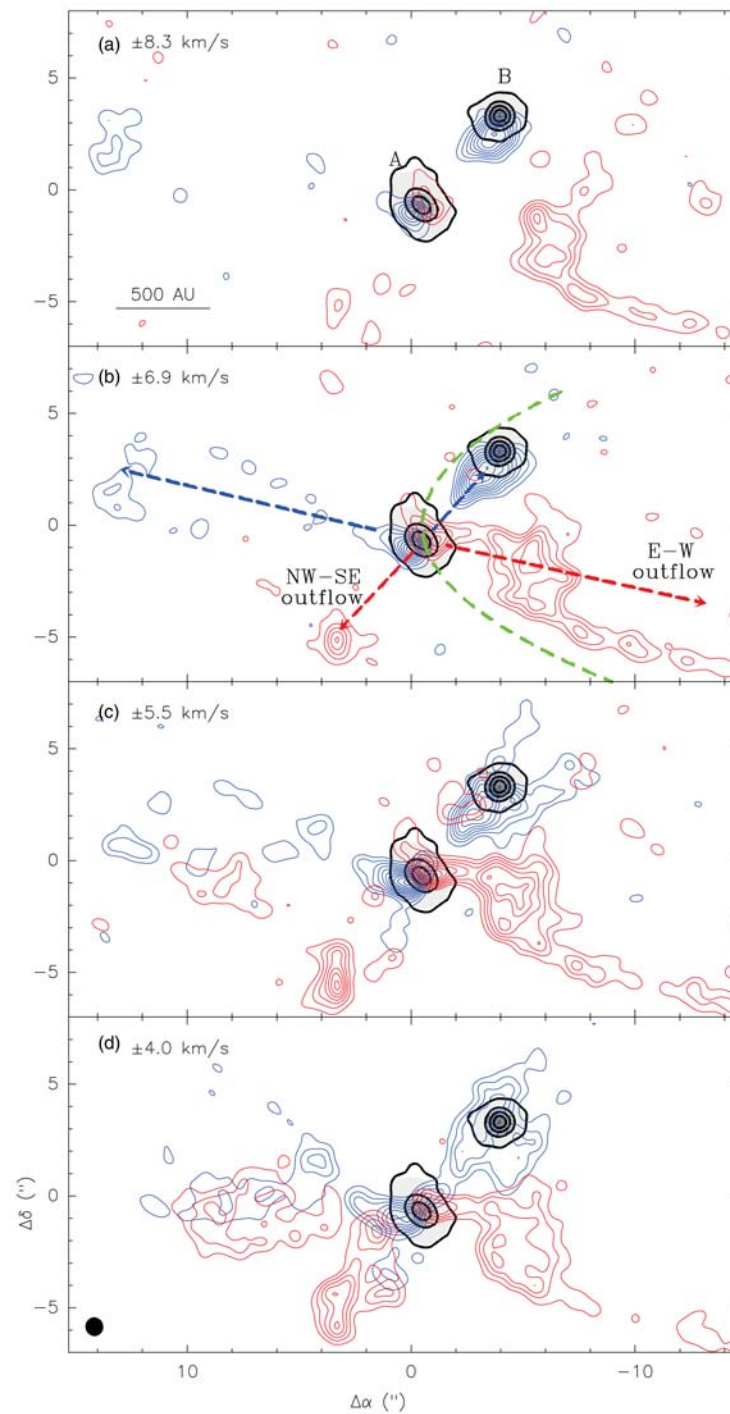
Figure 1.20. SMA channel maps of the CO (3–2) transition for the blueshifted (blue contours) and redshifted emission (red contours) overlaid with the 878 μm dust continuum (black contours). The green dashed line shows a cavity traced by the E-W lobes at scales of ~ 3000 AU found by Yeh et al. (2008). Figure taken from Girart et al. (2014).

2422 splits into more sources than the usual A1, A2 and B (Loinard et al. 2007). In fact, these observations revealed that A2 splits in two sub-condensations called A2α and A2β (see Figure 1.21). These sources trace a recent bipolar ejection from A2, moving roughly symmetrically away from this source at a projected velocity of $30 - 80$ km s^{-1}. This ejection corresponds to the first detection of the birth of a Herbig-Haro (HH) pair. Assuming that the emission from these ejecta is optically thin free-free emission, Pech et al. (2010) estimated the mass of each ejecta to be about $10^{-8} M_\odot$.
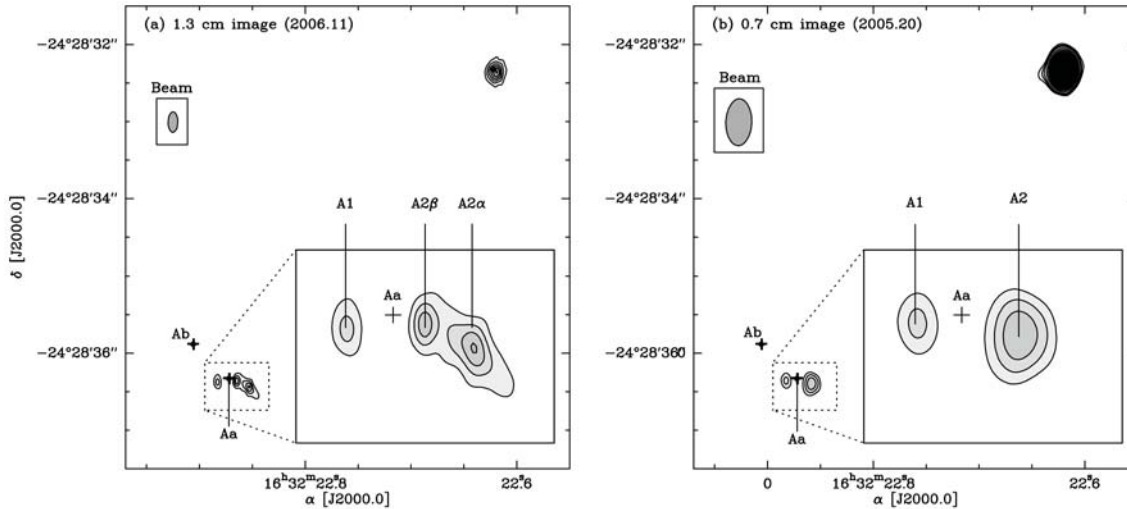
Figure 1.21. (a) 1.3 cm continuum image of IRAS 16293–2422 obtained in 2006.11. The first contour is 0.2 mJy beam^{-1}. (b) 0.7 cm continuum image obtained in 2005.20. The first contour is 1.5 mJy beam^{-1}. The contour step is 0.3 mJy beam^{-1} for the two maps. In both figures, the submillimeter sources Aa and Ab are indicated. The component A is triple in the 1.3 cm image, while it remains double in the 0.7 cm map. Taken from Loinard et al. (2007).

A new ejecta from A2 called A2δ was observed by Loinard et al. (2013) at 4 cm and 0.7 cm (see Figure 1.22) and they noted that this new radio source together with A2, A2α, A2β are very well aligned, although the P.A. ($\sim 70°$) is somewhat larger than the P.A. ($\sim 55°$) of the large-scale outflow known to originate from A2. This would suggest that the jet driven by A2 is precessing as consequence of the A1-A2 binarity.

The position angle (P.A.) between A1 and A2 has been found to increase roughly linearly from 45° in the late 1980s to about 80° in 2003-2005 (Loinard 2002; Chandler et al. 2005). During the same time span, the separation between these sources remained roughly constant ($\sim 0\rlap{.}''34$). Two scenarios have been proposed to explain this fact. The first one considers that A1 and A2 form a tight binary protostellar system in an almost face-on, nearly circular Keplerian orbit. Following the P.A. between A1 and A2 up to 2007, Pech et al. (2010) fitted this value and obtained a change with time of 1.98° yr^{-1}, corresponding to an orbital period of 182 yr. In addition, they estimated a total mass of 1.5 $M_\odot$ for A2 and 0.5 $M_\odot$ for A1. The second scenario interprets the source A1 as a shock feature resulting from the impact of a precessing jet driven by an undetected third protostar. In the first case, the P.A. should always
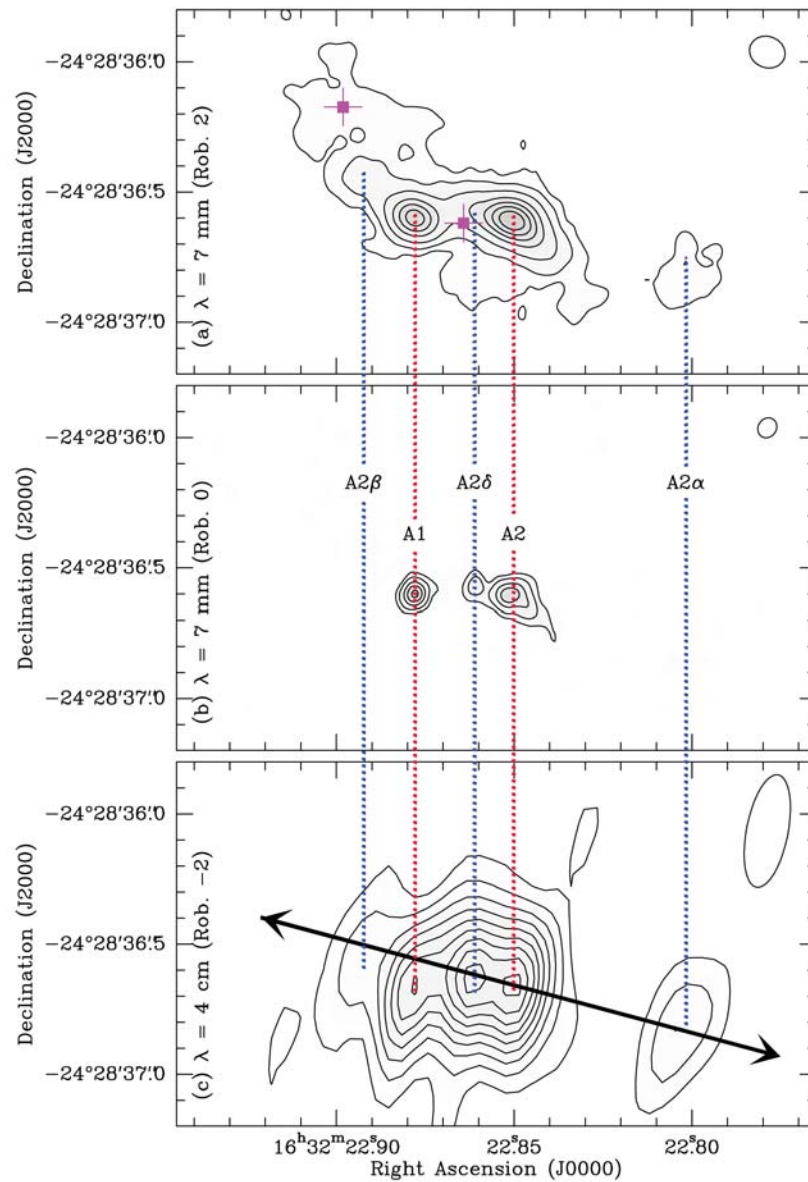
Figure 1.22. VLA continuum images of IRAS 16293–2422. On the left of each panel the observed wavelength and robust parameter associated with the weighting used in the reconstruction of the image is shown. The magenta square shows the position of the Aa and Ab sources. The position of A, B, A2α, A2β and the new ejecta A2δ is presented. The double arrow in the c) panel indicates the direction at a P.A. of ~ 70° along which the ejecta were launched. Figure taken from Loinard et al. (2013).

increase indefinitely, while in the second case it should decelerate since the jet must oscillate around an equilibrium position.

All the new detected ejections from source A might indicate that it could be entering a period of enhanced outflow activity.

1.4.4 The kinematic structure of IRAS 16293–2422A

The formation and evolution of circumstellar disks around low-mass protostars is of particular relevance. High angular observations of certain molecular species could provide us with information on the kinematics at small scales. Since IRAS 16293–2422 is a very good candidate to observe such structures, recent works have focused in the study of disks in this source. Favre et al. (2014) made observations with the SMA of the $C^{17}O$ (3–2) and $C^{34}S$ (7–6) transitions toward source A and found a velocity gradient along the NE-SW direction, which is consistent with the presence of a rotating structure at scales of 50–400 AU. However, a Keplerian rotation can be explained only if the enclosed envelope mass at the radii where the observed lines are excited is considered.

Girart et al. (2014) observed also the $C^{34}S$ (7–6) transition tracing the circumstellar gas around source A elongated in the NW-SW direction (P.A. ∼ 41°) (see Figure 1.23). They obtained a radius from the fit of about 140 AU and a mass of $M = 2.3 \pm 0.1\ M_\odot$ assuming Keplerian rotation.
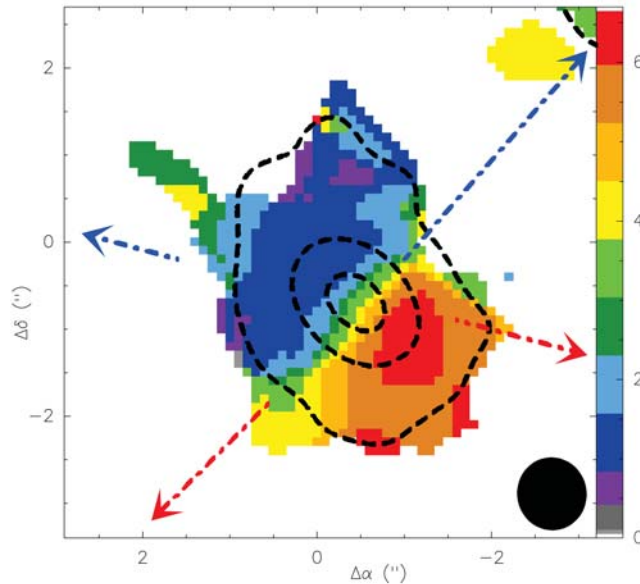
Figure 1.23. Moment 1 map (velocity field) of the $C^{34}S$ (7–6) transition observed with the SMA towards source A. The color bar at the right indicate the scale in km s^{-1}. The black dashed contours show the continuum emission at 878 μm, while the red and blue dashed arrows indicate the direction of the outflows. The synthesized beam is located at the bottom right. Figure taken from Girart et al. (2014).

The properties from ALMA observations suggest that the submillimeter continuum in source A is dominated by the circumbinary envelope rather than the individual disks around the protostars (Loinard et al. 2013).

More recently, Jacobsen et al. (2018) presented a 3D radiative transfer model of IRAS 16293-2422 using CO isotopologues and continuum emission from ALMA. They used a protoplanetary disk model for source A and found that they cannot constrain the density

structure since both inclined disk and edge-on disk configurations matched the continuum emission.

1.4.5 IRAS 16293–2422B

In contrast with source A, source B shows no clear complex substructure at all when observed with the highest angular resolutions available ($0\rlap{.}''05$), although Rodríguez et al. (2005) reported the presence of a marginal spiral-like structure from VLA continuum observations at 7 mm. It is not yet clear if it does have molecular outflows activity (e.g. see Loinard et al. 2013; Girart et al. 2014). Overall, the nature of this source remains elusive until now. Several evolutionary states have been proposed to explain the observational properties of source B. For instance, Stark et al. (2004) suggested that source B could be a T Tauri star based on the lack of molecular outflows. However, Chandler et al. (2005) inferred infall motions in source B from SMA observations at 300 GHz. Also, Pineda et al. (2012) detected inverse P-Cygni profiles in three molecular lines (CH_3OCHO-A, CH_3OCHO-E and H_2CCO) with ALMA and derived an infall rate of $4.5 \times 10^{-5} M_\odot$ yr^{-1} which is a typical value for low-mass protostars. Its spectral index from centimeter to millimeter observations is between 2 and 2.5, indicating that dust continuum dominates its emission (Chandler et al. 2005). Zapata et al. (2013) presented maps of $H^{13}CN$, $HC^{15}N$ and CH_3OH made with ALMA at 690 GHz and reported a small velocity gradient in the E-W direction, suggesting that, if source B is assumed to be a disk, its plane is likely located very close to the plane of the sky (see Figure 1.24).
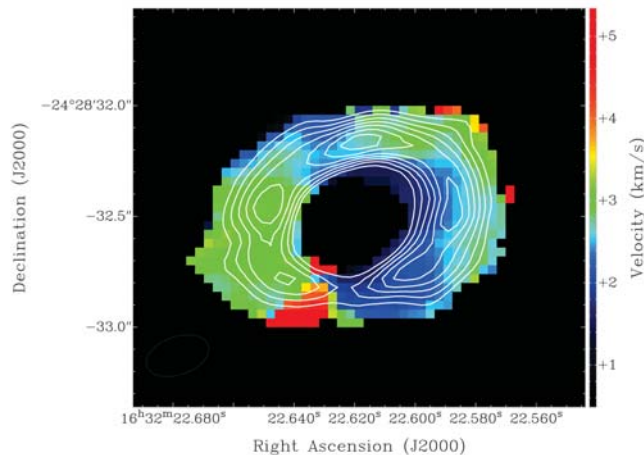
Figure 1.24. Moment 1 map (velocity field) of the $H^{13}CN$ emission in source B. The white contours indicate the integrated intensity contours. The colour-scale bar on the right indicates the LSR velocities in km s^{-1}. Figure taken from Zapata et al. (2013).

Zapata et al. (2013) noted that the maps presented a depression or "hole" of about the size of the continuum, interpreted as a very optically thick dust located in the innermost parts of source B. They also found that the line emission region was about twice the size of the observed continuum at 0.45 mm (see Figure 1.25). More recently, Oya et al. (2018) studied

the emission from other molecules with ALMA and found that the emission from CH_3OH and $HCOOCH_3$ seem to be concentrated toward the center of the source.
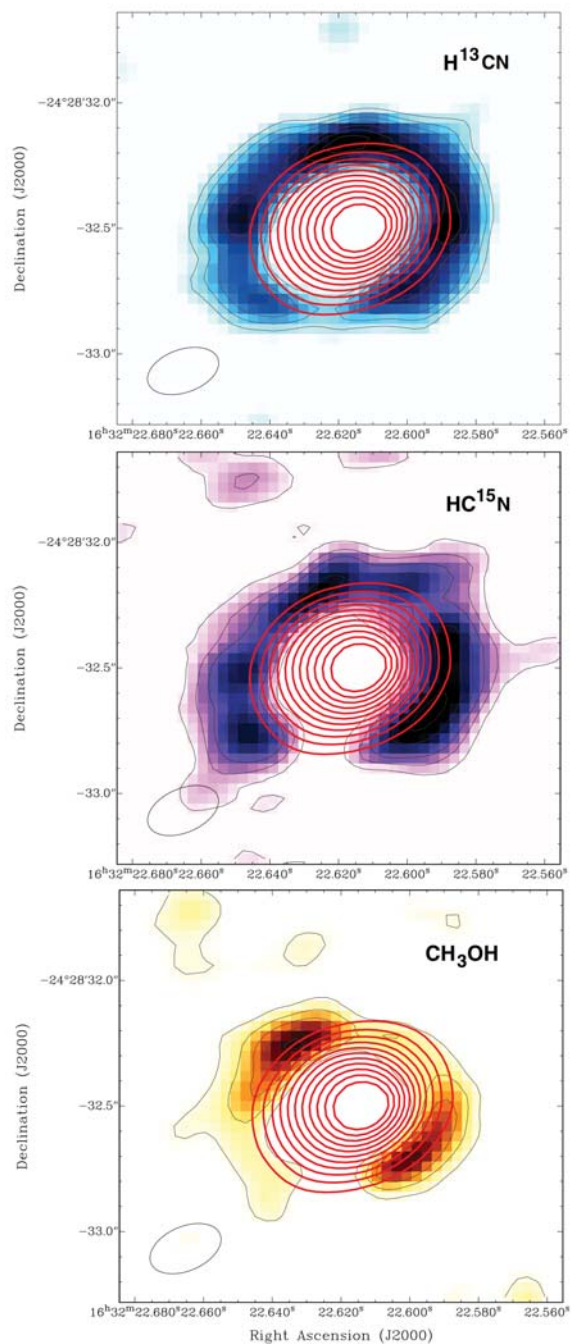
Figure 1.25. ALMA color scale integrated intensity maps of the $H^{13}CN$ $(8-7)$, $HC^{15}N$ $(8-7)$ and CH_3OH $(9_{3,6} - 8_{27})$ molecules on source B overlaid with the continuum emission at 0.45 mm (red contours). Figure taken from Zapata et al. (2013).

Oya et al. (2018) also found that the OCS and the H_2CS were more extended and were probably associated with an infalling rotating envelope. In fact, they argue that both infall and outflow motions could exist in source B.

1.4.6 The continuum spectrum

The continuum spectrum for sources A and B was derived by Chandler et al. (2005) (see Figure 1.26). They used observations with the VLA, the SMA and the PdBI from Bottinelli et al. (2004) at 110 and 230 GHz and Kuan et al. (2004) at 354 GHz. The spectrum of source A can be described by two power laws ($F_\nu \propto \nu^\alpha$). The first fit at frequencies $\nu < 40$ GHz with a spectral index $\alpha = 0.53 \pm 0.04$ is consistent with partially optically thick free-free emission. The second fit with $\nu > 40$ GHz gives $\alpha = 2.91 \pm 0.06$, which is consistent with thermal dust emission. On the other hand, source B has a spectral index between $2.09 \pm 0.07 < \alpha < 2.51 \pm 0.09$.
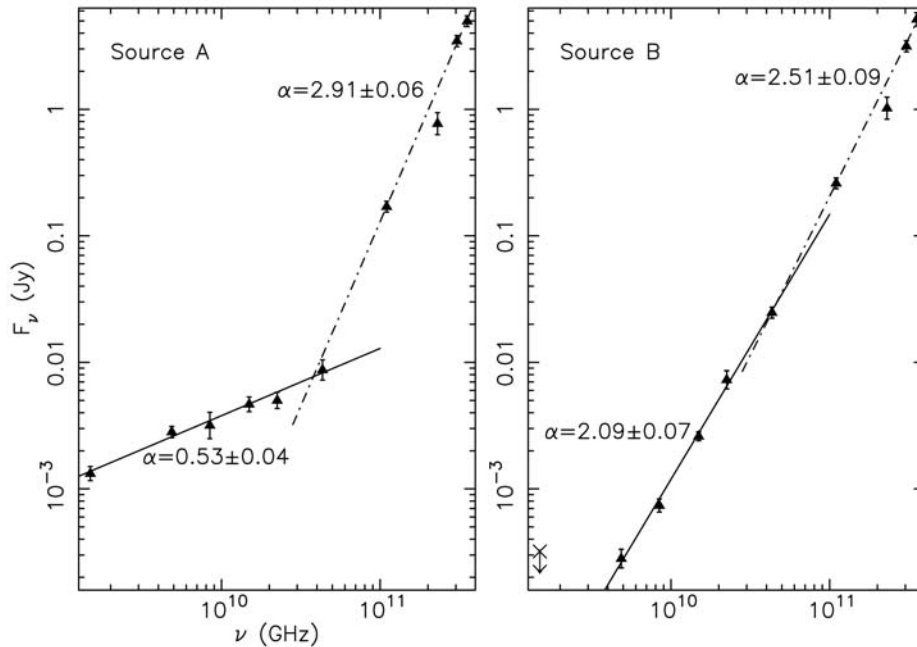
Figure 1.26. Continuum spectrum of sources A and B obtained from SMA and VLA observations up to 2004. Figure taken from Chandler et al. (2005).

The spectrum from source A is typical of a protostar. While a contribution from ionized jets in young stellar objects is expected to dominate at lower frequencies, at higher frequencies, the emission is dominated by dust grains in their envelope. For source B, no clear contribution from ionized winds is found.

1.4.7 The magnetic field structure

Several studies of the dust polarized emission in IRAS 16293–2422 with the SMA have shown that while source A has an hourglass magnetic field structure, source B shows a relatively ordered magnetic field with no evidence for deformation (see Figure 1.27) (Rao et al. 2009, 2014)
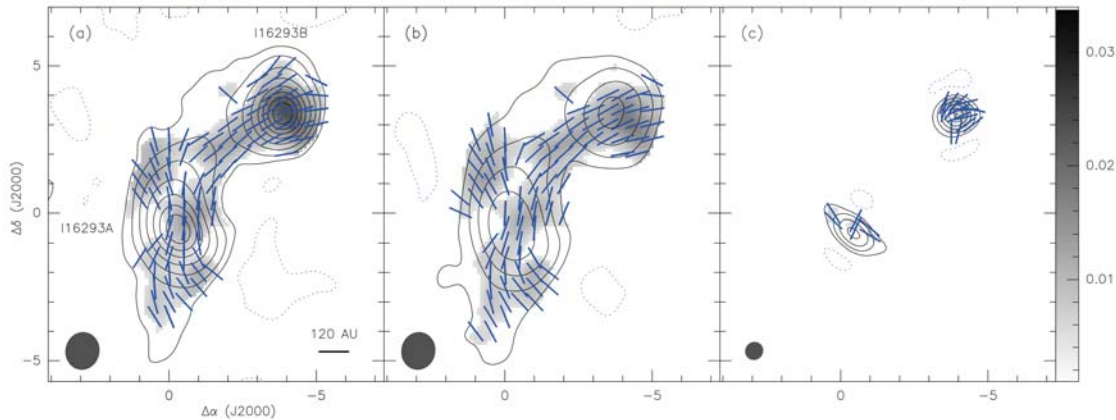
Figure 1.27. Contour maps of the dust continuum emission at 878 μm overlaid with the grayscale images of the polarized dust intensity and the magnetic fields on the plane of the sky (blue segments) as derived from polarized data. (a) Maps using both extended and compact configurations of the SMA. (b) Maps only for the envelope contribution. (c) Maps obtained by using only the baselines between 80 and 220 kλ. Figure taken from Rao et al. (2014).

Rao et al. (2014) found that the magnetic field pattern for source B resembles the expected configuration of a magnetized disk. The existence of rotationally supported disk in the earliest stages of the protostellar phase (Class 0) is still a matter of debate since it is believed that magnetic breaking can efficiently suppress the formation of a disk in the protostellar phase. However, if the rotation and the magnetic field axis are misaligned the magnetic breaking can be inefficient. From the well-formed magnetized disk on source B, Rao et al. (2014) inferred that this source is more evolved than source A.
Alves et al. (2012) found also that the magnetic field in IRAS 16293–2422 ($\sim$ 113 mG) is comparable to the outflow ram pressure. This would imply that the magnetic field is dynamically important for this system.

1.4.8 Masers in IRAS 16293–2422

Maser emission from a number of species has been reported in regions of star-formation. Normally, the emission from masers is found to be compact and strong, so the measurement of their displacement on the sky provide a useful tool to determine the distance to the regions where they originate. The first detection of H_2O maser emission at 22 GHz in IRAS 16293–2422 was made by Wilking and Claussen (1987). This emission was found to originate from a small region of $\sim$0.''6 (Terebey et al. 1992). It was discovered then that this water maser

emission was rapidly changing on a time scale of several days (Furuya et al. 2003). Imai et al. (1999) reported rotation-infall motions of a disk associated with source A from VLBI observations of H_2O maser features. More recently, Imai et al. (2007) followed the astrometry of water maser features with the VLBI Exploration of Radio Astrometry (VERA) instrument and estimated a distance to IRAS 16293–2422 of 178^{+18}_{-37} pc. However, this distance is notably larger than the typically used distance in the literature of 120 pc (Loinard et al. 2008).

1.4.9 The chemistry of IRAS 16293–2422

IRAS 16293–2422 is often considered as the template source for astrochemistry due to the wealth of molecular emission observed in its spectrum (see Figure 1.28) One could argue that IRAS 16293–2422 is the prototype of solar-type protostar in astrochemical studies as Orion KL is for high-mass protostars. In this section we explain why IRAS 16293–2422 is considered as such.
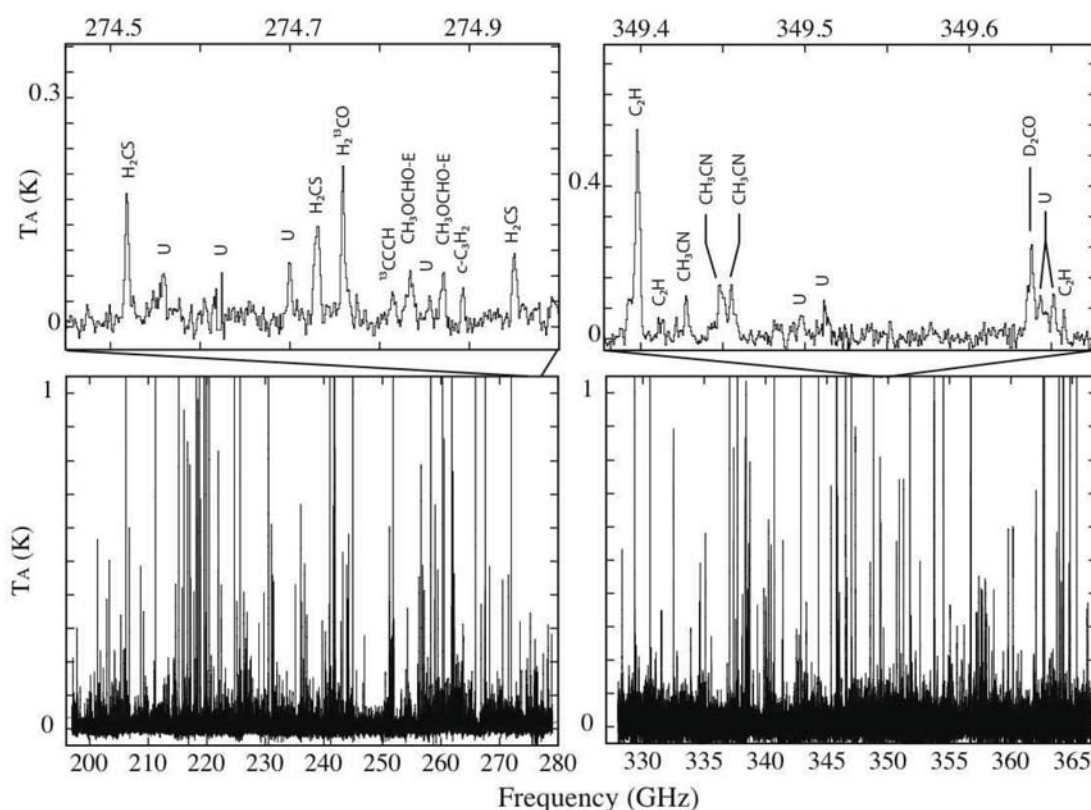
Figure 1.28. Bottom panels: Molecular spectra between 200–280 GHz (left panel) and between 300–365 GHz (right panel). Upper panel: zoom on a small frequency window on each of the spectra. Figure taken from Caux et al. (2011).

1.4.10   The first hot corino

IRAS 16293–2422 is the first low-mass protostar where complex organic and prebiotic molecules were identified to arise from a region where the dust grain mantles sublimate (e.g. Blake et al. 1994; van Dishoeck et al. 1995; Cazaux et al. 2003; Bottinelli et al. 2004). This made IRAS 16293–2422 earn the title of the first hot corino, the low-mass analogue of the high-mass hot cores (e.g. see Ceccarelli 2004). The term "hot corino" is nowadays widely used in the literature when referring to a low-mass hot core, and for convenience I will use it in the rest of the thesis. Many of the detected species in IRAS 16293–2422 were found in its envelope since single-dish observations used in these studies are sensitive to the most extended emission (e.g. see Caux et al. 2011).

1.4.11   The chemistry at small scales

The presence of a large number of complex organic molecules toward the sources A and B was revealed from early studies with interferometers (e.g. Kuan et al. 2004; Bottinelli et al. 2004; Huang et al. 2005; Jørgensen et al. 2011, 2016). Source A has been found to present a larger number of nitrogen and sulfur-bearing species which are weaker or absent in source B. In contrast, source B shows strong emission of oxygen-bearing complex organic molecules (Bisschop et al. 2008; Jørgensen et al. 2011). Caux et al. (2011) performed a molecular survey on IRAS 16293–2422 (called TIMASSS) with the IRAM-30m and the JCMT-15 m telescopes and found more than 4000 lines from 70 molecular species. They recognized that in source A the line widths increase with the upper energy level of the transition, which is compatible with having gas infalling toward a ~ 1 $M_\odot$ object. Since source B does not show this behaviour, it was inferred to have a lower mass ~ 0.1 $M_\odot$. Caux et al. (2011) argue that the difference of rest velocities is consistent with the hypothesis that source B rotates around source A. Because of the small separation between sources A and B ($\sim 5''$), single-dish observations include both sources in the beam and therefore the origin of the line emission is not easy to deduce. Jørgensen et al. (2011) performed a molecular survey of the components in IRAS 16293–2422 with the SMA and found more than 500 transitions from 54 molecular species. They find a systematic velocity V_{LSR} of 3.2 and 2.7 km s^{-1} for sources A and B, respectively. They also found that the line widths from the lines in source B are narrower than the line widths in source A (1.9 vs 2.6 km s^{-1}). IRAS 16293–2422 was also a science target of a molecular survey performed with HIFI on-board the Herschel Space Observatory (CHESS, Ceccarelli et al. 2010). This survey revealed molecular transitions at higher frequencies (and higher excitation energies) in the envelope. More recently, Jørgensen et al. (2016) performed a survey with ALMA (PILS) and found more than 10,000 lines from a few dozens of species, including many complex and organic molecules of astrobiological relevance.

1.4.12 The absorbing material

The presence of an absorbing component at a systematic velocity of 4.2 km s^{-1} (and line width of ~ 0.5 km s^{-1}) has been inferred from observations of HDO fundamental transitions at 465 and 894 GHz in IRAS 16293–2422 (Coutens et al. 2012). The doubly deuterated form of water D$_2$O with this features was also detected in this source. The material responsible for this absorption is associated with a water-rich absorbing layer resulting from the photodesorption of the ices at the edges of the molecular cloud by the UV field as predicted by chemical models (e.g. Hollenbach et al. 2009). Other studies have shown that this foreground component is needed to explain the line profiles for other molecules such as CH (Bottinelli et al. 2014) or HCO$^+$ (Quénard et al. 2018).

1.4.13 Deuteration

IRAS 16293–2422 was the first source where "super-deuteration" was discovered. This phenomenon refers to the very high abundance ratio of D-bearing molecules with respect to their H-bearing isotopologues (e.g. see Ceccarelli et al. 2007). Nowadays, it has been observed that the envelopes of low-mass Class 0 protostars present high levels of molecular deuteration (see e.g. Loinard 2002). Multiple deuterated molecules such as H$_2$CO, CH$_3$OH, H$_2$O and NH$_3$, among others, have been observed in IRAS 16293–2422 (see e.g. Ceccarelli et al. 1998; Vastel et al. 2003; Parise et al. 2003; Butner et al. 2007; Bacmann et al. 2010; Coutens et al. 2012; Caux et al. 2011; Parise et al. 2012).

Coutens et al. (2012) reported that water shows a different behaviour from other molecules such as CH$_3$OH and H$_2$CO whose deuteration increases with density, because the water fractionation ratio does not seem to vary with density. Interestingly, the low HDO/H$_2$O ratio deduced by Persson et al. (2013) in IRAS 16293–2422 suggested that the difference between the inner regions of protostars and Earth oceans and comets is smaller than previously thought.

1.4.14 Prebiotic molecules

Understanding the origin of life is one the main challenges of modern science. The study of complex molecules that could form in space and that are relevant for organic and prebiotic chemistry is, therefore, of prime importance. The abundance of these molecules is usually compared with the molecular content of comets in our Solar System, since they could have been formed in the early stages of star-formation and delivered later to the Earth by the bombarding of these objects.

A number of prebiotic complex organic molecules have been detected toward IRAS 16293–2422 such as CH$_3$NCO (methyl isocyanide, Martín-Doménech et al. 2017), glycolaldehyde (Jørgensen et al. 2012; Zhou et al. 2018), c-C$_2$H$_4$O (ethylene oxide, Lykke et al. 2017), C$_2$H$_5$CHO (propanal, Lykke et al. 2017), CH$_3$COCH$_3$ (acetone, Lykke et al. 2017) and NH$_2$CHO (formamide, Kahane et al. 2013).

From the astrochemical point of view, IRAS 16293–2422 is thus an interesting source to study the conditions that give birth to these complex molecules that are vital to build the blocks of life as we know it.

1.4.15   IRAS 16293–2422 : a unique source

This chapter summarizes very briefly some of the properties of IRAS 16293–2422. At small scales, IRAS 16293–2422 presents a complex structure with a binary system composed by IRAS 16293–2422A and IRAS 16293–2422B. Even at smaller scales, IRAS 16293–2422A breaks into two sources, A1 and A2, whose nature has been proposed to be protostellar. The very recent material expulsion from source A2 also represents the opportunity of studying the properties of very recent bipolar ejections. In addition, the nature of IRAS 16293–2422B remains elusive since different evolutionary stages (from protostellar phase to T Tauri star) have been proposed to describe its observational properties. These are based on the shape of its continuum spectrum, the fact that it shows very-well resolved P Cygni profiles and its lack of strong ionized winds.

IRAS 16293–2422 overall presents a very active chemistry. At larger scales, the envelope of this source has been fully modelled and it is presumed to have different molecular abundances at different radii whereas the density and temperature excitation conditions are also expected to change along it. Because the emission and absorption line profiles from molecular species provide a powerful tool to study the chemistry and the physics of star-forming regions, IRAS 16293–2422 represents the ideal target to model the excitation conditions of such species by means of radiative transfer and chemical modelling. In addition, its binarity makes IRAS 16293–2422 a suitable laboratory to study the properties of clustered star formation in detail.

Finally, since IRAS 16293–2422 resembles our Sun at its early stages of evolution, understanding and modelling the processes present in this source will help us learn more about the history of the formation of our Sun and our Solar System.

1.5   Outline of the thesis

The main goal of this thesis is to determine the three-dimensional structure of the low-mass solar-type protostar IRAS 16293-2422. Because this Class 0 object is in fact a multiple system embedded in a large envelope, we have analyzed the structure of the source at different spatial scales. First, we have studied the properties at small scales of the individual components in IRAS 16293-2422 based on high angular resolution millimeter to centimeter observations obtained with the VLA and ALMA interferometers. For the envelope at large scales, we extracted the information from the line profiles associated with nitrogen-bearing molecules such as CN and HNCO observed with IRAM, APEX, JCMT and Herschel/HIFI telescopes from centimeter to far infrared wavelengths. We have used radiative transfer models to predict the morphology of these line profiles, producing synthetic spectra to mimic the observations and at the same time constraining the structure in 3D of IRAS 16293-2422.

These models are compared with chemical models to corroborate our results. This analysis of the interferometric and single-dish observations allows to derive a complete model for the three-dimensional structure of IRAS 16293-2422 from a multi-frequency point of view. The thesis is organized as follows:

- Because the distance to IRAS 16293–2422 is fundamental for the analysis and modelling of the observations in this work, we performed in Chapter 2 a revision of the distance to this protostar based on the analysis of VLBA observations of water masers at 22 GHz. We discuss why our new measurement for the distance to IRAS 16293–2422 of 141^{+30}_{-21} pc is more accurate than previous measurements.

- Chapter 3 presents a detailed analysis of the individual components of IRAS 16293–2422 based on VLA and ALMA high resolution observations. We followed the astrometry of the multiple system over 30 years. We also present the analysis of the variability of the sources and give an interpretation of their measured continuum spectrum.

- In Chapter 4 we focus in constraining the physical structure of source B. A radiative transfer model in 3D of the continuum and P-Cygni profiles of CH_3OH and $H^{13}CN$ give us new insights on the nature of this source.

- Chapter 5 is devoted to constraining the abundance structure of the HNCO molecule in IRAS 16293–2422 based on single-dish observations over a wide range of frequencies. A radiative transfer model out of LTE, combined with the use of recently computed HNCO collision rate coefficients and a chemical model with Nautilus allow us to determine the structure of IRAS 16293–2422 consistently. This enables us to place constraints on the structure of the envelope along the line of sight.

- Chapter 6 is dedicated to the analysis of the emission and absorption of CN by the modelling of its complex line profiles with a radiative transfer model in LTE. We show that CN reveals evidence of rotation of the envelope and in fact its emission seems to be more extended than the envelope of IRAS 16293-2422. We compare the results with the predictions of the chemical model with Nautilus and find a good overall agreement. We computed the $^{12}C/^{13}C$ and $^{14}N/^{15}N$ ratios and discuss why some of these values are different for the envelope and the compact sources.

- Finally, in Chapter 7 we summarize our main results in the conclusions and provide some perspectives of the work.

Chapter 2

La distancia a IRAS 16293-2422 a partir de la astrometría de sus máseres de agua

Determinar la distancia hacia fuentes astronómicas en un problema fundamental en la astronomía. Esto es porque una gran cantidad de parámetros estelares tales como la masa, la luminosidad o el tamaño físico dependen directamente de su distancia. Por esta razón, una medición precisa de esta cantidad es vital para interpretar correctamente y modelar las observaciones hacia fuentes astronómicas. La distancia hacia la nube densa en Ofiuco, en donde IRAS 16293-2422 se encuentra profundamente embebida, ha sido tradicionalmente utilizada como ∼ 160 pc (Whittet and van Breda 1975). A partir de mediciones de extinción (Lombardi et al. 2008) y de observaciones con VLBI (Loinard et al. 2008), se determinó que la distancia hacia IRAS 16293-2422 era de 120 pc. Imai et al. (2007) midió la paralaje trigonométrica de máseres de agua de este objeto estelar joven y obtuvo una distancia mayor de 178^{+18}_{-37} pc. Más recientemente, Ortiz-León et al. (2017) determinaron paralajes trigonométricas de una muestra de estrellas jóvenes distribuidas en Ofiuco y obtuvieron distancias medias de 137.3 ± 1.2 pc para el núcleo de Ofiuco y 147.3 ± 3.4 pc para Lynds 1689, en donde IRAS 16293-2422 está localizada. Entre todos estos cálculos, la medición más directa de la distancia hacia IRAS 16293-2422 fue hecha por Imai et al. (2007). Sin embargo, su precisión fue fuertemente afectada debido a que no pudieron seguir con precisión el movimiento de las condensaciones maser debido a su variabilidad en el tiempo. Dado que la determinación de la estructura tridimensional de IRAS 16293-2422 depende directamente de su distancia, hemos revisado la distancia hacia esta fuente analizando la astrometría de sus máseres asociados observados con el VLBA a 22 GHz. Hemos realizado un análisis cuidadoso y hemos medido la paralaje de las condensaciones maser a lo largo de un año, obteniendo un valor de 7.1 ± 1.3 mas, lo que corresponde a una distancia de 141^{+30}_{-21} pc. Además, asociamos el movimiento relativo de las condensaciones maser con uno de los lóbulos corridos al rojo de uno de los flujos presentes en IRAS 16293-2422 que tiene un ángulo de posición de ∼ 110°. Adoptamos esta nueva distancia hacia IRAS 16293-2422 en el análisis e interpretación de las observaciones presentadas en los capítulos subsecuentes.

Para este trabajo en particular, estuve involucrado en la calibración de datos y elaboración de imágenes, en la discusión general y la redacción de algunas secciones del artículo resultante.

Chapter 2

La distance d'IRAS 16293-2422 à partir de l'astrométrie de ses masers d'eau

Déterminer la distance aux sources astronomiques est un problème fondamental en astronomie. En effet, un certain nombre de paramètres stellaires, tels que la masse, la luminosité ou la taille physique, dépendent directement de leur distance. Pour cette raison, une mesure précise de cette quantité est essentielle pour interpréter et modéliser correctement les observations vers les sources astronomiques. La distance à Ophiuchus, où IRAS 16293-2422 est profondément enfoui, était traditionnellement supposée être de 160 pc (Whittet and van Breda 1975). D'après les mesures d'extinction (Lombardi et al. 2008) et les observations VLBI (Loinard et al. 2008), il a été déterminé que la distance d'IRAS 16293-2422 était de 120 pc. Imai et al. (2007) a mesuré la parallaxe trigonométrique des masers de ce jeune objet stellaire et a obtenu une distance plus grande, de 178^{+18}_{-37} pc. Plus récemment, Ortiz-León et al. (2017) a déterminé une parallaxe trigonométrique sur un échantillon de jeunes étoiles réparties dans Ophiuchus et a obtenu des distances moyennes de 137.3 ± 1.2 pc pour le noyau d'Ophiuchus et de 147.3 ± 3.4 pc pour le nuage Lynds 1689, où IRAS 16293-2422 est situé. Parmi tous ces calculs, la mesure la plus directe de la distance à IRAS 16293-2422 a été effectuée par Imai et al. (2007). Cependant, leur précision était fortement affectée, car ils ne pouvaient pas suivre le mouvement des spots maser précisément en raison de leur variabilité dans le temps. Étant donné que la structure tridimensionnelle dépend de la distance, nous avons examiné la distance de cette source en analysant l'astrométrie de ses masers à 22 GHz avec le VLBA. Nous avons effectué une analyse minutieuse et mesuré la parallaxe des condensations maser pendant environ un an et avons obtenu une valeur de 7.1 ± 1.3 mas, correspondant à une distance de 141^{+30}_{-21} pc. De plus, nous relions le mouvement relatif des condensations masers avec l'un des lobes décalés vers le rouge de l'un des jets sortant de IRAS 16293-2422 avec un angle de position de ~ 110°. Nous avons adopté cette nouvelle valeur de la distance de IRAS 16293-2422 dans l'analyse et l'interprétation des observations présentées dans les chapitres suivants.

Pour ce travail particulier, j'ai été impliqué dans la calibration et l'imagerie des données, la discussion générale et la rédaction de certaines sections de l'article résultant.

Chapter 2

The distance to IRAS 16293-2422 from the astrometry of its associated water masers

Determining the distance to astronomical sources is a fundamental problem in astronomy. This is because a number of stellar parameters such as the mass, the luminosity or the physical size depend directly on their distance. For this reason, a precise measurement of this quantity is vital to correctly interpret and model the observations toward astronomical sources. The distance to the Ophiuchus cloud, where IRAS 16293-2422 in deeply embedded, was traditionally assumed to be ~ 160 pc (Whittet and van Breda 1975). From extinction measurements (Lombardi et al. 2008) and VLBI observations (Loinard et al. 2008), the distance to IRAS 16293-2422 was determined to be 120 pc. Imai et al. (2007) measured the triginometric parallax of the water masers to this young stellar object and obtained a larger distance of 178^{+18}_{-37} pc. More recently, Ortiz-León et al. (2017) determined trigonometric parallaxes to a sample of young stars distributed over Ophiuchus and obtained mean distances of 137.3 ± 1.2 pc for the Ophiuchus core and 147.3 ± 3.4 pc for Lynds 1689, where IRAS 16293-2422 is located. Among all these calculations, the most direct measurement for the distance to IRAS 16293-2422 was made by Imai et al. (2007). However, their accuracy was strongly affected since they could not follow the movement of the maser spots precisely due to their variability in time. Since the determination of the three-dimensional structure of IRAS 16293-2422 depends directly on its distance, we have revisited the distance of this source by analysing the astrometry of its associated water masers observed with the VLBA at 22 GHz. We performed a careful analysis and measured the parallax of the maser cloudlets over about one year and obtained a value of 7.1 ± 1.3 mas, corresponding to a distance of 141^{+30}_{-21} pc. In addition, we associated the relative motion of the masers spots with one of the redshifted lobes from one of the outflows present in IRAS 16293-2422 with a position angle of ~ 110°. We adopt this new distance to IRAS 16293-2422 in the analysis and interpretation of the observations presented in the subsequent chapters.

For this work in particular, I was involved in the data calibration and imaging, the general discussion and redaction of some sections of the resulting paper.

A revised distance to IRAS 16293-2422 from VLBA astrometry of associated water masers

S. A. Dzib[1], G. N. Ortiz-León[1,2], A. Hernández-Gómez[3,4], L. Loinard[3,5], A. J. Mioduszewski[6], M. Claussen[6], K. M. Menten[1], E. Caux[4], and A. Sanna[1]

[1] Max-Planck-Institut für Radioastronomie, Auf dem Hügel 69, 53121 Bonn, Germany
   e-mail: sdzib@mpifr-bonn.mpg.de
[2] Humboldt Fellow, Berlin, Germany
   e-mail: gortiz@mpifr-bonn.mpg.de
[3] Instituto de Radioastronomía y Astrofísica, Universidad Nacional Autónoma de México, Morelia 58089, Mexico
   e-mail: a.hernandez@irya.unam.mx
[4] IRAP, Université de Toulouse, CNRS, UPS, CNES, Toulouse, France
[5] Instituto de Astronomía, Universidad Nacional Autónoma de México, Apartado Postal 70-264, CdMx C.P. 04510, Mexico
[6] National Radio Astronomy Observatory, PO Box 0, Socorro, NM 87801, USA

ABSTRACT

IRAS 16293-2422 is a very well-studied young stellar system seen in projection towards the L1689N cloud in the Ophiuchus complex. However, its distance is still uncertain; there is a range of values from 120 pc to 180 pc. Our goal is to measure the trigonometric parallax of this young star by means of H_2O maser emission. We use archival data from 15 epochs of VLBA observations of the 22.2 GHz water maser line. By modeling the displacement on the sky of the H_2O maser spots, we derived a trigonometric parallax of 7.1 ± 1.3 mas, corresponding to a distance of 141^{+30}_{-21} pc. This new distance is in good agreement with recent values obtained for other magnetically active young stars in the L1689 cloud. We relate the kinematics of these masers with the outflows and the recent ejections powered by source A in the system.

Key words. astrometry – masers – stars: formation – stars: individual: IRAS 1629-2422 – techniques: interferometric

1. Introduction

As a result of the development and improvement of Very Long Base Interferometry (VLBI) techniques in recent decades, it has become possible to measure the trigonometric parallax of deeply embedded young stellar objects (YSOs) with very high accuracy. This information is crucial for the determination of some of the most fundamental stellar parameters, such as age, luminosity, and mass. Low-mass YSOs with nonthermal emission (such as gyrosynchrotron or synchrotron emission) are good candidates to be observed with VLBI since they have a high surface brightness over a few solar radii (e.g. Loinard et al. 2008; Dzib et al. 2016; Ortiz-León et al. 2017). However, VLBI observations of Class 0 objects, the youngest stars, are more complicated because their nonthermal emission can suffer strong free-free absorption effects from the ionized winds that they typically power.

Emission from water masers has been observed in a variety of objects and has been used to determine their trigonometric parallax and hence their distance (e.g., Imai et al. 2007; Hirota et al. 2008; Reid et al. 2009; Sanna et al. 2017b). Although water masers can vary on short timescales (Claussen et al. 1996), and their structure can be resolved at angular resolutions of VLBI instruments in nearby regions (Imai et al. 2007), they are a fundamental tool used to determine distances to far away star-forming regions. Recent VLBI observations of strong water masers have provided an accurate determination of the distance to a star-forming region at 20 kpc from the Sun (Sanna et al. 2017b).

Water maser emission has been observed towards IRAS 16293-2422 (hereafter I16293), a very well-studied young stellar system located to the north of the Lynds 1689 (L1689) cloud, in the Ophiuchus complex (Fig. 1). This system is comprised of two main sources, A and B, identified from interferometric observations at centimeter wavelengths (Wootten 1989; Mundy et al. 1992) that are separated by 5″ and have properties of Class 0 objects, i.e., YSOs in very early evolutionary phases. Source A itself is resolved into two subsources, A1 and A2, separated by 0.″3 (Chandler et al. 2005; Loinard et al. 2007). Recently, other continuum sources associated with an episodic ejection from A were observed with the VLA (Loinard et al. 2007; Pech et al. 2010; Loinard et al. 2013). Source A seems to power two outflows in the E-W and NW-SE directions observed through the emission of CO and SiO lines (Mizuno et al. 1990; Girart et al. 2014). There is also a compact outflow extending along the axis between sources A and B in the SE-NW direction. Since I16293 is an interesting laboratory for studying the kinematics and dynamics of clustered star formation, it is of crucial importance to determine its distance very precisely and, therefore, to infer its physical parameters correctly. Furthermore, relating the small-scale kinematics of the water masers with those of the larger scale outflows would be interesting.

Previously, Imai et al. (2007) reported on the emission of H_2O masers observed with the VLBI Exploration of Radio Astrometry (VERA) array towards this source and obtained an annual parallax for a maser feature of $5.6^{+1.5}_{-0.5}$ mas, corresponding to a distance of 178^{+18}_{-37} pc. On the other hand,
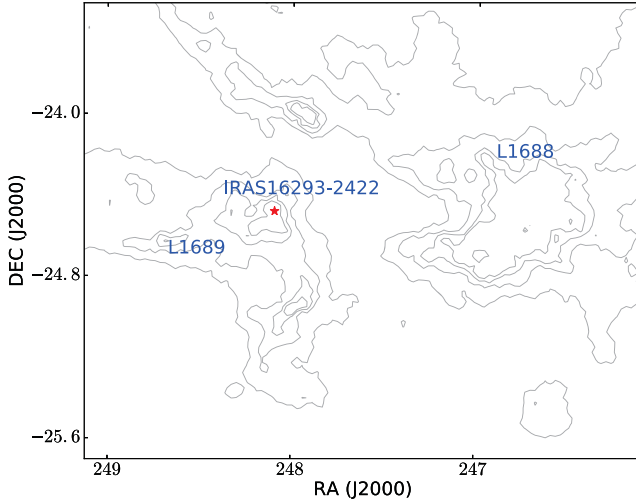
Fig. 1. Molecular cloud of Ophiuchus traced by optical extinction obtained as part of the COMPLETE project (Ridge et al. 2006). The location of I16293, the core (L1688), and Lynds 1689 (L1689) are indicated. The contours corresponds to $A_V = 4, 7, 10$, and 13.

Fig. 2. Observed spectrum of the water emission toward the brightest spot in epoch M (also called spot 2 in Sect. 3.2).

Loinard et al. (2008) measured the distance to the core of the Ophiuchus complex (also known as Lynds 1688 or L1688) from VLBA observations of nonthermal emission from two YSOs and found a distance of $120^{+4.5}_{-4.2}$ pc. This distance is now commonly used in the literature as the distance to I16293. More recently, Ortiz-León et al. (2017) measured the distance to the L1689 streamer using VLBA observations of three stellar systems, finding a mean parallax of 6.79 ± 0.16 mas, which corresponds to a distance of 147.3 ± 3.4 pc. They also revisited the mean distance to the Ophiuchus core and found a mean parallax of 7.28 ± 0.06 mas, corresponding to a distance of 137.3 ± 1.2 pc. As the distance to I16293 measured by Imai et al. (2007) is significantly larger than that to other stars in the L1689 cloud, it is not yet clear whether it is a background object seen along the line of sight to L1689. However, it is hard to think that such a deeply embedded young star should not be part of a cloud when it appears in projection on the densest part of that cloud (see Fig. 1). It is clear that the distance to I16293 needs to be revisited.

In this paper, we present high-sensitivity VLBI observations of H_2O masers towards I16293. From these observations, we were able to identify the positions of several masers spots and perform a precise astrometry, finding a distance to I16293 that is in good agreement with the recent measured values to other young stars in the Ophiuchus complex.

2. Observations and data calibration

We analyzed a series of 18 observations of water masers at 22.2 GHz carried out with the Very Long Baseline Array (VLBA) as part of project BC152 (PI: M. Claussen). These observations cover a period of eight months from 2005 August 2 to 2006 April 13 (see Table 1), and were taken at intervals of about 15 days. Each epoch consisted of cycles switching between I16293 and the quasar J1625-2527 ($\sim 1\overset{\circ}{.}8$ away), with two minutes of integration time on the target and one minute on the quasar. Data were taken in right and left circular polarizations with four baseband channels (BBCs) of 8 MHz bandwidth each. The BBC containing the maser line, which was centered at 22.2371 GHz, was also correlated with a channel separation of 15.6250 kHz (corresponding to a velocity resolution of
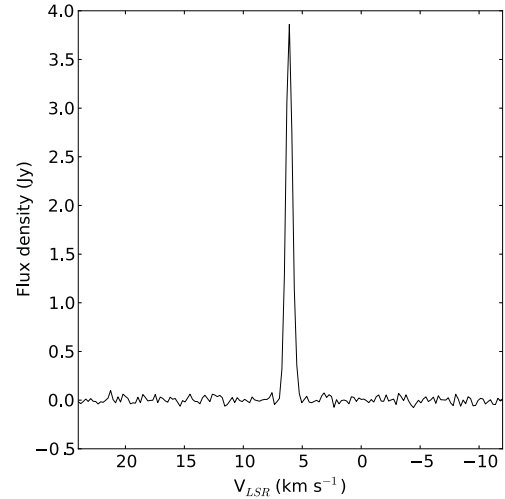
0.215 km s^{-1}) to produce 512 spectral channels. Throughout the whole data analysis, we only considered the BBC containing the maser emission.

The strong quasar 3C345 was observed at the beginning and at the end of each epoch and was used as a fringe finder. In total, three hours of observation were spent on I16293 during each observation[1], which was correlated at position $\alpha_{J2000} = 16^h 32^m 22\overset{s}{.}889$ and $\delta_{J2000} = -24°28'36''25$.

Data calibration and imaging were performed using the Astronomical Image Processing System (AIPS; Greisen 2003). First, we removed the delays introduced by the ionospheric content; then we applied corrections to the Earth Orientation Parameters used by the correlator, and corrections for voltage offsets in the samplers. Instrumental single-band delays were then determined and removed using fringes detected on 3C345. Amplitude calibration was done using the provided gain curves and system temperatures to derive the System Equivalent Flux Density (SEFD) of each antenna. At this stage, the bandpass shape calibration, which was obtained from the scans on 3C345, was applied to the data. In order to set the velocity information for I16293, we used the radio velocity definition and adopted a line rest frequency of 22.23508 GHz. Then we corrected the data for the Doppler shift due to the rotation of the antennas with the Earth around the Sun during observations. Finally, global fringe fitting was run on J1625-2527 in order to find residual phase rates and delays; the solutions from this final step were then applied to the maser line data. Due to poor weather conditions or technical faults at some antennas of the array, the first three epochs presented very poor data quality and were discarded from the analysis.

We found strong maser emission at an LSR velocity, $v_{\rm LSR}$, of ≈ 6.1 km s^{-1} (channel 252; see Fig. 2 for an example) in all the 15 remaining epochs. Images were produced for this velocity channel (see Sect. 3.1) using a pixel size of 50 μas and a weighting scheme intermediate between natural and uniform (ROBUST = 0 in AIPS). The emission from this channel was found to be offset from the phase center by $\sim 1''2$. Therefore, the phase center was shifted (using the task UVFIX in AIPS) to the position of the emission and then used to produce our

---

[1] The source YLW16A was also observed in each epoch, but these data are not discussed in the present work.

Table 1. Main parameters of all images obtained for each VLBA observation data set.

Epoch	Date of observation (yyyy-mm-dd/hh:mm)	Synthesized beam (mas × mas); PA	Noise (mJy beam^{-1})	Peak (Jy beam^{-1})
A	2005-Aug-02/03:00	. . .	. . .	. . .
B	2005-Aug-16/02:05	. . .	. . .	. . .
C	2005-Aug-30/01:10	. . .	. . .	. . .
D	2005-Sep-12/23:17	1.14 × 0.29; −20.1°	19	0.35
E	2005-Sep-25/22:19	0.74 × 0.25; −10.2°	10	0.21
F	2005-Oct-13/20:38	0.77 × 0.26; −10.9°	40	0.55
G	2005-Nov-01/19:55	0.91 × 0.29; −7.9°	40	2.23
H	2005-Nov-12/19:12	0.87 × 0.27; −11.6°	33	0.70
I	2005-Nov-27/18:14	0.84 × 0.25; −8.7°	38	0.53
J	2005-Dec-08/17:31	1.33 × 0.31; 7.2°	21	1.10
K	2005-Dec-22/16:34	0.83 × 0.26; −9.7°	18	0.56
L	2006-Jan-06/15:36	0.78 × 0.28; −8.9°	15	0.69
M	2006-Jan-18/14:53	0.74 × 0.25; −11.1°	33	0.83
N	2006-Feb-04/13:41	0.81 × 0.25; −11.0°	28	0.48
O	2006-Mar-02/12:00	0.93 × 0.30; −3.4°	20	0.46
P	2006-Mar-17/11:02	0.83 × 0.26; −8.6°	26	0.38
Q	2006-Mar-30/10:05	0.87 × 0.28; −7.0°	17	0.53
R	2006-Apr-13/09:07	0.78 × 0.26; −9.2°	30	0.53

Table 2. Other water maser features detected toward I16293 with the VLBA.

Epoch	Date of observation	Channel	v_{LSR} (km s^{-1})	RA (^{h} ^{m} ^{s})	Dec (° ′ ″)	Peak (Jy beam^{-1})
F	2005-Oct-13	268	2.8	16 32 22.864679(3)	−24 28 36.32705(5)	0.31 ± 0.03
I	2005-Nov-27	271	2.1	16 32 22.865514(1)	−24 28 36.33138(5)	0.25 ± 0.02
J	2005-Dec-08	271	2.1	16 32 22.865709(1)	−24 28 36.33135(2)	1.05 ± 0.03
R	2006-Apr-13	262	4.0	16 32 22.800719(1)	−24 28 36.57525(5)	0.20 ± 0.02
R	2006-Apr-13	272	1.9	16 32 22.882063(1)	−24 28 36.42483(4)	0.27 ± 0.01

final images, shown in Fig. 3. The resulting r.m.s. noises in these images are given in Table 1.

The final images were exported to FITS format for further analysis using the CASA software package. This software provides more flexibility for fitting multiple Gaussians in regions containing a large number of pixels (task IMFIT in CASA versus task JMFIT in AIPS). The Gaussian fittings were used to determine the position and flux of the water masers spots. We compared the fitted positions from the two software tools and found that they agree within 1σ. JMFIT and IMFIT provide an estimate of the position errors based on the expected theoretical astrometric precision of an interferometer (Condon 1997). The barycentric coordinates of the Earth and the Julian date of each observation, which are necessary for the astrometric fits, were calculated using the NOVAS routines distributed by the US Naval Observatory.

3. Results

3.1. Structure and properties of the emission

Maser emission is detected at radial velocities v_{LSR} ∼ 1.9, 2.1, 2.8, 4.0, and 6.1 km s^{-1}. These velocities are very similar to the systemic LSR velocity of I16293 A, for which Jørgensen et al. (2011) give +3.2 km s^{-1}. Only the emission at

6.1 km s^{-1} is detected in all of the 15 epochs, while emission at the other velocities is not seen in more than two epochs (see Table 2). For this reason, we focus our analysis on the persistent emission at 6.1 km s^{-1}. We note that Imai et al. (2007) also detected emission in their VERA observations from 2005 to 2006, at a velocity of v_{LSR} = 6.0 km s^{-1} with S_ν ∼ 2 Jy, which may correspond to the emission detected here.

For the astrometric analysis we only consider the spots detected in the maps for this velocity channel (channel 252). In general, several spots are detected at each epoch. Some spots show an elongated structure, just as was previously reported by Imai et al. (2007). As noticed by these authors, the brightness distribution of the emission is spatially resolved and variable. The brightest spot at one epoch is not necessarily the brightest one in the other epochs and many of them were detected in one epoch only. For all these reasons, choosing the correct positions for the astrometry implies a careful analysis of the images.

3.2. Selection of positions for astrometry

In order to perform accurate and reliable astrometry, the position of the same object needs to be measured at several consecutive epochs. For compact objects, such as stellar nonthermal continuum sources, there is little or even null confusion of the
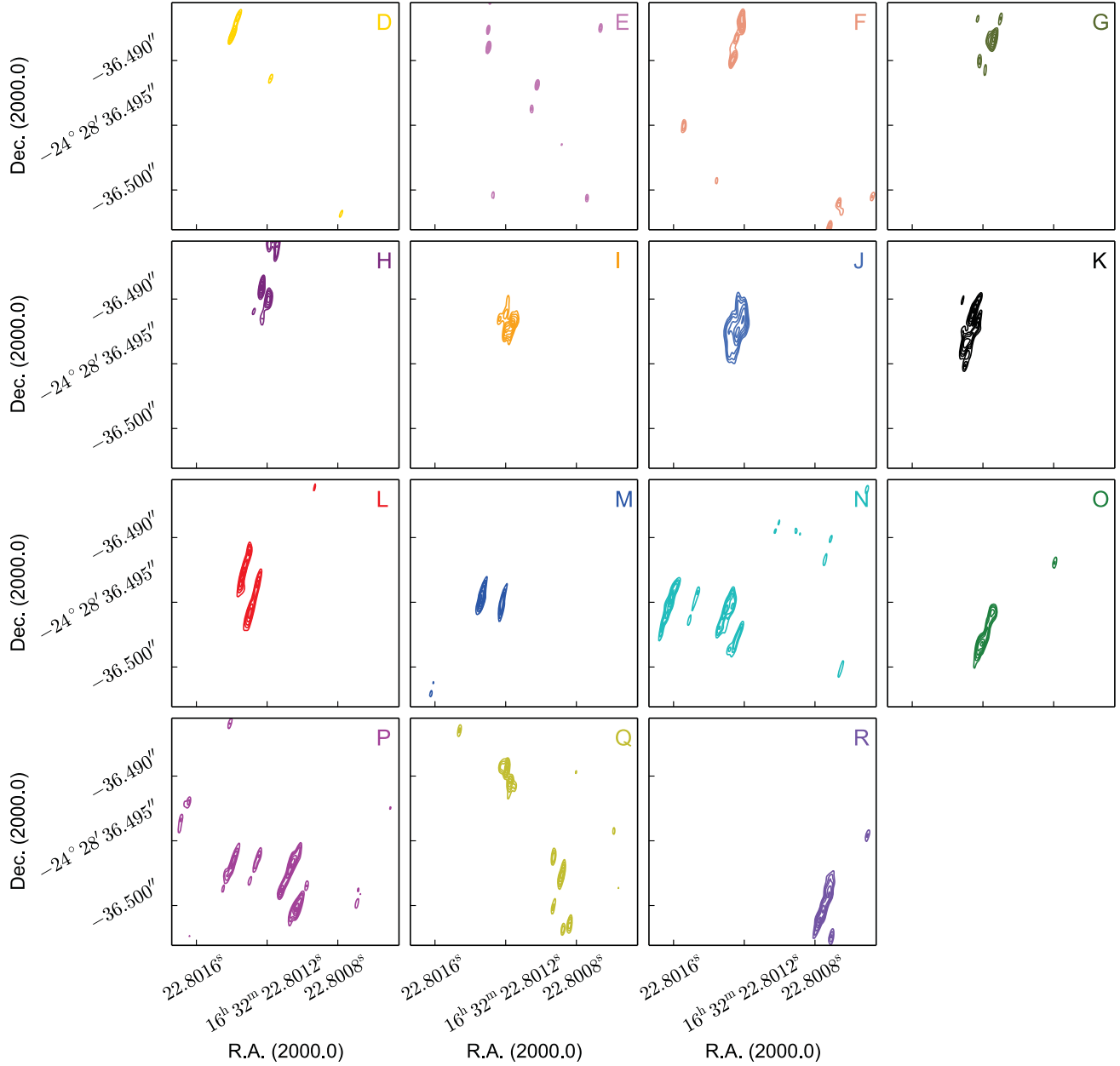
Fig. 3. Water masers detected in our VLBA images above 10σ at each epoch. The images show the emission from the channel at $v_{LSR} = 6.1$ km s^{-1}. Contour levels are 0.3, 0.4, 0.5, 0.65, 0.80, and 0.95 times the peak level on the images, which are given in Table 1. The blue strips indicate the RA position with error bars of the shock front (see Sect. 3.2.)

source position from epoch to epoch: it is the position of the emitting star. However, the case of water masers in nearby star-forming regions is much more complex. Due to their variability and motions, it is not easy to associate different spots even between contiguous epochs, especially when the emission is heavily resolved. The water maser shocks are located at the base of YSOs outflows (Torrelles et al. 2003; Sanna et al. 2012). Their motion on the plane of the sky is the result of the superposition of a proper motion plus a reflex motion introduced by the parallax. Especially important is their movement in the right ascension (R.A.) direction, since their position in this direction is better determined and allows better determinations of the trigonometric parallax (Reid et al. 2009).

To select the spots we made the following assumptions: (i) all the spots lie at the same distance, (ii) they have similar proper motions, and (iii) their radial velocity is constant at the different epochs. According to these assumptions, we expect that the position angle and projected angular distance between two different spots do not significantly change in a time interval of 15 days. With this in mind, we can identify individual spots between consecutive epochs as shown in Fig. 4. In the left panel, we superpose the maser emission detected in epochs D–G, which were observed from 2005 September to November. We can clearly identify a spot that is detected in these four epochs and that shows a coherent motion toward the southwest of the map. We refer to this spot as "spot 1". In the right panel of Fig. 4,
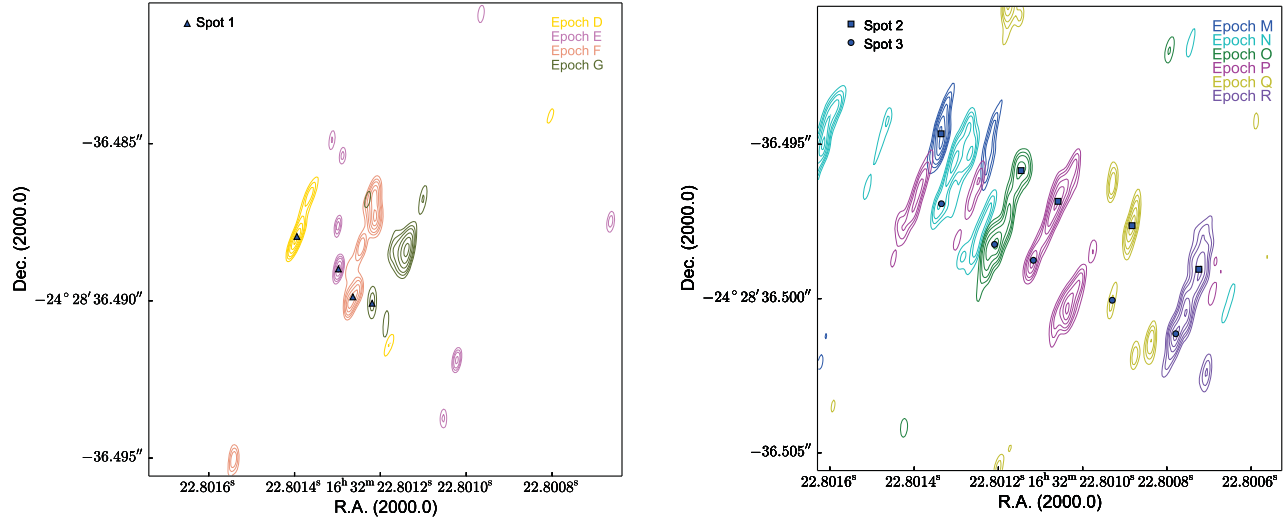
Fig. 4. Superposition of the detected spots. For clarity and to guide the eye, *left panel*: spots detected in the first four epochs (epoch D–G; see Table 1). *Right panel*: spots detected from epochs M to R. The contour levels are 0.3, 0.4, 0.5, 0.65, 0.80, and 0.95 times the peak flux of each image. Triangles indicate the emission peaks of spot 1; squares and circles correspond to spot 2 and 3, respectively.

we now show the detected emission in epochs M–R, which were taken from 2006 January to April. In these epochs, the structure of the emission is much more complex. We can still distinguish two spots with coherent motions, also toward the southwest. Both emission spots are detected in epochs O, P, Q, and R. These two spots show a similar position angle and angular separation (of about 2.5 mas) in the four epochs. We call them "spot 2" and "spot 3" (see Fig. 4). Spot 2 is also detected in epoch M, but not in epoch N, and, conversely, spot 3 is detected in epoch N but not in epoch M. We discarded epochs H–L because the maser emission shows multiple blended peaks, which cannot be distinguished unambiguously. The positions of spots 1, 2, and 3 are listed in Table 3, and they are used in Sect. 3.3 to estimate the parallax of I16293.

It is clear from this analysis that the spots are very variable and that their associated emission lasts for only a few months. A second approach for the determination of the trigonometric parallax is to track the motion of the shock front, which is traced by the collection of several spots at each epoch, and then fit the positions of this shock front in the RA direction. We adopted the mean position of the spots associated with it, which were identified by their proximity in the maps, as the position of the shock front at each epoch. These positions are listed in Table 4 and are shown as blue strips in Fig. 3. In the epochs where we see a lot of structure in the emission (for example in epochs N and P) we only consider the spots at the expected positions according to the advancing motion of the shock front.

Having identified three main spots that persisted in at least four epochs and the mean positions of the shock front, we now proceed with the astrometric fits. For this purpose, we apply the single value decomposition (SVD) fitting scheme described by Loinard et al. (2007).

3.3. Astrometry

In radio astrometry, the source positions are commonly registered at multiple epochs spanning long periods, usually of one-year duration, in order to trace the full parallax sinusoid. The observations presented here cover only a time period of

Table 3. Detected epochs and positions of the different maser spots used for the astrometry.

JD	α (s) 16^h32^m	σ_α $\times 10^{-7}$ (s)	δ ('') $-24°28'$	σ_δ $\times 10^{-5}$ ('')
(Spot 1)				
2453626.46	22.8013945	8	36.48795	3
2453639.43	22.8012977	4	36.48899	2
2453657.36	22.8012641	9	36.48988	3
2453676.33	22.8012193	5	36.49008	2
(Spot 2)				
2453754.12	22.8013360	6	36.49466	2
2453797.00	22.8011462	3	36.49585	2
2453811.96	22.8010585	7	36.49685	3
2453824.92	22.8008828	3	36.49764	2
2453838.88	22.8007241	6	36.49905	2
(Spot 3)				
2453771.07	22.8013353	9	36.49693	3
2453797.00	22.8012091	6	36.49824	3
2453811.96	22.8011170	6	36.49876	3
2453824.92	22.8009297	4	36.50005	2
2453838.88	22.8007789	6	36.50114	2

seven months. However, the first and last data were taken close to the time when the maximum parallax angle is reached, i.e., in September and March. Radio astrometry has been performed with similar time spans for other star-forming regions with good determination of parallaxes (e.g., Hirota et al. 2008; Kim et al. 2008). As described in Sect. 3.2, only three spots are detected in four or five epochs each (see Table 3), with time spans of only 2 to 3 months. The shock front, on the other hand, is tracked over the full seven months. We can compare the astrometry derived from the individual spots to that derived from the positions of the shock front.

We first fit each of the three maser spots separately (Fig. 5, first panel). The resulting values of the trigonometric parallax and distance from these fits are given in Table 5. Since the results from the three fits are consistent with each other within
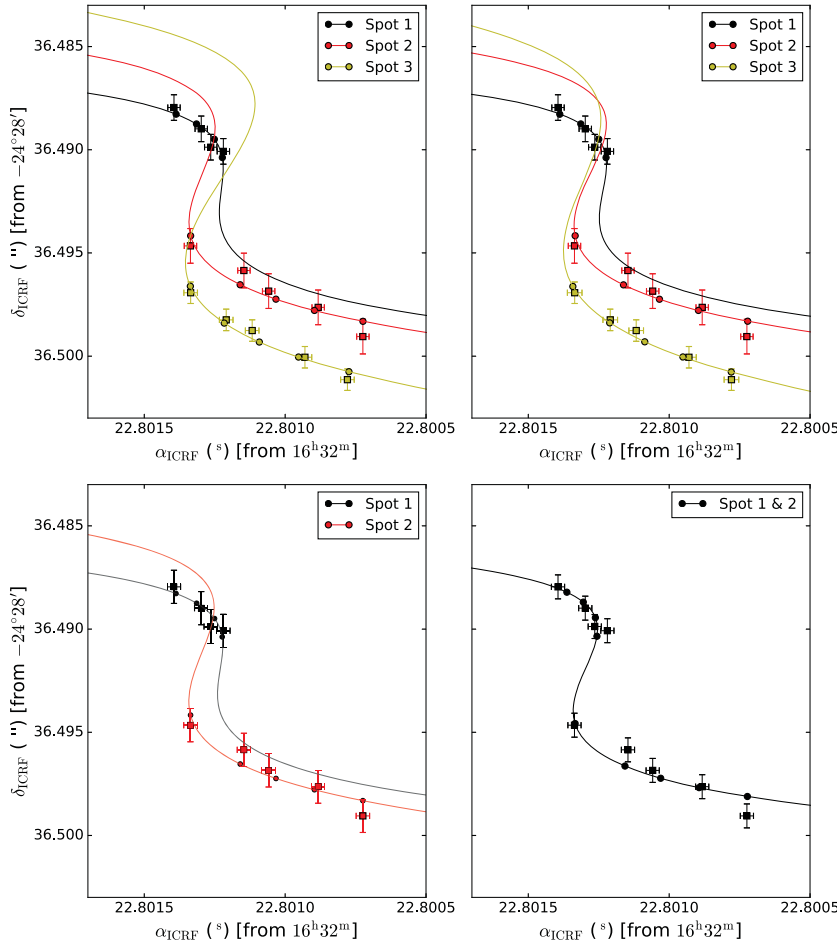
Fig. 5. Resulting fits to the water maser spots detected toward I16293 (see Table 5). The black, red, and yellow lines show the best fits for spot 1, 2, and 3, respectively. The solid squares with the error bars indicate measured positions and their corresponding uncertainties. The solid circles mark the expected positions from the fits at the observing epochs. *Top left*: individual fits to each of the three maser spots. *Top right*: simultaneous fit assuming that the parallax is the same for the three spots. *Bottom left*: simultaneous fit to positions of Spot 1 and 2, by allowing them to have a positional offset and different proper motions. *Bottom right*: simultaneous fit to spots 1 and 2, assuming that they belong to the same cloudlet.

Table 4. Observed epochs and RA positions of the water maser shock front.

Epoch	Julian date	RA (s) 16^h32^m	σ_{RA} $\times10^{-6}$ (s)
D	2453626.46	22.801381	2
E	2453639.43	22.801298	1
F	2453657.36	22.801242	8
G	2453676.33	22.801173	6
H	2453687.30	22.801209	4
I	2453702.26	22.801206	4
J	2453713.23	22.801244	4
K	2453727.19	22.801277	5
L	2453742.15	22.801318	5
M	2453754.12	22.801336	4
N	2453771.07	22.801303	10
O	2453797.00	22.801178	2
P	2453811.96	22.801090	6
Q	2453824.92	22.800915	3
R	2453838.88	22.800752	8

1σ, we simultaneously fit the three maser spots by requiring a single parallax, and allowing the proper motions to vary between the different spots. The parallax obtained in this case is 7.4 ± 1.1 mas, corresponding to a distance of 135^{+23}_{-16} pc. The values of the proper motions do not significantly change when compared to those derived from the individual fits.

We note that if we extrapolate the positions of spot 1 to the epochs when spot 2 is detected (by using the best models from the previous two fits), then their corresponding positions are consistent within the errors. This suggests that these two spots are related and may indeed correspond to the same gas condensation (or cloudlet; Sanna et al. 2017a). To test this hypothesis, we perform a simultaneous fit to both spots and consider that there is a positional offset between them. The resulting astrometric parameters from this fit are also given in Table 5 and are shown in Fig. 5 (bottom left). The best-fit parallax yields a distance of 141^{+30}_{-21} pc. It is important to mention that the resulting positional offset is relatively small and the proper motions of the spots are consistent within errors (see Table 5). Thus, an additional fit was done by assuming that spots 1 and 2 trace the motion of the same cloudlet. From this fit, we found that the parallax uncertainty is at least a factor of two lower than that obtained in the previous fits. However, given the strong variability of the maser emission, the spots could be bright at different times, and thus we consider the fit with nonzero positional offset to be more robust.

Second, we performed an astrometric fit to the mean position of the shock front and derive a trigonometric parallax of $\pi = 6.6 \pm 0.6$ mas, corresponding to a distance of $d = 152^{+16}_{-12}$ pc. We show the parallax sinusoid from this fit in Fig. 6, and give the resulting parameters in Table 5. The values of the parallax derived from the fits to the three main spots are in good agreement with that obtained from the fit to the R.A. motion of the shock front.

Table 5. Parameters obtained from the astrometric fits. The systematic errors that were added quadratically are also presented.

Fit	Spot	$\pi \pm \sigma_\pi$ (mas)	d (pc)	$\mu_\alpha \cos\delta \pm \sigma_{\mu_\alpha \cos\delta}$ (mas yr^{-1})	$\mu_\delta \pm \sigma_{\mu_\delta}$ (mas yr^{-1})	Offsets (mas) α	δ	Post-fit rms (mas) α	δ	Systematic errors (mas) α	δ
	1	6.9 ± 4.7	145^{+314}_{-59}	-44 ± 19	-13 ± 6	...	...	0.17	0.32	0.33	0.63
Individual	2	7.1 ± 1.3	141^{+30}_{-21}	-39 ± 2	-16 ± 5	...	...	0.21	0.54	0.33	0.84
	3	8.3 ± 2.1	120^{+40}_{-24}	-37 ± 3	-21 ± 4	...	...	0.24	0.34	0.36	0.52
	1			-47 ± 5	-13 ± 6	...	...	0.17	0.32	0.33	0.62
Simultaneous	2	7.4 ± 1.1	135^{+23}_{-16}	-40 ± 2	-16 ± 5	...	...	0.22	0.54	0.33	0.84
	3			-38 ± 3	-21 ± 4	...	...	0.25	0.33	0.39	0.52
	1			-42 ± 3	-13 ± 8	0.0 ± 0.0	0.0 ± 0.0	0.17	0.32	0.36	0.80
With offset		7.1 ± 1.3	141^{+30}_{-21}								
	2			-36 ± 2	-16 ± 5	-0.4 ± 1.0	1.4 ± 2.3	0.22	0.54	0.36	0.80
Spots 1 & 2	1+2	7.1 ± 0.5	141^{+10}_{-9}	-39 ± 2	-13 ± 1	...	...	0.29	0.48	0.36	0.58
Shock front	–	6.6 ± 0.6	152^{+16}_{-12}	-32 ± 3	...	...	...	0.14	...	0.64	...

The correlation coefficient matrices for all fits are shown in Appendix A. From these matrices we noticed a high (anti-) correlation between the parallax and the other fitted parameters in all the fits, as is expected given the short timescale covered by the observations. To check the reliability of our results, in view of these high correlations, we performed a series of Monte Carlo simulations which are presented in Appendix B. The result from these simulations is that, given the statistical and systematic errors in our measurements, the true astrometric parameters can be recovered from our fits even when the observations cover a period of only 3–7 months. The worst case is the individual fit to spot 1; this spot was only detected in four epochs and, consequently, the uncertainties on the fitted parameters are significantly larger.

4. Discussion

4.1. Distance to I16293

As we mentioned in the introduction, Imai et al. (2007) obtained a distance of 178^{+18}_{-37} pc to I16293 by measuring the trigonometric parallax of water masers associated with this YSO. Imai et al. (2007) mentioned that the most severe factor causing their modest astrometric accuracy was the temporal variation in the brightness structure of the maser spots they detected. If water masers have short lifetimes of a few months, as is the case with water masers in I16293, it is possible to misidentify maser spots even from one epoch to the next. Taking into account this possibility, these authors performed several fits by using different combinations of observed positions. By excluding the oddest positions, they obtained an upper limit to the trigonometric parallax of 7.1 mas (corresponding to a lower limit in the distance of $d = 141$ pc). In the following, we discuss the differences between our analysis and that of Imai et al. (2007).
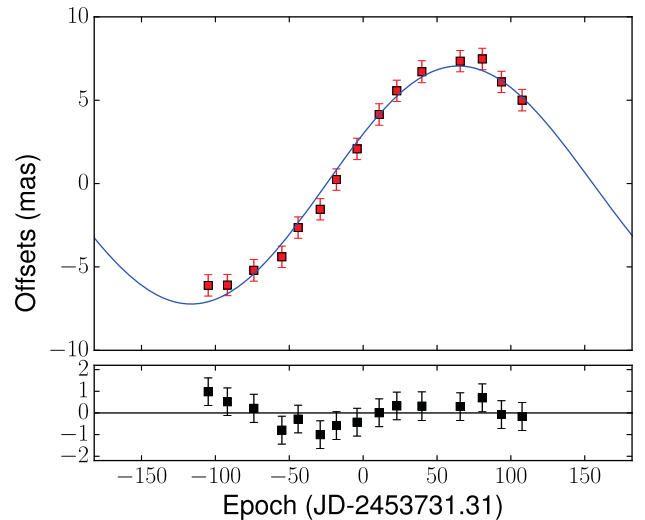
Fig. 6. Parallax fit to the mean positions of the shock front. *Top:* parallax sinusoid from the best fit to these data (blue line). The red squares are the mean positions of the shock front. In both cases, we have subtracted the proper motion and the RA position at JD 2453731.31 (the mean epoch from our observations) from the best fit. *Bottom:* residuals in right ascension.

The first difference comes from their criterion for the selection of maser spots. They assumed that the brightest peak always traces the same spot, and used its measured positions for the astrometric fits. As we can see in Fig. 4, this assumption is not valid, for instance from epoch M to epoch N. Additionally, the radial velocities of their spots vary from one epoch to the other by ~1 km s^{-1}, suggesting that they are not tracing the same gas
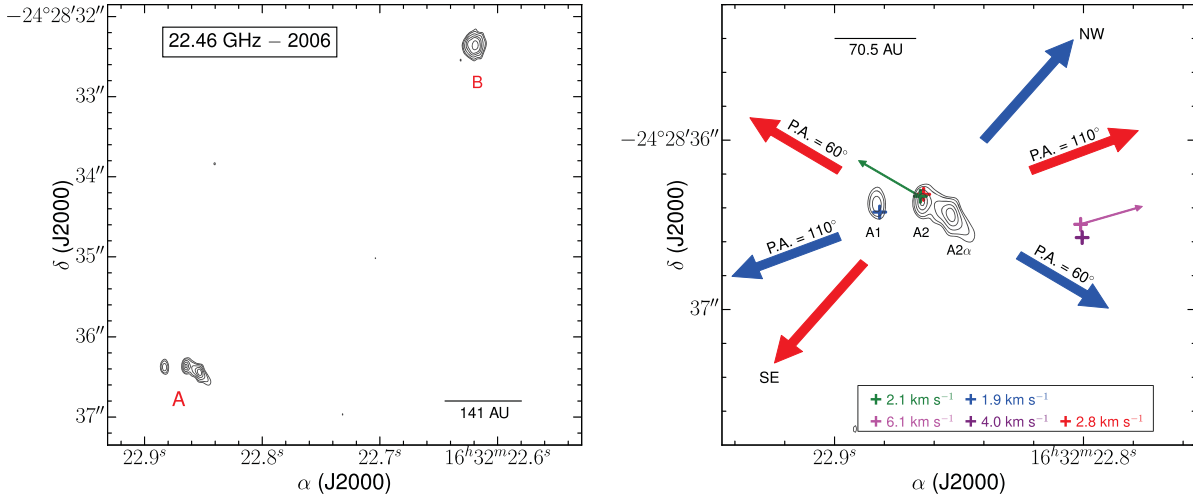
Fig. 7. Stellar system I16293. *Left*: continuum map at 22 GHz taken with the VLA on 2006 February 10. The noise level of this image is 47 μJy beam^{-1}, and the contour levels are -4, 4, 6, 10, 15, 20, and 30 times this value. *Right*: zoom-in on source A. Shown are the sources composing this system: A1, A2, and the ejecta A2α. Also shown are the directions of the three outflows (blue and red arrows). The colored crosses represent the positions of the maser spots detected at different velocities (see Table 2). The magenta cross indicates the position of the masers at 6.1 km s^{-1} and the magenta arrow arising from it shows the mean proper motion direction, while the green arrow indicates the proper motion direction of the maser spot at 2.1 km s^{-1} identified on epochs I and J. The blue cross indicates the position of the maser emission detected in epoch R at 1.9 km s^{-1}, very close to source A1, and the red cross marks the position of the maser spot at 2.8 km s^{-1} close to source A2 and detected in epoch F. The position of the maser spot detected in epoch R at 4.0 km s^{-1} is shown with a purple cross. The arrow lengths do not represent velocity magnitudes, but only the direction of the outflows and the proper motions of the masers. Also included is a reference of the physical scale on both images.

(e.g., Moscadelli et al. 2006). Finally, the time intervals between their observed epochs range from 22 days up to three months, whereas our measurements are spaced 15 days apart, on average. This higher cadence improves our ability to trace the same maser spots and, particularly, the shock front in time.

The estimated trigonometric parallaxes from all our fits agree with the lower limit of 141 pc obtained by Imai et al. (2007). However, the fits that exhibit the smallest parallax errors may be affected by the assumptions we made regarding the associations between the detected spots (see Sects. 3.2 and 3.3). The most conservative result is thus the fit "With offset" (Table 5) since it allows the spots to have non-identical positions and also spans the longest period of observation (7 months). The resulting trigonometric parallax from this fit is 7.1 ± 1.3 mas, corresponding to a conservative value of 141^{+30}_{-21} pc for the distance. This result also agrees within 1σ with a recent value of 147.3 ± 3.4 pc measured to three other systems in Lynds 1689 (Ortiz-León et al. 2017).

4.2. Relationship between water maser emission and molecular outflows in I16293

In Fig. 7 we show a radio continuum map of the I16293 system at 22.46 GHz, as observed with the VLA on 2006 February 10 (and previously reported by Pech et al. 2010). This image shows the sources A and B that were introduced in Sect. 1. On the right side of this figure we zoom in on source A and show its two components, A1 and A2, and the A2α ejecta as well. In Fig. 7 the magenta cross shows the position of the persistent water maser peak observed at $v_{\text{LSR}} = 6.1$ km s^{-1}.

The proper motions of the continuum sources A1 and A2 are $(-3.0 \pm 0.4, -27.9 \pm 0.8)$ mas yr^{-1} and $(-7.8 \pm 0.6, -21.8 \pm 0.5)$ mas yr^{-1}, respectively (Hernández-Gómez et al., in prep.). To convert proper motions into transverse velocities we use the

relation 1 mas $\equiv$ 0.67 km s^{-1}, which is appropriate for a distance of 141 pc. Here, we have measured a proper motion of $(-39 \pm 2, -13 \pm 1)$ mas yr^{-1} for the persistent maser cloudlet (Spots 1 and 2). The proper motion in declination of this cloudlet is similar in magnitude and direction to that of source A2, but is significantly larger in the R.A. direction. After subtracting the velocity vector of source A2, we found that the intrinsic proper motion of the spot is $(-31.2 \pm 2.1, 8.8 \pm 1.1)$ mas yr^{-1} = $(-20.9 \pm 1.4, 5.9 \pm 0.7)$ km s^{-1}, i.e., toward the northwest of the continuum source. It is indicated with the magenta arrow in Fig. 7.

Another maser spot at a radial velocity of 2.1 km s^{-1} was detected in the consecutive epochs I and J and is indicated in Fig. 7 with a green cross. We measured its positions and corrected for the trigonometric parallax in order to arrive at a proper motion of $(43.6 \pm 0.9, 7.5 \pm 1.9)$ mas yr^{-1}. Thus, its relative proper motion with respect to source A2 is $(51.4 \pm 0.9, 29.3 \pm 2.0)$ mas yr^{-1} = $(34.5 \pm 0.7, 19.7 \pm 1.3)$ km s^{-1}, i.e., toward the northeast of the continuum source, as indicated by the green arrow in Fig. 7. The maser spots at other radial velocities were only detected once, and their positions are shown in Fig. 7 as crosses of different colors. We note that two of them are close to source A2 and the other is close to source A1.

As mentioned before, several molecular outflows have been observed towards I16293 (see, e.g., Mizuno et al. 1990; Loinard et al. 2013; Girart et al. 2014). There are two bipolar outflows arising from source A with position angles (P.A.) of approximately 60° and 110°. There is also a third outflow in the SE-NW direction extending between sources A and B. The red- and blueshifted lobes have radial velocities between 6 and 20 km s^{-1}, and -10 and 2 km s^{-1}, respectively (Mizuno et al. 1990). The direction of the lobes of these three outflows are also indicated in Fig. 7. The water masers in I16293 are at the starting point of these much larger scale outflows. Given that the water maser shocks are usually found at the base of YSOs outflows (Torrelles

et al. 2003; Sanna et al. 2012), we suggest that the maser emission at 2.1 km s^{-1} and at 6.1 km s^{-1} are associated with these outflows. In particular, the radial velocity, position, and proper motions of the spot at 6.1 km s^{-1} suggest that this is directly related to the redshifted lobe of the outflow with PA = 110°. The radial velocity of the maser spot at 2.1 km s^{-1} suggests that it may be associated with a blueshifted lobe, possibly with the outflow with PA = 110°. However, the direction of its proper motions are similar to the redshifted lobe of the outflow with PA = 60°. Thus, we cannot unambiguously associate the maser emission with a specific flow.

5. Conclusions

We analyzed 15 archival VLBA observations at 22.2 GHz to measure the trigonometric parallax of water masers associated with the YSO I16293 in the Ophiuchus molecular cloud, and to determine its distance. In our analysis the main source of uncertainty is the maser variability and the short time span covered by the observations.

After a careful analysis of the maps, we identified three maser spots, and fitted their displacement on the plane of the sky as being due to a linear motion and the reflex motion of the trigonometric parallax. Additionally, we also tracked the position of the shock front and fitted its motion in the RA direction. All our fits agree within the errors, and suggest a distance of around 140 pc. Our most conservative approach yields a trigonometric parallax of 7.1 ± 1.3 mas, corresponding to a distance of 141^{+30}_{-21} pc.

This distance estimate is smaller than that reported by Imai et al. (2007) by nearly 40 pc, but the two results are consistent within 1σ. Our value for the I16293 distance is also 21 pc larger than the 120 pc obtained by Loinard et al. (2008) based on two objects in L1688 (their results were later corrected by Ortiz-León et al. (2017), who derived greater distances for both objects). Furthermore, our measured distance is in good agreement with recent measurements by Ortiz-León et al. (2017) of trigonometric parallaxes of magnetically active YSOs in the Ophiuchus complex, and especially in the L1689 cloud at a distance of 147.3 ± 3.4 pc. Thus, our results support the widely held view that I16293 is a member of the L1689 cloud in Ophiuchus.

The radial velocities and direction of the relative proper motions of the water masers (with respect to source A2), agrees with those of the outflow emission previously reported in this system. In the case of the water masers with v_{LSR} = 6.1 km s^{-1} it was possible to associate them with the redshifted lobe of the outflow with a PA = 110°.

References

Chandler, C. J., Brogan, C. L., Shirley, Y. L., & Loinard, L. 2005, ApJ, 632, 371
Claussen, M. J., Wilking, B. A., Benson, P. J., et al. 1996, ApJS, 106, 111
Condon, J. J. 1997, PASP, 109, 166
Dzib, S. A., Ortiz-León, G. N., Loinard, L., et al. 2016, ApJ, 826, 201
Girart, J. M., Estalella, R., Palau, A., Torrelles, J. M., & Rao, R. 2014, ApJ, 780, L11
Greisen, E. W. 2003, Information Handling in Astronomy – Historical Vistas, 285, 109 (Netherlands: Springer)
Hirota, T., Bushimata, T., Choi, Y. K., et al. 2008, PASJ, 60, 37
Imai, H., Nakashima, K., Bushimata, T., et al. 2007, PASJ, 59, 1107
Jørgensen, J. K., Bourke, T. L., Nguyen Luong, Q., & Takakuwa, S. 2011, A&A, 534, A100
Kim, M. K., Hirota, T., Honma, M., et al. 2008, PASJ, 60, 991
Loinard, L., Chandler, C. J., Rodríguez, L. F., et al. 2007, ApJ, 670, 1353
Loinard, L., Torres, R. M., Mioduszewski, A. J., & Rodríguez, L. F. 2008, ApJ, 675, L29
Loinard, L., Zapata, L. A., Rodríguez, L. F., et al. 2013, MNRAS, 430, L10
Mizuno, A., Fukui, Y., Iwata, T., Nozawa, S., & Takano, T. 1990, ApJ, 356, 184
Moscadelli, L., Testi, L., Furuya, R. S., et al. 2006, A&A, 446, 985
Mundy, L. G., Wootten, A., Wilking, B. A., Blake, G. A., & Sargent, A. I. 1992, ApJ, 385, 306
Ortiz-León, G. N., Loinard, L., Kounkel, M. A., et al. 2017, ApJ, 834, 141
Pech, G., Loinard, L., Chandler, C. J., et al. 2010, ApJ, 712, 1403
Reid, M. J., Menten, K. M., Brunthaler, A., et al. 2009, ApJ, 693, 397
Ridge, N. A., Di Francesco, J., Kirk, H., et al. 2006, AJ, 131, 2921
Sanna, A., Reid, M. J., Carrasco-González, C., et al. 2012, ApJ, 745, 191
Sanna, A., Moscadelli, L., Surcis, G., et al. 2017a, A&A, 603, A94
Sanna, A., Reid, M. J., Dame, T. M., Menten, K. M., & Brunthaler, A. 2017b, Science, 358, 227
Torrelles, J. M., Patel, N. A., Anglada, G., et al. 2003, ApJ, 598, L115
Urban, S., & Seidelmann, P. 2013, The Explanatory Supplement to the Astronomical Almanac (California, USA: University Science Books)
Wootten, A. 1989, ApJ, 337, 858

Appendix A: Correlation matrices

The purpose of this appendix is to show the correlations matrices for all the fits made to our data. In the following subsections we keep the name of the fits as they were introduced in Table 5.

A.1. Individual

Spot 1

	α	δ	$\mu_\alpha \cos(\delta)$	μ_δ	π
α	1.00	−0.21	−0.55	0.16	0.68
δ	−0.21	1.00	0.31	0.82	−0.31
$\mu_\alpha \cos(\delta)$	−0.55	0.31	1.00	−0.23	−0.99
μ_δ	0.16	0.82	−0.23	1.00	0.24
π	0.68	−0.31	−0.99	0.24	1.00

Spot 2

	α	δ	$\mu_\alpha \cos(\delta)$	μ_δ	π
α	1.00	−0.07	−0.27	−0.07	−0.93
δ	−0.07	1.00	−0.01	−0.94	0.07
$\mu_\alpha \cos(\delta)$	−0.27	−0.01	1.00	−0.01	−0.10
μ_δ	−0.07	−0.94	−0.01	1.00	0.08
π	−0.93	0.07	−0.10	0.08	1.00

Spot 3

	α	δ	$\mu_\alpha \cos(\delta)$	μ_δ	π
α	1.00	−0.23	−0.79	−0.08	−0.97
δ	−0.23	1.00	0.15	−0.92	0.23
$\mu_\alpha \cos(\delta)$	−0.79	0.15	1.00	0.05	0.62
μ_δ	−0.08	−0.92	0.05	1.00	0.08
π	−0.97	0.23	0.62	0.08	1.00

A.2. Simultaneous

	$\alpha[1]$	$\delta[1]$	$\mu_\alpha \cos(\delta)[1]$	$\mu_\delta[1]$	$\alpha[2]$	$\delta[2]$	$\mu_\alpha \cos(\delta)[2]$	$\mu_\delta[2]$	$\alpha[3]$	$\delta[3]$	$\mu_\alpha \cos(\delta)[3]$	$\mu_\delta[3]$	π
$\alpha[1]$	1.00	−0.11	−0.74	−0.04	−0.18	0.07	0.70	−0.05	0.79	−0.05	0.07	−0.06	−0.88
$\delta[1]$	−0.11	1.00	0.04	−0.95	0.03	−0.01	−0.10	0.01	−0.11	0.01	−0.01	0.01	0.12
$\mu_\alpha \cos(\delta)[1]$	−0.74	0.04	1.00	0.01	0.07	−0.03	−0.28	0.02	−0.32	0.02	−0.03	0.02	0.35
$\mu_\delta[1]$	−0.04	−0.95	0.01	1.00	0.01	−0.00	−0.03	0.00	−0.04	0.00	0.00	0.00	0.04
$\alpha[2]$	−0.18	0.03	0.07	0.01	1.00	−0.02	0.41	0.01	−0.19	0.01	−0.02	0.01	0.21
$\delta[2]$	0.07	−0.01	−0.03	−0.00	−0.02	1.00	0.06	0.96	0.07	0.00	0.01	0.00	−0.07
$\mu_\alpha \cos(\delta)[2]$	0.70	−0.10	−0.28	−0.03	0.41	0.06	1.00	−0.04	0.72	−0.05	0.07	−0.05	−0.8
$\mu_\delta[2]$	−0.05	0.01	0.02	0.00	0.01	0.96	−0.04	1.00	−0.05	0.00	0.00	0.00	0.06]
$\alpha[3]$	0.79	−0.11	−0.32	−0.04	−0.19	0.07	0.72	−0.05	1.00	−0.06	−0.34	−0.06	−0.90
$\delta[3]$	−0.05	0.01	0.02	0.00	0.01	0.00	−0.05	0.00	−0.06	1.00	−0.01	−0.94	0.06
$\mu_\alpha \cos(\delta)[3]$	0.07	−0.01	−0.03	0.00	−0.02	0.01	0.07	0.00	−0.34	−0.01	1.00	−0.01	−0.08
$\mu_\delta[3]$	−0.06	0.01	0.02	0.00	0.01	0.00	−0.05	0.00	−0.06	−0.94	−0.01	1.00	0.06
π	−0.88	0.12	0.35	0.04	0.21	−0.07	−0.80	0.06	−0.90	0.06	−0.08	0.06	1.00

A.3. With offset

	$\alpha[1]$	$\mu_\alpha \cos(\delta)[1]$	$\mu_\alpha \cos(\delta)[2]$	Offset(α)	π
$\alpha[1]$	1.00	−0.90	−0.09	−0.93	−0.98
$\mu_\alpha \cos(\delta)[1]$	−0.90	1.00	0.08	0.82	−0.83
$\mu_\alpha \cos(\delta)[2]$	−0.09	0.08	1.00	−0.26	−0.09
Offset(α)	−0.93	−0.82	0.26	1.00	−0.93
π	−0.98	−0.83	−0.09	−0.93	1.00

	$\delta[1]$	$\mu_\delta[1]$	$\mu_\delta[2]$	Offset(δ)	π
$\delta[1]$	1.00	−0.75	−0.78	−0.84	−0.98
$\mu_\delta[1]$	−0.75	1.00	0.52	0.63	−0.65
$\mu_\delta[2]$	−0.78	0.52	1.00	0.33	0.80
Offset(δ)	−0.84	0.63	0.33	1.00	0.82
π	−0.98	−0.65	0.80	0.82	1.00

A.4. Spot 1 & 2

	α	δ	$\mu_\alpha \cos(\delta)$	μ_δ	π
α	1.00	−0.01	−0.27	0.07	0.22
δ	−0.01	1.00	0.04	−0.21	−0.04
$\mu_\alpha \cos(\delta)$	−0.27	0.04	1.00	−0.30	−0.96
μ_δ	0.07	−0.21	−0.30	1.00	0.31
π	0.22	−0.04	−0.96	0.31	1.00

A.5. Shock front

	α	$\mu_\alpha \cos(\delta)$	π
α	1.00	0.56	−0.60
$\mu_\alpha \cos(\delta)$	0.56	1.00	−0.94
π	−0.60	−0.94	1.00

Appendix B: Monte Carlo simulations

To test the reliability of our results, particularly in relation to the short observing time span, we performed the following simulations. We created new data sets consisting of simulated observed positions at the epochs when the spots 1, 2, and 3 were detected. We then evaluated their positions following the equations appropriated for a particle moving with a linear proper motion (μ) plus the trigonometric parallax (π) as

$$P(0) = X(0) + f_\pi(0) * \pi,$$
$$P(1) = X(0) + \mu * t(1) + f_\pi(1) * \pi,$$
$$\vdots$$
$$P(n) = X(0) + \mu * t(n) + f_\pi(n) * \pi,$$

(B.1)

where the parameter are as follows: $P(n)$ is the simulated position at the epoch n; the start position, $X(0)$, is the position of our detected water maser spots in their first detection; and $f_\pi(n)$ is the projection of the parallactic ellipse at epoch n (e.g., Urban & Seidelmann 2013).

To each simulated position we added a random error drawn from a normal distribution of mean equal to zero and standard deviations of 0.4 mas and 0.8 mas in R.A. and Dec., respectively. These values are similar to the maximum values of our systematic errors ($E_{\rm sys}$; see Table 5). Each data set was then fitted using the same scheme that we used for the actual observations.

We created 10 000 realizations of the simulated positions and then calculated the mean and standard deviation of the resulting distributions of the astrometric parameters. The input values used in the simulation and the resulting values are given in Table B.1. As an example, a distribution histogram of one of the simulation sets is presented in Fig. B.1.

Table B.1. Input and output parameters of the Monte Carlo simulations.

|			Input parameters			Output parameters							
		π	d	$\mu_\alpha \cos\delta$	μ_δ	π		d		$\mu_\alpha \cos\delta$		μ_δ	
	Test	(mas)	(pc)	(mas yr^{-1})	(mas yr^{-1})	(mas)		(pc)		(mas yr^{-1})		(mas yr^{-1})	
Fit	particle					Mean	SD	Mean	SD	Mean	SD	Mean	SD
	1					8.1	3.7	124	57	−40.2	3.6	−20.5	7.4
	2	8.3333	120	−40	−20	8.3	1.5	121	22	−40.1	2.2	−20.2	4.5
	3					8.2	2.3	122	34	−40.3	3.5	−20.3	5.4
	1					6.8	3.9	148	85	−40.1	3.5	−20.3	7.3
Individual	2	6.7889	147.3	−40	−20	6.7	1.5	149	34	−40.1	2.2	−20.2	4.5
	3					6.8	2.3	147	50	−40.1	3.6	−20.1	5.6
	1					5.4	3.8	184	129	−40.2	3.5	−20.4	7.5
	2	5.5556	180	−40	−20	5.5	1.5	182	51	−40.1	2.2	−20.2	4.7
	3					5.4	2.3	185	78	−40.1	3.5	−20.3	5.7
	1									−40.3	7.0	−20.5	7.7
	2	8.3333	120	−40	−20	8.3	1.5	120	21	−40.1	2.2	−20.3	4.4
	3									−40.1	3.1	−20.3	5.6
	1									−40.2	6.8	−20.2	7.8
Simultaneous 1	2	6.7889	147.3	−40	−20	6.7	1.5	148	32	−40.0	2.2	−20.2	4.5
	3									−40.1	3.1	−20.2	5.6
	1									−40.3	6.8	−20.3	7.6
	2	5.5556	180	−40	−20	5.5	1.5	180	48	−40.1	2.2	−20.2	4.6
	3									−40.1	3.1	−20.4	5.5
	1			−45	−25					−45.6	6.8	−25.0	8.0
	2	8.3333	120	−35	−15	8.3	1.4	120	21	−35.1	2.2	−15.1	4.6
	3			−40	−20					−40.1	3.2	−20.1	5.5
	1			−45	−25					−45.5	7.0	−25.3	7.8
Simultaneous 2	2	6.7889	147.3	−35	−15	6.8	1.5	147	32	−35.1	2.2	−15.2	4.5
	3			−40	−20					−40.1	3.0	−20.1	5.6
	1			−45	−25					−40.2	3.6	−20.5	7.4
	2	5.5556	180	−35	−15	5.5	1.5	180	57	−40.1	2.2	−20.2	4.7
	3			−40	−20					−40.1	3.5	−20.3	5.7
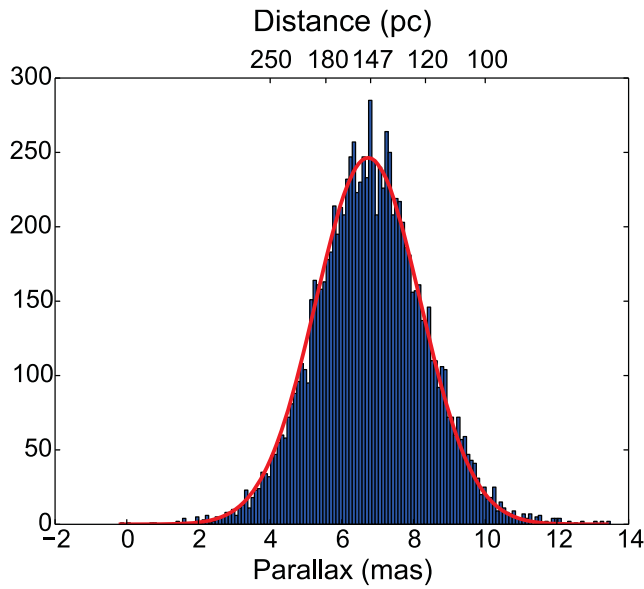
Fig. B.1. Distribution histogram of the simulation set corresponding to the Simultaneous 1 set, at the input distance 147.3 pc.

Chapter 3

Sobre la naturaleza de las fuentes compactas en IRAS 16293-2422

Presentamos un estudio observacional de las propiedades de las componentes individuales del sistema protoestelar IRAS 16293-2422 basados en observaciones multi-época con el VLA (3–45 GHz) y ALMA (220–690 GHz). Todas las fuentes dentro de la fuente A en este sistema, llamadas A1, A2, A2α, A2β y A2δ, se encuentran resueltas en nuestras observaciones. Hemos seguido la astrometría absoluta de las fuentes A1, A2 y B en un período de tiempo de 30 años. Mediciones previas han mostrado que el ángulo de posición entre las fuentes A1 y A2 se ha incrementado con el tiempo, lo cual es consistente con el escenario en el que A1 y A2 forman un sistema binario. Sin embargo, nuestros datos demuestran que desde 2015, el ángulo de posición ha comenzado de disminuir. Esto podría indicar que A1 corresponde más bien al impacto en el material circundante de un jet que precesa, o que A1/A2 son dos miembros de un sistema jerárquico triple. Hemos estudiado el espectro continuo de ambas fuentes A y B y confirmamos que la emisión de la fuente A tiene una contribución de gas ionizado (probablemente debido a la presencia de jets en esta fuente), y una contribución de emisión térmica de polvo. Los índices espectrales negativos medidos para A2α, A2β y A2δ son consistentes con emisión libre-libre delgada proveniente de una eyección ionizada de baja densidad. Los valores positivos para A1 and A2 son consistentes con emisión libre-libre parcialmente ópticamente gruesa, la cual es típica para jets térmicos de objetos estelares jóvenes. Por otra parte, la fuente B muestra un espectro en forma de ley de potencias que es compatible con emisión térmica de polvo, inclusive para las longitudes de onda más largas. Hemos calculado el exceso de emisión libre-libre en el espectro de la fuente B a partir de su luminosidad y concluimos que esta fuente no tiene ningún jet ionizado prominente. Además, el tamaño de la fuente B aumenta con la frecuencia en los datos del VLA (hasta 50 GHz), mientras permanece aproximadamente constante en los datos de ALMA (de 220 GHz a 690 GHz). Esto se interpreta en términos de la fuente B siendo una estructura de polvo con altas densidad y temperatura centrales. La variabilidad en el tiempo también ha sido explorada en este trabajo. Confirmamos que la fuente A, comparada con la fuente B, muestra una fuerte variabilidad (de alrededor de 50%) en el rango centimétrico.

Chapter 3

Sur la nature des sources compactes dans IRAS 16293-2422

Nous présentons une étude observationnelle des composants individuels du système proto-stellaire IRAS 16293-2422, basée sur des observations VLA (3–45 GHz) multi-époques et ALMA (220–690 GHz). Toutes les sources du composant A dans ce système, appelées A1, A2, A2α, A2β et A2δ, sont résolues dans nos observations. Nous avons suivi l'astrométrie absolue des sources A1, A2 et B sur une période de 30 ans. Des mesures antérieures avaient montré que l'angle de position entre les sources A1 et A2 avait augmenté avec le temps, ce qui est en accord avec le scénario selon lequel A1 et A2 seraient un système binaire. Cependant, nos données démontrent que depuis 2015, l'angle de position a commencé à diminuer. Cela pourrait indiquer que A1 correspond à l'impact d'un jet en précession sur la matière environnante ou que A1/A2 sont deux membres d'un système triple hiérarchique serré. Nous avons étudié les spectres du continuum des sources A et B et avons confirmé que l'émission de la source A avait une contribution en provenance de gaz ionisé (probablement due aux jets issus de cette source) et une contribution due à l'émission thermique de poussières. Les indices spectraux legèrement negatifs mesurés pour A2α, A2β et A2δ sont cohérents avec une émission libre-libre optiquement mince provenant d'éjecta ionisés de faible densité. Les valeurs positives pour A1 et A2 correspondent à une émission libre-libre partiellement op-tiquement épaisse, attendue pour les jets thermiques de jeunes objets stellaires. D'autre part, la source B présente un spectre de loi de puissance compatible avec l'émission thermique de poussières, même aux plus grandes longueurs d'onde. Nous avons calculé l'excès d'émission libre-libre attendue dans le spectre de la source B à partir de sa luminosité et nous concluons que cette source ne génère aucun jet ionisé puissant. En outre, la taille de la source B aug-mente avec la fréquence dans les données VLA (jusqu'à 50 GHz), tandis qu'elle reste à peu près constante dans les données ALMA (de 220 à 690 GHz). Nous interprétons cela comme une preuve que la source B est une structure poussiéreuse avec une densité et une température centrale élevées. La variabilité dans le temps a aussi été explorée dans ce travail, nous avons confirmé que la source A, par rapport à la source B, présentait une forte variabilité (d'environ 50%) dans le domaine centimétrique.

Chapter 3

On the nature of the compact sources in IRAS 16293-2422

We present an observational study of the properties of the individual components of the proto-stellar system IRAS 16293-2422 based in multi-epoch VLA (3–45 GHz) and ALMA (220–690 GHz) observations. All sources within source A in this system, called A1, A2, A2α, A2β and A2δ, are resolved in our observations. We have followed the absolute astrometry of sources A1, A2 and B over a period of 30 years. Previous measurements have shown that the position angle between sources A1 and A2 has increased over time, which is consistent with the scenario of A1 and A2 being a binary system. However, our data demonstrates that since 2015, the position angle has begun to decrease. This might indicate that A1 corresponds to the impact of a precessing jet onto the surrounding material, or that A1/A2 are two members of a tight hierarchical triple system. We have studied the continuum spectra from both A and B sources and confirmed that the emission from source A has a contribution from ionized gas (probably due to the presence of jets in this source), and a contribution from thermal dust emission. The measured negative spectral indices for A2α, A2β and A2δ are consistent for thin free-free emission from low density ionized ejecta. The positive values for A1 and A2 are consistent with partially optically thick free-free emission expected for the thermal jet of young stellar objects. On the other hand, source B shows a power-law spectrum that is compatible with thermal dust emission even at the largest wavelengths. We have computed the expected free-free emission excess in the spectrum of source B from its luminosity and conclude here that this source does not drive any powerful ionized jet. Also, the size of source B seems to increase with frequency in the VLA data (up to 50 GHz), while it remains roughly constant in the ALMA data (from 220 to 690 GHz). This is interpreted in terms of source B being a dusty structure with high central density and temperature. The variability over time has also been explored in this work. We confirmed that source A, compared with source B, shows a strong variability (of about 50%) in the centimeter range.

ON THE NATURE OF THE COMPACT SOURCES IN IRAS 16293–2422 SEEN IN AT CENTIMETER TO SUB-MILLIMETER WAVELENGTHS

ANTONIO HERNÁNDEZ-GÓMEZ,[1,2] LAURENT LOINARD,[1,3] CLAIRE J. CHANDLER,[4] LUIS F. RODRÍGUEZ,[1] LUIS A. ZAPATA,[1] DAVID J. WILNER,[5] PAUL T.P. HO,[6,7] EMMANUEL CAUX,[2] DAVID QUÉNARD,[8] SANDRINE BOTTINELLI,[2] CRYSTAL L. BROGAN,[9] LEE HARTMANN,[10] AND KARL M. MENTEN[11]

[1]*Instituto de Radioastronomía y Astrofísica, Universidad Nacional Autónoma de México, 58089 Morelia, Mexico*
[2]*IRAP, Université de Toulouse, CNRS, UPS, CNES, Toulouse, France*
[3]*Instituto de Astronomía, Universidad Nacional Autónoma de México, Apartado Postal 70-264, 04510 Cuidad de México, Mexico*
[4]*National Radio Astronomy Observatory, 1003 Lopezville Rd, Socorro, NM 87801, USA*
[5]*Harvard-Smithsonian Center for Astrophysics, 60 Garden Street, Cambridge, MA 02138, USA*
[6]*Institute of Astronomy and Astrophysics, Academia Sinica, P.O. Box 23-141, Taipei 10617, Taiwan*
[7]*East Asian Observatory, 660 N. Aohoku Place University Park, Hilo, Hawaii 96720, USA*
[8]*School of Physics and Astronomy, Queen Mary University of London, Mile End Road, London E1 4NS, UK*
[9]*National Radio Astronomy Observatory, 520 Edgemont Rd, Charlottesville, VA 22903, USA*
[10]*Department of Astronomy, University of Michigan, 1085 S. University Ave., Ann Arbor, MI 48109, USA*
[11]*Max-Planck-Institut für Radioastronomie, Auf dem Hügel 69, D-53121 Bonn, Germany*

ABSTRACT

We present multi-epoch continuum observations of the Class 0 protostellar system IRAS 16293–2422 taken with the Very Large Array (VLA) at multiple wavelengths between 7 mm and 15 cm (41 GHz down to 2 GHz), as well as single-epoch Atacama Large Millimeter/submillimeter Array (ALMA) continuum observations covering the range from 0.4 to 1.3 mm (700 GHz down to 230 GHz). The new VLA observations confirm that source A2 is a protostar driving episodic mass ejections, and reveal the complex relative motion between A2 and A1. The spectrum of component B can be described by a single power law ($S_\nu \propto \nu^{2.28}$) over the entire range from 3 to 700 GHz (10 cm down to 0.4 mm), suggesting that the emission is entirely dominated by dust even at $\lambda = 10$ cm. Finally, the size of source B appears to increase with frequency up to 41 GHz, remaining roughly constant (at $0\overset{''}{.}39 \equiv 55$ AU) at higher frequencies. We interpret this as evidence that source B is a dusty structure of finite size that becomes increasingly optically thick at higher frequencies until, in the millimeter regime, the source becomes entirely optically thick. The lack of excess free-free emission at long wavelengths, combined with the absence of high-velocity molecular emission indicates that source B does not drive a powerful outflow, and might indicate that source B is at a particularly early stage of its evolution.

1. INTRODUCTION

A paradigm exists for the formation of isolated low-mass stars through the gravitational collapse of dense cores embedded in a large molecular cloud (Shu et al. 1987). The different evolutionary stages considered in this scenario, from Class 0 to Class I, Flat Spectrum, and Class II and III sources, have been amply described in the literature (Lada & Wilking 1984; Andre et al. 1993; Greene et al. 1994). Although many features of this paradigm can be extended to low-mass stars forming in multiple systems, several standing questions remain regarding the formation and early evolution of multiple systems. For instance, the dominant route(s) leading to the formation of multiple stellar systems are still debated. The two leading (and not necessarily mutually exclusive) contending theories are turbulent and disk fragmentation (Padoan et al. 2007; Adams et al. 1989). The turbulent fragmentation theory considers that a bound core can break into multiple fragments due to turbulent fluctuations of the density. These fragments will have masses larger that the Jean mass and will collapse faster than the original core. In this scenario, the binary or multiple systems are expected to form if these fragments remain gravitationally bound (see e.g. Goodwin et al. 2004). On the other hand, the disk fragmentation model considers that strong gravitational instabilities can fragment a pre-existing disk to form stars that will form a multiple system (Adams et al. 1989). Both theories make different predictions on the architecture of the resulting multiple systems that can be tested through high spatial resolution observations (Tobin et al. 2016a,b). For instance, determining parameters from the observations such as the distance between the companions, their relative orientation or eccentricity might help us distinguish between these scenarios.

Furthermore, multiplicity directly affects early stellar evolution through a number of tidal mechanisms (e.g. Artymowicz & Lubow 1994; Kraus et al. 2011) that have been discussed in detail by Reipurth et al. (2014) and that can be particularly severe in young triple systems. These effects can, in particular, affect the accretion history and time evolution of members of multiple systems, rendering the interpretation of their observational properties in terms of theoretical models somewhat uncertain (e.g. Stassun et al. 2008). To study them, young multiple systems must be characterized in detail and at high angular resolution. Very young (Class 0) systems are particularly interesting in this context, because they probe the initial conditions of multiple stellar evolution.

IRAS 16293–2422 is a very well known Class 0 protostellar system located in the Lynds 1689N dark cloud within the Ophiuchus star-forming region. For some time, the distance to the entire Ophiuchus complex was assumed to be 120 pc following Loinard et al. (2008). In a recent work, Ortiz-León et al. (2017) determined trigonometric parallaxes to a sample of young stars distributed over the region and inferred mean distances of 137.3 ± 1.2 pc for the Ophiuchus core, Lynds 1688, and 147.3 ± 3.4 pc for Lynds 1689. Dzib et al. (2018), using astrometric observations of water masers, recently confirmed that the distance to IRAS 16293–2422 is 141^{+30}_{-21} pc, which is consistent with both Loinard et al. (2008) and Ortiz-León et al. (2017), so we will use 141 pc for the distance to IRAS 16293–2422 in the rest of the paper.

IRAS 16293–2422 has been amply studied over the years for a variety of reasons. Initially, it drew attention because it was the coldest known protostar (see e.g. Walker et al. 1986). Later on, it was found that this source presented very rich spectra with numerous complex molecules, indicating a chemistry particularly active. Indeed, it harbors the archetypical "hot corino" at its center (e.g. Ceccarelli et al. 2000; Caux et al. 2011; Jørgensen et al. 2016). Finally, IRAS 16293–2422 happens to be one of the first very young (Class 0) multiple stellar systems ever identified. Interferometric observations at centimeter and millimeter

wavelengths by Wootten (1989) and Mundy et al. (1992) revealed two compact sources (called A and B) near the center of the extended envelope of IRAS 16293–2422. At about the same time, Mizuno et al. (1990) identified two compact outflows driven from IRAS 16293–2422, confirming that it must contain a young multiple system. High resolution radio observations (Wootten 1989; Loinard 2002) have further revealed that source A contains two sub-condensations called A1 and A2. Multi-epoch radio observations (Loinard 2002; Chandler et al. 2005; Loinard et al. 2007; Pech et al. 2010) have shown that, while the separation between A1 and A2 remained constant at about $0\rlap{.}''34$ between 1986 and 2008, their relative position angle monotonically increased by $40°$ over the same time period. Loinard et al. (2007) and Pech et al. (2010) interpreted this relative motion in terms of a nearly face-on, nearly circular orbit, and therefore considered A1 and A2 to form a tight binary system (see Figures 1 and 2).

One of the two compact outflows identified by Mizuno et al. (1990) is oriented almost exactly in the E–W direction, while the other is oriented in the NE–SW direction (at a position angle of about $65°$). High resolution observations by Yeh et al. (2008) demonstrated unambiguously that the E–W outflow originates from within source A. On the other hand, source A2 was shown by Loinard et al. (2007) to be at the origin of multiple bipolar ejections giving rise to additional radio sources (called A2α, A2β, etc.) oriented along the same direction as the NE–SW ouflow. Pech et al. (2010) used multi-epoch radio observations to show that A2α and A2β are symmetrically moving away from A2, as expected for bipolar ejecta. Thus, the NE–SW outflow can be unambiguously traced back to A2, and both compact outflows identified by Mizuno et al. (1990) appear to be driven from within source A. A third compact outflow (oriented in the NW–SE direction) was identified in IRAS 16293–2422 by Rao et al. (2009) and studied in more detail by Girart et al. (2014). In their interpretation, this out-flow also originates from within source A and impinges on source B where it splits, producing an arc-like structure. Loinard et al. (2013) offered a different interpretation in terms of a slow and poorly collimated outflow driven by source B. Regardless of the origin of this third outflow, it appears abundantly clear that source A drives multiple outflows and must host a very young multiple system.

Source B in IRAS 16293–2422 has also been studied in detail. Although it is resolved and does exhibit some substructure when observed at very high angular resolution (e.g. Rodríguez et al. 2005), there is no evidence to suggest that it might harbour a multiple system. Source B exhibits two remarkable properties that are worth mentioning here. The first one is that its spectrum can be accurately described as a single power law, with a spectral index of order 2 to 2.5 from $\nu = 5$ GHz ($\lambda = 6$ cm) to $\nu = 330$ GHz ($\lambda = 0.8$ mm) (Chandler et al. 2005). This suggests that a single emission mechanism, thermal dust emission, is at work over that entire frequency range. This is highly unusual, since emission from low-mass protostars at centimeter wavelengths is almost always dominated by free-free radiation from an ionized wind (e.g. Anglada et al. 2015). The interpretation of the centimeter flux from source B in terms of dust emission was further confirmed by the observation by Chandler et al. (2005) that the size of source B *increases* with frequency in the centimeter regime as expected for optically thick thermal dust emission. In contrast, optically thick free-free emission is expected to result in a source size that *decreases* with frequency (e.g. Panagia & Felli 1975). The lack of free-free emission in source B would be expected in the scenario put forward by Girart et al. (2014) where all molecular outflow activity in IRAS 16293–2422 is driven from source A. We note, however, that it would not necessarily be incompatible with the slow and poorly collimated outflow proposed by Loinard et al. (2013) which

Table 1. Parameters of the interferometric observations used in this paper.

Project	Date (DD/MM/YYYY)	Frequency (GHz)	Synthesized beam ($\theta_{max} \times \theta_{min}$; P.A.)	r.m.s. noise (mJy bm^{-1})	S_A (mJy)	S_B (mJy)
VLA Data:						
15A-363	28/06/2015	3.0	$1\rlap{.}''10 \times 0\rlap{.}''46$; $-20\rlap{.}°7$	0.013	1.70 ± 0.17	0.052 ± 0.005
15A-363	15/07/2015	10.0	$0\rlap{.}''35 \times 0\rlap{.}''14$; $-17\rlap{.}°5$	0.014	2.95 ± 0.30	1.08 ± 0.11
15A-363	17/07/2015	15.0	$0\rlap{.}''23 \times 0\rlap{.}''10$; $+19\rlap{.}°6$	0.008	3.84 ± 0.38	2.64 ± 0.26
14A-313	25/02/2014	15.0	$0\rlap{.}''24 \times 0\rlap{.}''09$; $-23\rlap{.}°7$	0.005	4.39 ± 0.44	2.68 ± 0.27
14A-313	27/02/2014	10.0	$0\rlap{.}''39 \times 0\rlap{.}''14$; $-26\rlap{.}°9$	0.006	3.61 ± 0.36	1.05 ± 0.11
12B-088	25/11/2012	7.0	$0\rlap{.}''44 \times 0\rlap{.}''19$; $-168\rlap{.}°4$	0.006	2.58 ± 0.26	0.55 ± 0.06
12B-088	01/12/2012	33.0	$0\rlap{.}''11 \times 0\rlap{.}''04$; $-15\rlap{.}°6$	0.027	3.63 ± 0.54	15.3 ± 2.3
12B-088	23/12/2012	41.0	$0\rlap{.}''09 \times 0\rlap{.}''04$; $-4\rlap{.}°6$	0.072	4.87 ± 0.73	26.2 ± 3.9
10C-222	15/03/2011	41.0	$0\rlap{.}''36 \times 0\rlap{.}''16$; $-10\rlap{.}°0$	0.030	6.59 ± 0.99	31.3 ± 4.7
10C-222	19/03/2011	41.0	$0\rlap{.}''30 \times 0\rlap{.}''14$; $+11\rlap{.}°5$	0.060	6.86 ± 1.03	28.9 ± 4.3
10C-222	05/06/2011	41.0	$0\rlap{.}''13 \times 0\rlap{.}''10$; $-13\rlap{.}°9$	0.027	5.27 ± 0.79	26.9 ± 4.0
10C-222	08/06/2011	41.0	$0\rlap{.}''08 \times 0\rlap{.}''05$; $-174\rlap{.}°4$	0.037	5.81 ± 0.87	29.1 ± 4.4
10C-222	13/08/2011	6.0	$0\rlap{.}''50 \times 0\rlap{.}''20$; $-12\rlap{.}°5$	0.006	2.72 ± 0.27	0.38 ± 0.04
ALMA Data:						
01005762	17/08/2014	227.0	$0\rlap{.}''53 \times 0\rlap{.}''25$; $+87\rlap{.}°2$	1.81	1.47 ± 0.22	1.79 ± 0.27
01003905	14/06/2014	318.0	$0\rlap{.}''39 \times 0\rlap{.}''34$; $-62\rlap{.}°2$	3.89	3.81 ± 0.57	3.21 ± 0.48
01003908	14/06/2014	318.0	$0\rlap{.}''35 \times 0\rlap{.}''31$; $-62\rlap{.}°2$	2.27	3.92 ± 0.59	3.23 ± 0.48
01003968	16/06/2014	323.0	$0\rlap{.}''39 \times 0\rlap{.}''32$; $+87\rlap{.}°3$	3.15	3.79 ± 0.57	3.35 ± 0.50
01028453	28/06/2015	338.2	$0\rlap{.}''17 \times 0\rlap{.}''13$; $-83\rlap{.}°9$	3.49	2.46 ± 0.37	3.60 ± 0.54
01028026	29/08/2015	342.3	$0\rlap{.}''25 \times 0\rlap{.}''13$; $-76\rlap{.}°9$	6.03	2.78 ± 0.42	3.12 ± 0.57
01019938	06/06/2015	404.0	$0\rlap{.}''28 \times 0\rlap{.}''22$; $-78\rlap{.}°3$	7.95	6.06 ± 1.21	4.67 ± 0.93
01019922	07/06/2015	453.0	$0\rlap{.}''31 \times 0\rlap{.}''21$; $-81\rlap{.}°9$	8.86	8.86 ± 1.77	6.14 ± 1.23
SV	17/04/2012	695.0	$0\rlap{.}''29 \times 0\rlap{.}''16$; $-70\rlap{.}°4$	19.90	11.9 ± 2.4	13.5 ± 2.7

NOTE—Observational details for VLA data obtained before 2011 can be found in Chandler et al. (2005), Loinard et al. (2007), and Pech et al. (2010). The ALMA project numbers correspond to the ID numbers given in the Japanese Virtual Observatory (JVO) from where the data sets were obtained. For the ALMA observation at 695 GHz, SV stands for Science Verification.
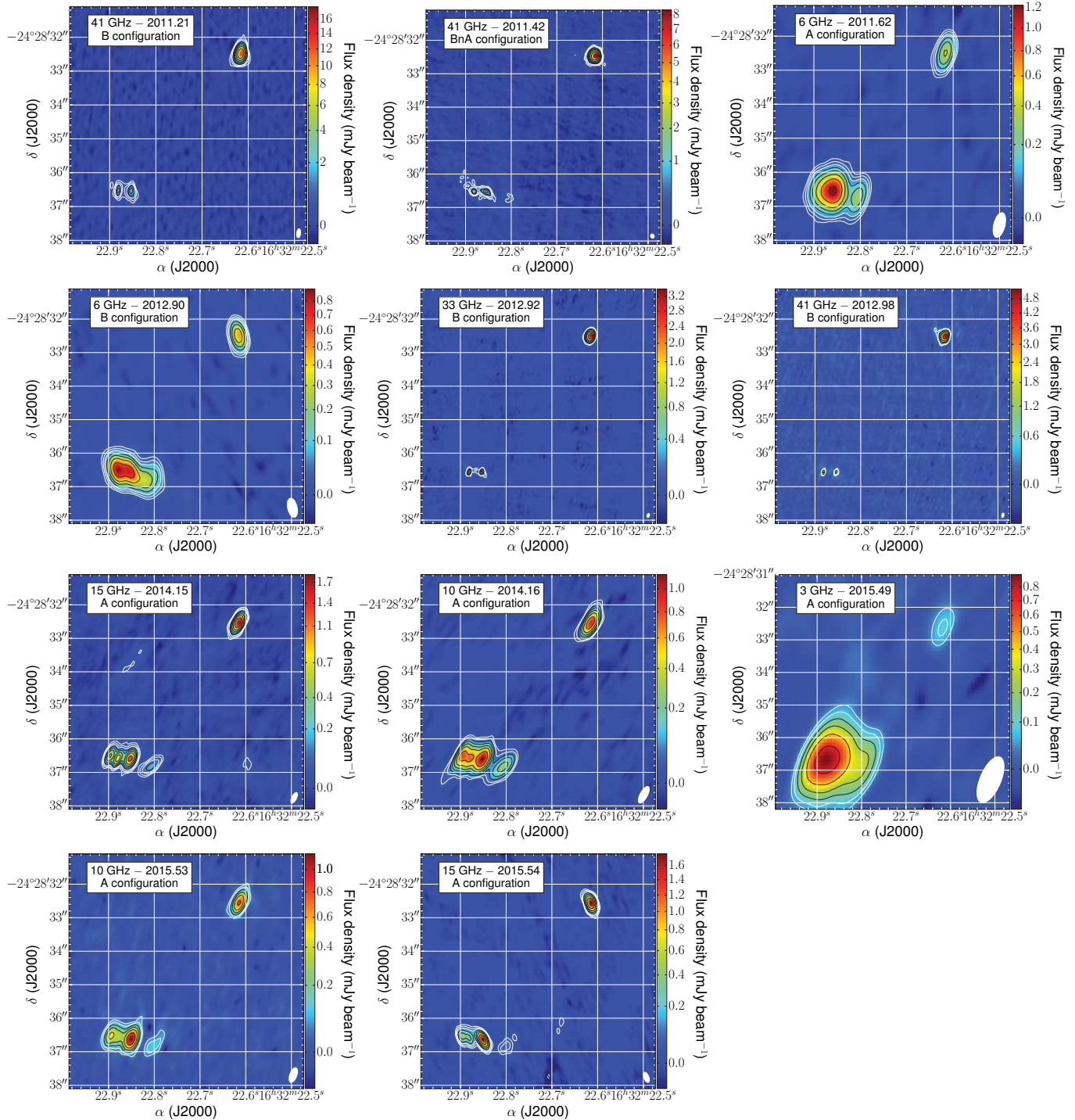
Figure 1. Continuum images of IRAS 16293–2422 for all new VLA observations presented in this paper. For all of them, the first contour corresponds to five times the r.m.s. noise of each image, and successive contours increase by a factor $\sqrt{3}$. The two main components, A and B, are located, respectively, to the south-east and north-west of the images (see also Figure 2).
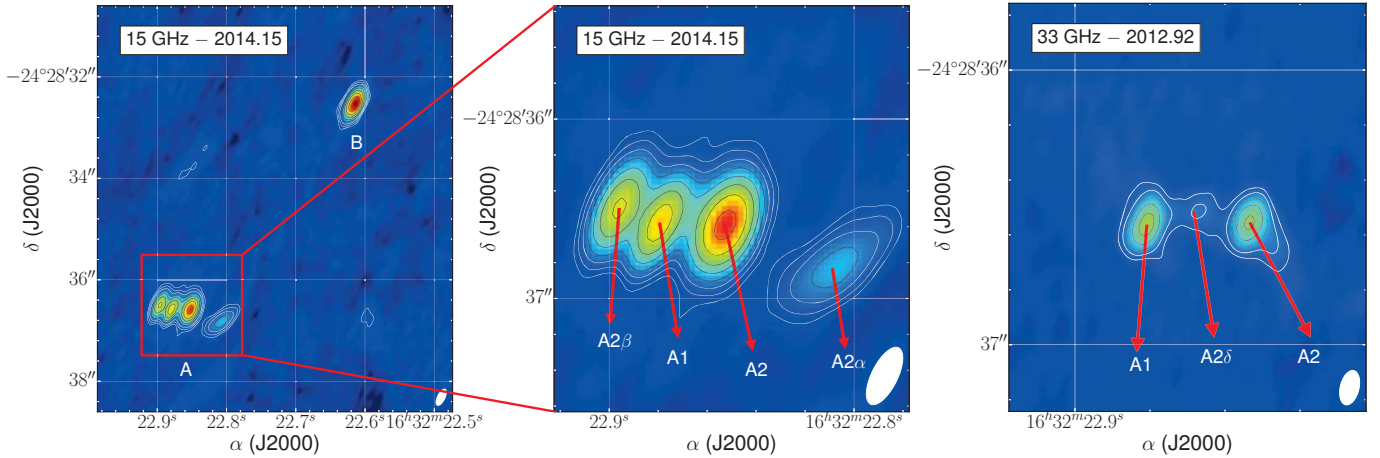
Figure 2. Labelling of the various sources in IRAS 16293–2422. Left panel: VLA image at 15 GHz indicating the position of sources A and B. Middle panel: zoom on source A at 15 GHz. The sources A1 and A2 are indicated as well as the ejecta A2α, A2β (see text). Right panel: VLA image at 33 GHz. The sources A1, A2 and A2δ are labeled. The contours and the color scale corresponding to the flux density are the same as in Figure 1.

might not generate the highly supersonic speeds required to produce shock-ionized gas.

The second remarkable feature of source B worth mentioning here is that it exhibits what is arguably the clearest known example of an inverse P-Cygni profile (Pineda et al. 2012; Zapata et al. 2013). This is naturally interpreted as evidence for infall, and Pineda et al. (2012) derived a mass accretion rate on source B of 4.5×10^{-5} M$_\odot$ yr^{-1}. Zapata et al. (2013) confirmed the interpretation of the P-Cygni profiles in terms of infall, and interpret source B itself as an optically thick disk seen nearly face-on. The high accretion rate onto source B is somewhat difficult to reconcile with the lack of a strong wind inferred from the absence of free-free emission, and of outflowing material proposed by Girart et al. (2014). Indeed, theoretical models of accreting protostars predict a mass ratio between accreted and ejected material of order 10 to 30% (e.g. Shu et al. 1988).

It is clear from the description presented above that IRAS 16293–2422 is in the process of forming a multiple (at least triple) stellar system. As such, it offers a unique opportunity to investigate the effect of multiplicity on the earliest stages of stellar evolution. Nevertheless, the exact number of protostars within IRAS 16293–2422, their relative evolutionary stages, and their relationship with known radio sources and outflows in the system, remain elusive. In this paper, we present new radio, millimeter, and sub-millimeter continuum observations aimed at elucidating several of these aspects. The observations will be presented in Section 2, the results given in Section 3, and used to discuss the nature of the sources in Section 4. Section 5 summarizes our conclusions and provides some perspectives.

2. OBSERVATIONS

2.1. *Very Large Array observations*

New Very Large Array (VLA) observations of IRAS 16293–2422 were obtained between 2011 and 2015 in the most extended configurations (A, BnA, and B) of the array (see Table 1 for a summary). They covered the frequency range from 2 to 42 GHz, and resulted in angular resolutions better than 0$''$5 at all frequencies except at 3 GHz. We used the VLA calibration pipeline (version 1.3.1) provided by NRAO to flag and calibrate all our datasets with the CASA software package (version 4.2.2). The quasars 3C 286 and J1256−0547 were used for the bandpass calibration, while the source
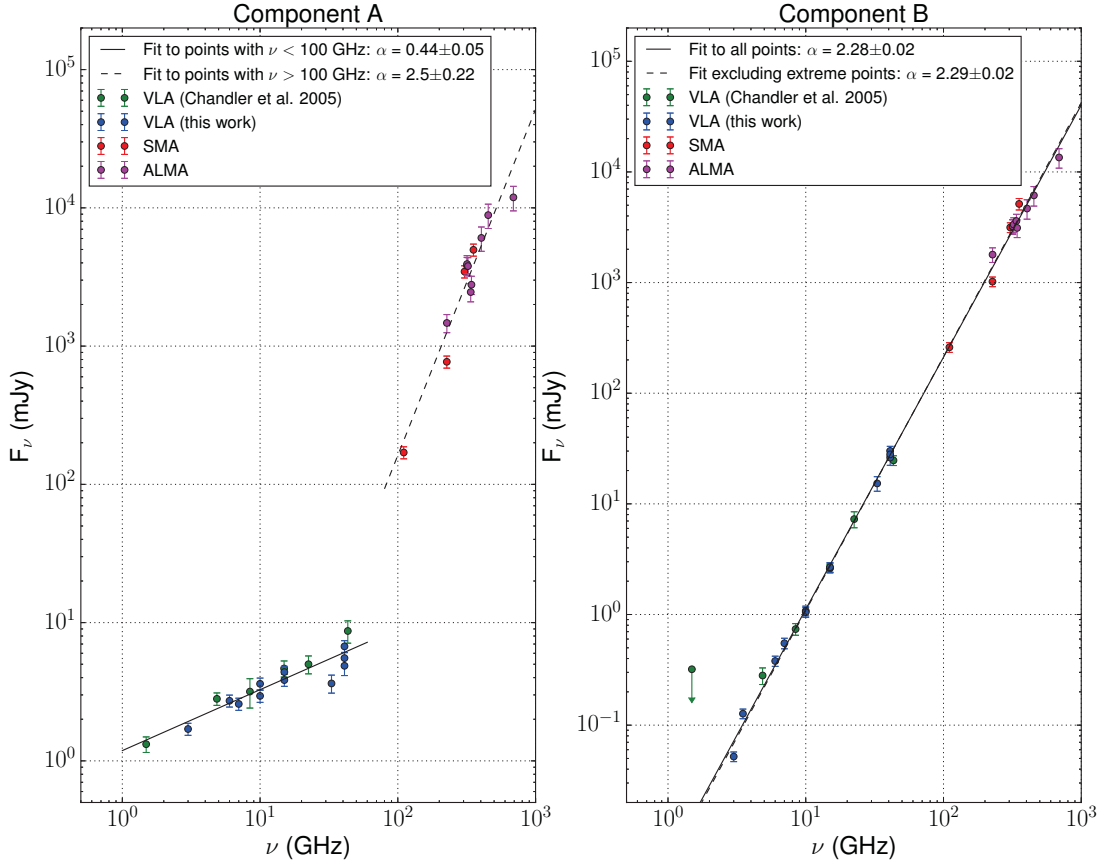
Figure 3. Spectra of sources A and B derived from SMA and VLA observations (Chandler et al. 2005) as well as the VLA and ALMA results presented in the present paper.

J1625−2527 was used for the complex gain calibration. The flux scale was set using the standard calibrator 3C 286. The uncertainty in the absolute flux calibration is estimated to be about 10% for the observations up to 15 GHz. For the observations at higher frequencies, the estimated uncertainty is about 15%.

The continuum emission from this source is strong enough that self-calibration can be performed in order to correct for atmospheric fluctuations on timescales shorter than the cycle between the target and the phase calibrators. The calibrated visibilities were imaged using a weighting scheme intermediate between natural and uniform (RO-BUST = 0 in CASA) to optimize the compromise between high angular resolution and high sensi-

tivity. The resulting synthesized beams and r.m.s. noise levels are given in Table 1. To complete our study, we will also make use of the continuum VLA observations from Chandler et al. (2005) and Pech et al. (2010) carried out between 1986 and 2008. The reduction and calibration of these data are described in details in the original papers.

2.2. ALMA observations

We have also used interferometric ALMA observations covering the frequency range from 230 GHz to 700 GHz (see Table 1). We selected only observations with an angular resolution better than 0″.4 so that the source size of source B could be properly deconvolved (see Section 3.3 below). Images at frequencies between 227 and 453 GHz were downloaded from the database
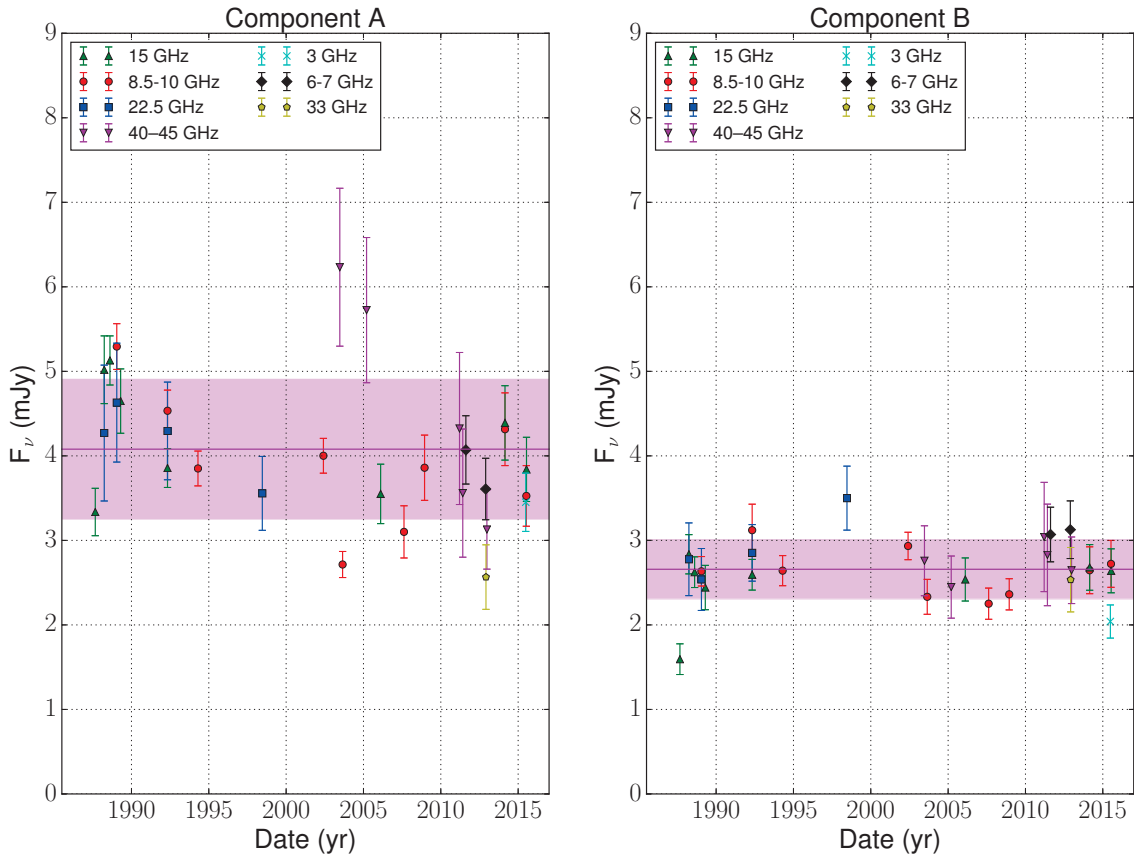
Figure 4. Variability of sources A and B. For clarity, the fluxes have been renormalized to the reference frequency of 15 GHz, using the spectral indices calculated on Section 3.1. Different frequencies are shown with different symbols and colours. The magenta line and magenta band in each panel show the mean flux and 1-sigma dispersion around that mean, respectively.

hosted by the Japanese ALMA Observatory (JAO; jvo.nao.ac.jp/portal/alma/archive.do). These images correspond to data that have not been self-calibrated, and we assume a 10% error on the source sizes derived from them. The absolute flux uncertainty, on the other hand, is assumed to be 15% for frequencies below 400 GHz, and 20% above 400 GHz. In addition, we used the Band 9 Science Verification observation of IRAS 16293–2422 as available on almascience.nrao.edu, these data were self-calibrated.

3. RESULTS

In Figure 1 we show all the continuum images of IRAS 16293–2422 obtained with the VLA be-

tween 2011 and 2015. Similar figures for observations prior to 2011 are included in Chandler et al. (2005) and Pech et al. (2010). For the 41 GHz observations obtained during 2011, we have averaged the data taken in the B configuration on 15 and 19 March (mean epoch 2011.21) to produce the first panel of Figure 1, and the data taken in the BnA configuration on 5 and 8 June (mean epoch 2011.42) to produce the second panel. This combining procedure results in images with higher signal-to-noise and better fidelity. To exhibit more clearly the structure of source A, labelled zooms of the images at 33 GHz (epoch 2012.92) and 15 GHz (epoch 2014.15) are provided in Figure 2.

Table 2. Deconvolved size of source B as a function of frequency

Frequency	θ_{max}	θ_{min}
(GHz)	(mas)	(mas)
10.0	122.0±5.9	42.5±39.0
15.0	137.7±5.6	130.0±2.5
22.46	160.6±3.2	141.4±5.4
33.02	192.2±6.7	159.9±4.5
41.1	198.6±8.2	172.6±6.8
227.0	416.0±28.0	369.0±18.0
318.0	410.0±16.0	376.0±15.0
318.0	407.0±13.0	373.0±11.0
323.0	415.0±18.0	380.0±18.0
338.2	374.0±13.0	355.0±13.0
342.3	391.0±12.0	365.0±12.0
404.0	410.0±16.0	386.0±16.0
453.0	402.0±12.0	370.0±10.0
695.88	408.9±9.4	368.1±6.9

Table 3. Absolute proper motions for all sources in IRAS 16293–2422.

Source	$\mu_\alpha \cos\delta$	μ_δ
	(mas yr^{-1})	(mas yr^{-1})
A1	−3.0±0.4	−27.9±0.8
A2	−7.8±0.6	−21.8±0.5
A2α	−63.8±5.9	−51.5±2.6
A2β	+53.2±3.4	−17.9±1.3
B	−5.7±1.4	−21.0±1.1

NOTE—These values were obtained by fitting a linear and uniform proper motion to the measured absolute positions.

As expected, source B to the north-west of the system remains largely featureless in all images, and –due to its positive spectral index– it appears much more prominent at the highest frequencies. Source A, on the other hand, appears highly structured, containing a number of sources that depends on time and frequency. These different sources correspond, on the one hand, to the A1 and A2 objects initially identified by Wootten (1989) and subsequently monitored by Loinard (2002), Chandler et al. (2005) and Pech et al. (2010), and, on the other, to the ejecta recently expelled by source A2 (Loinard et al. 2007; Pech et al. 2010; Loinard et al. 2013).

In the following sub-sections, we will use these VLA images as well as the ALMA images described in Section 2.2 to characterize, separately,

the spectra[1] of components A and B as well as their temporal variability. We will also use them to examine the size of several of the sources, and monitor the astrometry (both absolute and relative) of the different sources in the system.

3.1. *Spectra*

The integrated flux densities obtained for sources A and B from resolved SMA and VLA observations between 5 and 300 GHz were previously reported by Chandler et al. (2005). Here we extend these observations both to higher frequencies (up to 700 GHz) using ALMA observations and to lower frequencies (down to 2 GHz) using new VLA observations. We have used CASA to measure the flux densities for A and B. For source B, we used a gaussian fit since its structure at all wavelengths is well defined. On the other hand, the emission from source A is more complex, so we used the task IMFIT with multiple components

---

[1] Plots of flux density as a function of frequency, such as those that will be presented here, as often called spectral energy distributions (SED). Strictly speaking, however, an SED is a plot of *energy* vs. frequency, while plots of flux density vs. frequency are spectra. In the present paper, we will adhere to this definition.

in CASA to measure individual fluxes, and defined region including all sources composing A to obtain the total flux. The resulting complete spectra are shown in Figure 3.

In the case of source A, we confirm the results by Chandler et al. (2005) that the fluxes can be fitted by two separate power laws $F_\nu \propto \nu^\alpha$. At $\nu > 100$ GHz, the spectral index derived from the data is 2.50 ± 0.22, as expected from thermal dust emission. At $\nu < 100$ GHz, the spectrum becomes shallower and is well characterized by a spectral index $\alpha = 0.44 \pm 0.05$ typical of partially optically thick free-free emission from ionized jets (e.g. Anglada et al. 2015). This situation is typical of deeply embedded low-mass protostars driving supersonic outflows.

As shown in Figure 2, source A is a composite of several components, so the spectral index derived above corresponds to the average of the spectral indices of the various sources within component A. The determination of the spectral indices of the individual sources is complicated by the blending between those sources in several of the images, and the fact that some features (particularly the ejecta) are only detected at some frequencies. To estimate the spectral indices of the individual components, we used the resolved observations obtained at 10 and 15 GHz in 2014.15. These data yield $\alpha_{A1} = 0.5 \pm 0.2$, $\alpha_{A2} = 0.7 \pm 0.2$, $\alpha_{A2\alpha} = -0.4 \pm 0.2$ and $\alpha_{A2\beta} = -0.1 \pm 0.2$. The positive values derived for A1 and A2 are consistent with the partially optically thick free-free emission expected for the thermal jet of young stellar objects (e.g. Anglada et al. 2015). This would be consistent with the interpretation of A1/A2 in terms of a tight binary system by Loinard et al. (2007) and Pech et al. (2010). The spectral indices of sources A2α and A2β, on the other hand, are consistent with the expectation ($\alpha = -0.1$) for optically thin free-free emission, as appropriate for low density ionized ejecta. We note that Loinard et al. (2013) had found a similar value for A2β from earlier VLA observations. It is important to point out

that the ejecta contribute relatively little to the total flux of component A, so the overall spectrum of source A is dominated by the compact sources A1 and A2; this explains the overall positive index of source A.

For source B, the entire spectrum from 2 to 700 GHz can be modelled by a single power-law with spectral index $\alpha = 2.28 \pm 0.02$. Note that to constrain better the behaviour of the spectrum at low frequency, we measured the flux separately in the entire 3 GHz band ($\Delta\nu$ from 2 to 4 GHz) covered by the S-band observations, and in sub-bands from 2 to 3 GHz (centered at 2.5 GHz), and from 3 to 4 GHz (centered at 3.5 GHz). Source B is only detected in the entire band and in the higher frequency (3.5 GHz) sub-band. It is not detected in the lower frequency sub-band centered at 2.5 GHz. This is fully consistent with the spectral index derived from the entire spectrum (Figure 3). To examine whether or not the highest and lowest frequency points (at 695 GHz and 2.0 GHz) suggested a departure from a single power law, we also fitted the data ignoring these two extreme points. This fit is very nearly identical to that obtained including all points. The value of the spectral index of source B ($\alpha = 2.28 \pm 0.02$) is consistent with thermal dust emission, and is statistically incompatible with the maximum value ($+2.0$) for optically thick free-free emission. Instead, the spectrum suggests that the emission is due to thermal dust radiation over the entire range from 700 GHz down to 2 GHz, with no detectable free-free contribution even at the lowest frequency (further evidence for this conclusion will be presented in section 3.3). This is, to the best of our knowledge, a unique situation. A number of other young stellar objects (e.g. Brogan et al. 2016) have been observed to be dominated by thermal dust emission down to ~ 10 GHz, but never down to 2 GHz.

Anglada et al. (2018) reviewed the properties of centimeter free-free emission from jets driven by young stellar objects. They confirmed the existence of an empirical relationship between the

bolometric luminosity of the object and the intensity of the free-free emission from its thermal jet. IRAS 16293–2422 has a total bolometric luminosity of about 25 $L_\odot$ (Makiwa 2014; Crimier et al. 2010; Correia et al. 2004; Schöier et al. 2002, when scaled to the distance of 141 pc adopted here). The empirical relationship derived by Anglada et al. (2018) for that luminosity predicts a total centimeter free-free flux density for IRAS 16293–2422 of order 4 mJy (to within a factor of a few). This is indeed, the total centimeter flux density measured here for the sum of source A and B. Jacobsen et al. (2018) estimate that around 85% of that the total luminosity of IRAS 16293–2422 is attributable to source A, while the remaining 15% come from source B. Thus, one would expect centimeter free-free flux densities of about 3.4 and 0.6 mJy for source A and B respectively. The measured centimeter flux density of source A is consistent with this expectation, but that of source B is not. Indeed, the predicted contribution from dust at $\sim$ 6–7 GHz (from the power law derived from the spectrum of source B) is about 0.5 mJy. Thus, the total flux expected for source B, if it fell on the empirical relationship of Anglada et al. (2018), would be about 1 mJy. In contrast, the measured flux density of source B is only about 0.5 mJy, and is fully compatible with the predicted thermal dust emission alone. The dispersion of the data points around the fit to the spectrum is of order 10%, so a reasonable upper limit to the free-free contribution is about 0.05 mJy, or about a tenth of the expected flux for a source with that luminosity. We conclude that source B does not drive a powerful ionized outflow.

3.2. Variability

Chandler et al. (2005) have shown that the centimeter radio flux of source A is somewhat time variable, with a variability of order $\sim$ 50% at any given frequency. This result is confirmed by the new VLA observations. To characterize the radio variability of sources A and B separately, we considered the fluxes measured with the VLA at all
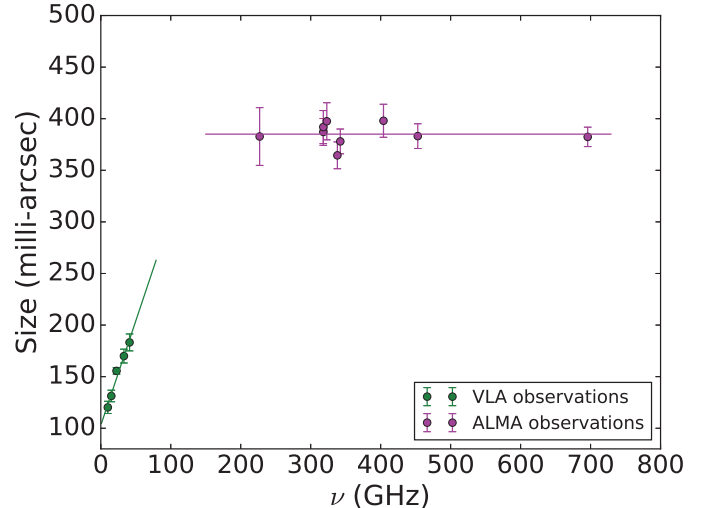

Figure 5. Size of source B as a function of frequency. The size increases linearly up to 50 GHz, while it remains roughly constant at frequencies higher than 200 GHz.

available epochs, and we re-scaled them to a single reference frequency (chosen, arbitrarily, to be 15 GHz) using the spectral indices of sources A and B measured in Section 3.1. Specifically, we multiplied the fluxes measured at a given frequency ν by $(15\,\text{GHz}/\nu)^\alpha$ where $\alpha = 0.45$ for source A and $\alpha = 2.28$ for source B. This eliminates the variations due to frequency and reveals intrinsic variability more explicitly. The results are shown in Figure 4 where it is immediately obvious that source A is more variable than source B. Quantitatively, the mean flux of source A (expressed at the reference frequency of 15 GHz) is found to be 4.08 mJy with a dispersion of 0.83 mJy around that mean. In comparison, the mean flux of source B is 2.66 mJy with a dispersion of only 0.35 mJy. Indeed, with the exception of the very first data point (at 15 GHz in 1987), the statistical distribution of all measured fluxes are compatible with the mean value. As discussed by Chandler et al. (2005), it is quite possible that the first data point is affected by an absolute flux calibration issue.

The variability of source A is certainly expected given that the centimeter emission traces mass ejection which, as evidenced by the recent ejecta

A2α and A2β, is clearly time dependent. The flux of source A2α at 10 GHz, for instance, is found to have faded by 30 to 40% between 2014.15 and 2015.53.

3.3. *Source sizes*

The components A1 and A2 of source A remain unresolved in our observations, and the ejecta source A2β is too heavily blended with A1 for a reliable size to be measured. The ejecta A2α, on the other hand, is well separated from the other components of source A in the 2014.15 and 2015.53 observations at 10 and 15 GHz. Epoch 2014.15 is especially interesting in this respect, because source A2α is detected with high signal to noise ratio. In comparison, the 2015.53 detections have a significantly lower signal to noise ratio, because these observations are intrinsically shallower, and because A2α has faded significantly between 2014.15 and 2015.53 (see Section 3.2). The deconvolved size of source A2α in 2014.15 is found to be (0$''$44$\pm$0$''$04) $\times$ (0$''$11$\pm$0$''$05) at position angle (116$°\pm$5$°$) at 15 GHz, and (0$''$47$\pm$0$''$04) $\times$ (0$''$17$\pm$0$''$06) at position angle (113$°\pm$7$°$) at 10 GHz. Thus, we find no statistical evidence for a different size at the two frequencies, as expected for optically thin free-free emission. On the other hand, source A2α is found to be significantly larger than in the 2007 and 2008 observations reported by Pech et al. (2010) who quote (0$''$21$\pm$0$''$06) $\times$ (0$''$08$\pm$0$''$04) at 8.5 GHz for epoch 2008.95. The position angle was poorly constrained for that epoch.

Source B is well resolved at all frequencies above 10 GHz in the interferometric observations presented here (Table 2). As noticed by Chandler et al. (2005), the size increases with frequency in the centimeter regime, from about 120 mas at 10 GHz to about 185 mas at 40 GHz (Figure 5). This tendency must continue between 40 and 230 GHz (at least in part of that frequency range), since the size measured at the latter frequency is 380 mas. As Chandler et al. (2005) pointed out, this increase of the size with frequency further confirms that the emission is dominated by partially optically thick thermal dust emission. Once in the millimeter regime, however, the size remains constant at 385$\pm$5 mas (54.3$\pm$0.7 AU assuming a distance of 141 pc – Dzib et al. 2018), suggesting that the source is entirely optically thick. In this scheme, the size measured at millimeter wavelengths corresponds to the full extent of source B.

3.4. *Astrometry*

The relative motion between sources A1 and A2 was first reported by Loinard (2002) from VLA observations at 8.4 GHz obtained between 1989 and 1994. Chandler et al. (2005) and Pech et al. (2010) expanded that study to include source B, using data obtained between 1987 and 2009. Pech et al. (2010) also monitored the motion of the ejecta A2α and A2β that were first reported by Loinard et al. (2007).

The absolute position as a function of time for sources A1, A2, and B are shown in Figure 6, and the derived proper motions are given in Table 3. While the positions are reasonably well fitted by linear and uniform proper motions, we find some evidence for a deviation from this expected behaviour in the data. Indeed, we find that a second order polynomial does reproduce the data significantly better. However, since accelerated absolute proper motions are unphysical in our case, we will use the linear fits to characterize the proper motions of the sources in IRAS 16293–2422. These fits confirm that sources A2 and B exhibit very similar proper motions. Their mean value ($\mu_\alpha \cos \delta = -7.5\pm0.8$ mas yr^{-1}; $\mu_\delta = -21.7\pm0.7$ mas yr^{-1}) provides a good proxy for the relative motion between the Sun and IRAS 16293–2422. We note that this motion is largely dominated by the reflex Solar motion. Assuming the values provided by Schönrich et al. (2010) for the Solar motion, we calculated that the reflex Solar motion for the direction of IRAS 16293–2422 is $\mu_\alpha \cos \delta = -8.1$ mas yr^{-1}, $\mu_\delta = -19.4$ mas yr^{-1}. In other words, the motion of IRAS 16293–2422 relative to the LSR is 0.6 ± 0.8 mas yr^{-1} and 2.3 ± 0.7 mas yr^{-1} in right
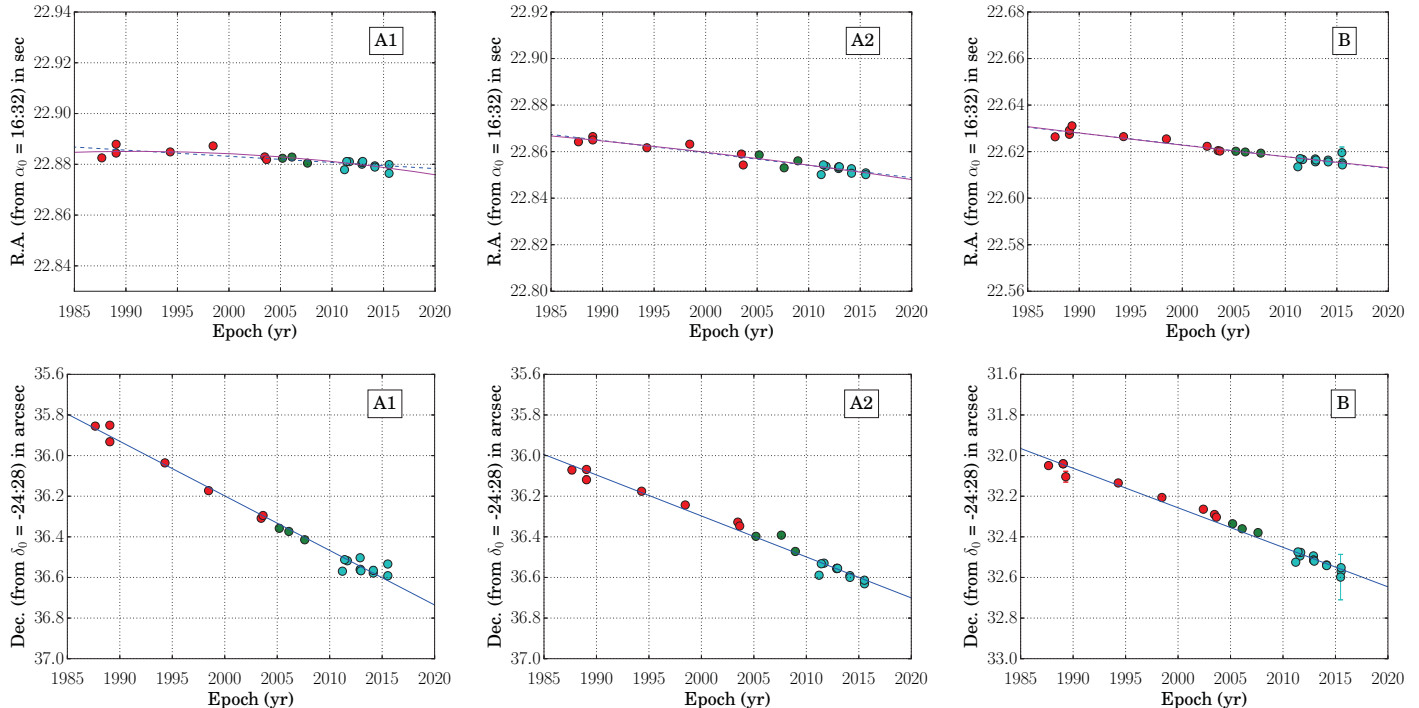
Figure 6. Absolute position as a function of time for sources A1, A2 and B (from left to right). The red points correspond to the observations from Chandler et al. (2005), the green points represent the observations from Pech et al. (2010) and the cyan points correspond to this work. The blue lines show the best fits with a first order polynomial.

ascension and declination, respectively. The proper motion of source A1, on the other hand, is somewhat different. To examine the relative motion between A1 and A2, Figure 7 shows the right ascension and declination offsets between A1 and A2 as a function of time (left column), as well as their separation and relative position angle as a function of time (right column). This shows that the separation between A1 and A2 is slowly increasing, from about 0″33 ($\equiv$ 46.5 AU) in the late 1980s to about 0″38 ($\equiv$ 53.6 AU) in 2015. Somewhat unexpectedly, the relative position angle between A1 and A2, which has increased by about 40° between the late 1980s and the early 2000s, has now started to decrease. We will discuss possible explanations in Section 4.

The relative motion between the ejecta A2α and A2β and their driving source A2 are, respectively 63±3 mas yr^{-1} at a position angle +62±10°, and 62±3 mas yr^{-1} at a position angle +266±10°. Both position angles are in agreement with the

orientation (P.A. $\sim$ 65°) of the NE-SW outflow driven from within component A (e.g. Mizuno et al. 1990). We conclude, as did Loinard et al. (2007) and Pech et al. (2010), that this specific outflow is driven by A2. The amplitudes of the proper motions of A2α and A2β relative to A2 are very similar, and imply transverse velocities of order 45 km s^{-1}.

4. DISCUSSION

Starting from their radio and millimeter properties described in section 3, we now proceed to discuss the nature of the various sources in IRAS 16293–2422.

4.1. *The protostellar source A2*

Source A2 is clearly associated with a protostar. Its centimeter emission is compact and exhibits a positive spectral index ($\alpha = +0.7\pm0.2$) typical of the thermal jets driven by low-mass protostars (Anglada et al. 2015). Moreover, it has recently ejected two condensations (A2α and A2β) that are
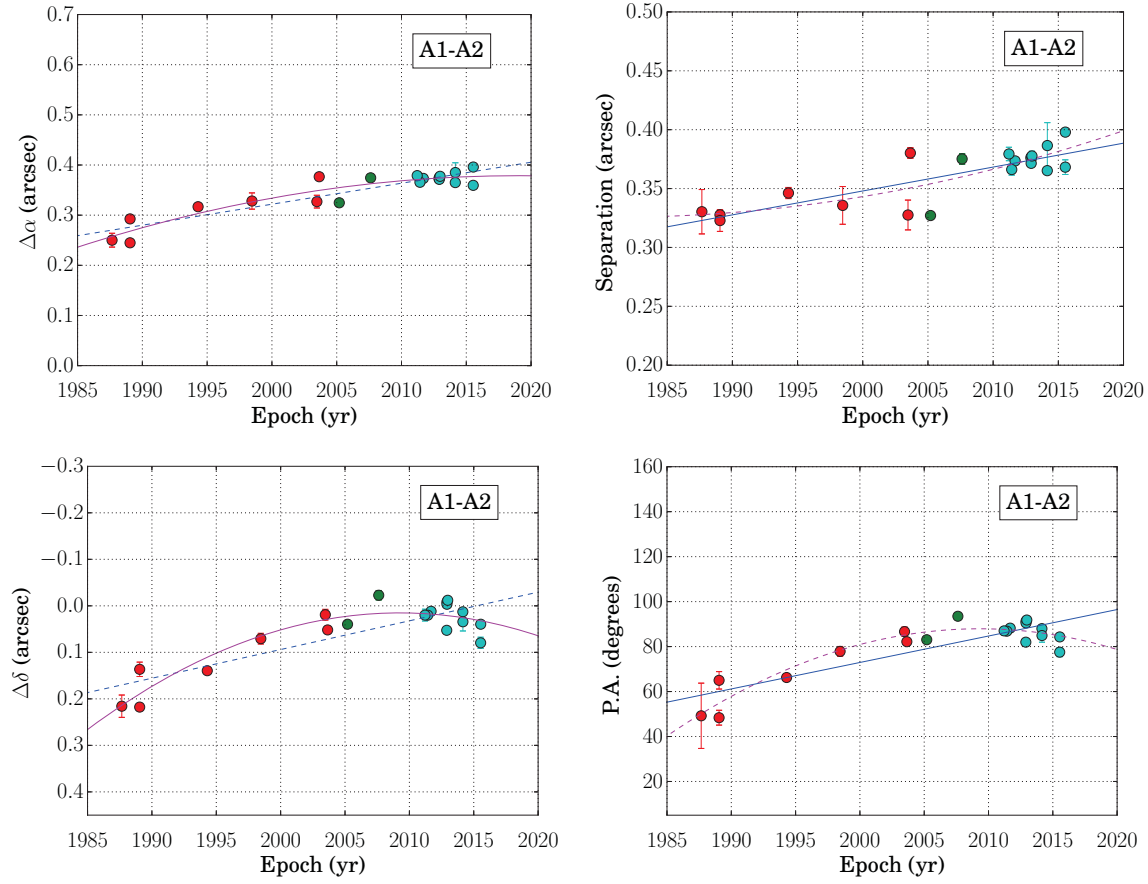
Figure 7. Relative motion between A1 and A2 in right ascension (upper left panel), declination (lower left panel), separation (upper right panel) and position angle (lower right panel). The blue lines (solid and dashed) show first order polynomial fits, while the magenta lines show a second order fit. The symbol colours have the same meaning as in Figure 6.

observed to move symmetrically away from A2 along a position angle that corresponds to that of the NE–SW outflow first observed by Mizuno et al. (1990). Incidentally, we note that this association between A2 and the NE–SW outflow is the only one that can currently be ascertained. The other outflows known to exist in the system cannot yet be unambiguously associated with specific proto-stars.

4.2. *The ejecta A2α and A2β*

The sources A2α and A2β were ejected from A2 around 2005 (Pech et al. 2010). The present observations confirm that the emission mechanism of the centimeter emission is optically thin thermal bremsstrahlung. Furthermore, the size of the well resolved source A2α is found to have increased

significantly between 2009 and 2014, demonstrating that it is diluting into its surroundings. It is, to our knowledge, the first time that such an expansion of a protostellar ejecta is observed.

4.3. *Source A1*

The nature of source A1 has been a matter of some debate. Chandler et al. (2005) proposed that A1 is a *shock feature* that corresponds to the impact on the surrounding medium of a jet driven by a protostar located close to A2. Initially, it was thought that A2 itself might be the source of that jet, but the recent ejections of A2α and A2β by A2 demonstrate that the jet from A2 does not point in the direction of A1. Thus, a different protostar (presumably a very close companion of A2) would have to be at the origin of the jet. Chandler et al. (2005) interpreted the relative motion between A1 and A2 as a consequence of the precession of that putative jet, and attribute the strong precession to the binary nature of the driving source. This interpretation would explain naturally the recent reversal in the behaviour of the relative position angle between A1 and A2 (Figure 7d). On the other hand, this interpretation is difficult to reconcile with the permanency of source A1 as a compact source of nearly constant flux over the last three decades. Indeed, A1 has been observed to move (on the plane of the sky) by about 35 AU over the course of the last 30 years. If A1 is interpreted as a shock feature from a precessing jet, then the properties of the shocked ambient material would be expected to change drastically over that time span, and this could easily have resulted in significant changes in the radio properties of A1.

The alternative interpretation, that has been put forward by Loinard et al. (2007) and Pech et al. (2010), is that A1 is a protostar which, together with A2, form a tight binary system. This interpretation explains more naturally the steadiness of A1 over the last 30 years. In addition, the spectral index of A1 (α = +0.5±0.2) is consistent with that of a protostar driving a thermal jet (Anglada et al. 2015). On the other hand, the recent behaviour of the relative position angle between A1 and A2 is clearly incompatible with a Keplerian orbit.

Here, we propose a third possibility, closely related to the tight binary interpretation just mentioned: that A1 is a member of a very tight binary system which, together with A2, form a hierarchical triple system. In that scheme, the relative motion between A1 and A2 would be the combination of the motion of the center of mass of the tight binary around A2, and the motion of A1 around the center of mass of that putative very tight binary. This would result in "epicycles" that could easily explain the complex behavior of the relative position between A1 and A2. Future astrometric observations will be needed to test this possibility, but we note that the existence of three protostars in source A is not unexpected. As we described in Section 1, two outflows (one oriented E–W and the other oriented NE–SW) have long been known to be powered from within A, and Girart et al. (2014) proposed that a third outflow (oriented NW–SE) also originated from source A. This would clearly require the existence of three protostars in source A.

4.4. *Source B*

Two of the radio properties of source B are quite extraordinary. The first one is that its spectrum can be described as a single power law from 2 to 700 GHz, with a spectral index (2.28±0.02) that is incompatible with thermal bremsstrahlung. Since the emission in the millimeter/sub-millimeter regime is clearly due to dust, the emission in the centimeter regime is likely of the same origin. This is confirmed by the second remarkable property of source B: that its size increases with frequency between 10 and 50 GHz, but stays constant from 230 to 700 GHz. We interpret this as evidence that the source becomes increasingly optically thick as the frequency increases until, in the millimeter and sub-millimeter regimes it is entirely optically thick. Given this conclusion, the brightness temperature measured at the central position of source B in the well-resolved images obtained with the VLA at 33 GHz (T_b = 870 K) and 41 GHz (T_b =

700 K) provide a stringent lower limit[2] to the kinetic temperature in the central parts of source B.

The brightness temperature derived from the ALMA observations is somewhat lower (~ 180 K). For instance, from the Science Verification Band 9 ALMA data at 700 GHz with a spatial resolution of $\sim 0.3''$, we have $T_b = 182$ K in the central pixel. In principle, this could be due to beam dilution since the beam area of the ALMA data used here is typically five to ten times larger than that of the VLA observations at 33 and 41 GHz. However, we have obtained higher angular resolution maps at ~ 300 GHz (E. Caux private communication), which show that the brightness temperature in the central pixel at $0.''12$ angular resolution is also about 185 K. This strongly suggests that beam dilution is not the cause of the lower brightness temperature measured with ALMA as compared with the VLA. Instead, a second effect could naturally explain the difference in brightness temperature. Given the dependence of opacity on wavelength, we expect lower frequency observations to probe regions deeper inside source B, and higher frequency data to only see the relatively outer layer, where the temperature is lower.

We conclude that source B is a dusty structure with a very high central density (this is required to explain the high opacity of source B) and high central temperature (at least 1,000 K). The lack of excess centimeter emission that would indicate the presence of a strong ionized wind and the absence of high-velocity molecular emission around source B (Mizuno et al. 1990; Girart et al. 2014) might indicate that source B is at a very early stage of its protostellar evolution.

5. CONCLUSIONS AND PERSPECTIVES

[2] The brightness temperature becomes equal to the kinetic temperature when (i) Local Thermodynamical Equilibrium (LTE) conditions apply (this is very likely at the high densities found near the center of source B), and (ii) when the optical depth tends to the infinite.

In this paper, we presented multi-epoch continuum observations of the Class 0 protostellar system IRAS 16293–2422 taken with the Very Large Array (VLA) at multiple wavelengths between 7 mm and 15 cm (41 GHz down to 2 GHz), as well as single-epoch Atacama Large Millimeter Array (ALMA) continuum observations covering the range from 0.4 to 1.3 mm (700 GHz down to 230 GHz). These observations all have sufficient angular resolution (typically better than $0.''4$) to resolve the various compact sources known to exist in the system.

The new VLA observations presented here, combined with previously published observations dating back to the late 1980s, were used to follow the proper motions of the different sources in the system. This confirms that the two sources known as A2 and B move on the plane of the sky with nearly identical velocities, tracing the overall relative motion between the Sun and the parent molecular cloud of IRAS 16293–2422, Lynds 1689N. The sources $A2\alpha$ and $A2\beta$, previously identified with recent ejecta from the protostellar object A2 are observed to symmetrically move away from A2, and one of them ($A2\alpha$) shows some evidence of diluting into its surroundings. Somewhat unexpectedly, the position angle between A1 and A2, which had been observed to increase steadily during the period from the late 1980s to the early 2000s, is now found to have started to decrease. This might indicate that A1 corresponds to the impact of a precessing jet onto the surrounding material, or that A1/A2 are two members of a tight hierarchical triple system.

Combining our new observations with data taken from the literature, we refined the determination of the spectrum of both component A and B. As expected for a protostar with an active outflow, the spectrum of component A changes from a shallow power law ($S_\nu \propto \nu^{0.44}$) at centimeter wavelengths to a steeper one ($S_\nu \propto \nu^{2.5}$) at millimeter wavelengths. In contrast, the spectrum of component B can be described by a single power law ($S_\nu \propto \nu^{2.28}$)

over the entire range from 2 to 700 GHz (10 cm down to 0.5 mm). This suggests that emission from component B is entirely dominated by dust even at λ = 10 cm, and that it drives no detectable outflow. We also find that the size of source B increases with frequency up to 41 GHz, remaining roughly constant (at $0''39 \equiv 55$ AU) at higher frequencies. We interpret this as evidence that source B is a dusty structure of finite size that becomes increasingly optically thick at higher frequencies. Finally, we find that the kinetic temperature at the center of source B is at least $\sim 1,000$ K.

REFERENCES

Adams, F. C., Ruden, S. P., & Shu, F. H. 1989, ApJ, 347, 959

Andre, P., Ward-Thompson, D., & Barsony, M. 1993, ApJ, 406, 122

Anglada, G., Rodríguez, L. F., & Carrasco-Gonzalez, C. 2015, Advancing Astrophysics with the Square Kilometre Array (AASKA14), 121

Anglada, G., Rodríguez, L. F., & Carrasco-González, C. 2018, A&A Rv, 26, 3

Artymowicz, P., & Lubow, S. H. 1994, ApJ, 421, 651

Brogan, C. L., Hunter, T. R., Cyganowski, C. J., et al. 2016, ApJ, 832, 187

Caux, E., Kahane, C., Castets, A., et al. 2011, A&A, 532, A23

Ceccarelli, C., Loinard, L., Castets, A., Tielens, A. G. G. M., & Caux, E. 2000, A&A, 357, L9

Chandler, C. J., Brogan, C. L., Shirley, Y. L., & Loinard, L. 2005, ApJ, 632, 371

Correia, J. C., Griffin, M., & Saraceno, P. 2004, A&A, 418, 607

Crimier, N., Ceccarelli, C., Maret, S., et al. 2010, A&A, 519, A65

Dzib, S. A., Ortiz-León, G. N., Hernández-Gómez, A., et al. 2018, ArXiv e-prints, arXiv:1802.03234

Girart, J. M., Estalella, R., Palau, A., Torrelles, J. M., & Rao, R. 2014, ApJL, 780, L11

Goodwin, S. P., Whitworth, A. P., & Ward-Thompson, D. 2004, A&A, 414, 633

Greene, T. P., Wilking, B. A., Andre, P., Young, E. T., & Lada, C. J. 1994, ApJ, 434, 614

Jacobsen, S. K., Jørgensen, J. K., van der Wiel, M. H. D., et al. 2018, A&A, 612, A72

Jørgensen, J. K., van der Wiel, M. H. D., Coutens, A., et al. 2016, A&A, 595, A117

Kraus, A. L., Ireland, M. J., Martinache, F., & Hillenbrand, L. A. 2011, ApJ, 731, 8

Lada, C. J., & Wilking, B. A. 1984, ApJ, 287, 610

Loinard, L. 2002, RMxAA, 38, 61

Loinard, L., Chandler, C. J., Rodríguez, L. F., et al. 2007, ApJ, 670, 1353

Loinard, L., Torres, R. M., Mioduszewski, A. J., & Rodríguez, L. F. 2008, ApJL, 675, L29

Loinard, L., Zapata, L. A., Rodríguez, L. F., et al. 2013, MNRAS, 430, L10

Makiwa, G. 2014, PhD thesis, University of Lethbridge (Canada

Mizuno, A., Fukui, Y., Iwata, T., Nozawa, S., & Takano, T. 1990, ApJ, 356, 184

18

Mundy, L. G., Wootten, A., Wilking, B. A., Blake, G. A., & Sargent, A. I. 1992, ApJ, 385, 306

Ortiz-León, G. N., Loinard, L., Kounkel, M. A., et al. 2017, ApJ, 834, 141

Padoan, P., Nordlund, Å., Kritsuk, A. G., Norman, M. L., & Li, P. S. 2007, ApJ, 661, 972

Panagia, N., & Felli, M. 1975, A&A, 39, 1

Pech, G., Loinard, L., Chandler, C. J., et al. 2010, ApJ, 712, 1403

Pineda, J. E., Maury, A. J., Fuller, G. A., et al. 2012, A&A, 544, L7

Rao, R., Girart, J. M., Marrone, D. P., Lai, S.-P., & Schnee, S. 2009, ApJ, 707, 921

Reipurth, B., Clarke, C. J., Boss, A. P., et al. 2014, Protostars and Planets VI, 267

Rodríguez, L. F., Loinard, L., D'Alessio, P., Wilner, D. J., & Ho, P. T. P. 2005, ApJL, 621, L133

Schöier, F. L., Jørgensen, J. K., van Dishoeck, E. F., & Blake, G. A. 2002, A&A, 390, 1001

Schönrich, R., Binney, J., & Dehnen, W. 2010, MNRAS, 403, 1829

Shu, F. H., Adams, F. C., & Lizano, S. 1987, ARA&A, 25, 23

Shu, F. H., Lizano, S., Ruden, S. P., & Najita, J. 1988, ApJL, 328, L19

Stassun, K. G., Mathieu, R. D., Cargile, P. A., et al. 2008, Nature, 453, 1079

Tobin, J. J., Kratter, K. M., Persson, M. V., et al. 2016a, Nature, 538, 483

Tobin, J. J., Looney, L. W., Li, Z.-Y., et al. 2016b, ApJ, 818, 73

Walker, C. K., Lada, C. J., Young, E. T., Maloney, P. R., & Wilking, B. A. 1986, ApJL, 309, L47

Wootten, A. 1989, ApJ, 337, 858

Yeh, S. C. C., Hirano, N., Bourke, T. L., et al. 2008, ApJ, 675, 454

Zapata, L. A., Loinard, L., Rodríguez, L. F., et al. 2013, ApJL, 764, L14

Chapter 4

IRAS 16293–2422 B: Un primer núcleo hidrostático ignorado?

IRAS 16293–2422B, un miembro del sistema protoestelar IRAS 16293–2422, muestra propiedades observacionales que son notables. Observaciones interferométricas en longitudes de onda centimétricas y milimétricas han revelado que su espectro en el continuo está dominado por emisión térmica de polvo. Además, perfiles P-Cygni inversos encontrados en esta fuente indican movimientos de caída, revelando que IRAS 16293–2422B es un objeto estelar joven que presenta acreción. El comportamiento del tamaño como función de la frecuencia sugiere que la fuente se vuelve cada vez más ópticamente gruesa conforme aumenta la frecuencia, hasta que a longitudes de onda sub-milimétricas, se vuelve completamente ópticamente gruesa, indicando que la estructura de densidad de IRAS 16293–2422B tiene una densidad central muy alta. La temperatura de brillo medida en la posición central con el VLA también indica que la temperatura central es alta ($\sim$ 1000 K). A pesar de estos hechos, la naturaleza de IRAS 16293–2422B aún es un misterio. Motivados por los resultados encontrados en el capítulo anterior, nos hemos concentrado en el análisis de las propiedades de esta fuente. Presentamos un modelo completo de transferencia radiativa de esta fuente hecho con el código GASS-LIME, basado en observaciones interferométricas con el VLA y ALMA entre 10 y 690 GHz que fueron presentadas previamente en el capítulo 3. También hemos utilizado mapas moleculares de algunas transiciones de CH_3OH y $H^{13}CN$ vistas con ALMA y que presentan perfiles P-Cygni inversos. Nuestro modelo para IRAS 16293–2422B consiste de una estructura de polvo con una densidad central alta (10^{13} cm^{-3}), un perfil de densidad empinado y una temperatura central de 1000 K. Encontramos que los perfiles de densidad y temperatura necesarios para reproducir los mapas observacionales de continuo presentados en el capítulo anterior y los perfiles de línea son muy similares a los esperados para primeros núcleos hidrostáticos. Esto, combinado con el hecho de que no encontramos evidencia de exceso de emisión en el rango centimétrico que pudiera ser causado por la presencia de un jet ionizado, podría indicar que IRAS16293–2422B apenas está alcanzando la fase protoestelar. Mi contribución en este artículo está relacionada con la calibración de los datos y la elaboracón de las imágenes de las observaciones en las que esta basado el modelo. También estuve a cargo de la redacción de una parte del artículo, excepto por la sección del modelado.

Chapter 4

IRAS 16293–2422 B: Un premier noyau hydrostatique ignoré?

IRAS 16293–2422B, membre du système protostellaire IRAS 16293–2422, présente des propriétés remarquables. Les observations interférométriques aux longueurs d'onde centimétriques et millimétriques ont révélé que son spectre continuum est dominé par l'émission thermique de la poussière. De plus, les profils P-Cygni inverses observés dans cette source indiquent des mouvements d'effondrement, ce qui révèle qu'IRAS 16293–2422B est un jeune objet stellaire en croissance. La variation de la taille de la source avec la fréquence suggère que celle-ci devient de plus en plus optiquement épaisse à des fréquences élevées, jusqu'à devenir complétement optiquement épaisse aux longueurs d'onde sub-millimétriques, ce qui indique que la structure d'IRAS 16293–2422B présente une densité centrale très élevées. La température de brillance centrale dans les données VLA indique, en outre, une température central élevée ($\sim$ 1000 K). En dépit de ces faits, la nature d'IRAS 16293–2422B reste mystérieuse. Motivés par les résultats du dernier chapitre, nous nous sommes concentrés sur l'analyse des propriétés de cette source. Nous présentons un modèle de transfert radiatif complet de cette source, calculé avec le code GASS-LIME, basé sur les observations interférométriques VLA et ALMA entre 10 et 690 GHz, précédemment présentées au Chapitre 3. Nous avons également utilisé des observations cartographiques de certaines transitions des molécules CH_3OH et $H^{13}CN$ observées avec ALMA et présentant des profils P-Cygni inverses. Notre modèle pour IRAS 16293–2422B comprend une structure poussiéreuse de densité centrale élevée à très élevée (10^{13} cm $^{-3}$), un profil de densité très raide et une température centrale de 1000 K. Nous avons constaté que les profils de densité et de température nécessaires pour reproduire les cartes de continuum observées présentées dans le dernier chapitre sont très similaires à ceux attendus pour les premiers noyaux hydrostatiques. Ces constatations, combinées au fait que nous n'avons trouvé aucune preuve d'un excès d'émission centimétrique associée à la présence d'un jet ionisé, pourraient indiquer qu'IRAS16293–2422B a tout juste atteint la phase protostellaire.

Ma contribution à cet article concerne la calibration des données et l'imagerie des observations dans lesquelles le modèle est basé. De plus, j'étais en charge de la rédaction de certaines parties du document, à l'exception de la partie consacrée à la modélisation.

Chapter 4

IRAS 16293–2422 B: An overlooked first hydrostatic core?

IRAS 16293–2422B, a member of the IRAS 16293–2422 protostellar system, shows observational properties that are remarkable. Interferometric observations at centimeter and millimeter wavelengths have revealed that its continuum spectrum is dominated by thermal dust. In addition, inverse P-Cygni profiles found in this source indicate infall motions, revealing that IRAS 16293–2422B is an accreting young stellar object. The behaviour of the size as a function of the frequency suggest that the source becomes increasingly optically thick at higher frequencies until it becomes entirely optically thick at sub-millimeter wavelengths, indicating that the density structure of IRAS 16293–2422B has a very high central density. The brightness temperature measured at the central position with the VLA also indicates that the central temperature is high (~ 1000 K). Despite all these facts, the nature of IRAS 16293–2422B is still puzzling. Motivated by the results found in the last chapter, we have focused in the analysis of the properties of this source. We present a full radiative transfer model of this source computed with the GASS-LIME code based on the VLA and ALMA interferometric observations between 10 and 690 GHz that were previously presented in Chapter 3. We have also used molecular mapping observations of some CH_3OH and $H^{13}CN$ transitions seen with ALMA that present inverse P-Cygni profiles. Our model for IRAS 16293–2422B consists of a dusty structure of a high central density (10^{13} cm^{-3}), a steep density profile and a central temperature of 1000 K. We found that the density and temperature profiles needed to reproduces the observed continuum maps presented in the last chapter and the line profiles are very similar to those expected for first hydrostatic cores. This, combined with the fact that we found no evidence of excess of emission in the centimeter range that could be caused by the presence of a ionized jet might indicate that IRAS16293–2422B just reached the protostellar phase.

My contribution for this paper in particular is related with the data calibration and imaging of the observations in which the radiative transfer model is based on. In addition, I was in charge of the redaction of some sections of the paper, except for the part of the modelling.

IRAS 16293–2422 B: An overlooked first hydrostatic core?

David Quénard,[1] Antonio Hernández-Gómez,[2,3] Laurent Loinard,[3,4] Emmanuel Caux,[2] Sandrine Bottinelli,[2] and al.[5]

[1]*School of Physics and Astronomy, Queen Mary University of London, Mile End Road, London E1 4NS, UK*
[2]*IRAP, Université de Toulouse, CNRS, UPS, CNES, Toulouse, France*
[3]*Instituto de Radioastronomía y Astrofísica, Universidad Nacional Autónoma de México, 58089 Morelia, Mexico*
[4]*Instituto de Astronomía, Universidad Nacional Autónoma de México, Apartado Postal 70-264, 04510 Ciudad de México, Mexico*
[5]

ABSTRACT

IRAS 16293–2422B is arguably the clearest known example of an accreting young stellar object, where infall in unambiguously revealed by a **spatially resolved** inverse P Cygni profile. In addition, the spectral energy distribution of IRAS 16293–2422B reveals that the emission mechanism from the sub-millimeter to the radio regime is entirely due to thermal dust radiation, with no contribution from outflowing ionized material. The behavior of source size with wavelength further indicates that the source becomes increasingly optically thick at higher frequencies until, in the millimeter and sub-millimeter regimes, it is entirely optically thick; this implies a very high central density. Finally, observed brightness temperatures in the centimeter regime indicate a central temperature of about 1,000 K. In this work, we present a full radiative transfer modelling of the structure of IRAS 16293–2422B informed by line and continuum VLA and ALMA interferometric high angular resolution observations between 10 and 690 GHz. The ensemble of observational properties can be reproduced by a model where the source is a spherical dusty structure with a very high central density ($\sim 10^{13}$ cm^{-3}), a steep density profile, and a central temperature of 1,000 K. Our model is able to reproduce accurately the continuum observations at all wavelengths, as well as the molecular maps. In addition, it strongly suggests that there is no collapsed (protostellar) object at the center of IRAS 16293–2422B. Remarkably, the density and temperature profiles obtained from the modelling mimic those expected for first hydrostatic cores. These facts, together with the observed absence of excess centimeter emission that would reveal the presence of a strong ionized wind, might indicate that IRAS 16293–2422B has not yet reached the protostellar stage. In this scenario, the inverse P Cygni profiles would trace infall onto the first hydrostatic core rather than onto the protostar.

Keywords: ISM: individual (IRAS 16293–2422) — line: profiles — methods: numerical — radiative transfer — radio continuum: ISM — stars: formation

1. INTRODUCTION

The formation of single low-mass stars is now widely accepted to be adequately described by the paradigm presented in Shu et al. (1987). The process begins with the fragmentation of a large molecular cloud into dense and cold condensations that collapse gravitation-

ally. The initial collapse phase proceeds until individual cores become optically thick, at which point they reach an equilibrium stage to become *first hydrostatic cores* (FHSC; Larson 1969). During the FHSC stage, accretion from the envelope onto the core continues, resulting in an adiabatic increase of the core temperature. When the temperature reaches $\sim$ 2,000 K, the dissociation of H$_2$ occurs, allowing the core to resume collapse at free-fall speed. This second collapse phase proceeds until the internal pressure is sufficient to halt it, and leads to

Corresponding author: Antonio Hernández
a.hernandez@irya.unam.mx

the formation of a second hydrostatic core, corresponding to the Class 0 protostellar phase. Class 0 protostars are characterized by energetic collimated outflows that are not expected during the FHSC stage. While many Class 0 sources are known (e.g. André et al. 1993), FHSC have remained elusive in spite of intensive searches (e.g. Enoch et al. 2010).

IRAS 16293–2422 is located in the dark cloud Lynds 1689 N within the Ophiuchus star-forming complex at a distance of 141^{+30}_{-21} pc (Dzib et al. 2018). IRAS 16293–2422 is composed of two compact sources called IRAS 16293–2422A and B (Wootten 1989; Mundy et al. 1992) separated by about $5''$ ($\equiv 700$ au). A fairly comprehensive description of the system as a whole is provided in the companion paper by Hernández-Gómez et al. (2018). In the present paper, we will focus exclusively on IRAS 16293–2422B, and now proceed to describe several of its remarkable properties.

IRAS 16293–2422B is a fairly compact source, with a size measured with ALMA at (sub-)millimeter wavelengths of $0''.4$ or 55 au (Hernández-Gómez et al. 2018). As shown in Chandler et al. (2005) and Hernández-Gómez et al. (2018), the spectral energy distribution of IRAS 16293–2422B over the entire frequency range where it has been measured (from 2 to 700 GHz) is consistent with thermal dust radiation. This is highly unusual, because the centimeter emission ($1 < \nu < 50$ GHz) of low-mass young stars is normally dominated by free-free radiation associated with partially ionized winds (e.g. Anglada et al. 2018). The lack of such free-free emission in the case of IRAS 16293–2422B strongly suggests that it does not drive a powerful outflow. Both the spectral index and the behavior of the size of IRAS 16293–2422B as a function of frequency further show that the dust emission is increasingly optically thick at higher frequencies until, at millimeter and sub-millimeter wavelengths, the source is entirely optically thick. This implies a very high central density. The brightness temperature measured with the VLA at $\lambda \approx 1$ cm places stringent lower limits of order 700 K on the central temperature of IRAS 16293–2422B (Hernández-Gómez et al. 2018).

IRAS 16293–2422B is also arguably the young stellar object where evidence of infall is most clearly established. The first clear evidence for infall motion was reported by Chandler et al. (2005) from SMA observations at 300 GHz. Using ALMA observations at ∼220 GHz, Pineda et al. (2012) reported infall movements as well based on the detection of an inverse P-Cygni profile from complex molecules such as CH_3OCHO and H_2CCO and derived an infall rate of $4.5 \times 10^{-5} M_\odot yr^{-1}$. Zapata et al. (2013) used ALMA observations at 690 GHz of other

molecular transitions (of $H^{13}CN$, $HC^{15}N$ and CH_3OH) to further study the inverse P-Cygni profile. They find that the molecular lines are seen entirely in absorption toward the central position of IRAS 16293–2422B due to the high opacity of the dust there. That central absorption region is surrounded by a ring of molecular emission with a deconvolved size of 40 mas. In other words, the inverse P-Cygni profile is spatially resolved. Zapata et al. (2013) also reported a velocity gradient in the east-west direction, suggesting a disk geometry almost exactly aligned with the plane of the sky. More recently, Jacobsen et al. (2018) modelled the structure of the envelope of IRAS 16293–2422 and its protostellar components based on ALMA observations of ^{13}CO, $C^{17}O$ and $C^{18}O$ at scales up to $\sim 8,000$ AU. They adopted a disk-like structure for IRAS 16293–2422B but showed that the disk needed to have a large scale-height in order to reproduce the observed continuum dust emission level. Oya et al. (2018) also studied the line profiles of several molecules towards IRAS 16293–2422B with ALMA. They found that while some species are concentrated towards the center of the source, others are more extended, and probably associated with an infalling rotating envelope. However, since the P-Cygni profiles from those species are interpreted as free-fall motion of the gas around the location where the infalling rotating envelope turns into a rotationally supported disk (called centrifugal barrier), they argue that both infall and outflow motions could coexist in IRAS 16293–2422B.

Although much effort has been devoted to understanding the physics and the chemistry of IRAS 16293–2422B, its structure has not been yet completely established. This is a fundamental ingredient for chemical modeling and the correct interpretation of the observations toward this source. For this reason, in this paper, we focus on determining the physical structure of IRAS 16293–2422B based on high angular resolution interferometric observations with the VLA and ALMA over a wide range of frequencies. To do so, we have used a radiative transfer code to produce synthetic continuum and molecular maps and compare our predicted emission/absorption line profiles and continuum maps directly with the observations. In Section 2, we briefly present the relevant observations, while in Section 3 we present our physical model and explain how it was derived. In Section 4 we discuss the results of our model, providing, in particular, a comparison with first hydrostatic core simulations. Finally Section 5 contains our conclusions.

2. OBSERVATIONS

The continuum observations we use have been obtained using the VLA and ALMA between 10 and

Table 1. Observational properties used in CASA

Frequency (GHz)	Beam size (arcsec)	Beam P.A. (degree)	rms (Jy/beam)
10	0.39×0.14	-26.90	6.2×10^{-6}
15	0.24×0.09	-23.68	4.7×10^{-6}
22	0.13×0.06	-35.42	4.8×10^{-5}
33	0.11×0.04	-15.61	2.5×10^{-5}
41	0.09×0.04	-03.45	6.5×10^{-5}
44	0.08×0.07	-35.42	3.1×10^{-5}
306	0.17×0.12	-85.55	6.0×10^{-3}
338	0.18×0.13	$+83.90$	3.5×10^{-3}
342	0.25×0.13	-76.88	4.9×10^{-3}
404	0.28×0.22	$+78.31$	9.6×10^{-3}
453	0.31×0.21	-81.88	1.4×10^{-2}
690	0.29×0.16	-70.77	1.6×10^{-2}

44 GHz, and 306 and 690 GHz, respectively. These observations were performed between 2011 and 2015 and have typical spatial resolutions between about $0\rlap{.}''05$ and $0\rlap{.}''3$. The data reduction and analysis are described in the companion paper by Hernández-Gómez et al. (2018). We refer the reader to Table 1 of this paper for the details on these observations.

We have also extracted data cubes around the frequencies of $H^{13}CN$ and CH_3OH from ALMA Science Verification data obtained with the Double Sideband (DSB) Band 9 receivers. These observations were carried out on 16 and 17 April 2012 with a total observing time of about 9.2 hours. The phase center was $\alpha_{2000} = 16^h32^m 22\rlap{.}^m7$, $\delta_{2000} = -24°28'\ 32\rlap{.}''5$. Four basebands were used for obtaining data with Frequency Division Mode (FDM). Each spectral window contained 3840 channels and a bandwidth of 1.875 GHz, providing a channel separation of 0.488 MHz (~ 0.2 km s^{-1}). These data were obtained using the Cycle 0 Early Science extended configuration which resulted in an angular resolution of about $0\rlap{.}''2$. The overall absolute flux uncertainty was estimated to be about 20%.

3. MODELLING

3.1. *Methodology*

To determine the structure of IRAS 16293–2422B from the multiple continuum observations presented in Section 2, we have used a combination of three codes: GASS[1] (Quénard et al. 2017), LIME[2] (Brinch & Hoger-

heijde 2010) and CASA[3], the Common Astronomy Software Applications.

The first code, GASS, allows us to define the structure of the source. Considering the observed circular appearance of IRAS 16293–2422B (see Hernández-Gómez et al. 2018), we adopted a spherical structure. The maximum source radius is assumed to be 282 au ($2''$ at 141 pc). This radius corresponds to the volume of influence of the sphere defined by IRAS 16293–2422B and we define the physical model within this limit. We make no *a priori* assumption on the physical structure of the source and we ran various grids (a few thousands of models in total) by varying three physical properties:

1. **The temperature profile**. The inner temperature, the number of temperature jumps, the radii at which these jumps occur and the slope of the power-law profile have been varied (4 parameters).

2. **The density profile**. The inner density, the number of density jumps, the radii at which these jumps occur and the slope of the power-law profile have been varied (4 parameters).

3. **The dust opacity as a function of wavelength**. The dust opacity profile is assumed to be described by

$$\kappa_\nu = \kappa_0 \left(\frac{\nu}{\nu_0}\right)^\beta = \alpha\,\nu^\beta.$$

   We varied α and β in the models (2 parameters).

Thus, our models have a total of 10 free parameters. If we pretend to vary all these parameters at the same time and we explore just 5 values for each, a grid of $\sim 10^7$ models would have to be considered and this is not a manageable amount. Instead, we first constructed smaller grids varying only one or two parameters at the same time for both the temperature and densities. This way, we were able to rapidly constrain the density and temperature profiles.

Once a model is defined (by specifying a set of 10 parameters), we perform the radiative transfer modelling using LIME v1.5. LIME is fast at producing continuum images thanks to its *continuum only* mode. We used 10,000 points in GASS to define the model, which is a sufficiently large number considering the simple physical structure of IRAS 16293–2422B. The output image intensity unit is set to Jy/pixel with 201 pixels per dimension and a resolution of $0\rlap{.}''01$ per pixel. The total image size is therefore $2'' \times 2''$, large enough to cover the

---

[1] https://quenarddavid.wixsite.com/astrophysics/gass-code
[2] https://github.com/lime-rt/lime
[3] https://casa.nrao.edu/index.shtml

emission region of IRAS 16293–2422B that we are interested in. The output of the LIME modelling is a set of 12 continuum images, stored as FITS files, corresponding to the 12 continuum frequencies listed in Table 1. We used CASA to post-process these images by adding the appropriate noise level at each frequency, and by convolving the images by the synthesized beam of the relevant interferometric observations. Table 1 presents these values for each frequency. These new images are then compared to the observations.

3.2. *Best fit model*

In order to derive the best fit, we have compared the observed and modelled continuum images by minimizing the difference in pixel intensities along a horizontal cut, as well as over the entire image. The images at all frequencies were taken into account in the minimization process.

The best fit physical structure is shown in Figure 1. The central temperature is 1,000 K, remaining constant until 4.2 au. Then it follows a power-law profile (with a slope of –0.8) until 9.4 au where the slope becomes –1 until the edge of the source (at 282 au). The central density is found to be 10^{13} cm^{-3}, constant until 4.2 au. Then it follows a power-law profile (with a slope of –5.5) until 9.4 au where the slope becomes –1.6. At 32.9 au, the slope becomes –3.5 until the edge of IRAS 16293–2422B.

The dust opacity value is also varied to derive the best profile and it is a highly constrained parameter because of the numerous continuum images we are using covering a wide range of frequencies. We ran large grids of models with tiny steps to efficiently constrain both α and β. First, we considered only one dust opacity profile (corresponding to a single dust size) but the fit to the data was poor. By nature, LIME cannot consider a grain size distribution over the model. Therefore, only one dust opacity distribution can be considered at a time. In the case of IRAS 16293–2422B, dust growth likely occurs because of the high densities in the inner region of the object (Jørgensen et al. 2016). Bigger grains are likely to be present near the center, changing the dust opacity profile as the radius varies. To take this effect into account using LIME, we used two dust opacity profiles: one for the VLA observations, resolving the very inner structure of IRAS 16293–2422B and one for the ALMA observations, sensitive to the external dust distribution of the source. By doing so, we can constrain the dust size distribution of the source and derive correct dust properties. The best fit dust opacity profiles we obtain are the following:

$$\kappa_\nu^{\mathrm{ALMA}} = 0.55\,\nu^{0.30} = 3.04\left(\frac{\nu}{300\ \mathrm{GHz}}\right)^{0.30}, \quad (1)$$

$$\kappa_\nu^{\mathrm{VLA}} = 0.25\,\nu^{0.30} = 0.25\left(\frac{\nu}{10\ \mathrm{GHz}}\right)^{0.30}. \quad (2)$$

We emphasize that in this case, the two slopes are the same for both ALMA and VLA observations with $\beta = 0.30$, and they are both in very good agreement with the $\beta = 0.28 \pm 0.02$ value derived from the SED of the source (Hernández-Gómez et al. 2018). Only the scaling power-law factor (the α parameter) is different between the two dust opacity laws, revealing that dust growth is indeed occurring in the source, with bigger grains in the innermost region.

From our best fit physical structure we have determined that the total mass of IRAS 16293–2422B is $\sim 0.06\,\mathrm{M}_\odot$ with a total H$_2$ column density N(H$_2$) $= 1.34 \times 10^{27}$ cm^{-2}. Recent studies performed by Jørgensen et al. (2016) and Martín-Doménech et al. (2017) derived the H$_2$ column density from continuum observations of the source at 353 and 232 GHz, respectively, assuming $\tau = 1$. They derived N(H$_2$)>1.2 × 10^{25} cm^{-2} and N(H$_2$) = 2.8 × 10^{25} cm^{-2}, respectively. Using our density profile, at $\tau = 1$, we obtain N(H$_2$) = 1.03×10^{25} cm^{-2} at 353 GHz and N(H$_2$) = 1.17×10^{25} cm^{-2} at 232 GHz, in good agreement with the results obtained by Jørgensen et al. (2016) and Martín-Doménech et al. (2017).

Of course, the profiles derived here are only parametric characterizations of the true density and temperature profiles in IRAS 16293–2422B. We note, also, that the behavior of the density and temperature at radii smaller than about 5 au is not constrained at all by the observations since the source remains partially optically thick even at the lowest frequencies. In particular, the presence of higher densities near the very center of IRAS 16293–2422B cannot be discarded. Similarly, the interferometric observations used to constrain the model of IRAS 16293–2422B are not sensitive to faint extended emission on angular scales larger than 1–2″. This corresponds to radii of about 75-150 au. Appendix A presents images at all the modelled frequencies, with comparisons to the observations.

3.3. *Molecular modelling*

In this section we aim at checking the validity of our physical structure by using it to generate synthetic molecular maps. Indeed, molecular lines are good probes of physical structures, especially of density and temperature profiles. We will use two molecules: H^{13}CN and CH$_3$OH. The molecular maps corresponding to these lines are calculated under LTE assumption, as the H$_2$ density is much higher than the critical densities of the transitions we are interested in. We have confirmed this by checking that both LTE and non-LTE
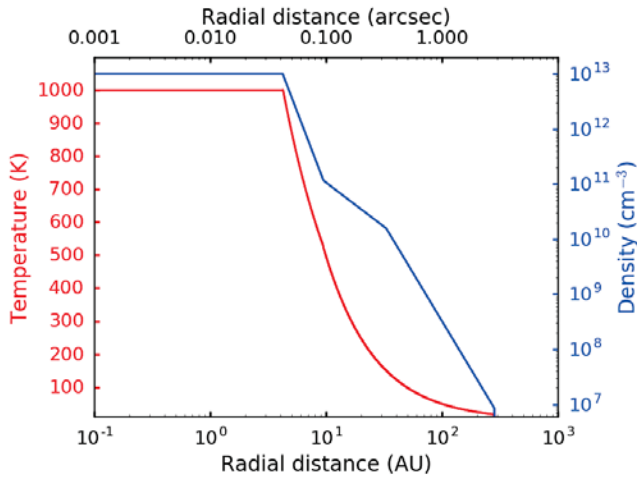
Figure 1. Density (blue) and temperature (red) profiles of IRAS 16293–2422B derived by the best fit model compared to the observations.

radiative transfer calculations are giving the same result (for both molecules) with LIME.

3.3.1. *$H^{13}CN$ modelling*

For $H^{13}CN$, we used the best fit physical profile and dust opacity as a basis. We then ran thousands of abundance profile models to fit the molecular maps. The best fit abundance profile gives a value for the abundance of 9×10^{-9}, which remains constant until 61.1 au. After this radius, the $H^{13}CN$ abundance drops by several orders of magnitude (we used a value of 10^{-15} for the abundance outside of 61.1 au, to avoid numerical difficulties associated with using abundances of zero). This can be explained by the depletion of the molecules onto the dust grain surface because of the lower temperature ($\sim 70 - 80$ K) at this radius combined to the very high densities ($> 10^9$ cm^{-3}). The resulting $H^{13}CN$ emission map is shown in Figure 2, where the agreement between the model and the observations can be appreciated. In reality, the $H^{13}CN$ distribution around the source might not be perfectly homogeneous, explaining the small residual differences. Overall, we consider the agreement between the observations and the model to be very satisfactory.

3.3.2. *CH_3OH modelling*

As for $H^{13}CN$, the CH_3OH molecular maps are fitted using the best fit physical structure and by running several grids of abundance profiles. The best fit yields an abundance of 2×10^{-7} until 61.1 au (same radius as for $H^{13}CN$), which then drops by several order of magnitude at larger radii (again, we used 10^{-15} for the outer abundance). As with $H^{13}CN$, this can be explained by the heavy depletion of molecules occurring at lower temperatures, combined with very high densities. The resulting

CH_3OH emission map is shown in Figure 2. The residual is at the noise level, except in a small southern region where the model predicts less emission than is actually observed. This might be caused by inhomogeneities in the distribution of the molecule around IRAS 16293–2422B.

The modelling of the continuum emission presented in Section 3.2 results in a density profile (Figure 1) that can be used to self-consistently predict the molecular line widths. The measured line width (for both $H^{13}CN$ and CH_3OH) happen to be slightly larger than the values expected from our model. The discrepancy can be resolved by adding a point-like mass condensation, $M_B^\star = 0.006 \pm 0.002$ M$_\odot$, at the center of IRAS 16293–2422B. We interpret this as evidence that the density profile in the inner few au increases above the value of 10^{13} cm^{-3} that we adopted in our model (recall that the density in the few central au cannot be constrained from the data; see end of Section 3.2). For instance, a mean density of $\sim 3 \times 10^{14}$ cm^{-3} in the central au would be sufficient to produce the excess mass needed to self-consistently reproduce the line profiles. From this analysis, we conclude that there is no evidence supporting the existence of a collapsed (protostellar object) near the center IRAS 16293–2422B.

4. DISCUSSION

The model presented in Section 3.2 shows that the continuum observations of IRAS 16293–2422B can be reproduced assuming a spherical source structure with the density and temperature profiles shown in Figure 1. The analysis of the molecular line widths (Section 3.3) suggests that the central density might even be higher. The high values of the central densities and temperatures, as well as the size of IRAS 16293–2422B, are reminiscent of those expected in first hydrostatic cores (FHSC), so we will now carry out a direct comparison between our results and theoretical simulations of FHSC. We have used the recent simulations performed by Vaytet & Haugbølle (2017), who produced numerous calculations of the gravitational collapse of an isolated sphere of gas with uniform temperature and a Bonnor-Ebert density profile. They varied initial masses from 0.2 to 8 M$_\odot$, temperatures between 5–30 K and radii $3,000 \leq R_0 \leq 30,000$ au.

Among all 143 calculations performed by Vaytet & Haugbølle (2017), we have found two models (run 023 and run 119) whose density and temperature profiles correspond well with those we derived for IRAS 16293–2422B. Figure 3 presents these models for different time steps of the FHSC simulation. In both cases, there
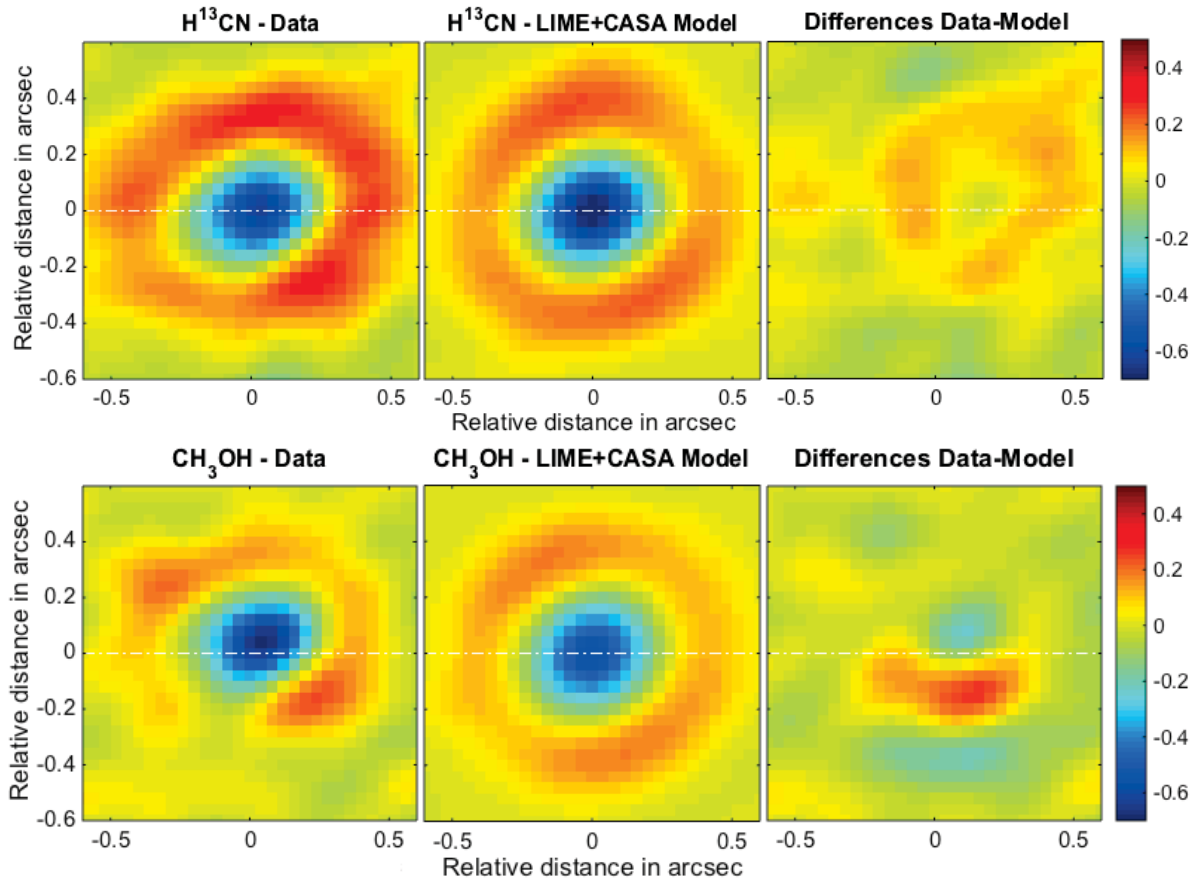
Figure 2. Molecular map of H^{13}CN (top) and CH$_3$OH (bottom). The left column shows the observed maps, the central column shows the model, and the right column shows the residual between the model and the observed maps.

is a very significant discrepancy between our model of IRAS 16293–2422B and the theoretical models for the density in the central few au. As mentioned earlier, however, the behavior of the density in that region is not constrained by the observations, so this discrepancy is not relevant. Indeed, the higher central densities suggested by the molecular line widths (end of Section 3.3) would bring the model of IRAS 16293–2422B and the FHSC theoretical models in better agreement. Similarly, the comparison between our model for IRAS 16293–2422B and the FHSC theoretical models should not be extended beyond radii of about 100 au because the interferometric observations used here are not sensitive to extended emission (end of Section 3.2).

For run 023 (top panels), the temperature coincides well with the one of IRAS 16293–2422B but the density profile is slightly higher, affecting the total mass as a function of the radius (top-right panel). On the contrary, the density profile in run 119 (bottom panels) agrees much more with the one of IRAS 16293–2422B but the temperature profile less so –there seems to be a small shift in radius between the profiles for IRAS 16293–2422B and for the theoretical model. Re-

gardless of these small differences, the density and temperature profiles derived here for IRAS 16293–2422B are generally similar to those expected theoretically for FHSC.

So, could IRAS 16293–2422 B be a first hydrostatic core? Aside from the similarity in the density and temperature profiles, there are several elements that would be consistent with this possibility. The first one is the very fact that IRAS 16293–2422B is optically thick; high optical thickness is precisely one of the defining characteristics of FHSC, since radiation pressure is what maintains them in a state of equilibrium. The second one is the aforementioned fact that there is little to no evidence pointing to the existence of a collapsed (protostellar) object at the center of IRAS 16293–2422B. The third one is that there is no evidence for an excess of free-free emission at low frequencies that would indicate the existence of a powerful wind driven from IRAS 16293–2422B (see Hernández-Gómez et al. 2018 for details). In contrast, Class 0 protostars are expected to produce such powerful winds. We note finally that the accretion rate on IRAS 16293–2422B (4.5×10^{-5} M$_\odot$ yr^{-1}; Pineda
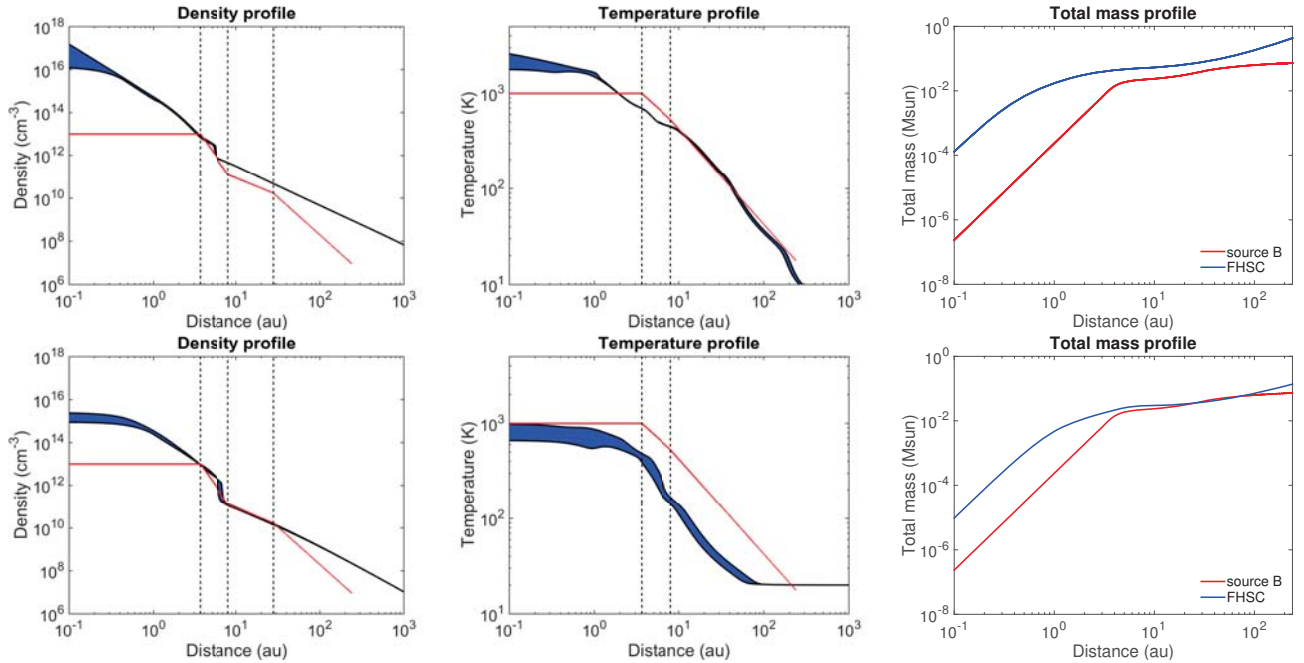
Figure 3. Density, temperature and total mass profiles for run 023 (top panels) and run 119 (bottom panels) obtained by Vaytet & Haugbølle (2017) are shown in blue, while the predicted profiles from our model are shown in red. The width of the blue renderings of the model reflects their time evolution.

et al. 2012) combined with its mass (0.06–0.07 $M_\odot$) indicate a dynamical age of order 1,000 yr. This is comparable with the expected lifetime of a FHSC with that accretion rate (Figure 8 in Vaytet & Haugbølle 2017).

One could argue that there is a contradiction between the claim that IRAS 16293–2422B is a FHSC (i.e. that it has not yet reached the protostellar phase) and the fact that it is one of the most clearly accreting know young stellar objects. This contradiction does not exist, however, since FHSC are expected to be continuously accreting from their surrounding envelopes (at rates between 10^{-3} and 10^{-5} $M_\odot$ yr^{-1}; Vaytet & Haugbølle 2017). This accretion is precisely what is needed for their internal temperature to rise, and eventually for the collapse to resume toward the formation of a protostar. Indeed, it might well be that the reason why the inverse P Cygni profile toward IRAS 16293–2422B is spatially resolved and so clearly detected is because they trace accretion onto an extended structure rather than a collapsed object. Protostars have radii of order of the Solar radius ($\sim 10^{-3}$ au), so the spatial scale corresponding to infall structures onto a protostar should remain unresolved even at the $\sim 0\rlap{.}''1$ scales probed here. In contrast, infall onto a FHSC whose size is expected to be of order 10 au Vaytet & Haugbølle (2017) ought to be resolved at our angular resolution, as is observed here for IRAS 16293–2422B.

5. CONCLUSIONS

In this work, we have used VLA and ALMA continuum and line observations to constrain the physical structure of IRAS 16293–2422 B. We made no a priori assumption on the physical structure of the source and ran a grid of models by varying the temperature, density and dust opacity profiles by using GASS and LIME. We then produced continuum maps in CASA by adding the observed rms noise level and convolving the images with the synthesized beam provided by the interferometric observations to compare directly with the data. Since the dust size can change along the radius of the source, affecting the dust opacity profile, we have considered separate dust profiles for the VLA and ALMA observations but with the same slope of 0.30, which is in full agreement with the 0.28 ± 0.02 value derived from the observations. To validate our physical structure, we computed the expected H^{13}CN and CH$_3$OH molecular maps by calculating appropriate abundance profiles for these species. We found that our model can successfully reproduce the complex molecular maps as observed with ALMA.

Our best model for the density and temperature profiles of IRAS 16293–2422B resembles those expected for first hydrostatic cores, and implies a mass of ~ 0.06 $M_\odot$ for IRAS 16293–2422B. In addition, we find that there is no compelling evidence to suggest that a collapsed (protostellar) object is located at the center of the compact but resolved IRAS 16293–2422B. Combined with the previously known lack of excess free-free emis-

sion at centimeter frequencies, our results suggest that IRAS 16293–2422B might be a first hydrostatic core rather than a protostar.

REFERENCES

André, P., Ward-Thompson, D., & Barsony, M. 1993, ApJ, 406, 122

Anglada, G., Rodríguez, L. F., & Carrasco-González, C. 2018, A&A Rv, 26, 3

Bisschop, S. E., Jørgensen, J. K., Bourke, T. L., Bottinelli, S., & van Dishoeck, E. F. 2008, A&A, 488, 959

Brinch, C. & Hogerheijde, M. R. 2010, A&A, 523, A25.

Chandler, C. J., Brogan, C. L., Shirley, Y. L., & Loinard, L. 2005, ApJ, 632, 371

Dzib, S. A., Ortiz-León, G. N., Hernández-Gómez, A., et al. 2018, A&A, 614, A20

Enoch, M. L., Lee, J.-E., Harvey, P., Dunham, M. M., & Schnee, S. 2010, ApJL, 722, L33

Girart, J. M., Estalella, R., Palau, A., Torrelles, J. M., & Rao, R. 2014, ApJL, 780, L11

Jacobsen, S. K., Jørgensen, J. K., van der Wiel, M. H. D., et al. 2018, A&A, 612, A72

Jørgensen, J. K., Bourke, T. L., Nguyen Luong, Q., & Takakuwa, S. 2011, A&A, 534, A100

Jørgensen, J. K., van der Wiel, M. H. D., Coutens, A., et al. 2016, A&A, 595, A117

Kuan, Y.-J., Huang, H.-C., Charnley, S. B., et al. 2004, ApJL, 616, L27

Liu, H. B., Hasegawa, Y., Ching, T.-C., et al. 2018, arXiv:1805.02012

Larson, R. B. 1969, MNRAS, 145, 271

Loinard, L., Zapata, L. A., Rodríguez, L. F., et al. 2013, MNRAS, 430, L10

Martín-Doménech, R., Rivilla, V. M., Jiménez-Serra, I., et al. 2017, MNRAS, 469, 2230

Mizuno, A., Fukui, Y., Iwata, T., Nozawa, S., & Takano, T. 1990, ApJ, 356, 184

Mundy, L. G., Wootten, A., Wilking, B. A., Blake, G. A., & Sargent, A. I. 1992, ApJ, 385, 306

Oya, Y., Moriwaki, K., Onishi, S., et al. 2018, ApJ, 854, 96

Persson, M. V., Jørgensen, J. K., Müller, H. S. P., et al. 2018, A&A, 610, A54

Pineda, J. E., Maury, A. J., Fuller, G. A., et al. 2012, A&A, 544, L7

Quénard, D., Bottinelli, S., & Caux, E. 2017, MNRAS, 468, 685

Quénard, D., Bottinelli, S., Caux, E., & Wakelam, V. 2018, MNRAS, accepted

Rao, R., Girart, J. M., Marrone, D. P., Lai, S.-P., & Schnee, S. 2009, ApJ, 707, 921

Reipurth, B., Clarke, C. J., Boss, A. P., et al. 2014, Protostars and Planets VI, 267

Shu, F. H., Adams, F. C., & Lizano, S. 1987, ARA&A, 25, 23

Stark, R., Sandell, G., Beck, S. C., et al. 2004, ApJ, 608, 341

Vaytet, N., Audit, E., Chabrier, G., Commerçon, B., & Masson, J. 2012, A&A, 543, A60

Vaytet, N., Chabrier, G., Audit, E., et al. 2013, A&A, 557, A90

Vaytet, N., & Haugbølle, T. 2017, A&A, 598, A116

Wootten, A. 1989, ApJ, 337, 858

Zapata, L. A., Loinard, L., Rodríguez, L. F., et al. 2013, ApJL, 764, L14

APPENDIX

A. CONTINUUM IMAGE OF THE MODELS COMPARED TO THE OBSERVATIONS

In this section we present the continuum maps obtained from the VLA and ALMA observations and the continuum maps produced by our best model. These synthetic maps where produced by adding the observed rms noise level and convolving the resulting images from the LIME radiative transfer modelling with the beam size and shape recovered from the observations in each case. In all figures, we show the data (top left panel), our best model (top right panel) and the residual between these maps (bottom left panel). We also made a cut along IRAS 16293–2422B (white dotted line) in both maps and produced an intensity profile (bottom right panel). The blue profile correspond to the data, while the red one is taken from our model.
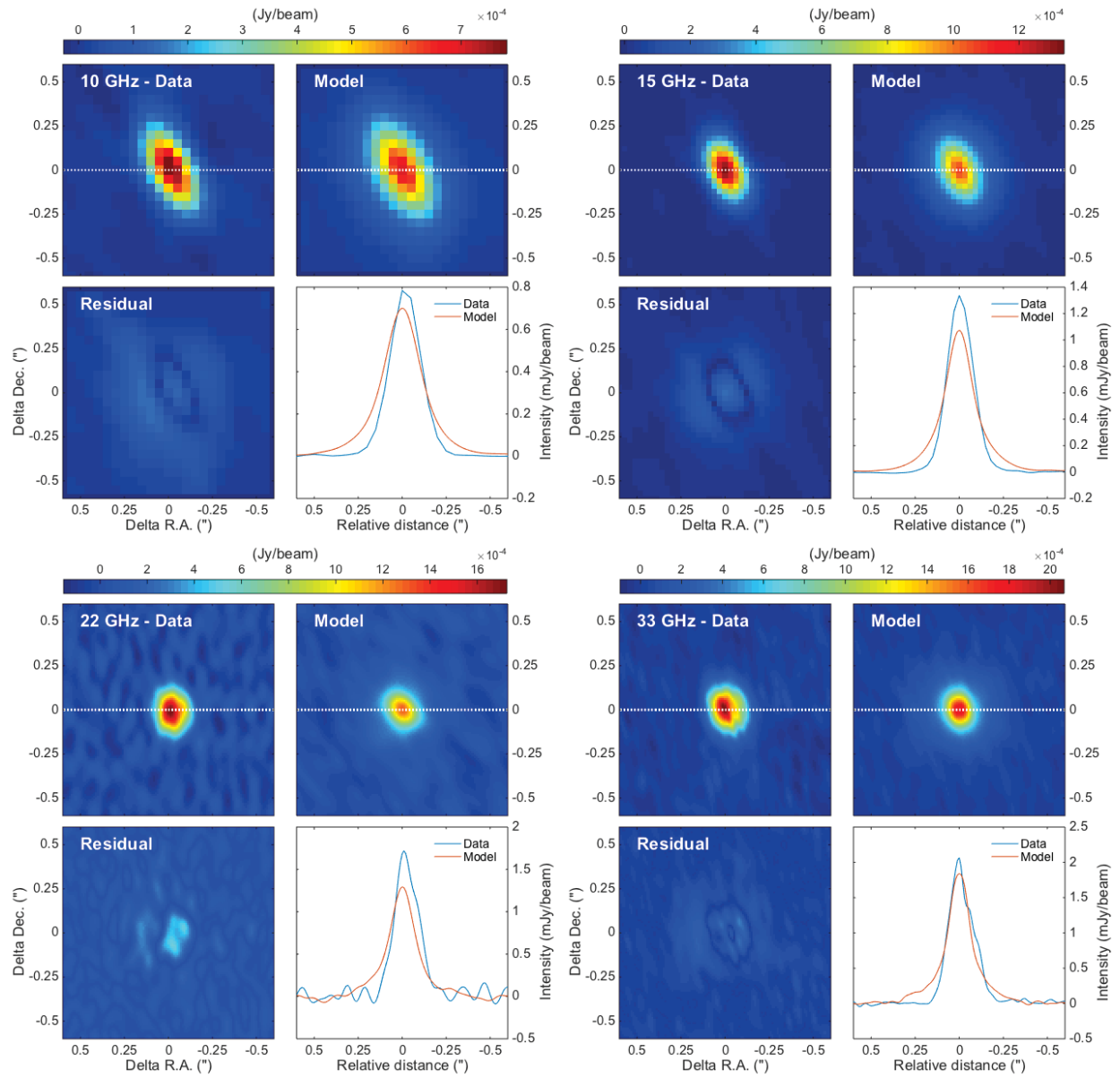
Figure 4. VLA observed and modelled continuum images at 10, 15, 22 and 33 GHz.
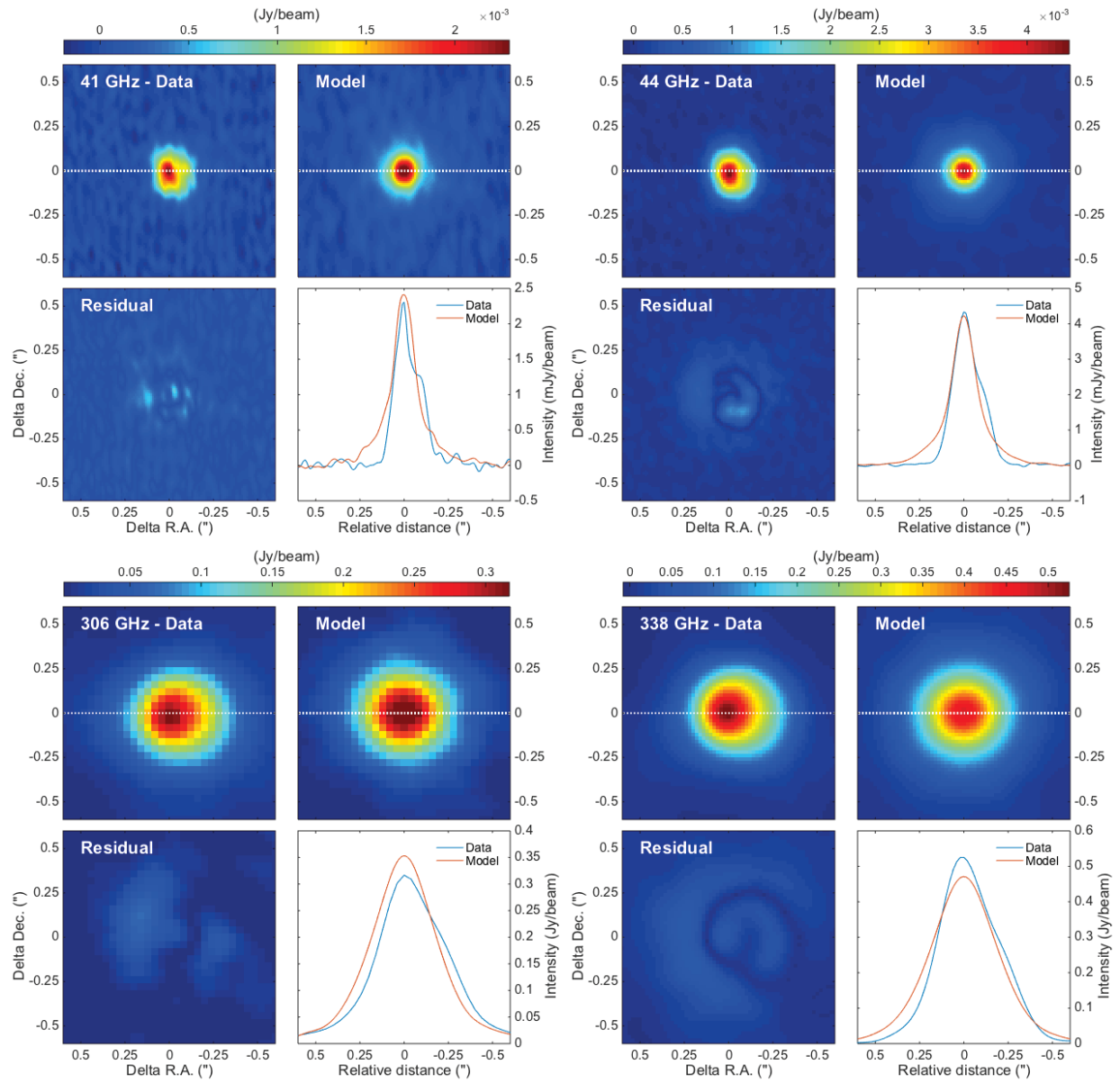
Figure 5. VLA (top panels) and ALMA (bottom panels) observed and modelled continuum images at 41 and 45 GHz, and 306 and 338 GHz respectively.
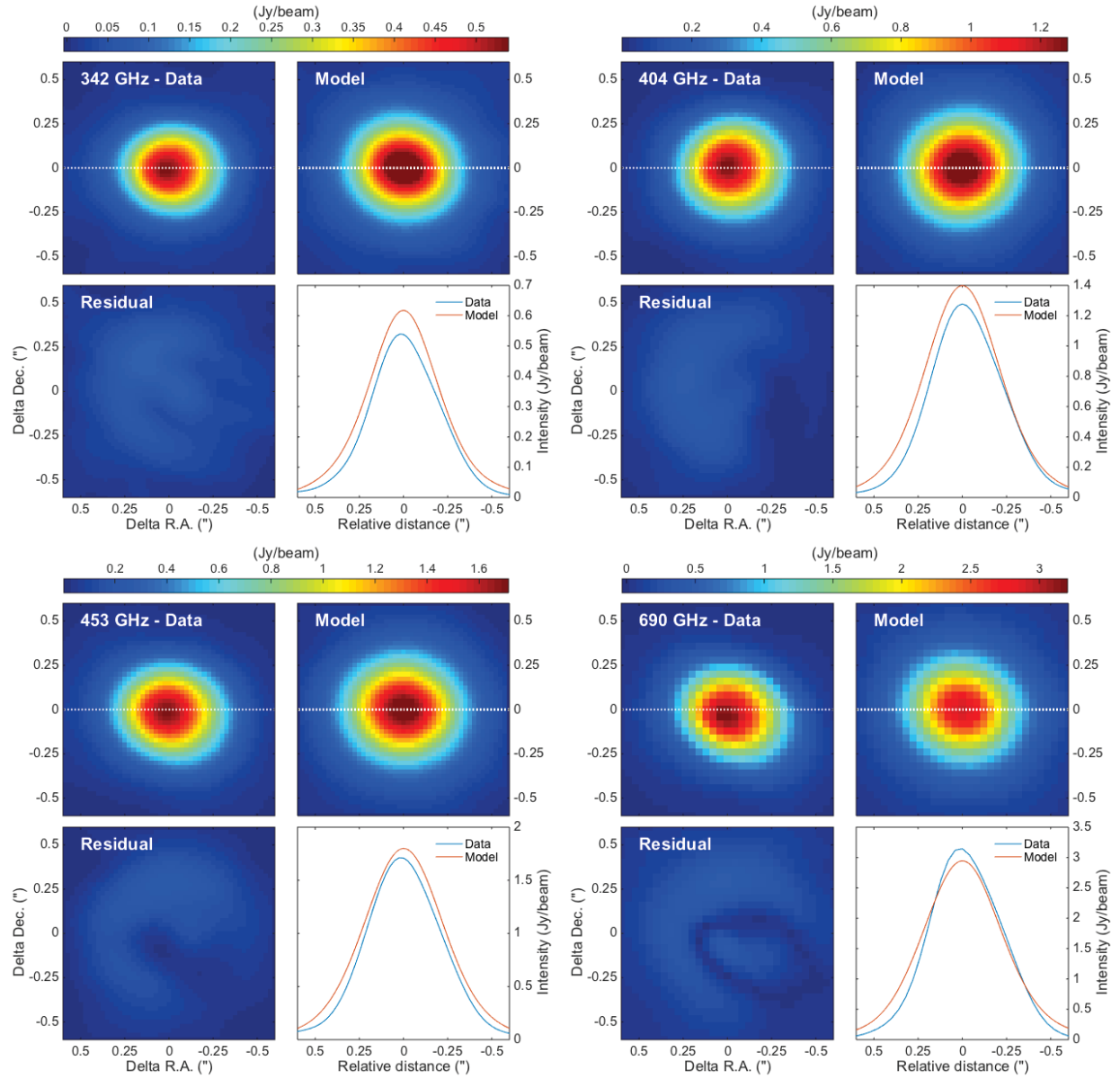
Figure 6. Observed and modelled ALMA continuum images at 342, 404, 453 and 690 GHz.

Chapter 5

Modelando la estructura de abundancia del HNCO hacia IRAS 16293-2422

La segunda parte de esta Tesis está enfocada en el análisis de la química en IRAS 16293-2422 a partir de observaciones de un solo plato desde longitudes de onda milimétricas hasta el lejano infrarrojo.

La protoestrella IRAS 16293-2422 es la fuente prototípica para estudios astroquímicos debido a su riqueza de emisión molecular y ha sido objeto de muchos estudios espectroscópicos. En particular, una gran cantidad de moléculas nitrogenadas han sido detectadas en la envolvente de esta fuente. Entre ellas, el ácido isocianuro (HNCO), una de las moléculas nitrogenadas más simples que contienen los cuatro elementos esenciales para la vida como la conocemos, ha sido detectada en IRAS 16293-2422. Tenemos en manos los estudios espectrales más amplios hechos hacia esta fuente con instrumentos de un solo plato: el estudio TIMASSS (hecho con IRAM, JCMT y APEX en un rango de frecuencias entre $80 - 500$ GHz), y el estudio CHESS (hecho con el intrumento HIFI en un rango de frecuencias entre $0.5 - 1$ THz). Dado que en regiones de formación estelar la emisión de HNCO no se encuentra siempre en Equilibrio Termodinámico Local (ETL), los coeficientes colisionales son necesarios para predecir la emisión de líneas usando códigos de transferencia radiativa fuera de ETL como RADEX. Para modelar las líneas de HNCO observadas en esta fuente, usamos un nuevo conjunto de coeficientes colisionales para HNCO con orto-H_2 y para-H_2, calculados a partir de un conjunto de tasas de excitación rotacional entre HNCO y H_2 basados en una nueva superficie de energía potencial para las interacciones entre moléculas rígidas. Hemos encontrado que la mayoría de los perfiles de línea de HNCO son reproducidos satisfactoriamente si consideramos que el HNCO proviene de una fuente compacta, densa y caliente asociada con el núcleo caliente, una componente tibia asociada con la parte interna de la envolvente protoestelar, y una componente fría más extendida asociada con la parte externa de la envolvente. Hemos calculado la abundancia en cada una de estas componentes físicas y la comparamos con el perfil de abundancia radial obtenido con el código químico Nautilus, encontrando un buen acuerdo. El código de transferencia radiativa que usamos trata las diferentes capas de una manera auto-consistente, lo cual nos permite establecer su secuencia en el espacio, y examinar la estructura de la envolvente a lo largo de la línea de visión.

Chapter 5

Modélisation de la structure d'abondance de HNCO dans IRAS 16293–2422

La deuxième partie de la thèse est consacrée à l'analyse de la chimie dans IRAS 16293-2422 à partir d'observations dans les domaines millimétriques à infrarouge lointain.

La proto-étoile IRAS 16293-2422 est un modèle pour les études astrochimiques en raison de sa richesse en émission de raies moléculaire, elle a donc fait l'objet de nombreuses études spectroscopiques. En particulier, un certain nombre de molécules azotées ont été détectées dans l'enveloppe de cette source. Parmi celles-ci, l'acide isocyanique (HNCO), l'une des molécules simples contenant de l'azote et contenant les quatre éléments essentiels à la vie tels que nous la connaissons, a été détecté dans IRAS 16293–2422. Nous avons entre les mains les relevés spectraux les plus complets obtenus sur cette source avec des instruments à antenne unique, les relevés TIMASSS (avec IRAM, JCMT et APEX dans la gamme des 80 – 500 GHz) et CHESS (dans la gamme 0.5 – 1 THz avec l'instrument HIFI à bord de l'Observatoire Spatial Herschel). Dans les environnements d'étoiles en formation, l'émission de HNCO n'est pas toujours à l'équilibre thermodynamique (ETL). Pour prédire l'émission des raies, la connaissance des coefficients de collision est nécessaire pour utiliser des codes de transfert hors équilibre thermodynamique comme RADEX. Pour modéliser les raies de HNCO observées dans cette source, nous avons utilisé ici les nouveaux coefficients de collision de HNCO avec ortho-H_2 et para-H_2, calculés à partir d'un ensemble de taux d'excitation rotationnelle entre HNCO et H_2 et basés sur une nouvelle surface d'énergie potentielle pour les molécules rigides en interactions. Nous avons constaté que la plupart des raies de HNCO sont très bien reproduites si nous supposons qu'elles proviennent d'une source chaude, dense et compacte associée au "hot corino", d'un composant chaud associé à la partie interne de l'enveloppe protostellaire et d'un composant plus étendu et plus froid associé à l'enveloppe externe. Nous avons calculé l'abondance de HNCO pour chacun des composants physiques obtenus et l'avons comparé aux résultats du calcul d'un profil d'abondance radiale calculé à l'aide du code chimique Nautilus, et avons trouvé un bon accord. Il est important de souligner que le code de transfert radiatif que nous utilisons traite les différentes couches de manière cohérente. En conséquence, cela permet d'utiliser sa séquence dans l'espace et d'examiner la structure de l'enveloppe le long de la ligne de visée.

Chapter 5

Modelling the HNCO abundance structure towards IRAS 16293-2422

The second part of the thesis is devoted to the analysis of the chemistry in IRAS 16293–2422 based on single-dish millimeter to far infrared observations.

The protostar IRAS 16293-2422 is the prototypical source for astrochemical studies due to its wealth of molecular emission and it has been the subject of many spectroscopic studies. In particular, a number of nitrogen-bearing molecules have been detected in the envelope of this source. Among them, isocyanic acid (HNCO), one of the simplest nitrogen-bearing molecules containing all four essential elements for life as we know it, has been detected towards IRAS 16293–2422. We have in hands the broadest spectral surveys conducted towards this source with single-dish instruments: the TIMASSS survey (with IRAM, JCMT and APEX in the 80 – 500 GHz range), and the CHESS survey (in the 0.5 – 1 THz range with the HIFI instrument). Because, in star-forming environments the HNCO emission is not always at the Local Thermal Equilibrium (LTE), the knowledge of collisional coefficients is needed to predict the line emission using non-LTE transfer codes such as RADEX. To model the HNCO lines observed in this source, we used here a new set of HNCO collisional coefficients with ortho-H_2 and para-H_2, computed from a set of rotational excitation quenching rates between HNCO and H_2 based on a novel potential energy surface for the rigid molecules interactions. We have found that most of the HNCO lines profiles are very well reproduced if we assume that HNCO arises from a warm, dense and compact source associated with the hot corino, a warm component associated with the internal part of the protostellar envelope, and a cold and more extended component associated with the outer envelope. We have computed the abundance on each of these physical components and compared it with a radial abundance profile derived with the chemical code Nautilus, and found a good agreement. It is important to emphasize that the radiative transfer code that we used treats the different layers in a self-consistent fashion, enabling us to establish their sequence in space, and to examine the structure of the envelope along the line of sight.

Modelling the abundance structure of isocyanic acid (HNCO) towards the low-mass solar type protostar IRAS 16293–2422

Antonio Hernández-Gómez [iD],[1,2]★ Emna Sahnoun [iD],[3,4] Emmanuel Caux [iD],[2]
Laurent Wiesenfeld [iD],[4,5] Laurent Loinard [iD],[1,6] Sandrine Bottinelli [iD],[2]
Kamel Hammami [iD][3] and Karl M. Menten [iD][7]

[1]*Instituto de Radioastronomía y Astrofísica, Universidad Nacional Autónoma de México, Morelia 58089, Mexico*
[2]*IRAP, Université de Toulouse, CNRS, UPS, CNES, Toulouse, France*
[3]*Laboratory of Atomic Molecular Spectroscopy and Applications, Department of Physics, Faculty of Science, University Tunis El Manar, Campus Universities, 1060 Tunis, Tunisia*
[4]*IPAG, Université Grenoble Alpes, CNRS, F-38000 Grenoble, France*
[5]*Laboratoire Aimé-Cotton, Université Paris-Saclay, CNRS, Orsay, France*
[6]*Instituto de Astronomía, Universidad Nacional Autónoma de México, Apartado Postal 70-264, CdMx C.P. 04510, Mexico*
[7]*Max-Planck-Institut für Radioastronomie, Auf dem Hügel 69, D-53121 Bonn, Germany*

ABSTRACT

Isocyanic acid (HNCO), the most stable of the simplest molecules containing the four main elements essential for organic chemistry, has been observed in several astrophysical environments such as molecular clouds, star-forming regions, external galaxies, and comets. In this work, we model HNCO spectral line profiles towards the low-mass solar type protostar IRAS 16293−2422 observed with the ALMA interferometer, the IRAM, JCMT, and APEX single-dish radio telescopes, and the HIFI instrument on board the Herschel Space Observatory. In star-forming environments, the HNCO emission is not always in Local Thermodynamical Equilibrium (LTE). A non-LTE radiative transfer approach is necessary to properly interpret the line profiles, and accurate collisional rate coefficients are needed. Here, we used the RADEX package with a completely new set of collisional quenching rates between HNCO and both ortho-H_2 and para-H_2 obtained from quantum chemical calculations yielding a novel potential energy surface in the rigid rotor approximation. We find that the lines profiles towards IRAS 16293−2422 are very well reproduced if we assume that the HNCO emission arises from a compact, dense, and hot physical component associated with the hot corino, a warm component associated with the internal part of the protostellar envelope, and a cold and more extended component associated with the outer envelope. The derived HNCO abundances from our model agree well with those computed with the NAUTILUS chemical code.

Key words: astrochemistry – ISM: molecules – stars: individual (IRAS 16293–2422).

1 INTRODUCTION

Isocyanic acid (HNCO) is the most stable of the simplest molecules containing all four atoms essential for life as we know it.[1] In consequence, understanding the formation and evolution of this molecule in star-forming environments might prove relevant to organic chemistry in space. Interstellar HNCO was first reported by Snyder & Buhl (1972) towards the molecular cloud complex Sgr B2, where its emission was found to be abundant and spatially extended. Further studies confirmed the high abundance of HNCO with respect to H_2

towards molecular clouds in the direction of the Galactic centre (e.g. Turner 1991; Martín et al. 2008), and revealed its presence in various other environments such as hot molecular cores (e.g. Blake et al. 1987; van Dishoeck et al. 1995; MacDonald et al. 1996; Helmich & van Dishoeck 1997; Bisschop et al. 2008), molecular outflows (e.g. Rodríguez-Fernández et al. 2010), external galaxies (e.g. Meier & Turner 2005; Martín et al. 2006; Martín, Martín-Pintado & Mauersberger 2009), and comets (e.g. Lis et al. 1997; Crovisier 1998; Biver et al. 2006).

HNCO was proposed to be a tracer of dense gas since it has been observed in high-density regions (e.g. Jackson, Armstrong & Barrett 1984), as well as a tracer of shocks since its abundance appears to be enhanced towards shocked gas regions (e.g. Rodríguez-Fernández et al. 2010). Much effort has been devoted to understanding the chemistry of HNCO in a variety of astrophysi-

★ E-mail: a.hernandez@irya.unam.mx
[1]Cyanic acid (HOCN), fulminic acid (HCNO), and isofulminic acid (HONC), are all less stable.

cal environments (e.g. Marcelino et al. 2009, 2010; Quan et al. 2010), but it is not yet fully constrained. In an early study, Iglesias (1977) proposed that the formation pathway of HNCO in Sgr B2 could occur in the gas phase through the chemical ion–neutral reactions

$$NCO^+ + H_2 \rightarrow HNCO^+ + H, \tag{1}$$

$$HNCO^+ + H_2 \rightarrow HNCOH^+ + H, \tag{2}$$

$$HNCOH^+ + e^- \rightarrow HNCO + H. \tag{3}$$
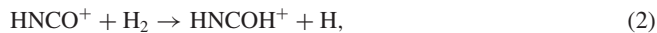
Turner (2000) also suggested some neutral–neutral reactions to form HNCO

$$CN + O_2 \rightarrow NCO + O, \tag{4}$$

$$NCO + H_2 \rightarrow HNCO + H, \tag{5}$$

where reaction (5) has an activation barrier. More recently, Marcelino et al. (2009, 2010) proposed a more complete gas phase model to explain the abundance of HNCO and its isomers in cold dense cores.

Other studies (e.g. Garrod, Widicus Weaver & Herbst 2008; Tideswell et al. 2010) have shown that HNCO could also be formed on dust grain surfaces through the thermal reaction

$$NH + CO \rightarrow HNCO, \tag{6}$$

(which has no activation barrier according to Garrod et al. 2008) and then be released into the gas phase through desorption. For sometime, it was believed that HNCO was directly related with the formation of NH_2CHO (formamide, a molecule important in prebiotic chemistry) via hydrogenation on grain surfaces. Recent laboratory experiments, however, have shown that this process is in fact inefficient (e.g. Fedoseev et al. 2015; Noble et al. 2015). Regardless, both gas phase and grain surface chemistry need to be taken into account to correctly model the observed abundances in astrophysical sources of HNCO and other related molecules of potential exobiological interest.

IRAS 16293–2422 (I16293 hereafter), a Class 0 protostar located at 141^{+30}_{-21} pc (Dzib et al. 2018) in the Ophiuchus star-forming region, is particularly interesting in this context. This protostar is often considered a template source for astrochemistry since it has the richest molecular line spectrum known for low-mass protostars, spanning over a wide range of frequencies (e.g. Caux et al. 2011; Jørgensen et al. 2016). In interferometric observations, I16293 is found to be composed of two dense condensations, called A and B, separated by ∼705 au (at a distance of 141 pc), presumably tracing a newborn binary system (Wootten 1989; Mundy et al. 1992). HNCO has been detected towards the compact sources A and B (e.g. Bisschop et al. 2008) as well as in the surrounding large-scale envelope (e.g. van Dishoeck et al. 1995). This makes I16293 an ideal target to study the chemistry of HNCO at multiple scales in a low-mass star-forming environment (e.g. Bisschop et al. 2008; Marcelino et al. 2010). Recently, López-Sepulcre et al. (2015) modelled the emission of HNCO in I16293 with a radiative transfer code, using the collisional rate coefficients computed by Green (1986) for the HNCO–He system. They obtained abundances with respect to H_2 of $(5 \pm 4) \times 10^{-12}$ and $(6 \pm 3) \times 10^{-9}$ for the regions where the temperature is, respectively, smaller and higher than 90 K. According to their model, this temperature corresponds to the threshold for

thermal desorption of some species from icy dust mantles. Once in the gas phase, HNCO will be subject to collisions with other species. Since H_2 is, by far, the most abundant collider in dense astrophysical environments, it would be desirable to use coefficients for the HNCO–H_2 system – rather than HNCO–He. Such coefficients recently became available (Sahnoun et al. 2018) for both forms of H_2 (ortho and para) as a result of new quantum chemical calculations (see Section 3.1).

In this work, we make use this new set of collision coefficients to model the HNCO lines profiles observed at different spatial scales with the Atacama Large Millimeter/submillimeter Array (ALMA) and the single-dish telescopes IRAM, the Atacama Pathfinder Experiment (APEX), the James Clerk Maxwell Telescope (JCMT), and Herschel Heterodyne Instrument for the Far-Infrared (HIFI; de Graauw et al. 2010), over a wide range of frequencies. In Section 2, we describe the observations in detail, while in Section 3, we describe the new HNCO–H_2 collisional coefficients and the adopted physical model. In Section 4, we discuss our findings and compare them with a chemical model and previously published results. Section 5 summarizes our results.

2 OBSERVATIONS

To study the extended HNCO emission from I16293, we analysed a set of data obtained with the IRAM-30m, JCMT-15m, and APEX-12m, ground based single-dish (sub)millimeter wavelength telescopes, as well as from the HIFI instrument on board the Herschel Space Observatory covering a frequency range from 80 GHz to 1 THz. The compact emission from the hot corino was studied with interferometric ALMA observations between 329 and 363 GHz. All the observations are described in this section.

2.1 IRAM-30m and JCMT-15m observations

First, we use observations that were part of TIMASSS (The IRAS16293-2422 Millimeter And Submillimeter Spectral Survey; Caux et al. 2011) conducted with the IRAM-30m telescope (Granada, Spain) between 80 and 280 GHz and the JCMT-15m telescope (Mauna Kea, Hawaii) between 328 and 366 GHz with a spectral resolution ranging from 0.51 to 2.25 km s^{-1}. These observations were carried out between 2004 January and 2006 August. For more details on these observations, see Caux et al. (2011).

In addition, higher spectral resolution observations (100 kHz, 0.13 km s^{-1}) of the HNCO (5_{05}–4_{04}) transition were carried out with the IRAM-30m telescope between 2017 November 1st and 6th using the broad-band Eight Mixer Receiver (EMIR) receivers connected to a Fast Fourier Transform spectrometer (FFTS). The sky emission was cancelled using the wobbler switching observing mode and a throw of 150 arcsec. The total observing time for this run was about 5.6 h and the observed coordinates were $\alpha_{2000} = 16^h 32^m 22^s.64$, $\delta_{2000} = -24° 28' 33''.6$.

2.2 APEX observations

The observations of I16293 in the frequency range 265–323.5 GHz were performed with the APEX telescope on the Chajnantor plateau (Chile) during several runs in 2011 and 2012. The observations were carried out using the APEX-1 and APEX-2 receivers in the wobbler switching observing mode, with a throw of 150 arcsec. A FFTS was connected to the APEX receivers, providing a spectral resolution of 60 kHz and a total bandwidth of about 1.5 GHz per tuning. The

on-source integration time was 30–60 min per setting, depending on the frequency, to reach a similar rms noise level over the complete frequency range observed. The observed coordinates were $\alpha_{2000} = 16^h\ 32^m\ 22\overset{s}{.}87$, $\delta_{2000} = -24°\ 28'\ 36\overset{''}{.}6$.

The transitions between 372 and 462 GHz were observed during 2013 August under very good weather conditions using a modified version of the First Light Apex Submillimeter Heterodyne receiver (FLASH; Heyminck et al. 2006). The spectral resolution delivered by the backends was 38.15 kHz corresponding to a velocity resolution of 0.03 (372 GHz), 0.027 (418 GHz), and 0.025 km s^{-1} (462 GHz). Since I16293 is a very bright sub-millimeter source, the pointing of the telescope was checked regularly using I16293 itself. Thus, the observed position corresponds to the peak of the sub-millimeter emission at $\alpha_{2000} = 16^h\ 32^m\ 22\overset{s}{.}9$, $\delta_{2000} = -24°\ 28'\ 35\overset{''}{.}6$.

The final velocity resolution of all APEX observations was degraded to ∼ 0.6 km s^{-1} to increase the signal-to-noise ratio without losing much information on the line profile.

For both the IRAM 2017 November and the APEX observations, the data reduction was performed using the GILDAS/CLASS90[2] package. The telescopes and receivers parameters (main-beam efficiency B$_{eff}$, forward efficiency F$_{eff}$, half power beam width HPBW) were taken from the IRAM and the APEX webpages. The rms noise achieved is typically 10 mK (T_{mb}) per 0.6 km s^{-1} velocity channel for the APEX data, and 3 mK (T_{mb}) per 0.6 km s^{-1} velocity channel for IRAM data.

2.3 Herschel–HIFI observations

Observations with the HIFI instrument onboard the Herschel Space Observatory were conducted as part of the guaranteed-time key program CHESS (Chemical Herschel Surveys of Star-forming regions; Ceccarelli 2010), whose goal was to perform spectral surveys in the frequency range 480−1790 GHz with a high spectral resolution (∼1.1 MHz). The data used in this article are part of a full spectral coverage of bands 3b (860–960 GHz; Obs. Id 1342192330) and 4a (950–1060 GHz; Obs. Id 1342191619), which were obtained on March 19, and 2010 March 3, respectively. The Spectral Scan Double Beam Switch (DBS) with optimization of the continuum observing mode was used. A spectral resolution of 1.1 MHz (∼0.3 km s^{-1} at 1 THz) was provided by the HIFI acousto-optic Wide Band Spectrometer (WBS) with an instantaneous bandwidth of 4 × 1 GHz (Roelfsema et al. 2012). The observed coordinates were $\alpha_{2000} = 16^h\ 32^m\ 22\overset{s}{.}64$, $\delta_{2000} = -24°\ 28'\ 33\overset{''}{.}6$. The DBS reference positions were situated approximately 3 arcmin east and west of the source.

To carry out a spectral survey, multiple local oscillator tunings are used, in order to cover the required frequency bands. A single local oscillator tuning spectrum consists of eight separate spectra: four per polarization (horizontal and vertical) in four sub-bands of ∼1 GHz each. Using the HIPE (Ott 2010) 'flagTool' task, we removed the spurs not automatically eliminated by the pipeline. Standing waves and baselines removal on each sub-band were performed with the HIPE tasks 'fitHifiFringe' and 'fitBaseline'. The sideband deconvolution was performed using the HIPE task 'doDeconvolution', and the resulting deconvolved spectra observed in both polarizations were averaged to improve the noise in the final spectra, given that they had similar quality. The task 'fitBaseline' was then ran to obtain the continuum values which are well fitted
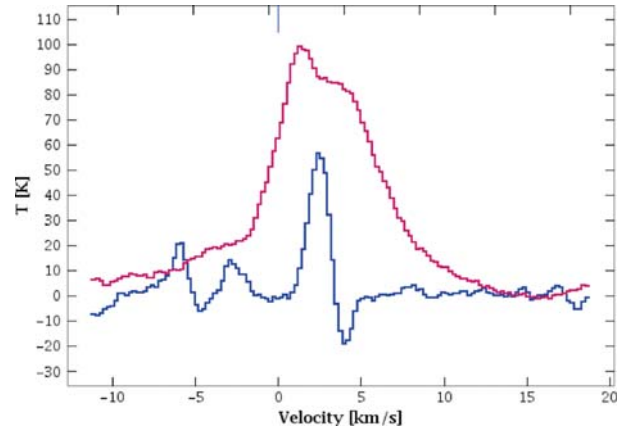

Figure 1. HNCO $15_{0,15}-14_{0,14}$ line emission as observed towards IRAS16293 in the PILS survey towards source A (red line) and source B (blue line).

by order 3 polynomials over the frequency range of the whole sub-bands. These single side band continuum values were then added to the spectra at the considered frequencies. Finally, we used the forward efficiency of 0.96 and the (frequency-dependent) beam-efficiency given in table 1 of Roelfsema et al. (2012) to convert the intensities from antenna to main-beam temperature scale.

2.4 ALMA observations

PILS, the ALMA Protostellar Interferometric Line Survey (Jørgensen et al. 2016), reported ALMA observations in the frequency range [329.15, 362.90] GHz with an ∼0.2 km s^{-1} channel spacing and an ∼0.5 arcsec spatial resolution. Five HNCO lines used in this work were observed in this survey, HNCO $(15_{0\,15}-14_{0\,14})$, $(15_{1\,14}-14_{1\,13})$, $(16_{0\,16}-15_{0\,15})$, $(16_{1\,16}-15_{1\,14})$, and $(16_{1\,16}-15_{1\,15})$. These interferometric observations, not sensible to the extended emission, were only used to determine some physical parameters of the hot corino component. As can be seen in Fig. 1, the HNCO $(15_{0\,15}-14_{0\,14})$ line integrated intensity is nine times larger for A than for B, allowing us to assume in this work that source A is solely responsible of the hot corino emission.

Table A1 summarizes the observation parameters as well as spectroscopic information for the observed lines from the Cologne Data base for Molecular Spectroscopy[3] (CDMS; Müller et al. 2001, 2005). This data base makes use of spectroscopic data from Kukolich (1971), Hocking (1975), Niedenhoff et al. (1995), and Lapinov et al. (2007). All line intensities are expressed in main-beam brightness temperature units (T_{mb}), after correction of rearward losses and main-beam efficiency and for the atmospheric attenuation for IRAM, APEX, and JCMT observations.

3 RESULTS

To identify and model the relevant HNCO spectral lines, we used CASSIS[4] (Caux et al. 2011), a software developed at IRAP-UPS/CNRS which makes use of the CDMS data base (Müller et al. 2001, 2005). 35 transitions are present in the IRAM observations, 16 in the APEX ones, and 6 in the JCMT ones. We also found 47 transitions falling within the HIFI observations range. Most of these
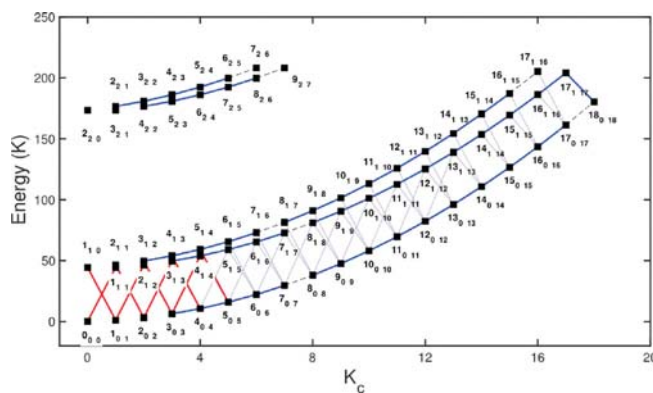
---

[2]http://www.iram.fr/IRAMFR/GILDAS/

[3]https://www.astro.uni-koeln.de/cdms
[4]http://cassis.irap.omp.eu

Figure 2. Sketch of the rotational levels of HNCO, labelled by $J_{K_a K_c}$, and energy in Kelvin. Lines connect observable transitions, at frequencies $80 < \nu < 1200$ GHz. Blue lines indicate transitions detected in emission and red lines indicate transitions detected in absorption. Light grey lines indicate transitions that were looked for but not detected, while dashed lines indicate transitions that were not observed.

latter lines were not detected (see Appendix), but the corresponding upper limits were used as constraints in the modelling. The details for all the transitions used are given in Table A1. We illustrate in Fig. 2 the transitions observed and their corresponding levels as a function of the quantum number K_c and the energy above the ground state.

To model the line profiles we used the statistical equilibrium non-LTE radiative transfer code RADEX (van der Tak et al. 2007) that uses the escape probability formalism. The HNCO collisional coefficients are taken from Sahnoun et al. (2018) and were obtained as we now describe.

3.1 HNCO collisional coefficients

The main aspects of the collisional coefficients computation are summarized in this section. The full description can be found in Sahnoun et al. (2018).

3.1.1 Potential energy surface

The potential energy surface (PES) for the HNCO–H$_2$ van der Waals system was recently computed by Sahnoun et al. (2018). This five-dimensional PES was computed in the rigid-rotor approximation. The HNCO and H$_2$ internuclear distances are frozen at the experimental average value for the vibrational ground state (distances in bohr, angles in degrees). For H$_2$, we set $r_{HH} = 1.4011$. The planar HNCO parameters are set to $r_{HN} = 1.9137$, $r_{NC} = 2.3007$, $r_{CO} = 2.2028$, $\alpha(HNC) = 124.0$, $\alpha(NCO) = 172.1$ (Fusina & Mills 1981). We computed the PES for distances R between centre of masses from 4.5 to 50 bohr. About 430 000 ab initio points were computed in the C1 symmetry group with the CCSD(T)-F12a method using for atomic bases the standard aug-cc-pVDZ basis set as implemented in the MOLPRO2011 package (Werner et al. 2012). The basis set superposition error has been corrected at all geometries with the counterpoise procedure (Nizam et al. 1988). The PES has a global minimum of $V = -235.26$ cm^{-1} located at $R = 7.9$ bohr and angles such that the H$_2$ molecule is perpendicular to the HNCO plane, and its centre is collinear with the NH bond. This PES presents a very large anisotropy because of the rod-like geometry of the HNCO molecule, with the H atom protruding out of the nearly linear NCO arrangement.

3.1.2 Rotational quenching cross-sections and rates

The PES ab initio points were fit in terms of polyspherical harmonic functions in order to be introduced in the MOLSCAT dynamical code.[5] Computation of the rotational quenching cross-sections was done within the coupled-states quantum time-independent formalism for collision energies up to 500 cm^{-1} (719 K), for both ortho-H$_2$, $J_{H_2} = 1$ and para-H$_2$, $J_{H_2} = 0, 2$. The cross-sections were averaged using the Maxwell–Boltzmann distribution to calculate the rate coefficients as a function of the kinetic temperature.

All details about the collisional coefficients computation may be found in a preceding paper (Sahnoun et al. 2018). It was shown that the quenching rates with ortho-H$_2$ are larger than the corresponding ones with para-H$_2$. Also, the rates connecting the $K_a = 0$ levels are somewhat larger than those corresponding to the $K_a = 1$ levels. Hence, quenching redistributes the level populations in a manner far from the black-body distribution.

3.2 The physical model

Several previous studies have shown that I16293 has a hot corino revealed by the emission of numerous complex molecules in both the A and B sources. In addition, a common, extended infalling envelope surrounding the binary system has also been observed by single-dish telescopes (e.g. Caux et al. 2011). Crimier et al. (2010) determined the physical structure of I16293 from single-dish and interferometric continuum observations, assuming a spherical source, and provided temperature and density profiles up to $R \sim 6000$ au. More recently, Jacobsen et al. (2018) studied the inner envelope of I16293 up to $R \sim 8000$ au ($\sim$113 arcsec size) with a three-dimensional dust and gas model based on ALMA observations. By comparing those studies, we noted that the model of the envelope in Jacobsen et al. (2018) is fully compatible with Crimier et al. (2010) in the same radius range. Last, OTF observations of CS (Menten et al. 1987), and CN (Hernández-Gómez et al. 2018), have shown the presence of an extended cold envelope component (size larger than 100 arcsec).

We therefore modelled the HNCO lines assuming I16293 can be represented by three physical components: a single hot corino of size 0.5 arcmin (see Section 2.4), a warm envelope ($R \leq 1000$ au), and a cold, extended envelope ($R \geq 1000$ au), see Fig. 3. In order to constrain the parameters of each of the three physical components, we have used the one-dimensional physical structure derived by Crimier et al. (2010), fixing thereby the main H$_2$ density for all components from their derived density profile.

A fundamental ingredient for the modelling is the continuum level in the spectra. However, because of the observing mode at IRAM and JCMT, no continuum was recovered during those observations. This is not the case for APEX and HIFI observations. To have a consistent model taking into account the continuum level for all lines, we have computed the spectral energy distribution (SED) for the envelope of I16293 with several instruments (such as PACS, SPIRE, MIPS, MAMBO2, LABOCA, IRS, SCUBA2, NIKA2, and HIFI) and derived the expected continuum from $\sim$1 mm to $\sim$70 μm ($\sim$150 GHz to $\sim$5 THz) (Bottinelli et al., in preparation). We have checked that the predicted continuum level is consistent with the observations within an error of about 15 per cent. We subtracted the
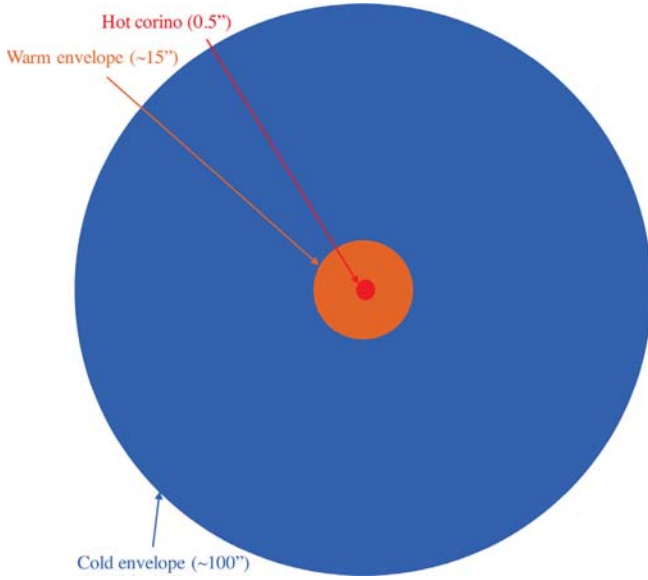
---

[5]http://ipag.osug.fr/~afaure/molscat/index.html

Hot corino (0.5")
Warm envelope (~15")
Cold envelope (~100")

Figure 3. Adopted three components physical structure to model the HNCO emission in I16293.

continuum for spectra that show continuum and added the predicted continuum for all lines.

3.3 Model fitting

In CASSIS, it is possible to model with RADEX (van der Tak et al. 2007) an observed spectrum with a set of physical components, each of them defined with six physical parameters that will serve as input for RADEX: the size of the component, its density $n(H_2)$, its kinetic temperature T_{kin}, the Full Width at Half Maximum (FWHM) and the velocity relative to the Local Standard of Rest V_{LSR} of the lines, and the column density N of the studied species. Since our observations have sufficient spectral resolution, we fixed V_{LSR} of the lines for the warm and cold envelopes to 4.1 km s^{-1}. Given that the component associated with the cold envelope has a narrow line width, we have fixed its FWHM to 0.4 km s^{-1}. The parameters left to vary during the optimization are therefore the column density and kinetic temperature for all components, FWHM and V_{LSR} for the hot corino, and FWHM and size for the warm envelope. For the hot corino, we adopted an ortho-to-para H_2 ratio of 3 but we checked that varying this value did not influence the final results. For both envelope layers, we assumed that para-H_2 is the dominant form since para-H_2 is more stable at lower temperatures. We have therefore modelled I16293 in terms of the superposition of three physical components represented on Fig. 3, with a total of 10 free parameters out of 18 possible.

We used the Monte Carlo Markov Chain (MCMC) method inside CASSIS (Hastings 1970; Guan et al. 2006) which explores the space of parameters to find the best solution by means of χ^2 mini-

mization, running 1000 models with these 10 free parameters randomly chosen. Table 1 shows the best values obtained from the χ^2 minimization, and Fig. 4 shows observed and simulated spectra of some of the HNCO transitions, while all spectra are shown in appendix B. In all cases, the predicted emission has been diluted with the appropriate telescope beam, considering the frequency of the transitions and the assumed size of the given physical component.

It should be noted that the observations used in this study cannot constrain the size of the hot corino, or that of the extended envelope, the single-dish beams being either too big or too small to provide useful information. The given column-densities and abundances are therefore those corresponding to the adopted sizes of these components (0.5 and 100 arcsec, respectively), and should be scaled if other sizes are used. Only the size of the HNCO emission in the warm envelope can be correctly constrained with the observations we have in hands.

4 DISCUSSION

4.1 HNCO physical parameters

The best results from our model give a temperature for the HNCO-bearing gas associated with the hot corino of about 200 K and a column density of $(1.9 \pm 0.4) \times 10^{16}$ cm^{-2}, which corresponds to an abundance relative to H_2 of $(7.1 \pm 0.6) \times 10^{-8}$ for a fixed size of 0.5 arcsec. This abundance is in agreement with typical values measured for other hot cores (e.g. Bisschop et al. 2007). Martín-Doménech et al. (2017) derived the column density of HNCO towards the hot corino associated with source B in I16293 measuring the HNC^{18}O column density and adopting an isotopic ratio of ^{16}O/^{18}O = 500. They obtained N(HNCO)=$(4.9 \pm 1.9) \times 10^{16}$ cm^{-2} and an abundance of $(1.8 \pm 0.7) \times 10^{-9}$. Although the column density for source A computed with our model is similar to the column density derived by Martín-Doménech et al. (2017) for source B, we predict a higher abundance for source A. For the warm envelope, we found a column density of $(2.5 \pm 0.5) \times 10^{13}$ cm^{-2}, a temperature of (31 ± 5) K, a size of (15.6 ± 2.4) arcsec and an abundance of $(1.8 \pm 0.4) \times 10^{-11}$. The line widths are smaller (4.9 km s^{-1}) than those found for the hot corino (6.2 km s^{-1}). This behaviour is expected if we consider that the infall and rotation speeds are larger towards the centre of the envelope. For the cold outer layer of the envelope, we derive a temperature of about 9 K and a column density of $(5.3 \pm 0.6) \times 10^{12}$ cm^{-2}. The resulting abundance is $(9.8 \pm 0.3) \times 10^{-12}$, which is very similar to that of the warm envelope.

In a previous study, van Dishoeck et al. (1995) derived a value for the HNCO column density in the envelope of I16293 based on data obtained with the JCMT and the CSO (Caltech Submillimeter Observatory located on Mauna Kea, Hawaii) of $(3.4 \pm 1.5) \times 10^{13}$ cm^{-2} and an abundance with respect to H_2 of 1.7×10^{-10} by using the rotational diagram technique, which assumes LTE conditions (although no source size for the envelope was derived from their

Table 1. Best physical parameters (those with * being fixed) obtained with the χ^2 minimization. The abundance was computed with respect to H_2.

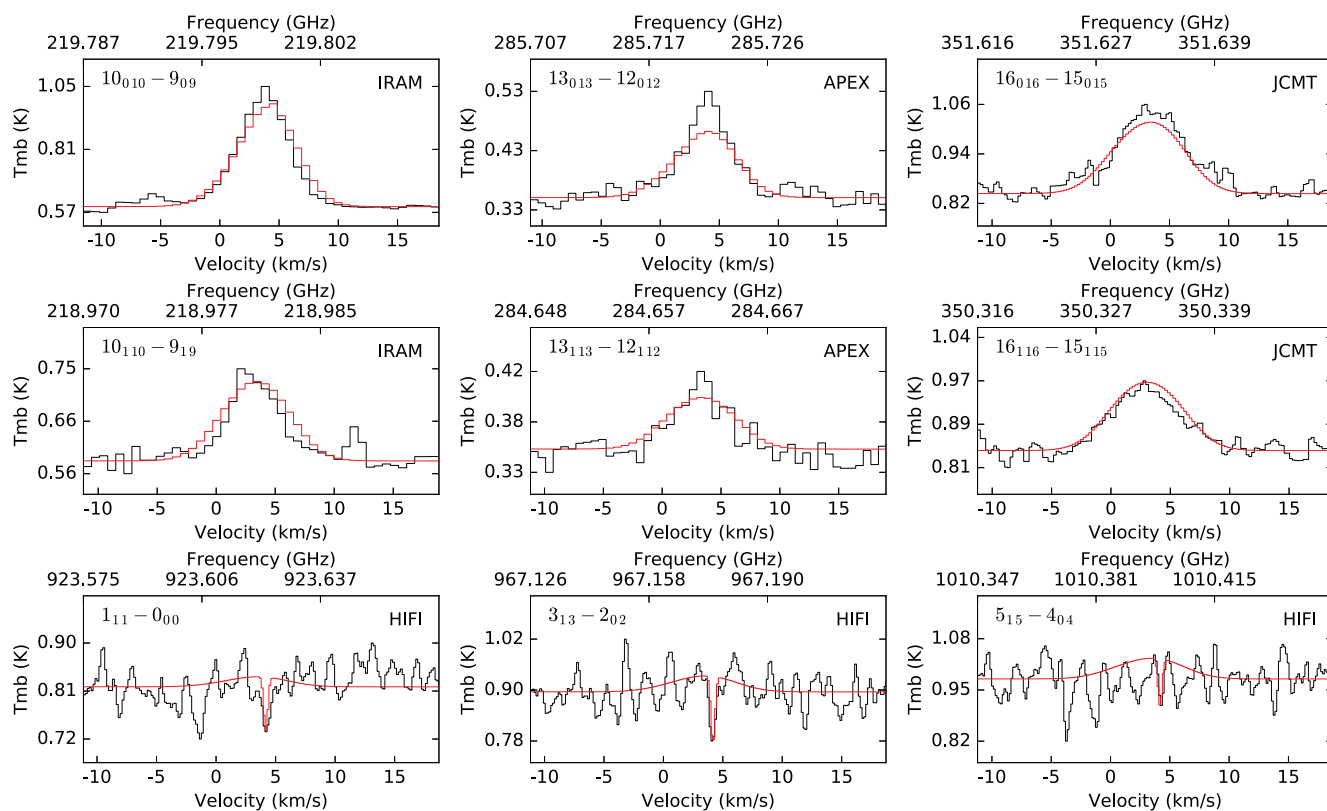| Component	N (cm^{-2})	T_{kin} (K)	FWHM (km s^{-1})	V_{LSR} (km s^{-1})	Size (arcsec)	$n(H_2)$ (cm^{-3})	$X(n_{HNCO}/n_{H_2})$
Hot corino	$(1.9 \pm 0.4) \times 10^{16}$	190 ± 50	6.2 ± 0.7	2.9 ± 0.1	0.5*	3×10^8	$(7.1 \pm 0.6) \times 10^{-8}$
Warm envelope	$(2.5 \pm 0.5) \times 10^{13}$	31 ± 5	4.9 ± 0.8	4.1*	15.6 ± 2.4	5×10^7	$(1.8 \pm 0.4) \times 10^{-11}$
Cold envelope	$(5.3 \pm 0.6) \times 10^{12}$	8.7 ± 0.8	0.4*	4.1*	100.0*	3×10^6	$(9.8 \pm 0.3) \times 10^{-12}$

Figure 4. In black, we show some of the observed HNCO line profiles as seen by different telescopes, while in red we show the predicted profiles from our model with the parameters reported in Table 1.

observed HNCO transitions). The column density derived by us is consistent with that reported by van Dishoeck et al. (1995) but our abundance is lower by a factor of 10. This difference could be related with the different assumed H_2 column densities. Moreover, assuming LTE conditions might not be appropriate for the envelope of I16293. Indeed, López-Sepulcre et al. (2015) already pointed out this problem. These latter authors computed the abundances for HNCO using a non-LTE radiative transfer model together with collision coefficients from Green (1986) and found abundances between $(6 \pm 3) \times 10^{-9}$ for $T > 90$ K in the warm envelope and $(5 \pm 4) \times 10^{-12}$ for $T < 90$ K corresponding to the cold envelope. We argue that the differences between our abundances and those of López-Sepulcre et al. (2015) reflect, in part, the different number of components considered in the different models: while ours considers three distinct components, López-Sepulcre et al. (2015) only includes two. Our hot corino component has a size of 0.5 arcsec, corresponding to a radius of 35 au. This is significantly more compact that the region (of radius, fortuitously, 90 au) where the temperature is higher than 90 K. As a consequence, this latter region in the model of López-Sepulcre et al. (2015) would correspond in our model to a mixture of the hot corino region and the warm envelope component. It is, therefore, not surprising that the abundance, $(6 \pm 3) \times 10^{-9}$, reported by López-Sepulcre et al. (2015) for this region is intermediate between the abundances we derive here for the hot corino and the warm envelope. For the region outside of 90 au, we derive an abundance of $(1–2) \times 10^{-11}$, which is within a factor of two of that derived by López-Sepulcre et al. (2015).

4.2 Spectral modelling

We see that most of the lines are very well reproduced by the model based on the physical parameters discussed previously (see Fig. 4). However, some of them are underestimated [see the predicted line profiles by the model in the Appendix; note that in some cases, the predicted emission could not be computed for some HNCO transitions since their corresponding collisional rate coefficient was lacking in the computation of Sahnoun et al. (2018)]. For the spectroscopic branch $K_a = 1$, the agreement between the model and the data is less good for transitions at lowest frequencies (e.g. $J = 4$, 5). We have searched for line blending with other species for these transitions in particular to verify if the line intensities were affected by this problem but we did not found a clear contribution from other molecules. For the transitions belonging to the $K_a = 2$ levels, the problem is more severe. It could be argued that collision coefficients are particularly inaccurate for such lines. However, examining the spectra of similar molecules, like H_2CO, one sees the same type of problems. A thorough discussion is given by Mangum & Wootten (1993) and Mangum & Shirley (2015). Formaldehyde has a rotational spectra similar to HNCO, with a heavy rod or rod-like part (NCO versus CO), and only light H atom(s) breaking the rod-like symmetry. Both molecules have thus very distinct $K_a = 0, 1, 2, \ldots$ branches well separated one from the other. Other molecules, less abundant, present a very similar type of spectroscopy (e.g. H_2CS and l-C_3H_2).

While for H_2CO the intensities and line-shapes are well understood for $K_a \le 2$ (see methods proposed by Mangum & Wootten 1993), this is not always true for the higher lying $K_a > 2$ branch,

very similarly to our case of HNCO. The higher $K_a = 2$ transitions, we observe connect levels which are not correctly modelled. That is, the levels with high-J and $K_a = 2$ or any level with $K_a > 2$ are not considered in the computation of the collisional coefficients used in this paper. These high levels could be populated by specific excitation, perhaps originating in some hotter photonic bath or some specific excitation, not properly taken into account.

Note that we have not considered infrared (IR) pumping to vibrationally excited states of HNCO. For this molecule, the ν_4, ν_6, and ν_5 fundamental bending vibrations have energies above ground by 1118, 949, and 831 K, respectively (see e.g. Yamada 1977). Various rotational lines with $J = 4$ and 5 from within the $\nu_5 = 1$ and $\nu_6 = 1$ (and possibly the $\nu_4 = 1$) states have been detected by Belloche et al. (2017) with ALMA towards the hot core Sgr B2 (N2). These lines intensities are characterized by a source model whose angular source size and rotational temperature are not too different from the values used by us for I16293. Some of the lines had even been detected in an earlier survey with the IRAM 30-m telescope Belloche et al. (2013). While quite weak for detection by the single dishes employed by us, future ALMA data could address HNCO excitation in the hot corino in I16293. Deciding whether vibrational excitation by IR photons or collisions are both feasible or whether such excitation and re-decay to the ground state could influence the intensities of the $K_a = 2$ lines lies beyond the scope of this paper.

4.3 Comparison with Green collisional coefficients

The new collisional coefficients with respect to those computed by Green (1986) bring three advantages:

(a) More temperatures are considered, 17 with the new set of coefficients (7, 10, and 20–300 K with a step of 20 K) with respect to 5 for Green coefficients (20, 40, 80, 160, and 320 K).
(b) More collisional transitions are considered (2272 against 2254).
(c) The coefficients are computed separately for collisions with p-H_2 and o-H_2, allowing to deal with the o/p ratio, an important factor in cold environments.

While the computed spectra using both set of collisional coefficients are similar for our I16293 three components model at frequencies ≤ 500 GHz, there are some differences at higher frequencies, as can be seen on Fig. 5, justifying the use of this new set for an optimal modelization.

4.4 Chemical modelling with NAUTILUS

To further investigate the chemistry of HNCO in the envelope of I16293 and to probe the abundances derived from our full non-LTE radiative transfer model, we computed the abundance profiles using the NAUTILUS chemical code. NAUTILUS is a three phase gas–grain chemical code that allows us to compute the chemical composition as a function of time. The details of the chemical reactions included in the code are explained in Ruaud, Wakelam & Hersant (2016). The gas phase network used by NAUTILUS is based on kida.uva.2014 (Wakelam et al. 2015), while the grain chemistry is presented in Ruaud et al. (2015). The modelling is made in two steps: first, we run a simulation for the parental cloud where the protostar I16293 was formed, and then we take the resulting abundances as input for the protostar phase, where we use the one-dimensional structure for the envelope defined by Crimier et al. (2010, i.e. the temperature and density profiles) to compute the corresponding abundance profile.
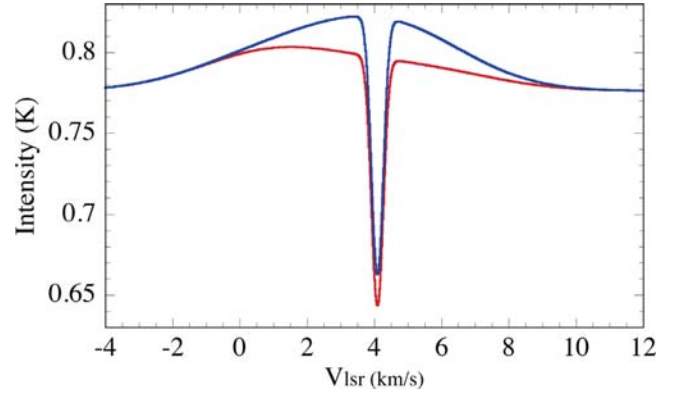
Figure 5. Comparison of the I16293 computed spectrum for the HNCO $(4_{1,3}-4_{0,4})$ transition ($\nu = 902\,505.9937$ MHz, $E_{up} = 53.86$ K, and $A_{ij} = 7.85 \times 10^{-3}$ s^{-1}) with our three-component model. Blue : Green coefficients, Red : new set of coefficients.

For the parental cloud, as Hincelin et al. (2011), we have used the atomic initial abundances and the following set of physical parameters, which are typical for cold dense clouds in the Solar neighbourhood: $n = 3 \times 10^4$ cm^{-3}, $T = 10$ K, C/O ratio $= 0.7$, gas-to-dust ratio $= 100$, and grain size $= 0.1$ μm, UV field $G_0 = 1$ Habing (1.6×10^{-3} erg cm^{-2} s^{-1}), visual extinction $A_v = 3$, cosmic-ray ionization rate $\zeta = 1.3 \times 10^{-17}$ s^{-1}, evolution time for the cloud to reach the pre-stellar phase $= 2.5 \times 10^5$ yr. We ran several simulations changing the value of A_v (from 3 to 30), density (from 3×10^3 to 3×10^5 cm^{-3}), evolution times (from 10^5 to 5×10^5 yr), C/O ratio (0.7 and 1.2), and cosmic ray ionization rate (from 10^{-17} to 10^{-16} s^{-1}), and found that the only parameters changing the abundance profiles are the visual extinction A_v and the cosmic-ray ionization rate ζ. The abundance profiles that best reproduces the observations are obtained with $A_v = 4$ and $\zeta = 8.0 \times 10^{-17}$ s^{-1}. Although this value of ζ is higher that the commonly assumed standard value for the Solar neighbourhood (1.3×10^{-17} s^{-1}), the Ophiuchus star-forming region is known to have a high cosmic ionization rate (e.g. Hunter et al. 1994).

4.5 Results of the NAUTILUS chemical model for HNCO

Once the final abundances are computed, we use them as input and run a simulation taking into account the density and temperature profiles defined by Crimier et al. (2010) for the envelope of I16293. To do that, we kept the same visual extinction and cosmic ionization rate used for the initial cloud. The resulting HNCO radial abundance profile for different ages of the protostar is shown in Fig. 6. The model for the warm envelope predicts a high abundance (larger than $\sim 10^{-9}$) close to the hot corino value (in agreement with the model described above), while for the warm envelope radius derived from our non-LTE radiative transfer model of 7.8 arcsec, the abundance varies from 10^{-12} to 10^{-10}, depending on the age of the protostar. For the external envelope, the abundance profile seems to change more rapidly with time. At a radius of 30 arcsec, where the difference between the predicted abundances seems to be larger, the model predicts a smaller abundance for largest age ($\sim 10^{-12}$ for 1.4×10^5 yr) and vice-versa ($\sim 10^{-9}$ for 1.0×10^4 yr). The final values for the abundance predicted with NAUTILUS (although smaller) are closer to the abundance predicted by the radiative transfer model for younger ages. In fact, the age of I16293 in the literature is reported to be between $\sim 10^4$ and 10^5 yr. For instance, Quénard et al. (2018) studied the emission of HNCO towards the hot corino as-
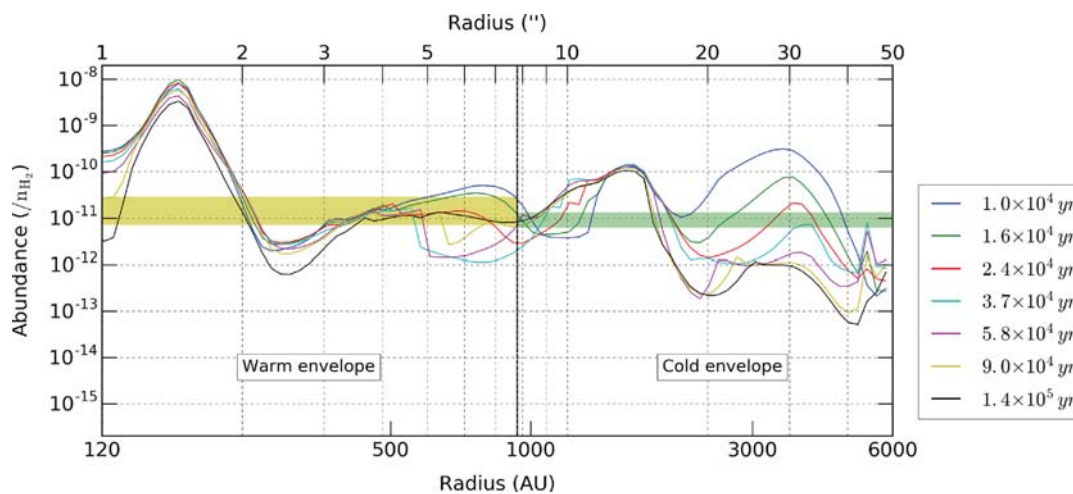
Figure 6. HNCO abundance profile computed with Nautilus for the envelope of I16293 assuming a cosmic ionization rate of 8.0×10^{-17} s^{-1}. The colours of the lines indicate the age of the protostar in years. The light yellow horizontal band represents the predicted abundance for the warm envelope from our CASSIS–RADEX model ($1.8 \pm 0.4 \times 10^{-11}$), while the light green colour band represents the predicted abundance for the cold envelope ($9.8 \pm 0.3 \times 10^{-12}$). Both bands have a 3σ error width. The black vertical line represents the radius of the warm envelope of 7.8 arcsec.

sociated with source B and the cold envelope of I16293 using the chemical code UCLCHEM. They compared the abundance for source B obtained by Martín-Doménech et al. (2017; 1.8×10^{-9}) and the abundance for the cold envelope derived by van Dishoeck et al. (1995; 1.7×10^{-10}) and found an age for the protostar close to $\sim(2–4) \times 10^4$ yr.

From the simulations, we conclude that we cannot use HNCO as a chemical clock to constrain the age of the protostar due to the strong dependence on the initial parameters for the model. If we take an age of about 5.8×10^4 yr, we observe that the abundance profile, although not constant, is in good agreement with the abundances derived directly from the observations with our radiative transfer model. We also found that the Nautilus input parameters used to reproduce the HNCO observed abundances are very similar to those derived by other authors using Nautilus and single-dish data for other molecules such as HDO (Coutens et al. 2012), CH (Bottinelli et al. 2014), CH_3SH (Majumdar et al. 2016), C_3H_2 (Majumdar et al. 2017), or $HOCO^+$ (Majumdar et al. 2018).

Recently, observations of the ortho- and para-ground-state lines of both H_2D^+ and D_2H, deuterated isotopologues of the fundamental H_3^+ ion, have been performed towards I16293 with the APEX telescope and the Stratospheric Observatory for Infrared Astronomy (SOFIA; Brünken et al. 2014; Harju et al. 2017). Given the observed simple line profiles, their narrow width and LSR velocities, the lines from these species originate in the extended envelope of I16293. For both species, their ortho-to-para ratio, OPR, is time-dependent. Modelling the observed OPR for H_2D^+, Brünken et al. (2014) derive an age of order 10^6 yr. This value is further constrained to 5×10^5 yr by Harju et al. (2017) who combines the observed values for the H_2D^+ and D_2H^+ OPR. This age is considerably older that the values from Nautilus modelling. While this might be understandable for the age of the hot corino, the discrepancy between the age derived from the H_2D^+ and HNCO in the extended envelope is difficult to explain.

5 CONCLUSIONS

In this work, we have presented an analysis of isocyanic acid (HNCO) line emission towards IRAS 16293−2422 as observed with single-dish telescopes (IRAM, APEX, JCMT, and Herschel/HIFI)

over a wide range of frequencies. The HNCO line profiles are interpreted as the superposition of three physical components along the line of sight: a dense, warm, and compact source associated with the hot corino in I16293, a more extended component associated with the warm part of the envelope, and a cold and extended component corresponding to the outer layer of the envelope. We have constrained most of the parameters for each physical component based on the structure derived by Crimier et al. (2010).

We used a full non-LTE radiative transfer model in CASSIS–RADEX to predict the line emission profiles by using the new HNCO collisional rate coefficients computed by Sahnoun et al. (2018) from a set of rotational excitation quenching rates between HNCO and both ortho and para H_2. We obtain physical values for the hot corino that are in very good agreement with what has been found for other hot cores (e.g. Bisschop et al. 2007). From the derived column densities, we found that the abundances in both warm and cold layers of the envelope are very similar (close to $\sim 10^{-11}$).

While the transitions on the $K_a = 0, 1$ bands are well reproduced, the transitions belonging to the upper rotational band $K_a = 2$ levels are not. We argue that those levels could be populated by specific excitation due to a hotter photonic or collisional bath and that the modelling is not able to take these excitations into account.

We used the three phase chemical gas–grain code Nautilus to compute the chemical composition of the envelope of I16293 and produce an HNCO radial abundance profile. We found that the younger ages for the protostar are in better agreement with our radiative transfer model results. However, HNCO cannot be used as a reliable chemical clock due to the high dependence on the initial parameters in our simulations.

REFERENCES

Belloche A., Müller H. S. P., Menten K. M., Schilke P., Comito C., 2013, A&A, 559, A47

Belloche A. et al., 2017, A&A, 601, A49

Bisschop S. E., Jørgensen J. K., Bourke T. L., Bottinelli S., van Dishoeck E. F., 2008, A&A, 488, 959

Bisschop S. E., Jørgensen J. K., van Dishoeck E. F., de Wachter E. B. M., 2007, A&A, 465, 913

Biver N. et al., 2006, A&A, 449, 1255

Blake G. A., Sutton E. C., Masson C. R., Phillips T. G., 1987, ApJ, 315, 621

Bottinelli S., Wakelam V., Caux E., Vastel C., Aikawa Y., Ceccarelli C., 2014, MNRAS, 441, 1964

Brünken S. et al., 2014, Nature, 516, 219

Caux E., Bottinelli S., Vastel C., Glorian J. M., 2011, Proc. IAU Symp. 280, The Molecular Universe, Kluwer, Dordrecht, p. 120

Caux E. et al., 2011, A&A, 532, A23

Ceccarelli C. et al., 2010, A&A, 521, L22

Coutens A. et al., 2012, A&A, 539, A132

Crimier N., Ceccarelli C., Maret S., Bottinelli S., Caux E., Kahane C., Lis D. C., Olofsson J., 2010, A&A, 519, A65

Crovisier J., 1998, Faraday Discuss., 109, 437

de Graauw T. et al., 2010, A&A, 518, L6

Dzib S. A. et al., 2018, A&A, 614, A20

Fedoseev G., Ioppolo S., Zhao D., Lamberts T., Linnartz H., 2015, MNRAS, 446, 439

Fusina L., Mills I. M., 1981, J. Mol. Spectros., 86, 488

Garrod R. T., Widicus Weaver S. L., Herbst E., 2008, ApJ, 682, 283

Green, S., 1986, NASA Technical Memorandum, 87791

Guan Y., Fleißner R., Joyce P., Krone S. M., 2006, Stat Comput, 16, 193

Harju J. et al., 2017, ApJ, 840, 63

Hastings W. K., 1970, Biometrika, 57, 97

Helmich F. P., van Dishoeck E. F., 1997, A&AS, 124, 205

Hernández-Gómez A. et al., 2018, submitted

Heyminck S., Kasemann C., Güsten R., de Lange G., Graf U. U., 2006, A&A, 454, L21

Hincelin U., Wakelam V., Hersant F., Guilloteau S., Loison J. C., Honvault P., Troe J., 2011, A&A, 530, A61

Hocking W. H., Gerry M. C. L., Winnewisser G., 1975, Can. J. Phys., 53, 1869

Hunter S. D., Digel S. W., de Geus E. J., Kanbach G., 1994, ApJ, 436, 216

Iglesias E., 1977, ApJ, 218, 697

Jackson J. M., Armstrong J. T., Barrett A. H., 1984, ApJ, 280, 608

Jacobsen S. K. et al., 2018, A&A, 612, A72

Jørgensen J. K. et al., 2016, A&A, 595, A117

Kukolich S. G., Nelson A. C., Yamanashi B. S., 1971, J. Am. Chem. Soc., 93, 6769

Lapinov G., Golubiatnikov Yu., Markov V. N., Guarnieri A., 2007, Astron. Lett., 33, 121

Lis D. C. et al., 1997, Icarus, 130, 355

López-Sepulcre A. et al., 2015, MNRAS, 449, 2438

MacDonald G. H., Gibb A. G., Habing R. J., Millar T. J., 1996, A&AS, 119, 333

Majumdar L., Gratier P., Andron I., Wakelam V., Caux E., 2017, MNRAS, 467, 3525

Majumdar L., Gratier P., Vidal T., Wakelam V., Loison J. C., Hickson K. M., Caux E., 2016, MNRAS, 458, 1859

Majumdar L., Gratier P., Wakelam V., Caux E., Willacy K., Ressler M. E., 2018, MNRAS, 477, 525

Mangum J. G., Shirley Y. L., 2015, PASP, 127, 266

Mangum J. G., Wootten A., 1993, ApJS, 89, 123

Marcelino N., Brünken S., Cernicharo J., Quan D., Roueff E., Herbst E., Thaddeus P., 2010, A&A, 516, A105

Marcelino N., Cernicharo J., Tercero B., Roueff E., 2009, ApJ, 690, L27

Martín-Doménech R., Rivilla V. M., Jiménez-Serra I., Quénard D., Testi L., Martín-Pintado J., 2017, MNRAS, 469, 2230

Martín S., Martín-Pintado J., Mauersberger R., 2009, ApJ, 694, 610

Martín S., Mauersberger R., Martín-Pintado J., Henkel C., García-Burillo S., 2006, ApJS, 164, 450

Martín S., Requena-Torres M. A., Martín-Pintado J., Mauersberger R., 2008, ApJ, 678, 245

Meier D. S., Turner J. L., 2005, ApJ, 618, 259

Menten K. M., Serabyn E., Guesten R., Wilson T. L., 1987, A&A, 177, L57

Mundy L. G., Wootten A., Wilking B. A., Blake G. A., Sargent A. I., 1992, ApJ, 385, 306

Müller H. S. P., Schlöder F., Stutzki J., Winnewisser G., 2005, J. Mol. Struct., 742, 215

Müller H. S. P., Thorwirth S., Roth D. A., Winnewisser G., 2001, A&A, 370, L49

Niedenhoff M., Yamada K. M. T., Belov S. P., Winnewisser G., 1995, J. Mol. Spectrosc., 174, 151

Nizam M., Bouteiller Y., Silvi B., Pisani C., Causa M., Dovesi R., 1988, J. Phys. C: Solid State Phys., 21, 5351

Noble J. A. et al., 2015, A&A, 576, A91

Ott S., 2010, in Mizumoto Y., Morita K.-I., Ohishi M., eds, ASP Conf. Ser. Vol. 434, Astronomical Data Analysis Software and Systems XIX, Astron. Soc. Pac., San Francisco, p. 139

Quan D., Herbst E., Osamura Y., Roueff E., 2010, ApJ, 725, 2101

Quénard D., Jiménez-Serra I., Viti S., Holdship J., Coutens A., 2018, MNRAS, 474, 2796

Rodríguez-Fernández N. J., Tafalla M., Gueth F., Bachiller R., 2010, A&A, 516, A98

Roelfsema P. R. et al., 2012, A&A, 537, A17

Ruaud M., Loison J. C., Hickson K. M., Gratier P., Hersant F., Wakelam V., 2015, MNRAS, 447, 4004

Ruaud M., Wakelam V., Hersant F., 2016, MNRAS, 459, 3756

Sahnoun E., Wiesenfeld L., Hammami K., Jaidane N., 2018, J. Phys. Chem. A, 122, 3004

Snyder L. E., Buhl D., 1972, ApJ, 177, 619

Tideswell D. M., Fuller G. A., Millar T. J., Markwick A. J., 2010, A&A, 510, A85

Turner B. E., 1991, ApJS, 76, 617

Turner B. E., 2000, ApJ, 542, 837

van der Tak F. F. S., Black J. H., Schöier F. L., Jansen D. J., van Dishoeck E. F., 2007, A&A, 468, 627

van Dishoeck E. F., Blake G. A., Jansen D. J., Groesbeck T. D., 1995, ApJ, 447, 760

Wakelam V. et al., 2015, ApJS, 217, 20

Werner H. et al., 2012, University College Cardiff Consultants Ltd. Wales, UK

Wootten A., 1989, ApJ, 337, 858

Yamada K., 1977, J. Mol. Spectrosc., 68, 423

APPENDIX A: OBSERVED HNCO TRANSITIONS PARAMETERS

In this section, we give the parameters of all the HNCO observed lines.

Table A1. Detected HNCO transitions in all observations and their main parameters. The negative sign for some transitions detected with Herschel/HIFI indicate that the line could be in absorption (after subtracting a baseline), although this is within the noise. Columns are frequency, quantum numbers, upper level energy, Einstein A value, value and error of the velocity-integrated main-beam brightness temperature. Telescope used: $[87, 245]$ GHz:IRAM-30m, $[260, 320]$ and $[370, 470]$ GHz:APEX, $[328, 360]$ GHz:JCMT, and $[>490]$ GHz:Herschel–HIFI.

Frequency (MHz)	Transition ($J_{K_a\,K_c}$)	E_{up} (K)	A_{ij} (s^{-1})	$\int T_{mb} dv$ (K km s^{-1})
875 97.330	$4_{1\,4}-3_{1\,3}$	53.78	8.04×10^{-6}	0.29 ($\pm$0.05)
878 98.425	$4_{2\,3}-3_{2\,2}$	180.83	6.28×10^{-6}	0.18 ($\pm$0.04)
878 98.628	$4_{2\,2}-3_{2\,1}$	180.83	6.28×10^{-6}	0.18 ($\pm$0.04)
879 25.237	$4_{0\,4}-3_{0\,3}$	10.54	8.78×10^{-6}	0.82 ($\pm$0.11)
882 39.020	$4_{1\,3}-3_{1\,2}$	53.86	8.22×10^{-6}	0.25 ($\pm$0.13)
109 495.996	$5_{1\,5}-4_{1\,4}$	59.04	1.65×10^{-5}	0.46 ($\pm$0.07)
109 872.337	$5_{2\,4}-4_{2\,3}$	186.10	1.41×10^{-5}	0.39 ($\pm$0.05)
109 872.765	$5_{2\,3}-4_{2\,2}$	186.10	1.41×10^{-5}	0.39 ($\pm$0.05)
109 905.749	$5_{0\,5}-4_{0\,4}$	15.82	1.75×10^{-5}	0.65 ($\pm$0.04)
110 298.089	$5_{1\,4}-4_{1\,3}$	59.15	1.68×10^{-5}	0.38 ($\pm$0.09)
131 394.230	$6_{1\,6}-5_{1\,5}$	65.34	2.92×10^{-5}	0.29 ($\pm$0.05)
131 845.890	$6_{2\,5}-5_{2\,4}$	192.43	2.61×10^{-5}	0.34 ($\pm$0.07)
131 846.600	$6_{2\,4}-5_{2\,3}$	192.43	2.61×10^{-5}	0.34 ($\pm$0.07)
131 885.734	$6_{0\,6}-5_{0\,5}$	22.15	3.08×10^{-5}	1.12 ($\pm$0.12)
132 356.701	$6_{1\,5}-5_{1\,4}$	65.50	2.99×10^{-5}	0.30 ($\pm$0.07)
153 291.935	$7_{1\,7}-6_{1\,6}$	72.70	4.73×10^{-5}	0.55 ($\pm$0.16)
153 818.880	$7_{2\,6}-6_{2\,5}$	199.81	4.33×10^{-5}	0.10 ($\pm$0.10)
153 820.016	$7_{2\,5}-6_{2\,4}$	199.81	4.33×10^{-5}	0.10 ($\pm$0.10)
153 865.086	$7_{0\,7}-6_{0\,6}$	29.53	4.94×10^{-5}	1.27 ($\pm$0.20)
154 414.765	$7_{1\,6}-6_{1\,5}$	72.91	4.84×10^{-5}	0.68 ($\pm$0.24)
197 085.416	$9_{1\,9}-8_{1\,8}$	90.57	1.03×10^{-4}	0.80 ($\pm$0.13)
197 762.939	$9_{2\,8}-8_{2\,7}$	217.74	9.66×10^{-5}	0.89 ($\pm$0.43)
197 765.372	$9_{2\,7}-8_{2\,6}$	217.74	9.66×10^{-5}	0.89 ($\pm$0.43)
197 821.461	$9_{0\,9}-8_{0\,8}$	47.47	1.07×10^{-4}	2.23 ($\pm$0.32)
198 528.881	$9_{1\,8}-8_{1\,7}$	90.91	1.05×10^{-4}	0.18 ($\pm$0.03)
218 981.009	$10_{1\,10}-9_{1\,9}$	101.07	1.42×10^{-4}	0.78 ($\pm$0.07)
219 733.850	$10_{2\,9}-9_{2\,8}$	228.29	1.35×10^{-4}	1.33 ($\pm$0.33)
219 737.193	$10_{2\,8}-9_{2\,7}$	228.29	1.35×10^{-4}	1.33 ($\pm$0.33)
219 798.274	$10_{0\,10}-9_{0\,9}$	58.01	1.47×10^{-4}	2.32 ($\pm$0.10)
220 584.751	$10_{1\,9}-9_{1\,8}$	101.50	1.45×10^{-4}	0.74 ($\pm$0.14)
240 875.727	$11_{1\,11}-10_{1\,10}$	112.63	1.90×10^{-4}	1.53 ($\pm$0.20)
241 703.853	$11_{2\,10}-10_{2\,9}$	239.89	1.81×10^{-4}	0.64 ($\pm$0.20)

Table A1 – *continued*

Frequency (MHz)	Transition ($J_{K_a\,K_c}$)	E_{up} (K)	A_{ij} (s^{-1})	$\int T_{mb} dv$ (K km s^{-1})
241 708.312	$11_{2\,9}-10_{2\,8}$	239.89	1.81×10^{-4}	0.64 ($\pm$0.20)
241 774.032	$11_{0\,11}-10_{0\,10}$	69.62	1.96×10^{-4}	2.67 ($\pm$0.23)
242 639.704	$11_{1\,10}-10_{1\,9}$	113.14	1.95×10^{-4}	2.25 ($\pm$0.31)
262 769.477	$12_{1\,12}-11_{1\,11}$	125.25	2.48×10^{-4}	0.75 ($\pm$0.18)
263 672.912	$12_{2\,11}-11_{2\,10}$	252.54	2.37×10^{-4}	1.32 ($\pm$0.51)
263 678.709	$12_{2\,10}-11_{2\,9}$	252.54	2.37×10^{-4}	1.32 ($\pm$0.51)
263 748.625	$12_{0\,12}-11_{0\,11}$	82.28	2.56×10^{-4}	0.70 ($\pm$0.07)
264 693.655	$12_{1\,11}-11_{1\,10}$	125.85	2.54×10^{-4}	0.21 ($\pm$0.06)
284 662.172	$13_{1\,13}-12_{1\,12}$	138.91	3.17×10^{-4}	0.38 ($\pm$0.08)
285 721.951	$13_{0\,13}-12_{0\,12}$	95.99	3.26×10^{-4}	0.76 ($\pm$0.09)
286 746.514	$13_{1\,12}-12_{1\,11}$	139.61	3.24×10^{-4}	0.29 ($\pm$0.11)
306 553.733	$14_{1\,14}-13_{1\,13}$	153.62	3.97×10^{-4}	0.42 ($\pm$0.09)
307 693.905	$14_{0\,14}-13_{0\,13}$	110.76	4.09×10^{-4}	1.08 ($\pm$0.20)
308 798.184	$14_{1\,13}-13_{1\,12}$	154.43	4.06×10^{-4}	0.72 ($\pm$0.15)
328 444.054	$15_{1\,15}-14_{1\,14}$	169.38	4.90×10^{-4}	0.68 ($\pm$0.21)
329 664.367	$15_{0\,15}-14_{0\,14}$	126.58	5.04×10^{-4}	1.79 ($\pm$0.19)
330 848.569	$15_{1\,14}-14_{1\,13}$	170.31	5.01×10^{-4}	1.63 ($\pm$0.40)
350 333.059	$16_{1\,16}-15_{1\,15}$	186.20	5.97×10^{-4}	1.01 ($\pm$0.06)
351 633.257	$16_{0\,16}-15_{0\,15}$	143.45	6.13×10^{-4}	1.63 ($\pm$0.12)
352 897.581	$16_{1\,15}-15_{1\,14}$	187.24	6.10×10^{-4}	0.88 ($\pm$0.09)
372 220.660	$17_{1\,17}-16_{1\,16}$	204.06	7.17×10^{-4}	0.56 ($\pm$0.10)
373 600.448	$17_{0\,17}-16_{0\,16}$	161.38	7.36×10^{-4}	1.64 ($\pm$0.24)
417 529.351	$19_{0\,19}-18_{0\,18}$	200.41	1.03×10^{-3}	1.37 ($\pm$0.12)
419 035.477	$19_{1\,18}-18_{1\,17}$	244.41	1.03×10^{-3}	1.08 ($\pm$0.15)
461 450.213	$21_{0\,21}-20_{0\,20}$	243.65	1.39×10^{-3}	1.54 ($\pm$0.22)
493 675.710	$17_{1\,17}-18_{0\,18}$	204.06	6.30×10^{-4}	0.40 ($\pm$0.06)
517 020.943	$16_{1\,16}-17_{0\,17}$	186.20	7.21×10^{-4}	-0.01 ($\pm$0.001)
540 288.323	$15_{1\,15}-16_{0\,16}$	169.38	8.21×10^{-4}	-0.01 ($\pm$0.002)
563 477.534	$14_{1\,14}-15_{0\,15}$	153.62	9.29×10^{-4}	0.05 ($\pm$0.02)
586 588.183	$13_{1\,13}-14_{0\,14}$	138.91	1.04×10^{-3}	-0.06 ($\pm$0.01)
609 619.927	$12_{1\,12}-13_{0\,13}$	125.25	1.17×10^{-3}	0.05 ($\pm$0.01)
632 572.365	$11_{1\,11}-12_{0\,12}$	112.63	1.30×10^{-3}	0.16 ($\pm$0.04)
655 445.310	$10_{1\,10}-11_{0\,11}$	101.07	1.44×10^{-3}	-0.01 ($\pm$0.004)
678 238.267	$9_{1\,9}-10_{0\,10}$	90.57	1.58×10^{-3}	-0.004 ($\pm$0.01)
700 951.182	$8_{1\,8}-9_{0\,9}$	81.11	1.74×10^{-3}	-0.03 ($\pm$0.01)
723 583.635	$7_{1\,7}-8_{0\,8}$	72.70	1.89×10^{-3}	0.01 ($\pm$0.01)
746 135.382	$6_{1\,6}-7_{0\,7}$	65.34	2.05×10^{-3}	-0.04 ($\pm$0.01)
768 606.238	$5_{1\,5}-6_{0\,6}$	59.04	2.21×10^{-3}	-0.01 ($\pm$0.01)
790 995.975	$4_{1\,4}-5_{0\,5}$	53.78	2.35×10^{-3}	-0.08 ($\pm$0.03)
813 304.397	$3_{1\,3}-4_{0\,4}$	49.58	2.47×10^{-3}	-0.06 ($\pm$0.01)
835531.328	$2_{1\,2}-3_{0\,3}$	46.42	2.49×10^{-3}	-0.03 ($\pm$0.003)
857 676.609	$1_{1\,1}-2_{0\,2}$	44.32	2.25×10^{-3}	-0.04 ($\pm$0.01)
901 800.081	$1_{1\,0}-1_{0\,1}$	44.33	7.84×10^{-3}	-0.09 ($\pm$0.01)
901 956.917	$2_{1\,1}-2_{0\,2}$	46.45	7.84×10^{-3}	-0.03 ($\pm$0.01)
902 192.207	$3_{1\,2}-3_{0\,3}$	49.62	7.84×10^{-3}	-0.08 ($\pm$0.01)
902 505.994	$4_{1\,3}-4_{0\,4}$	53.86	7.85×10^{-3}	-0.07 ($\pm$0.01)
902 898.335	$5_{1\,4}-5_{0\,5}$	59.15	7.86×10^{-3}	-0.05 ($\pm$0.01)
903 369.302	$6_{1\,5}-6_{0\,6}$	65.50	7.87×10^{-3}	-0.09 ($\pm$0.01)
903 918.982	$7_{1\,6}-7_{0\,7}$	72.91	7.88×10^{-3}	0.04 ($\pm$0.01)
904 547.473	$8_{1\,7}-8_{0\,8}$	81.38	7.89×10^{-3}	-0.01 ($\pm$0.004)
905 254.892	$9_{1\,8}-9_{0\,9}$	90.91	7.91×10^{-3}	0.04 ($\pm$0.01)
906 041.367	$10_{1\,9}-10_{0\,10}$	101.50	7.93×10^{-3}	-0.03 ($\pm$0.002)
906 907.042	$11_{1\,10}-11_{0\,11}$	113.14	7.95×10^{-3}	0.06 ($\pm$0.01)
907 852.072	$12_{1\,11}-12_{0\,12}$	125.85	7.97×10^{-3}	-0.004 ($\pm$0.003)
908 876.631	$13_{1\,12}-13_{0\,13}$	139.61	7.99×10^{-3}	0.04 ($\pm$0.004)
909 980.904	$14_{1\,13}-14_{0\,14}$	154.43	8.01×10^{-3}	-0.05 ($\pm$0.010)
911 165.091	$15_{1\,14}-15_{0\,15}$	170.31	8.04×10^{-3}	-0.007 ($\pm$0.002)
912 429.407	$16_{1\,15}-16_{0\,16}$	187.24	8.07×10^{-3}	-0.02 ($\pm$0.003)
913 774.079	$17_{1\,16}-17_{0\,17}$	205.24	8.10×10^{-3}	0.01 ($\pm$0.003)
923 621.180	$1_{1\,1}-0_{0\,0}$	44.32	5.61×10^{-3}	-0.07 ($\pm$0.01)
945 438.685	$2_{1\,2}-1_{0\,1}$	46.42	5.42×10^{-3}	-0.05 ($\pm$0.003)
967 173.925	$3_{1\,3}-2_{0\,2}$	49.58	5.52×10^{-3}	-0.06 ($\pm$0.01)
988 826.956	$4_{1\,4}-3_{0\,3}$	53.78	5.74×10^{-3}	-0.05 ($\pm$0.01)
101 0397.720	$5_{1\,5}-4_{0\,4}$	59.04	6.01×10^{-3}	-0.02 ($\pm$0.007)

Table A1 – *continued*

Frequency (MHz)	Transition ($J_{K_a K_c}$)	E_{up} (K)	A_{ij} (s^{-1})	$\int T_{mb} dv$ (K km s^{-1})
103 1886.200	6_{16}–5_{05}	65.34	6.32×10^{-3}	-0.06 (± 0.001)
105 3292.425	7_{17}–6_{06}	72.70	6.66×10^{-3}	-0.08 (± 0.01)
107 4616.365	8_{18}–7_{07}	81.11	7.03×10^{-3}	-0.17 (± 0.01)
109 5858.058	9_{19}–8_{08}	90.57	7.41×10^{-3}	-0.07 (± 0.01)
111 7017.603	10_{110}–9_{09}	101.07	7.81×10^{-3}	-0.14 (± 0.01)
113 8095.052	11_{111}–10_{010}	112.63	8.23×10^{-3}	0.06 (± 0.03)
115 9090.494	12_{112}–11_{011}	125.25	8.67×10^{-3}	-0.02 (± -0.003)
118 0004.039	13_{113}–12_{012}	138.91	9.13×10^{-3}	0.08 (± 0.02)

APPENDIX B: OBSERVED AND MODELLED HNCO TRANSITIONS

In this section, we show all the HNCO observed line profiles individually (in black) and the predicted emission/absorption profiles from our model described in Section 3 (in red). We have separated the observations by the K_a quantum number. Some transitions (indicated in each figure caption) could not be modelled since their collisional rate coefficients were not computed in the quantum chemical calculations of Sahnoun et al. (2018).
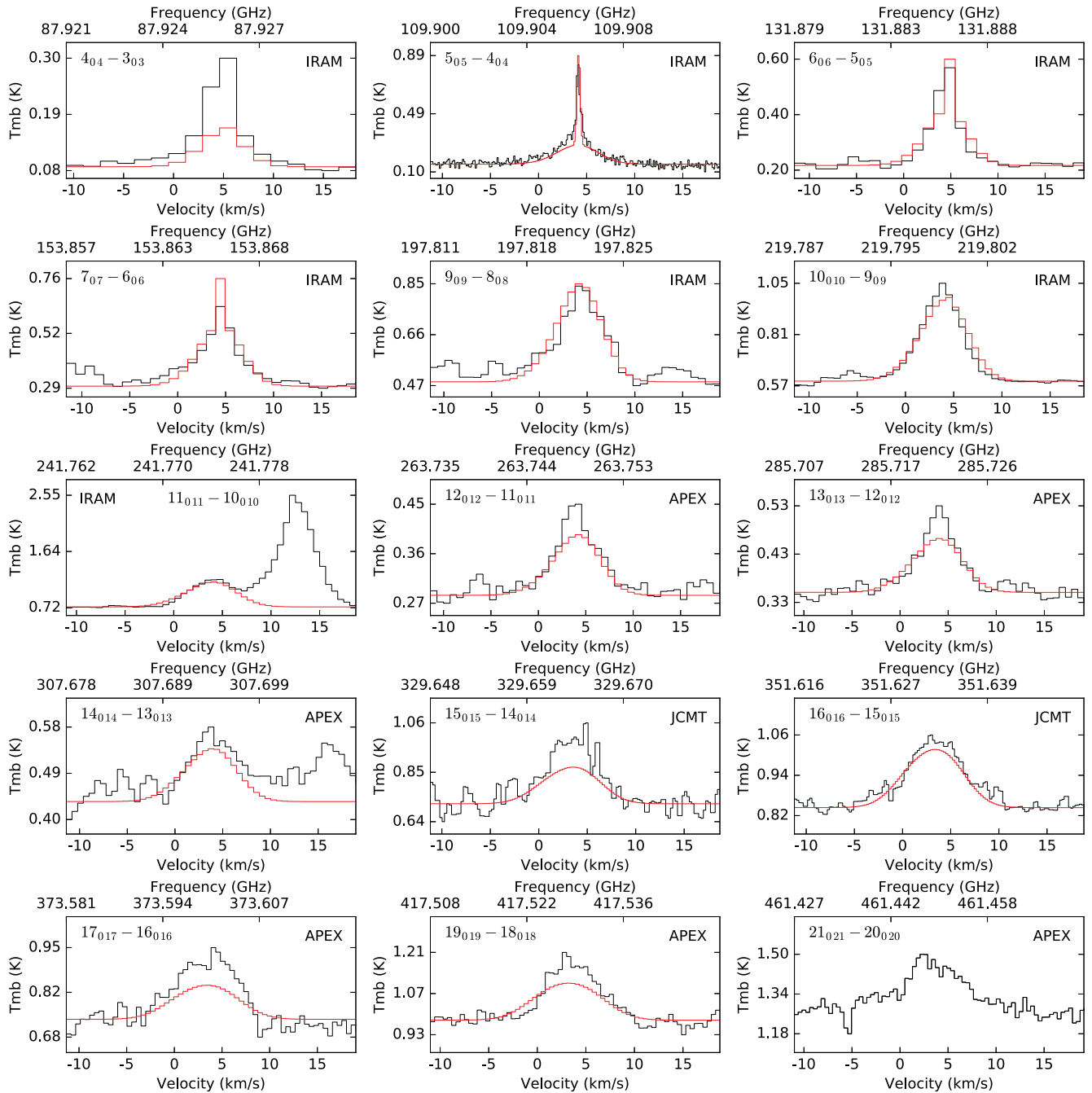
Figure B1. HNCO $K_a = 0$ transitions. The collision rate coefficient for the $21_{0\,21}$–$20_{0\,20}$ transition was lacking and therefore it could not be modelled.
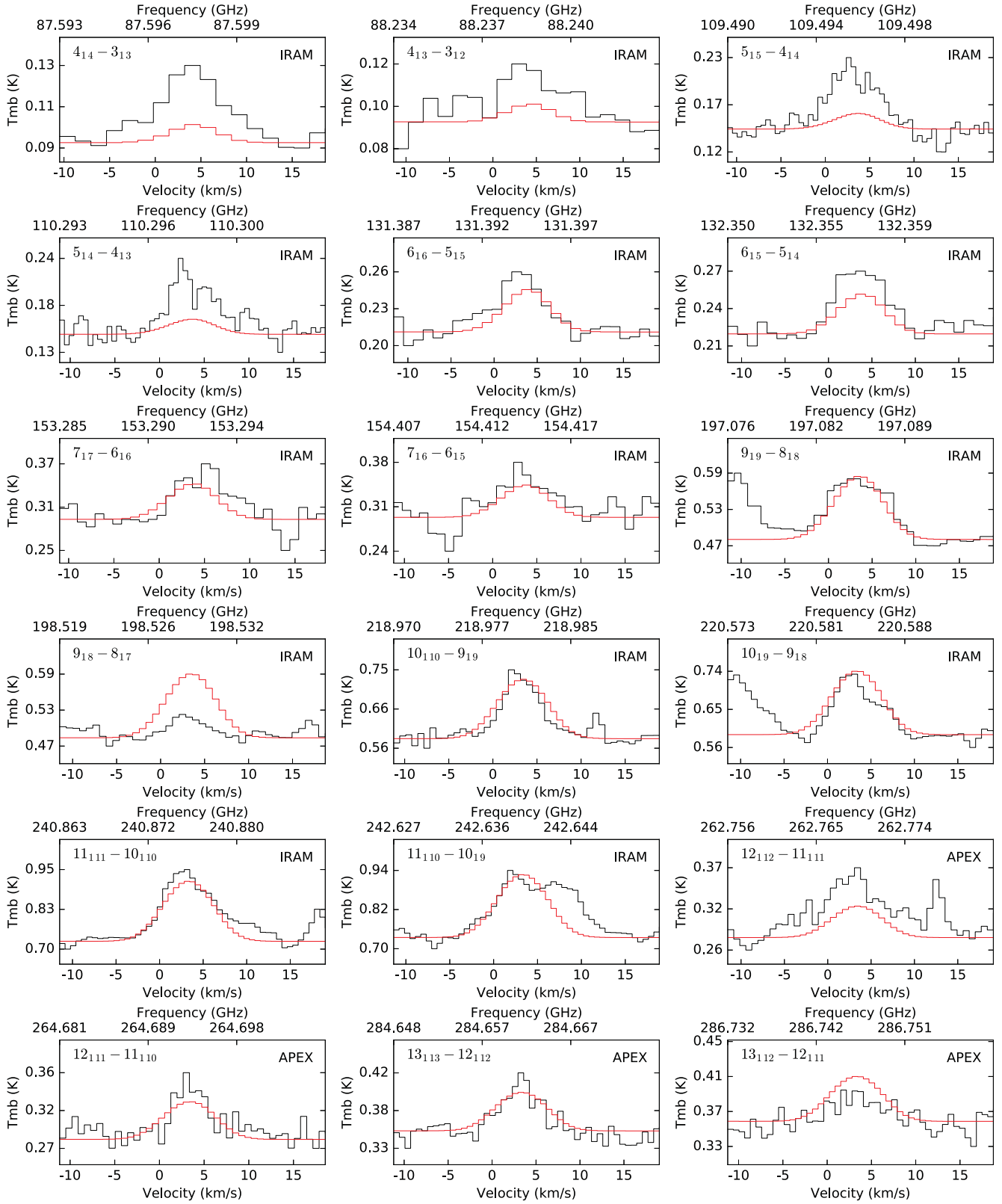
Figure B2. HNCO $K_a = 1$ transitions. The $19_{1\,18}-18_{1\,17}$ transition could not be modelled due to the lack of its collisional rate coefficient.
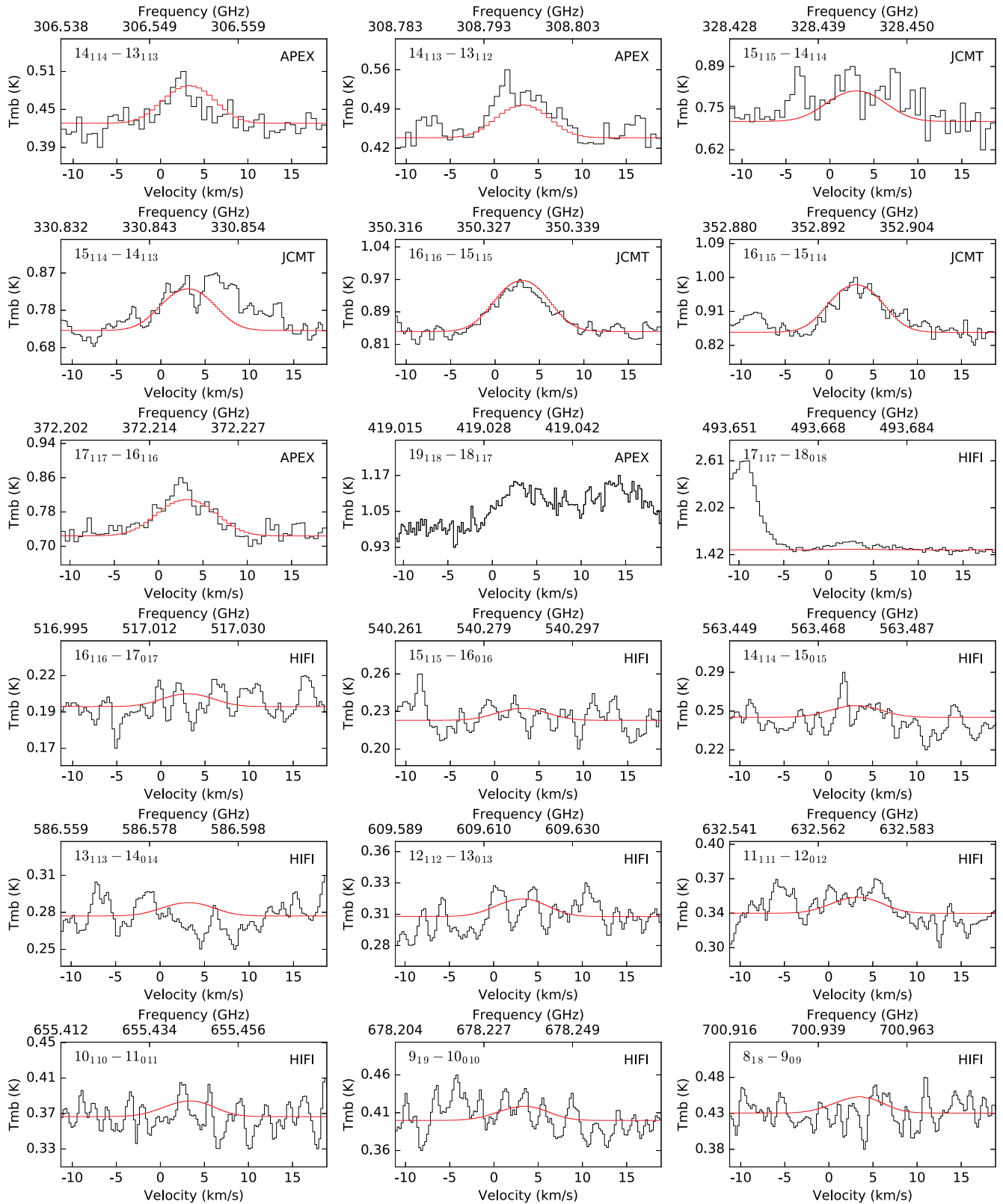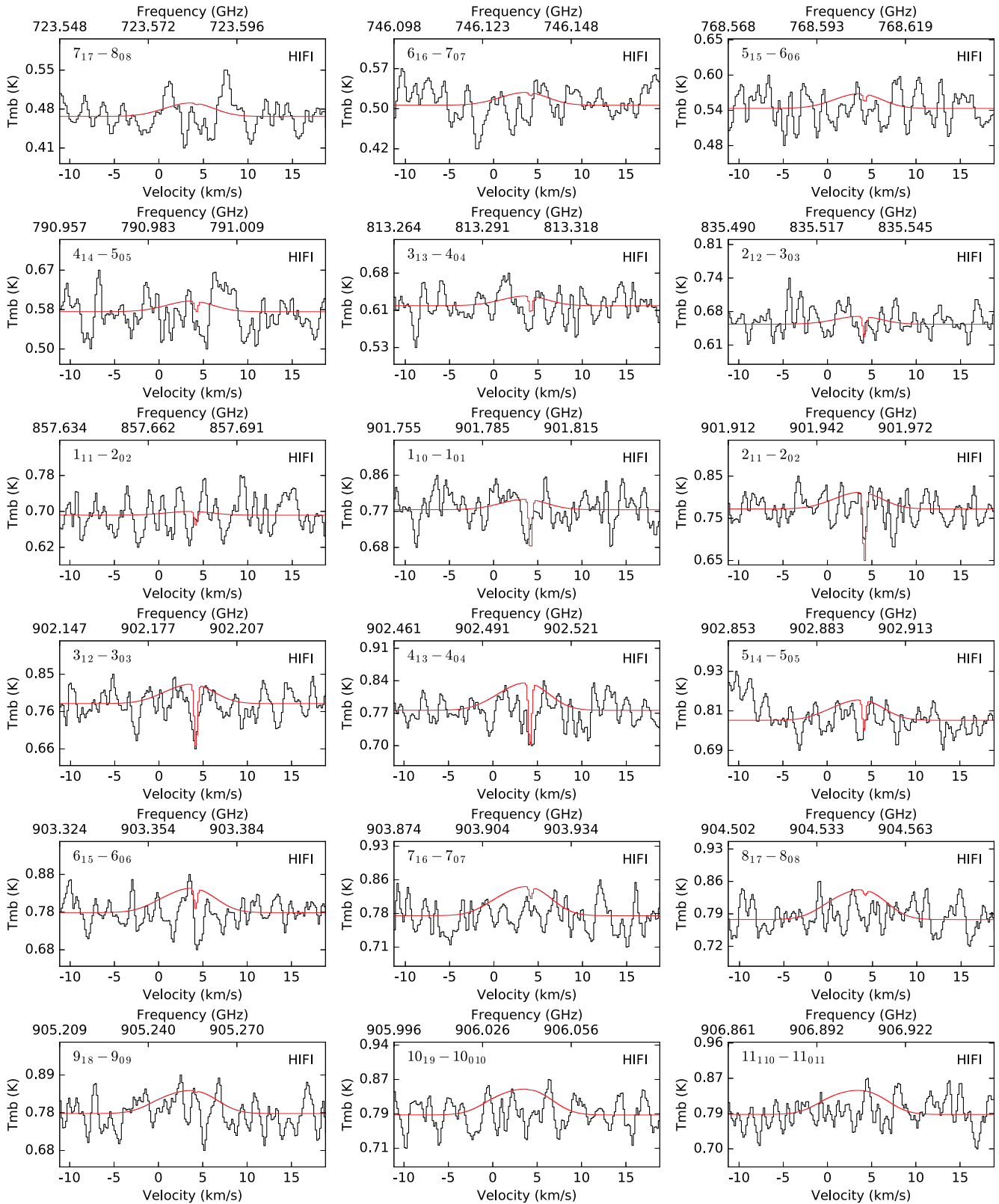
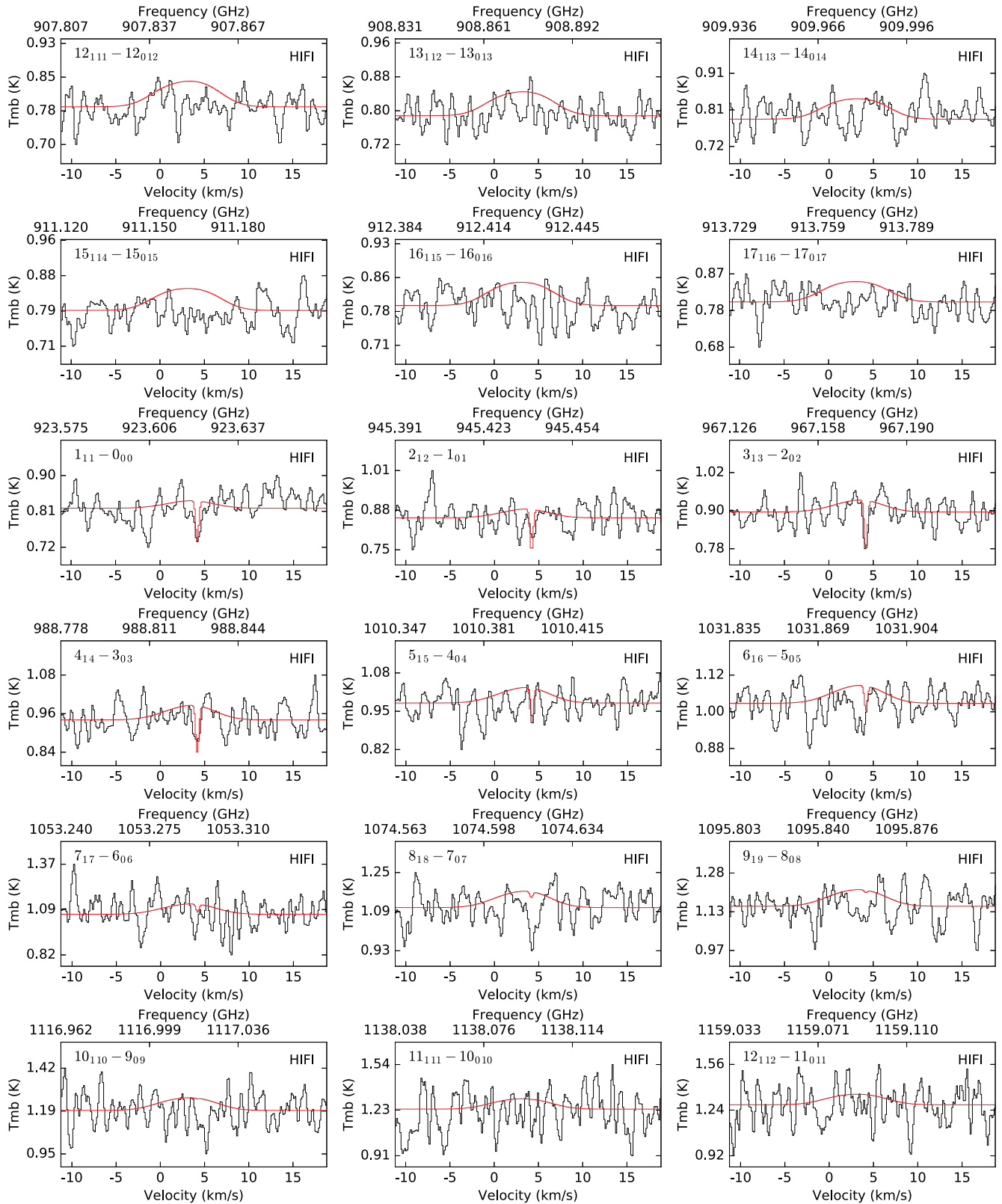**Figure B2.** *– continued*
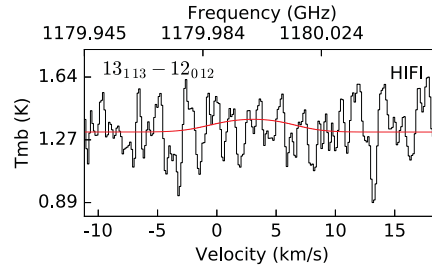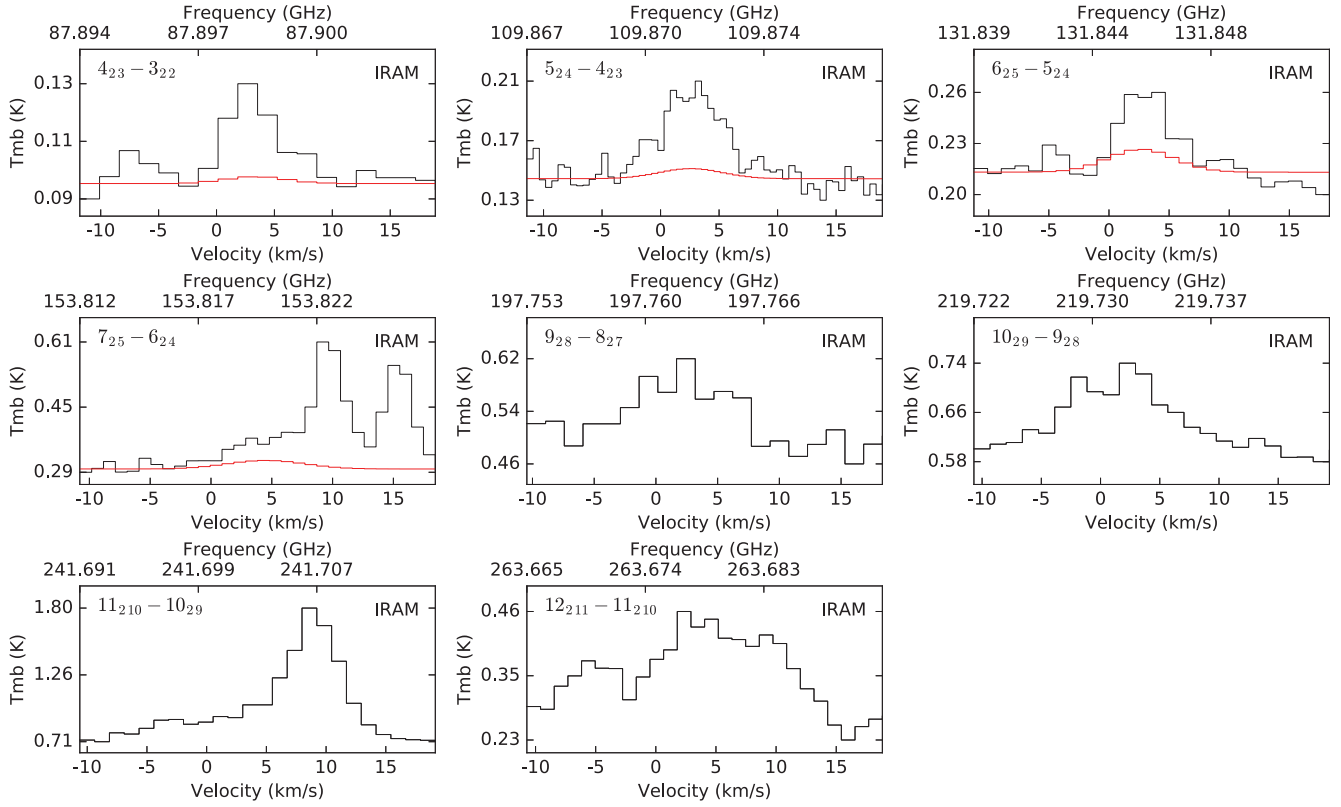
Figure B2. *– continued*

Figure B2. *– continued*

Figure B2. *– continued*

Figure B3. HNCO $K_a = 2$ transitions. In all cases, two transitions very close in frequency are always contained in the same line profile (see Table 1). The transitions with $J \geq 9$ were not modelled due to the lack of their corresponding collisional rate coefficients.

This paper has been typeset from a TEX/LATEX file prepared by the author.

Chapter 6

Análisis de la estructura de IRAS 16293–2422 a partir de los perfiles de absorción de cianuro (CN)

Se sabe que las moléculas nitrogenadas son buenos trazadores de las propiedades físicas y químicas en regiones de formación estelar. En el Capítulo 5, derivamos la estructura de abundancia del HNCO en IRAS 16293-2422 a partir de un modelo de transferencia radiativa fuera de ETL. En este último capítulo, nos enfocamos en las propiedades de IRAS 16293-2422 a partir del análisis de una de las moléculas nitrogenadas más simples: el cianuro (CN). Observaciones de alta resolución espectral en longitudes de onda milimétricas hasta el lejano infrarrojo hechas con APEX, IRAM y HIFI, han mostrado la presencia de varias transiciones rotacionales de CN en IRAS 16293-2422. Comparados con HNCO, los perfiles de línea de CN muestran una morfología mucho más compleja, incluyendo absorciones profundas. Estos perfiles de línea proveen una oportunidad para analizar la estructura de la protoestrella a diferentes escalas espaciales dado que se espera que los componentes de emisión o absorción de CN se originen en diferentes partes de la envolvente. Los mapas hechos con IRAM de las transiciones $J = 1 - 0$ y $J = 2 - 1$ revelaron la emisión extendida de CN en la envolvente. Además, el campo de velocidades de estas transiciones muestran un gradiente de velocidad en la dirección NE-SO, asociado con la rotación de la envolvente. Hemos utilizado un modelo de transferencia radiativa en ETL dentro de CASSIS y definimos un modelo separado para cada transición. Una componente de emisión extendida más grande que la envolvente de IRAS 16293-2422 definida por Crimier et al. (2010) es necesaria para modelar los perfiles de línea. De hecho, para reproducir correctamente la absorción observada, es necesario considerar que la envolvente fría se extiende hasta 75″ a partir del pico de emisión. Un modelo químico hecho con el código de gas-granos Nautilus nos permite calcular el perfil de abundancia de CN y verificamos que la abundancia encontrada en nuestro modelo en ETL es consistente con las observaciones. Además, derivamos el cociente para algunos isótopos analizando las líneas de ^{13}CN y $C^{15}N$. Encontramos un cociente de $^{12}C/^{13}C \sim 55$, el cual es similar al valor encontrado en el medio interestelar, pero diferente al reportado para IRAS 16293-2422B en la literatura (~ 30). Por otra parte, el cociente $^{14}N/^{15}N \sim 315$ es similar a valores estándares.

Chapter 6

Analyse de la structure d'IRAS 16293–2422 à partir des profils d'absorption du cyanure

On sait que les molécules azotées sont de bons traceurs des propriétés physiques et chimiques des régions qui forment des étoiles. Au Chapitre 5, nous avons dérivé la structure d'abondance HNCO dans IRAS 16293-2422 à partir de la modélisation du transfert radiatif de ses émissions hors LTE. Dans ce dernier chapitre, nous nous intéressons aux propriétés d'IRAS 16293–2422, issues de l'analyse d'une des molécules les plus simples contenant de l'azote: le cyanure (CN). Des observations spectroscopiques de haute résolution spectrale dans les domaines millimétrique à infrarouge lointain avec les radio-télescopes APEX, IRAM et HIFI ont montré la présence de nombreuses transitions rotationnelles de CN dans IRAS 16293-2422. Comparés à HNCO, les profils de raie du CN présentent une morphologie beaucoup plus complexe, y compris des absorptions profondes. Ces profils de raies fournissent une opportunité de sonder la structure de la proto-étoile à différentes échelles spatiales puisque les différentes composantes d'émission ou d'absorption du CN proviennent de différentes parties de l'enveloppe. Les cartes réalisées à l'IRAM avec le mode "on the fly" des transitions $J = 1 - 0$ et $J = 2 - 1$ de CN ont révélé l'émission étendue de CN dans l'enveloppe. De plus, le champ de vitesse de ces transitions montre un gradient de vitesse dans la direction NE-SW, associé à la rotation de l'enveloppe. Nous avons utilisé un modèle de transfert radiatif à l'ETL dans CASSIS et défini un modèle distinct pour chaque transition. Une émission de l'enveloppe d'IRAS 16293-2422 plus étendue que celle définie par Crimier et al. (2010) est nécessaire pour modéliser correctement les profils de raie observés. En effet, pour reproduire correctement l'absorption observée, il faut supposer que l'enveloppe froide s'étend jusqu'à 75″ du pic d'émission. Une modélisation chimique avec le code Nautilus nous a permis de calculer le profil d'abondance du CN et nous avons vérifié que l'abondance obtenue est compatible avec notre modèle ETL. De plus, nous avons dérivé les rapports isotopiques à partir de l'analyse des raies des isotopologues du CN, ^{13}CN et $C^{15}N$. Nous avons obtenu un rapport $^{12}C/^{13}C \sim 55$ et un rapport $^{14}N/^{15}N \sim 315$, similaires à ceux obtenus dans le voisinage solaire à partir d'autres observations.

Chapter 6

Probing the structure of IRAS 16293–2422 from the absorption line profiles of cyanide (CN)

Nitrogen-bearing molecules are known to be good tracers of the physical and chemical properties of star-forming regions. In Chapter 5, we derived the HNCO abundance structure in IRAS 16293-2422 from the radiative transfer modelling of its emission out of LTE. In this last chapter, we focus on the properties of IRAS 16293–2422 from the analysis of one of the simplest nitrogen-bearing molecules: the cyanide (CN). Millimeter to far infrared high spectral resolution single-dish observations with APEX, IRAM and HIFI have shown the presence of numerous rotational transitions of CN in IRAS 16293-2422. When compared to HNCO, CN line profiles appear to have a much more complex morphology, including deep absorptions. These line profiles provide an opportunity to probe the structure of the protostar at different spatial scales since the different CN emission or absorption components are expected to originate in different parts of the envelope. On the fly maps made with IRAM of the $J = 1 - 0$ and $J = 2 - 1$ transitions revealed the extended emission of CN in the envelope. Moreover, the velocity field of these transitions shows a velocity gradient in the NE-SW direction, associated with the rotation of the envelope. We have used an LTE model in CASSIS and defined a separate model for each transition. An extended emission larger than the envelope of IRAS 16293-2422 as defined by Crimier et al. (2010) is needed to correctly model the line profiles. Indeed, to correctly reproduce the observed absorption, it is necessary to assume that the cold envelope extends as far as $75''$ from the peak of emission. A chemical modelling with the gas-grain code Nautilus allow us to compute the abundance profile of CN and we verified that the abundance found in our LTE model is consistent with the observations. In addition, we derived the ratio for the CN isotopologues analysing the ^{13}CN and C^{15}N lines. We found a ratio of ^{12}C/^{13}C$\sim$ 55, which is similar to the value found in the interstellar medium, but different from that derived for IRAS 16293-2422B in the literature ($\sim$ 30). This might give us a clue on the different conditions where ^{13}C depletes compared with ^{12}C. On the other hand, the ratio ^{14}N/^{15}N$\sim$ 315 is similar to the standard values in the solar neighboorood.

Probing the structure of the low-mass solar type protostar IRAS 16293–2422 from the emission and absorption of cyanide (CN)

Antonio Hernández-Gómez,[1,2]⋆ Emmanuel Caux[2], Laurent Loinard[1,3],
Sandrine Bottinelli[2], and Karl M. Menten[4]

[1]*Instituto de Radioastronomía y Astrofísica, Universidad Nacional Autónoma de México, Morelia 58089, Mexico*
[2]*IRAP, Université de Toulouse, CNRS, UPS, CNES, Toulouse, France*
[3]*Instituto de Astronomía, Universidad Nacional Autónoma de México, Apartado Postal 70-264, CdMx C.P. 04510, Mexico*
[4]*Max-Planck-Institut für Radioastronomie, Auf dem Hügel 69, D-53121 Bonn, Germany*

ABSTRACT
Cyanide (CN), one of the simplest nitrogen-bearing molecules detected in space, is known to be a good tracer of the kinematic and chemical properties of the interstellar medium (ISM) over a wide range of physical conditions. In this work, we present a study of the properties of CN associated with the low-mass protostar IRAS 16293–2422. Observations with the IRAM and APEX single-dish telescopes, and the HIFI instrument onboard the Herschel Space Observatory revealed the presence of complex CN line profiles in the spectrum showing both emission and absorption features. We present molecular maps of the CN $J = 1 - 0$ and $J = 2 - 1$ transitions observed with the IRAM telescope that exhibit an extended structure associated with the object's envelope, and show a clear velocity gradient in the E-W direction, indicating that the envelope is slowly rotating. Because CN rotational transitions at different energies probe material at different spatial scales, we use a radiative transfer model in Local Thermodynamical Equilibrium (LTE) considering that IRAS 16293–2422 is formed by a warm and compact region associated with the hot corino, and a large envelope. The presence of a more extended and colder component is also needed to reproduce the line profiles. This model can satisfactorily reproduce the morphology of the line profiles and allows us to estimate the CN abundance for each region. We use the Nautilus gas-grain chemical code to compute the radial abundance profile and found it to be in full agreement with the values produced by our LTE model. Finally, we derive isotopic abundance ratios for the envelope around IRAS 16293–2422 of $^{14}N/^{15}N \sim 315$ and $^{12}C/^{13}C$ of ~ 55.

Key words: astrochemistry – radiative transfer – stars: individual (IRAS 16293–2422)

1 INTRODUCTION

Nitrogen, the sixth most abundant element in the Universe, has been found to be present in a large number of molecules detected in the interstellar medium (ISM). Understanding the chemistry of these molecules is particularly relevant since some of them are used to determine chemical, kinematic and dynamic properties of star-forming environments over a broad range of conditions (e.g. Hartquist & Dalgarno 1996; Le Gal et al. 2014). One of the simplest nitrogen-bearing

molecules is cyanide (CN). This molecule, together with nitrogen monoxide (NO), plays a key role in the formation of molecular nitrogen, which is at the heart of the formation of nitrogen hydrides such as NH_3. CN also presents Zeeman hyperfine splitting under the presence of a magnetic field and therefore it can be used as a diagnostic of magnetic activity in dense regions (Crutcher 2012).

⋆ E-mail: a.hernandez@irya.unam.mx

It is thought that the chemistry of molecular nitrogen in the gas phase at low temperatures (~ 10 K) begins with the chemical reactions:

$$N + CH \rightarrow CN + H, \tag{1}$$
$$N + CN \rightarrow N_2 + C. \tag{2}$$

Also, CN can be formed from the destruction of NO:

$$C + NO \rightarrow CN + O, \tag{3}$$

while the chemical reaction

$$CN + O \rightarrow CO + N, \tag{4}$$

can destroy CN. Thus, the C/O ratio will be directly related to the abundance of both CN and NO.

The analysis of the rotational transitions of CN provides a useful tool to derive physical and chemical properties in astrophysical environments. In particular, it can constrain the structure of young stellar objects (YSOs) because transitions at different energies probe regions at different temperatures –and, therefore, associated with different components within the YSO. In the present paper, we will perform such an analysis for the low-mass protostar IRAS 16293–2422, located in the Ophiuchus star-forming complex within the Lynds 1689 N dark cloud. Its distance has recently been revised to 141^{+30}_{-21} pc by Dzib et al. (2018) from the parallax measurement of water maser emission associated with one of its outflows. This protostar is a proto-binary system (Wootten 1989; Mundy et al. 1992) composed of two condensations called A and B, surrounded by an extended envelope with a mass of about 2 $M_{\odot}$ (Crimier et al. 2010). A and B are surrounded by a warm and dense archetypical hot corino (Ceccarelli 2004), a region giving rise to emission from numerous complex organic molecules.

The chemistry of IRAS 16293–2422 has been extensively studied. Three recent molecular surveys have revealed a plethora of the species identified towards this source. One of them is the CHESS spectral survey (Chemical Herschel Surveys of Star-forming regions, Ceccarelli et al. 2010), a guaranteed-time key program of the Herschel Space Observatory performed in the frequency range 480 –1790 GHz with a high spectral resolution (0.2–0.6 km s^{-1}). Another one is TIMASSS (The IRAS 16293–2422 Millimeter And Submillimeter Spectral Survey, Caux et al. 2011) which was obtained with the IRAM-30m telescope (near Pico Veleta, Spain) between 80 and 280 GHz and the James Clerk Maxwell Telescope (JCMT, Mauna Kea, Hawaii) between 328 and 366 GHz, at low spectral resolution (1 km s^{-1}). Finally, PILS (The ALMA Protostellar Interferometric Line Survey, Jørgensen et al. 2016), the most recent molecular survey towards this source, revealed over 10,000 transitions from many species in the frequency range of 329 – 363 GHz. These molecular surveys have revealed the presence of a large number of nitrogen-bearing molecules. In particular, a number of CN transitions with different excitation temperatures have been detected in these surveys.

In this work, we have extracted the observed CN line profiles from the CHESS survey, and obtained additional recent observations with the IRAM and APEX telescopes to model them with a radiative transfer model in LTE. In Section 2, we describe in detail all the observations. In Section 3, we present our physical model for IRAS 16293–2422 and the results of our LTE radiative transfer modelling. In Section 4, we compute the CN radial abundance profile with the chemical code Nautilus and compare it with our model. Finally, in Section 5 we summarize our results.

2 OBSERVATIONS

The data used in this paper resulted from observations with with the IRAM-30m and APEX-12m single-dish ground-based telescopes. We have also included observations with the HIFI instrument (de Graauw et al. 2010) onboard the Herschel Space Observatory. The details are described in this section.

2.1 IRAM-30m observations

Pointed observations of the ^{12}CN $J = 1 - 0$ (~ 113 GHz) and $J = 2 - 1$ (~ 226 GHz) transitions were carried out with the IRAM-30m telescope on 15–16 June 2017 using the broad-band Eight Mixer Receiver (EMIR) connected to a Fast Fourier Transform Spectrometer (FTS) in its narrow mode, providing a channel spacing of 50 kHz. This corresponds to a velocity resolution of about 0.132 and 0.066 km s^{-1} at 113 and 226 GHz respectively. The pointing direction was $\alpha_{2000} = 16^{\rm h}$ $32^{\rm m}$ $22\overset{s}{.}56$, $\delta_{2000} = -24° 28'31''\!.8$ with a total observing time of about 5 hours. The sky emission was cancelled using the wobbler with a throw of 150''. The rms noise level was about 60 and 100 mK at 113 and 226 GHz, respectively.

Additionally, on-the-fly (OTF) maps of the ^{12}CN $J = 1 - 0$ and $J = 2 - 1$ transitions were obtained between 1 and 6 November 2017. As for the pointed observations, EMIR modules E090 and E230 were simultaneously used and connected to the FTS backend in its narrow mode. 90'' × 90'' maps (both with horizontal and vertical scanning directions) were acquired with a map centre approximately between A and B sources, at $\alpha_{2000} = 16^{\rm h}$ $32^{\rm m}22\overset{s}{.}75$, $\delta_{2000} = -24°28'34''\!.2$. A step size of 4''.35 was chosen to fulfill the Nyquist sampling criteria at 226 GHz. Each map contains 22 rows of 25 seconds each, yielding a scanning speed of 3''.6/s (well below the maximum of 5''.4/s). The reference ("off") position, 240'' away from the map centre, was regularly observed (every ~100 s). The total observing time was about 5.6 hours with good weather conditions (opacity at 226 GHz of ~0.1–0.2 or precipitable water vapour of ~1–3 mm), yielding rms noise levels of about 90 mK and 150 mK at 113 and 226 GHz respectively.

2.2 APEX observations

Pointed observations of the ^{12}CN $J = 3 - 2$ and $J = 4 - 3$ transitions were made with the APEX telescope (Chajnantor plateau, Chile) during August 2013 under very good weather conditions. These were made with a modified version of the First Light Apex Submillimeter Heterodyne receiver (FLASH; Heyminck et al. 2006). The spectral resolution provided by the backends was 38.14 kHz, corresponding to a velocity resolution of about 0.03 km s^{-1} at a frequencies

(340 GHz and 453 GHz) of the transitions. The pointing direction was $\alpha_{2000} = 16^{\mathrm{h}}32^{\mathrm{m}}22\overset{s}{.}9$, $\delta_{2000} = -24°28'35''6$. The rms noise achieved was typically 10 mK per 0.6 km s^{-1} velocity channel.

For both IRAM and APEX observations we performed the data reduction and calibration with the GILDAS/CLASS[1] package. The line intensities are given in terms of main beam brightness temperature units (T_{mb}). These intensities were corrected for atmospheric attenuation, rear-ward losses and main beam efficiency. The telescopes and receiver parameters such as the main beam efficiency (B_{eff}), forward efficiency (F_{eff}) and half power beam width (HPBW) where taken from the IRAM[2] and APEX[3] webpages.

2.3 HIFI observations

The CN $J = 5-4$ transition was observed with HIFI/Herschel as part of the CHESS molecular survey mentioned in Section 1. The data used in this paper are part of a full spectral coverage of band 1b (560 – 640 GHz; obsid:1342191559), which was performed on 2 March 2010, using the HIFI Spectral Scan Double Beam Switch (DBS) observing mode with optimization of retrieving the continuum level. In this mode, the HIFI acousto-optic Wide Band Spectrometer (WBS) was used, providing a spectral resolution of 1.1 MHz ($\sim$ 0.6 km s^{-1} at 566 GHz) over an instantaneous bandwidth of 4×1 GHz (Roelfsema et al. 2012). The observed coordinates were $\alpha_{2000} = 16^{\mathrm{h}}32^{\mathrm{m}}22\overset{s}{.}64$, $\delta_{2000} = -24°28'33''6$. The DBS reference positions were situated approximately 3' east and west of the source.

In order to cover the required frequency bands to perform the spectral survey, multiple local oscillator tunings were used. For each tuning spectrum consists of eight separate spectra: one per polarization (horizontal and vertical) in 4 sub-bands of $\sim$1 GHz each. Each band was examined using the HIPE (Ott 2010) "flagTool" task to remove spurs that were not automatically removed by the pipeline. The HIPE tasks "fitHifiFringe" and "fitBaseline" were also used to remove the standing waves and baselines for each sub-band, while the task "doDeconvolution" was used to perform the sideband deconvolution. The deconvolved spectra observed in both polarizations were of similar quality, and averaged to lower the noise in the final spectra. The continuum values obtained from running fitBaseline are well fitted by polynomials of order 3 over the frequency range of the whole sub-bands and were added to the spectra at the appropiate frequencies. The intensities were converted from antenna to main-beam temperature scale using a forward efficiency of 0.96 and the (frequency-dependent) beam-efficiency given in Table 1 of Roelfsema et al. (2012).

3 RESULTS

3.1 The extended emission

The compact sources (A and B) in IRAS 16293–2422 are embedded in an extended envelope. Several studies have revealed the presence of a variety of molecular species in this envelope (e.g. Hily-Blant et al. 2010; Coutens et al. 2012; Bottinelli et al. 2014). A previous study by Menten et al. (1987) revealed extended molecular emission around IRAS 16293–2422 from CS maps ($J = 2-1$ and $J = 3-2$) over a region of 90''×90''. They found that the gas traced by this emission followed a modified Keplerian motion around the protostar. Crimier et al. (2010) modelled the density and temperature profiles for the envelope from 22 to 6000 AU (assuming a distance of 120 pc) and found that the density can be described with a Shu-like density profile. Recently, Jacobsen et al. (2018) modelled the 3D structure of the envelope up to $\sim$8000 AU with a dust and gas model from ALMA observations.

To investigate how CN is distributed in the envelope of IRAS 16293–2422, we use the OTF maps of the $J = 1-0$ and $J = 2-1$ transitions obtained with the IRAM-30m telescope and described in Section 2. In Figure 1, we show the CN emission map of the $J = 2-1$ transition at 226.659 GHz. There is emission in all pixels of the mapped area (as shown in the spectra map of Figure 2). Figure 1 has been clipped to show only the central brighter part of the envelope, but there is a more extended component (more extended indeed than the mapped area). The emission seen in Figure 1 does not appear to be completely spherical, unlike what has been found for the dust emission from submillimeter continuum observations (e.g. Correia et al. 2004; Siringo et al. 2009). A Gaussian fit with the CASA software yields a deconvolved size of $(59.0 \pm 3.8) \times (49.4 \pm 3.2)''$.

To examine the kinematics of this extended component, we have computed in CASA the moment 1 map for the $J = 1-0$ and $J = 2-1$ CN transitions which reveals the velocity field. In Figure 3 we show the moment 1 map for the $J = 1-0$ transition at 113.489 GHz. We find that the north-eastern (NE) part of the envelope shows a velocity peak of 3.6 km s^{-1} corresponding to blue-shifted emission, while in the southwest (SW) part of the envelope, the peak is 4.3 km s^{-1}, corresponding to red-shifted emission. Toward the centre of the extended structure, the measured velocity corresponds to a mean value of 3.9 km s^{-1}. We interpret this velocity pattern as rotation of the envelope in the NE-SW direction, with a rotation axis aligned about –45° east of north.

3.2 CN line profiles

We now proceed to the analysis of the pointed CN spectra (corresponding to the $J = 1-0$, $J = 2-1$, $J = 3-2$, $J = 4-3$, and $J = 5-4$ transitions) obtained toward the center of IRAS 16293–2422. For this analysis, we have used the software CASSIS[4] (Centre d'Analyse Scientifique de Spectres Instrumentaux et Synthétiques, Caux et al. 2011). We report the relevant parameters for these transitions in Appendix A. We have found a total of 9 hyperfine transitions in the IRAM data, 40 in the APEX data, and 12 in the

---

[1] http://www.iram.fr/IRAMFR/GILDAS/
[2] http://www.iram-institute.org/
[3] http://www.apex-telescope.org/telescope/
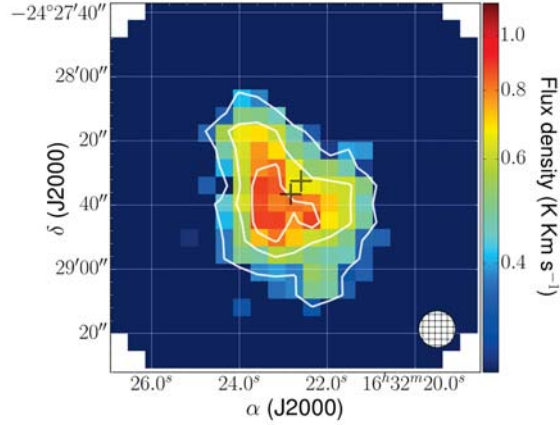
[4] http://cassis.irap.omp.eu

Figure 1. Moment 0 (integrated intensity) map of the $J = 2 - 1$ CN transition at 226.659 GHz. The white contours correspond to the emission of the same transition in steps of 0.2 K km s^{-1}. The beam is shown at the bottom right of the figure. The crosses indicate the positions of sources A and B; the pointing direction of the pointed observations coincides with the position of source B to better than a fraction of an arcsecond.
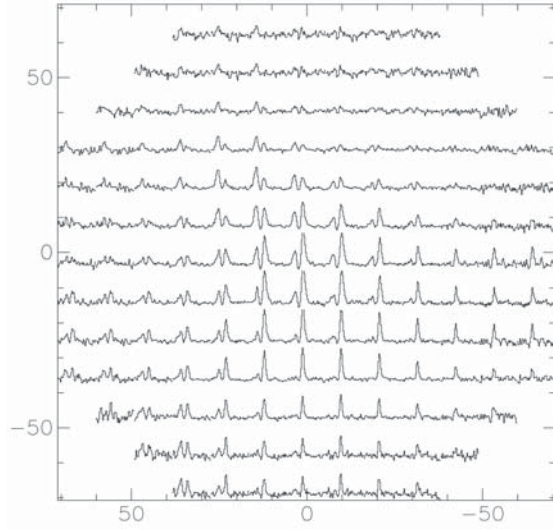

Figure 2. Map of the spectra in the same region as shown in Figure 1. The axis indicate the offset from the center of the map in arcseconds.

HIFI data. Since some of the hyperfine transitions are very close in frequency, many line profiles present blending. When imaged, the lines present a complex morphology with deep absorption features making the analysis of each individual transition complex.

3.3   Radiative transfer modelling

Several radiative transfer models (both LTE and non-LTE) have been implemented to explain and reproduce the properties of the observed line profiles toward IRAS 16293–2422 for molecules such as CH (Bottinelli et al. 2014), HDO (Coutens et al. 2012), HCO$^+$ (Quénard et al. 2018) and
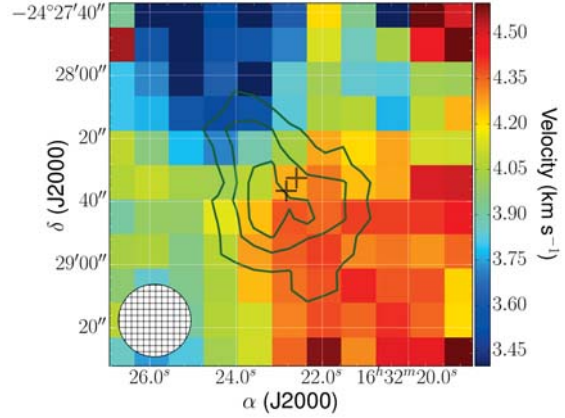

Figure 3. Moment 1 (velocity field) map of the $J = 1 - 0$ CN transition at 113.489 GHz. The green contours are the same as the white ones in Figure 1. A velocity gradient in NE-SW direction associated with the rotation of the envelope is seen. The beam is shown at the bottom left of the map. The black crosses indicate the position of A and B sources.

Table 1. Derived CN column densities and abundances.

Component	N(CN) (cm^{-2})	Size (″)	Abundance
Hot corino	$(2.5) \times 10^{14}$	2.0	$(2.2) \times 10^{-10}$
Envelope	$(2.2) \times 10^{14}$	50.0	$(1.7) \times 10^{-9}$
Extended emission	$(5.0) \times 10^{14}$	150.0	$(1.7) \times 10^{-8}$

Table 2. Computed physical parameters per transition.

CN transition	Component	T_{ex} (K)	FWHM (km s^{-1})	v_{LSR} (km s^{-1})
$1 - 0$	Envelope	5.5	1.3	3.95
	Extended emission	2.73	0.35	3.85
	Hot corino	200	5.0	3.6
$2 - 1$	Envelope	6.0	1.35	3.95
	Extended emission	3.0	0.4	3.85
	Hot corino	200	5.0	3.6
$3 - 2$	Envelope	8.0	1.6	3.95
	Extended emission	3.8	0.45	3.95
	Hot corino	200	5.0	3.6
$4 - 3$	Envelope	9.5	2.0	3.95
	Extended emission	6.0	0.45	3.95
	Hot corino	200	5.0	3.6
$5 - 4$	Envelope	9.5	2.0	3.95
	Extended emission	6.0	0.45	3.95
	Hot corino	200	5.0	3.6

HNCO (Hernández-Gómez et al. 2018). The presence of an external layer has been proposed to explain the absorptions observed at velocities between 3.8 and 4.2 km s^{-1} for these molecules.

Since we detect several transitions of CN over a wide range of energies, we could have used the rotational diagram method which takes into account the integrated intensities of the lines to compute the column density and rotational
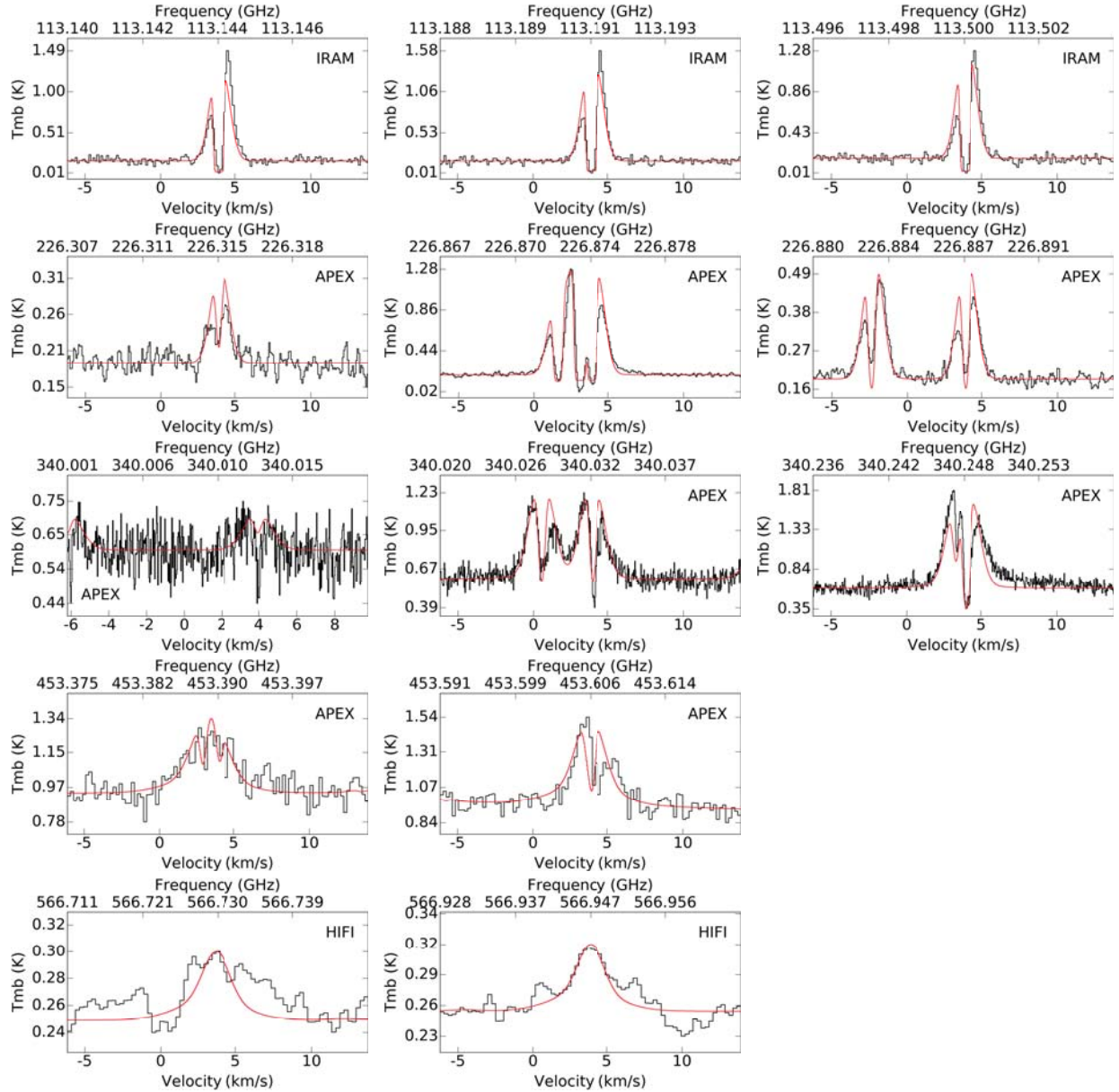
Figure 4. Observed CN line profiles (black) as seen by different telescopes, overlaid with the predicted profiles from our model (red) with the parameters reported in Table 2. Each row contains a set of modelled profiles starting from $J = 1 - 0$ to $J = 5 - 4$ transitions (from top to bottom).

temperature of the molecule. However, in most cases, the CN line profiles are very complex due to the absorption features they present. Moreover, the hyperfine line blending is severe in many cases, making a rotational diagram analysis far too complicated. As a consequence, we turned to an LTE radiative transfer analysis with CASSIS, which is more suitable in our case.

The CASSIS software allows us to define a set of physical components by constraining the following five parameters for each one: angular size of the region, column density, kinetic temperature, the Full Width at Half Maximum (FWHM) of the lines and their velocity in the Local Stan-

dard of Rest (LSR). Once these components are defined, we can solve the radiative transfer equation and produce a synthetic spectrum assuming LTE conditions.

For the physical model of IRAS 16293–2422, we have considered three physical components:

1. A compact and warm component associated with the hot corino present in IRAS 16293–2422. Because interferometric observations have shown that either source A and/or B could dominate the emission for a certain molecule, we have assumed a single source containing A and B with an angular size of 2″. This component is necessary to reproduce

the profiles of CN lines arising from higher energy levels observed with APEX and HIFI ($J = 4 − 3$ and $J = 5 − 4$).

2. A cooler component associated with the $\sim 50''$ envelope seen in Figure 1. This component dominates the emission of the $J = 3 − 2$, $J = 2 − 1$ transitions in APEX.

3. A more extended and colder component corresponding to the extended emission described in Section 3.1. This component is necessary to reproduce the observed emission profiles for the lowest transition ($J = 1 − 0$), but also to produce the absorption profiles.

For the model, we have 5 parameters for each of the three physical components, so a total of 15 free parameters. To model the line profiles, we have used the Monte Carlo Markov Chain (MCMC) method inside CASSIS (Hastings 1970; Guan et al. 2006). This allows us to run a set of models considering all three physical components and their respective parameters to find the best set of values that reproduces the observed line profiles by means of χ^2 minimization.

Because the continuum level is crucial to have the right absorption level in the spectra, we need to compute it and add it to the IRAM data since the continuum was removed during the data reduction. To do so, we have obtained continuum observations with these instruments: HIFI, PACS, SPIRE (Herschel Space Observatory), MIPS, IRS (Spitzer), MAMBO2, NIKA2 (IRAM), SCUBA (JCMT) and LABOCA (APEX). The observations from all the instruments cover a frequency range from ~ 300 GHz to ~ 0.35 THz (~ 1 mm to $\sim 850 \ \mu m$). For each data set, the integrated flux of the source was measured. Then, the spectral energy distribution (SED) was built from these observations and it was fitted to compute the continuum level expected at every given frequency. We have compared the expected continuum value with that obtained from APEX and HIFI observations and noted that our predicted continuum is in good agreement with the observations within an error of 15%. Hence, to be consistent regarding the continuum level we have in our data, we subtracted the continuum from all observations and added back the continuum level predicted by our SED fitting. Details on the comprehensive continuum data set will be discussed in a separate paper (S. Bottinelli et al. in prep.)

We must note that an attempt to model all ^{12}CN rotational transitions at the same time with a χ^2 minimization is not the best strategy. Indeed, it is expected that both the linewidths (FWHM) and the V_{LSR} increase with the E_{up} of the transitions as higher energy lines probe material deeper in the envelope, where the velocity dispersion increases (gas falling and/or rotating faster toward the center) and the V_{LSR} is redshifted for the same reason. As a consequence, we model separately each transition.

Before proceeding with the χ^2 minimization, we have fixed some values in order to reduce the number of free parameters. First, for the hot corino we have assumed an excitation temperature of 200 K (which is a typical value for hot corinos) and an angular size of $2''$ because we cannot disentangle if either source A or B dominates the emission. The FWHM for this component is set to 5 km s^{-1} since the observations at HIFI frequencies associated with this component help us constrain this value. Also, a Gaussian fit to these HIFI lines gives us a value for the V_{LSR} of 3.6 km s^{-1}, which is also fixed. For the warm envelope and the cold ex-

tended component, we have adopted sizes of $50''$ and $150''$. This assumption is not completely correct since the size of the region changes with J (i.e. with frequency) as stated before. However, we fixed those values since we have no observational constraints on them. After fixing these values, we are left with the following free parameters: the column density for all three components, the FWHM of the two extended components and their excitation temperature. This amounts to a total of 9 free parameters. We have also taken into account the corresponding beam dilution for each telescope according to the size of each physical component. We then ran a set of 1,000 models to find the best solution.

Table 1 shows the column densities and abundances derived from the modelling while Table 2 shows the T_{ex}, FWHM and V_{LSR} values derived from the modelling for each transition separately. Figure 4 presents some of the CN observed and modelled lines (see the rest of the observed and modelled line profiles in the Appendix B).

As we can see, the observed complex line emission/absorption are very well reproduced by our radiative transfer model in LTE. We see that the excitation temperature for the $J = 1 − 0$ transition in the most extended component is equal to that of the cosmic background. We have seen that this excitation temperature is absolutely needed in our model to produce the deepest absorptions at the right level.

3.4 Determination of the ^{12}C/^{13}C and ^{14}N/^{15}N ratios

In addition to cyanide transitions from the molecule main isotopic form, we have found three ^{13}CN and three C^{15}N transitions in the 3 mm IRAM pointed observations (see Section 2). The main parameters for these transitions are shown in Table 3. To compute the ^{12}C/^{13}C ratio, we have used our radiative model with three physical components as a template to reproduce the ^{13}CN lines and determine their column density. The hot corino component is not contributing at all in the emission of these 1-0 transitions, and therefore it is not used in this model for ^{13}CN. First, we note that the v_{LSR} of ^{13}CN for both the envelope and the extended components are different from those determined for ^{12}CN in our model (~ 0.1 and ~ 0.25 km s^{-1} smaller, for the envelope and the extended component, respectively, see Table 4). Second, the linewidth of the envelope component is narrower (~ 0.4 km s^{-1} smaller) than that found with our ^{12}CN model. We argue that these differences might arise from the fact that the ^{13}CN lines are not coming from the same material as the ^{12}CN lines. Indeed, when looking at the ^{13}CN OTF maps, we observe that the bulk of the emission is arising from a region smaller ($\sim 35''$ vs. $50''$), and displaced from the ^{12}CN peak (Figure 5). We note, in particular, that the pointed observations were not performed towards the peak of the ^{13}CN emission.

The data are not sufficient to constrain separately the ^{13}CN column densities in the envelope and the extended component. Thus, we assumed an identical ^{12}C/^{13}C ratio in both. The absorption created by the extended component is highly dependent on the excitation temperature, and we need a value about 0.12 K larger to explain the ^{13}CN absorption than the ^{12}CN absorption. The derived ^{13}CN column density for the envelope implies an isotopic ratio ^{12}C/^{13}C
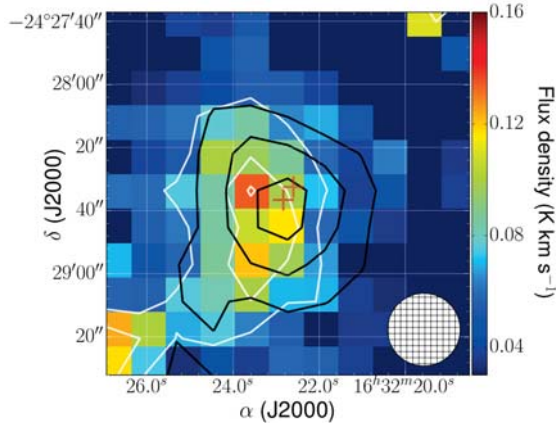
Figure 5. Moment 0 (integrated intensity) map of the $J = 1 - 0$ transition of ^{13}CN at 108.780 GHz. The white contours correspond to the emission of the same transition in steps of 0.03 K km s^{-1}, while the black contours correspond to the emission of the ^{12}CN $J = 1 - 0$ transition at 113.144 GHz in steps of 0.2 K km s^{-1}. The beam is shown at the bottom right of the figure. The red crosses indicate the position of A and B sources.

Table 3. CN isotopologues transitions.

Transition	Frequency (MHz)	E_u (K)	A_{ij} (s^{-1})
^{13}CN $(1_{1.523} - 0_{0.512})$	108780.201	5.25	1.05×10^{-5}
^{13}CN $(1_{1.522} - 0_{0.511})$	108782.374	5.25	7.75×10^{-6}
^{13}CN $(1_{1.521} - 0_{0.510})$	108786.982	5.25	5.72×10^{-6}
C^{15}N $(1_{0.51} - 0_{0.51})$	109689.610	5.27	7.10×10^{-6}
C^{15}N $(1_{1.51} - 0_{0.50})$	110023.540	5.28	7.16×10^{-6}
C^{15}N $(1_{1.52} - 0_{0.51})$	110024.590	5.28	1.09×10^{-5}

~ 55. This value is slightly smaller that the standard value for the local ISM of ~ 70 (e.g. Wilson & Rood 1994; Milam et al. 2005). Interestingly, this value is almost twice higher that the value of ~ 30 found by Jørgensen et al. (2016) for IRAS 16293–2422B.

The C^{15}N lines are too faint to accurately determine the v_{LSR}, FWHM and T$_{ex}$ of both components. We, therefore, used the values of these parameters determined with the ^{13}CN lines and just adjusted the C^{15}N column densities for both components, whose values are reported in Table 4. The obtained ^{14}N/^{15}N ratio is ~ 315, in agreement with that of the ISM (~ 370; Wilson & Rood 1994). Both ^{13}CN and C^{15}N transitions observed and modelled are presented in Figure 6.

4 DISCUSSION

4.1 CN abundance profile

From the column densities derived above, we can compute the CN abundance relative to H$_2$ for each of the physical components. To derive the necessary H$_2$ column densities, we have used the density profile derived by Crimier et al. (2010), and integrated the column densities separately in each region. For the extended cold component, which ex-

tends further than modelled by Crimier et al. (2010), we considered two limiting cases. In the first one, we assumed that the volume density stayed constant outside of the outer radius (6,000 AU) considered in the model. In the other, we extrapolated the density profile of Crimier et al. (2010) to larger radii. Given that the column densities are dominated by the denser (innermost) material, the difference between the two cases is only appreciable when considering the extended emission, and even then the difference is less than a factor of 2. The resulting abundances are given in Table 1; and shown graphically in Figure 7. Note that the error bars on the derived abundance for the extended emission do include the effect of considering different extrapolations to the model of Crimier et al. (2010) to compute the H$_2$ column densities.

To compare the derived abundances to theoretical estimates, we have used Nautilus, a three phase gas-grain chemical code. Nautilus allows us to compute the time evolution of the chemical composition a source of a given structure starting with a set of initial conditions. The details of the chemical reactions included in Nautilus are explained in Ruaud et al. (2016). The gas phase network used in Nautilus is based on kida.uva.2014 and can be found in Wakelam et al. (2015), while the grain chemistry is presented in Ruaud et al. (2015).

The chemical model is performed in two phases as follows. First, the birth of a protostar begins with the formation and evolution of a giant molecular cloud where it is born. To define this parental cloud in Nautilus, we have considered physical parameters that are typical of the Solar neighborhood. These values are: density $n = 3 \times 10^4$ cm^{-3}, temperature T = 10 K, C/O ratio = 0.7, gas to dust ratio = 100 and grain size = 0.1 μm, UV field G_0 = 1 Habing (1.6×10^{-3} erg cm^{-2} s^{-1}), visual extinction A$_v$ = 4 and cosmic ray ionization rate $\zeta = 8.0 \times 10^{-17}$ s^{-1}. Also, the initial abundances are assumed to be atomic as defined in Hincelin et al. (2011). Once these parameters are set, we let the cloud evolve for $t = 2.5 \times 10^5$ years, the time which is expected for the cloud to reach the pre-stellar phase. The result will be a set of final abundances for all the molecules that were formed in the gas and/or on the surface of the grains. Second, we take the resulting abundances of step 1 and use them as input for the protostellar phase. In this step, we need to define the physical structure of the protostar in order to correctly compute the abundance. Crimier et al. (2010) defined the density and temperature profiles of IRAS 16293–2422 directly from observations. Therefore, we used this structure for our static model.

Note that choosing the right physical parameters for this stage is not easy. In this case, we have run several simulations by changing the value of A$_v$ (from 3 to 30), density (from 3×10^3 to 3×10^5 cm^{-3}), evolution times (from 10^4 to 8×10^5 years), C/O ratio (0.7 and 1.2) and cosmic ray ionization rate (from 10^{-17} to 10^{-16} s^{-1}). We found that the only parameters changing the abundance profiles are the visual extinction A$_v$ and the cosmic ray ionization rate ζ. The abundance profiles that best reproduces the observations are obtained with A$_v$ = 4 and $\zeta = 8.0 \times 10^{-17}$ s^{-1}. Although this value of ζ is higher than the commonly assumed standard value for the Solar neighbourhood (1.3×10^{-17} s^{-1}), the Ophiuchus star-forming region is known to have a high cosmic ionization rate (e.g. Hunter et al. 1994).

Table 4. Best parameters for the physical components from the χ^2 minimization of CN isotopologues.

Component	N(^{13}CN) (cm^{-2})	N(C^{15}N) (cm^{-2})	T$_{ex}$ (K)	FWHM (km s^{-1})	V$_{LSR}$ (km s^{-1})	Size ($''$)
Envelope	$(4.0) \times 10^{12}$	$(7.0) \times 10^{11}$	5.62	0.9	3.85	50.0
Extended component	$(9.1) \times 10^{12}$	$(1.6) \times 10^{12}$	2.85	0.35	3.60	150.0
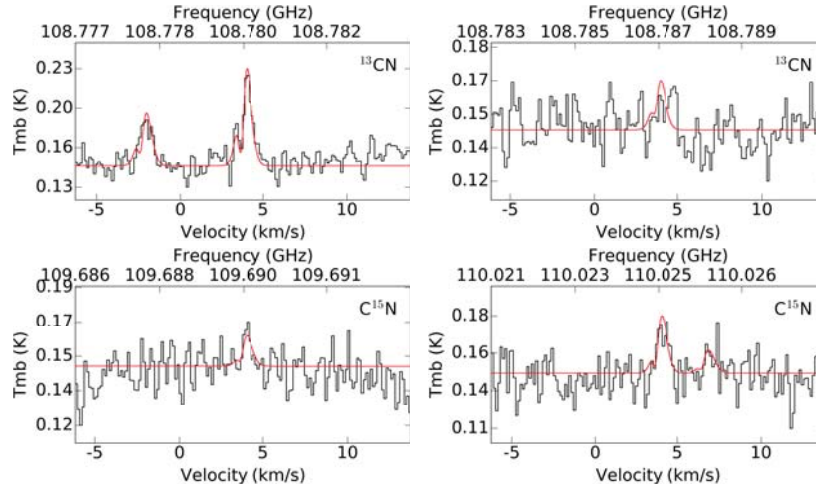
Figure 6. Observed and modelled spectra for the CN isotopologues found in the IRAM data.
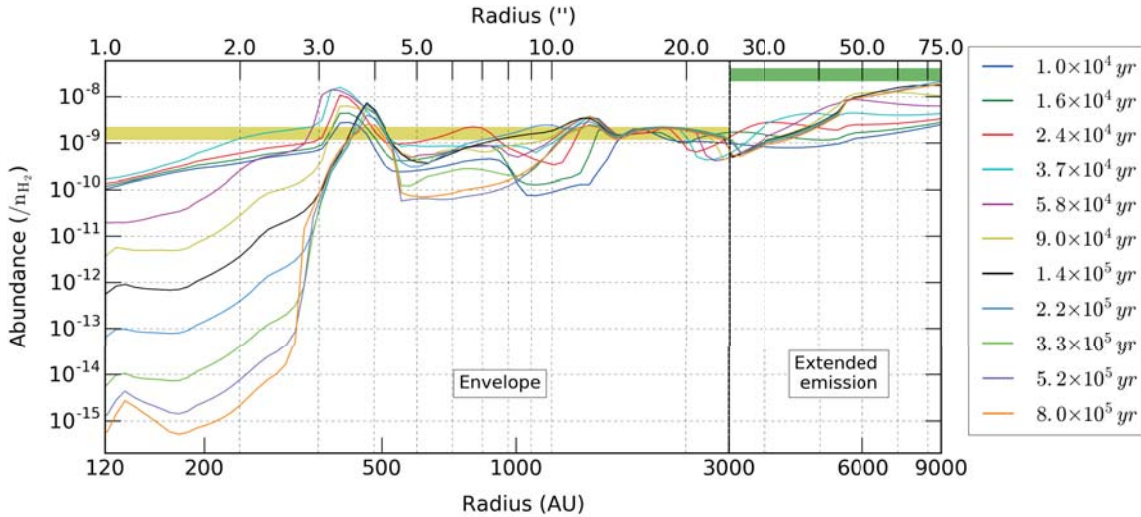
Figure 7. CN abundance profile obtained with the chemical code Nautilus. The color plots indicate different ages of the protostar as indicated in the legend shown on the right. The abundances derived from our data are indicated by the light and the darker green bars in the left and right panel, respectively.

In Figure 7, we show the resulting CN abundance profile with respect to H$_2$ for different ages of the protostar. For the hot corino, the structure derived by Crimier et al. (2010) is not accurate, and therefore we do not compute the abundances at spatial scales below 1$''$. For the envelope and the extended emission, our measured abundances are in good agreement with the model predictions. We note, however, that beyond a radius of about 500 AU, the CN abundances predicted by the model hardly depend on age, so the CN abundances are not a good discriminator between different ages. We note that, from modelling the ratio of ortho-to-para H$_2$D$^+$ observed, Brünken et al. (2014) derive an age of at least one million years for the IRAS 16293-2422 parent cloud.

4.2 Isotopic ratios

Jørgensen et al. (2016) found a fairly anomalous ^{12}C/^{13}C ($\sim$30) in IRAS 16293–2422B. Here we find a value of 55 for the extended envelope, which is more closer to the standard value in the ISM (e.g. Milam et al. 2005). Similarly, we find a standard value of the ^{14}N/^{15}N ratio in the envelope of IRAS 16293–2422. Our results are not unexpected since the physical conditions in the envelope of IRAS 16293–2422 are not extremely different from that of the dense ISM. The conditions in source B (densities in excess of 10^{12} cm^{-3}, temperatures in excess of 1,000 K; (Hernández-Gómez et al. 2018), on the other hand, could be conducive to significant variations in the isotopic ratios. It would be interesting to measure the ^{14}N/^{15}N ratio in IRAS 16293–2422B to see if the anomalous value found for carbon extends to other elements.

5 CONCLUSIONS

We have carried out a study of cyanide (CN) toward the low-mass Solar type protostar IRAS 16293–2422. Since CN is a good probe of the kinematic properties of the gas in dense regions over several scales, we have observed a number of CN transitions with the IRAM-30m and APEX ground-based telescopes at very high spectral resolution and obtained data from the CHESS survey made with the HIFI instrument on-board the Herschel Space Observatory. Maps of the $J = 1-0$ and $J = 2-1$ transitions revealed the extent and the rotation of the emission arising from the envelope. The rotation axis of this extended structure is oriented about –45° east of north.

The CN lines profiles observed toward the central position of IRAS 16293–2422 are complex because both emission and absorption features are present. We propose an LTE radiative transfer model in CASSIS to reproduce these line profiles. Because the excitation temperature and linewidths are expected to be different for different physical components in the system, we have modelled each J rotational transition separately. We have considered that the protostar is formed by three physical components: a warm and compact source associated with the hot corino, a cooler more extended component associated with the warm envelope and a cold and more extended layer. Each of these components is constrained by their column density, temperature, V$_{\text{LSR}}$, size and linewidths. Our model is able to reproduce the complex morphology of the line profiles and allows us to compute the abundance of CN with respect to H$_2$ in each of the components. We used the Nautilus gas-grain chemical code to compute the expected CN radial abundance profile and found that it is in good agreement with our LTE radiative transfer model. We note, however, that although we present a model which can reproduce satisfactorily the complex CN emission and absorption lines profiles, a full 3D radiative transfer model would be necessary to model consistently all lines at the same time, considering a more realistic velocity field and including the rotation effects for the envelope. Finally, we measure the ^{12}CN/^{13}CN and C^{14}N/C^{15}N isotopic ratios, and found them to be in good agreement with those in the standard ISM.

REFERENCES

Bottinelli, S., Wakelam, V., Caux, E., et al. 2014, MNRAS, 441, 1964

Brünken, S., Sipilä, O., Chambers, E. T., et al. 2014, Nature, 516, 219

Caux, E., Kahane, C., Castets, A., et al. 2011, A&A, 532, A23

Caux, E., Bottinelli, S., Vastel, C., & Glorian, J. M. 2011, The Molecular Universe, 280, 120

Correia, J. C., Griffin, M., & Saraceno, P. 2004, A&A, 418, 607

Coutens, A., Vastel, C., Caux, E., et al. 2012, A&A, 539, A132

Ceccarelli, C. 2004, Star Formation in the Interstellar Medium: In Honor of David Hollenbach, 323, 195

Ceccarelli, C., Bacmann, A., Boogert, A., et al. 2010, A&A, 521, L22

Crimier, N., Ceccarelli, C., Maret, S., et al. 2010, A&A, 519, A65

Crutcher, R. M. 2012, ARA&A, 50, 29

de Graauw, T., Helmich, F. P., Phillips, T. G., et al. 2010, A&A, 518, L6

Dzib, S. A., Ortiz-León, G. N., Hernández-Gómez, A., et al. 2018, arXiv:1802.03234

Guan Y., Fleißner R., Joyce P., Krone S. M., 2006, Stat Comput,16, 193

Hastings W. K., 1970, Biometrika, 57, 97

Hartquist, T. W., & Dalgarno, A. 1996, Ap&SS, 237, 267

Heyminck, S., Kasemann, C., Güsten, R., de Lange, G., & Graf, U. U. 2006, A&A, 454, L21

Hily-Blant, P., Maret, S., Bacmann, A., et al. 2010, A&A, 521, L52

Hincelin, U., Wakelam, V., Hersant, F., et al. 2011, A&A, 530, A61

Hunter, S. D., Digel, S. W., de Geus, E. J., & Kanbach, G. 1994, ApJ, 436, 216

Jacobsen, S. K., Jørgensen, J. K., van der Wiel, M. H. D., et al. 2018, A&A, 612, A72

Jørgensen, J. K., van der Wiel, M. H. D., Coutens, A., et al. 2016, A&A, 595, A117

Le Gal, R., Hily-Blant, P., Faure, A., et al. 2014, A&A, 562, A83

Menten, K. M., Serabyn, E., Guesten, R., & Wilson, T. L. 1987, A&A, 177, L57

Milam, S. N., Savage, C., Brewster, M. A., Ziurys, L. M., & Wyck-off, S. 2005, ApJ, 634, 1126

Mundy, L. G., Wootten, A., Wilking, B. A., Blake, G. A., & Sargent, A. I. 1992, ApJ, 385, 306

Ott, S., 2010, Astronomical Data Analysis Software and Systems XIX. Proceedings of a conference held October 4-8, 2009 in Sapporo, Japan. Edited by Yoshihiko Mizumoto, Koh-Ichiro Morita, and Masatoshi Ohishi. ASP Conference Series, Vol. 434, 139

Quénard, D., Bottinelli, S., Caux, E., & Wakelam, V. 2018, MN-RAS, 477, 5312

Roelfsema, P. R., Helmich, F. P., Teyssier, D., et al. 2012, A&A, 537, A17

Ruaud, M., Loison, J. C., Hickson, K. M., et al. 2015, MNRAS, 447, 4004

Ruaud, M., Wakelam, V., & Hersant, F. 2016, MNRAS, 459, 3756

Siringo, G., Kreysa, E., Kovács, A., et al. 2009, A&A, 497, 945

van der Tak, F. F. S., Black, J. H., Schöier, F. L., Jansen, D. J., & van Dishoeck, E. F. 2007, A&A, 468, 627

Wakelam, V., Loison, J.-C., Herbst, E., et al. 2015, ApJS, 217, 20

Wilson, T. L., & Rood, R. 1994, ARA&A, 32, 191

Wootten, A. 1989, ApJ, 337, 858

APPENDIX A: CN TRANSITIONS FOUND IN THE DATA.

In this section we show the main parameters of the CN transitions found in the data.

Table A1. Identified CN lines in the data. Some of the lines are not detected, but we used the corresponding upper limits to model the emission. Columns are rest frequency, transition, upper energy level, E_u/k (k is the Boltzmann constant), Einstein coefficient A, and telescope.

Frequency (MHz)	Transition	E_u/k (K)	A_{ij} (s^{-1})	Telescope
113123.3701	$1_{0\frac{1}{2}\frac{1}{2}} - 0_{0\frac{1}{2}\frac{1}{2}}$	5.43	1.29×10^{-6}	IRAM
113144.1573	$1_{0\frac{1}{2}\frac{1}{2}} - 0_{0\frac{1}{2}\frac{3}{2}}$	5.43	1.05×10^{-5}	IRAM
113170.4915	$1_{0\frac{1}{2}\frac{3}{2}} - 0_{0\frac{1}{2}\frac{1}{2}}$	5.43	5.14×10^{-6}	IRAM
113191.2787	$1_{0\frac{1}{2}\frac{3}{2}} - 0_{0\frac{1}{2}\frac{3}{2}}$	5.43	6.68×10^{-6}	IRAM
113488.1202	$1_{0\frac{3}{2}\frac{3}{2}} - 0_{0\frac{1}{2}\frac{1}{2}}$	5.45	6.74×10^{-6}	IRAM
113490.9702	$1_{0\frac{3}{2}\frac{5}{2}} - 0_{0\frac{1}{2}\frac{3}{2}}$	5.45	1.19×10^{-5}	IRAM
113499.6443	$1_{0\frac{3}{2}\frac{1}{2}} - 0_{0\frac{1}{2}\frac{1}{2}}$	5.45	1.06×10^{-5}	IRAM
113508.9074	$1_{0\frac{3}{2}\frac{3}{2}} - 0_{0\frac{1}{2}\frac{3}{2}}$	5.45	5.19×10^{-6}	IRAM
113520.4315	$1_{0\frac{3}{2}\frac{5}{2}} - 0_{0\frac{1}{2}\frac{3}{2}}$	5.45	1.30×10^{-6}	IRAM
226287.4185	$2_{0\frac{3}{2}\frac{1}{2}} - 1_{0\frac{3}{2}\frac{1}{2}}$	16.31	1.03×10^{-5}	APEX
226298.9427$^{a)}$	$2_{0\frac{3}{2}\frac{1}{2}} - 1_{0\frac{3}{2}\frac{3}{2}}$	16.31	8.23×10^{-6}	APEX
226303.0372$^{a)}$	$2_{0\frac{3}{2}\frac{3}{2}} - 1_{0\frac{3}{2}\frac{1}{2}}$	16.31	4.17×10^{-6}	APEX
226314.5400	$2_{0\frac{3}{2}\frac{3}{2}} - 1_{0\frac{3}{2}\frac{3}{2}}$	16.31	9.90×10^{-6}	APEX
226332.4986$^{b)}$	$2_{0\frac{3}{2}\frac{3}{2}} - 1_{0\frac{3}{2}\frac{5}{2}}$	16.31	4.55×10^{-6}	APEX
226341.9298	$2_{0\frac{3}{2}\frac{5}{2}} - 1_{0\frac{3}{2}\frac{3}{2}}$	16.31	3.16×10^{-6}	APEX
226359.8710	$2_{0\frac{3}{2}\frac{5}{2}} - 1_{0\frac{3}{2}\frac{5}{2}}$	16.31	1.61×10^{-5}	APEX
226616.5714	$2_{0\frac{3}{2}\frac{1}{2}} - 1_{0\frac{1}{2}\frac{3}{2}}$	16.31	1.07×10^{-5}	APEX
226632.1901	$2_{0\frac{3}{2}\frac{3}{2}} - 1_{0\frac{1}{2}\frac{3}{2}}$	16.31	4.26×10^{-5}	APEX
226659.5584	$2_{0\frac{3}{2}\frac{5}{2}} - 1_{0\frac{1}{2}\frac{3}{2}}$	16.31	9.47×10^{-5}	APEX
226663.6928	$2_{0\frac{3}{2}\frac{1}{2}} - 1_{0\frac{1}{2}\frac{1}{2}}$	16.31	8.46×10^{-5}	APEX
226679.3114	$2_{0\frac{3}{2}\frac{3}{2}} - 1_{0\frac{1}{2}\frac{1}{2}}$	16.31	5.27×10^{-5}	APEX
226874.1908	$2_{0\frac{5}{2}\frac{5}{2}} - 1_{0\frac{3}{2}\frac{3}{2}}$	16.34	9.62×10^{-5}	APEX
226874.7813	$2_{0\frac{5}{2}\frac{7}{2}} - 1_{0\frac{3}{2}\frac{5}{2}}$	16.34	1.14×10^{-4}	APEX
226875.8960	$2_{0\frac{5}{2}\frac{3}{2}} - 1_{0\frac{3}{2}\frac{1}{2}}$	16.34	8.59×10^{-5}	APEX
226887.4202	$2_{0\frac{5}{2}\frac{3}{2}} - 1_{0\frac{3}{2}\frac{3}{2}}$	16.34	2.73×10^{-5}	APEX
226892.1280	$2_{0\frac{5}{2}\frac{5}{2}} - 1_{0\frac{3}{2}\frac{5}{2}}$	16.34	1.81×10^{-5}	APEX
226905.3574$^{b)}$	$2_{0\frac{5}{2}\frac{3}{2}} - 1_{0\frac{3}{2}\frac{5}{2}}$	16.34	1.13×10^{-6}	APEX
340008.1263$^{b)}$	$3_{0\frac{5}{2}\frac{5}{2}} - 2_{0\frac{3}{2}\frac{5}{2}}$	32.63	6.20×10^{-5}	APEX
340019.6255$^{b)}$	$3_{0\frac{5}{2}\frac{3}{2}} - 2_{0\frac{3}{2}\frac{3}{2}}$	32.63	9.27×10^{-5}	APEX
340031.5494	$3_{0\frac{5}{2}\frac{7}{2}} - 2_{0\frac{3}{2}\frac{5}{2}}$	32.63	3.84×10^{-4}	APEX
340035.4080$^{*)}$	$3_{0\frac{5}{2}\frac{3}{2}} - 2_{0\frac{3}{2}\frac{1}{2}}$	32.63	2.89×10^{-4}	APEX
340035.4080$^{*)}$	$3_{0\frac{5}{2}\frac{5}{2}} - 2_{0\frac{3}{2}\frac{3}{2}}$	32.63	3.23×10^{-4}	APEX
340247.7700$^{*)}$	$3_{0\frac{7}{2}\frac{7}{2}} - 2_{0\frac{5}{2}\frac{5}{2}}$	32.67	3.80×10^{-4}	APEX
340247.7700$^{*)}$	$3_{0\frac{7}{2}\frac{9}{2}} - 2_{0\frac{5}{2}\frac{7}{2}}$	32.66	4.13×10^{-4}	APEX
340248.5440	$3_{0\frac{7}{2}\frac{5}{2}} - 2_{0\frac{5}{2}\frac{3}{2}}$	32.67	3.67×10^{-4}	APEX
340261.7734	$3_{0\frac{7}{2}\frac{5}{2}} - 2_{0\frac{5}{2}\frac{5}{2}}$	32.67	4.48×10^{-5}	APEX
340264.9490	$3_{0\frac{7}{2}\frac{7}{2}} - 2_{0\frac{5}{2}\frac{7}{2}}$	32.67	3.35×10^{-5}	APEX
340279.1201$^{b)}$	$3_{0\frac{7}{2}\frac{5}{2}} - 2_{0\frac{5}{2}\frac{7}{2}}$	32.67	9.27×10^{-7}	APEX
453368.1883$^{b)}$	$4_{0\frac{7}{2}\frac{7}{2}} - 3_{0\frac{5}{2}\frac{7}{2}}$	54.39	8.02×10^{-5}	APEX
453375.6007$^{b)}$	$4_{0\frac{7}{2}\frac{5}{2}} - 3_{0\frac{5}{2}\frac{5}{2}}$	54.39	1.07×10^{-4}	APEX
453389.9228	$4_{0\frac{7}{2}\frac{9}{2}} - 3_{0\frac{5}{2}\frac{7}{2}}$	54.39	9.77×10^{-4}	APEX
453391.4699	$4_{0\frac{7}{2}\frac{5}{2}} - 3_{0\frac{5}{2}\frac{3}{2}}$	54.39	8.69×10^{-4}	APEX
453391.6114	$4_{0\frac{7}{2}\frac{7}{2}} - 3_{0\frac{5}{2}\frac{5}{2}}$	54.39	8.97×10^{-4}	APEX
453606.5379	$4_{0\frac{9}{2}\frac{9}{2}} - 3_{0\frac{7}{2}\frac{7}{2}}$	54.43	9.65×10^{-4}	APEX
453606.6814	$4_{0\frac{9}{2}\frac{9}{2}} - 3_{0\frac{7}{2}\frac{9}{2}}$	54.43	1.02×10^{-3}	APEX
453607.1348	$4_{0\frac{9}{2}\frac{7}{2}} - 3_{0\frac{7}{2}\frac{5}{2}}$	54.44	9.52×10^{-4}	APEX
453621.3059$^{b)}$	$4_{0\frac{9}{2}\frac{7}{2}} - 3_{0\frac{7}{2}\frac{7}{2}}$	54.44	6.24×10^{-5}	APEX
453623.6292$^{b)}$	$4_{0\frac{9}{2}\frac{9}{2}} - 3_{0\frac{7}{2}\frac{9}{2}}$	54.43	4.99×10^{-5}	APEX
453638.3972$^{b)}$	$4_{0\frac{9}{2}\frac{7}{2}} - 3_{0\frac{7}{2}\frac{9}{2}}$	54.44	7.77×10^{-7}	APEX
566693.0039$^{b)}$	$5_{0\frac{9}{2}\frac{7}{2}} - 4_{0\frac{7}{2}\frac{9}{2}}$	81.59	1.54×10^{-6}	HIFI
566709.1064$^{b)}$	$5_{0\frac{9}{2}\frac{9}{2}} - 4_{0\frac{7}{2}\frac{9}{2}}$	81.59	9.81×10^{-5}	HIFI
566714.7384$^{b)}$	$5_{0\frac{9}{2}\frac{7}{2}} - 4_{0\frac{7}{2}\frac{7}{2}}$	81.59	1.23×10^{-4}	HIFI
566729.9044	$5_{0\frac{9}{2}\frac{11}{2}} - 4_{0\frac{7}{2}\frac{9}{2}}$	81.59	1.98×10^{-3}	HIFI
566730.7492	$5_{0\frac{9}{2}\frac{7}{2}} - 4_{0\frac{7}{2}\frac{5}{2}}$	81.59	1.86×10^{-3}	HIFI
566730.8409	$5_{0\frac{9}{2}\frac{9}{2}} - 4_{0\frac{7}{2}\frac{7}{2}}$	81.59	1.88×10^{-3}	HIFI
566946.8006	$5_{0\frac{11}{2}\frac{11}{2}} - 4_{0\frac{9}{2}\frac{9}{2}}$	81.64	1.96×10^{-3}	HIFI
566946.8933	$5_{0\frac{11}{2}\frac{13}{2}} - 4_{0\frac{9}{2}\frac{11}{2}}$	81.64	2.03×10^{-3}	HIFI
566947.2123	$5_{0\frac{11}{2}\frac{9}{2}} - 4_{0\frac{9}{2}\frac{7}{2}}$	81.64	1.95×10^{-3}	HIFI
566961.9803$^{b)}$	$5_{0\frac{11}{2}\frac{9}{2}} - 4_{0\frac{9}{2}\frac{9}{2}}$	81.64	8.02×10^{-5}	HIFI
566963.7484$^{b)}$	$5_{0\frac{11}{2}\frac{11}{2}} - 4_{0\frac{9}{2}\frac{11}{2}}$	81.64	6.68×10^{-5}	HIFI
566978.9281$^{b)}$	$5_{0\frac{11}{2}\frac{9}{2}} - 4_{0\frac{9}{2}\frac{11}{2}}$	81.64	6.66×10^{-7}	HIFI

Table A1 – *continued*

$^{a)}$ Line blended with SO$_2$ at 226300.0267 MHz.
$^{b)}$ Two transitions at the same frequency.

APPENDIX B: OBSERVED AND MODELLED CN TRANSITIONS

In this section, we show all the CN observed line profiles individually (in black) and the predicted emission/absorption profiles from our model.

This paper has been typeset from a TeX/LaTeX file prepared by the author.
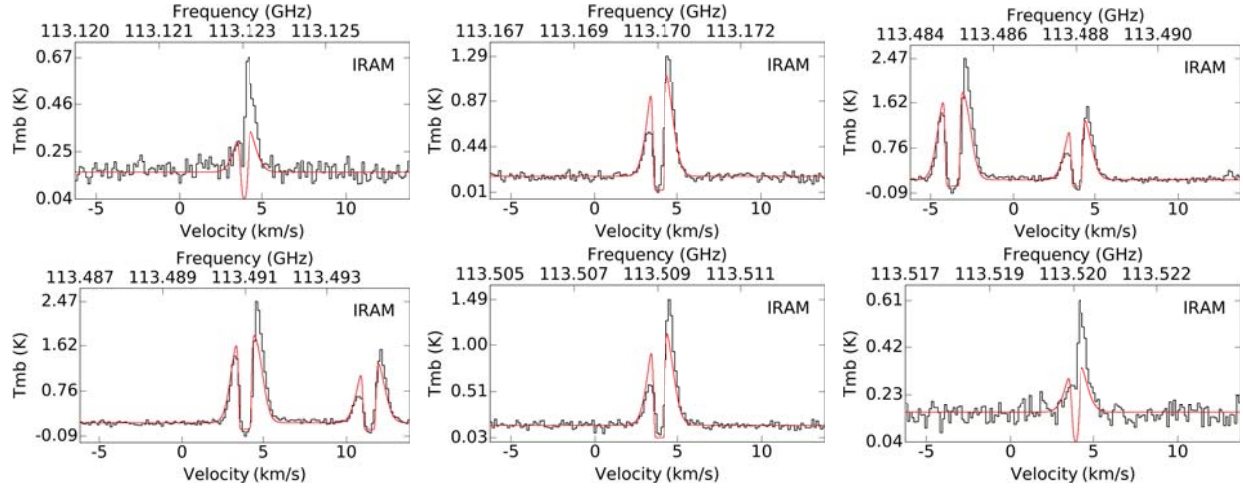
Figure B1. CN 1 − 0 transitions.

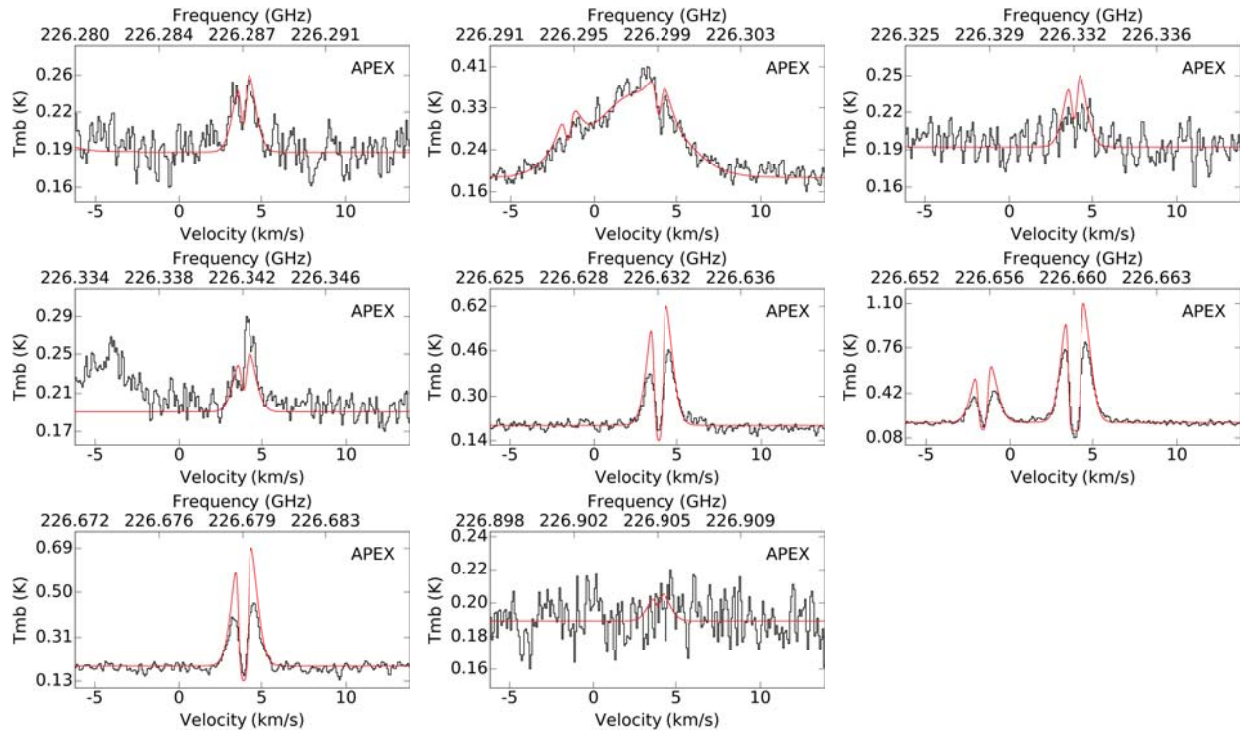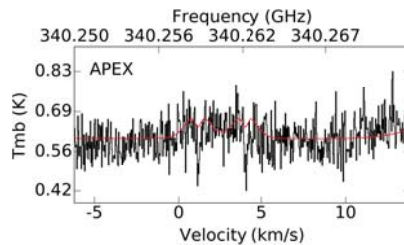Figure B2. CN 2 − 1 transitions.

Figure B3. CN 3 − 2 transitions.

Chapter 7

Conclusions and perspectives

The formation of isolated low-mass stars has been widely studied and nowadays is theoretically well described. However, the details regarding some of the earliest stages of star formation are not yet fully understood. In this work, we contribute to this problem by studying the properties of IRAS 16293-2422, a very well-known solar type low-mass protostar.

A summary of the thesis is as follows:

- The distance to IRAS 16293–2422 was still uncertain from a range of values between 120 to 180 pc. We measured the trigonometric parallax using the water maser emission associated with this protostar. We use VLBA archival observations of the 22.2 GHz water maser line and modelled the displacement on the sky of the maser spots. We derived a trigonometric parallax of 7.1 ± 1.3 mas, which corresponds to a distance of 141^{+30}_{-21} pc. We related the kinematics of the water masers with the outflows and recent ejections from source A in the system. The radial velocities and direction of the relative proper motions of the water masers agrees with the redshifted lobe of the outflow in the A system with a P.A. = 110°.

- New VLA observations of IRAS 16293–2422 from 2 to 41 GHz confirm that source A2 is a protostar driving episodic mass ejections and reveal the complex motion between A2 and A1. These new observations combined with previously published observations from the late 1980s allowed us to follow the proper motions of the individual sources in the system. Unexpectedly, the position angle between A1 and A2 which had been observed to increase steadily during the period from the late 1980s to the early 2000s, is now found to have started to decrease. This might indicate that A1 corresponds to the impact of a precessing jet onto the surrounding material, or that A1/A2 are two members of a tight hierarchical triple system.

- Observations with the VLA and ALMA from 3 to 700 GHz revealed that the spectrum of source B can be described by a single power-law $S_\nu \propto \nu^{2.28}$. This result suggests that the emission is completely dominated by thermal dust. The size of source B appears to increase with frequency up to 41 GHz, while it remains roughly constant at

higher frequencies. This is interpreted as evidence that source B is a dusty source that becomes optically thick at higher frequencies, being entirely optically thick in the millimeter/submillimeter regime. This implies a very high central density. In addition, the brightness temperature measured at the center of the source with the VLA indicates a high central kinetic temperature ($\sim$ 1,000 K).

- The properties of source B based on the VLA and ALMA interferometric observations can be reproduced by a radiative transfer model with GASS-LIME where this source is a dusty spherical source with very high central density (1×10^{13} cm^{-3}), a steep density profile and a central temperature of 1000 K. This model can also reproduce the inverse P cygni profiles from CH_3OH and $H^{13}CN$. Remarkably, the density and temperature profiles mimic those for first hydrostatic cores. The lack of excess of free-free emission indicates that source B does not drive a powerful ionized outflow. All these facts support the idea that B is at a particularly early stage of its evolution.

- Several molecular surveys performed in IRAS 16293–2422 have revealed the presence of a large number of molecular species. Among them isocyanid acid (HNCO) is present in IRAS 16293–2422 as revealed by single-dish observations toward this source with IRAM, APEX, JCMT and HIFI. Recent collisional rate coefficients computed from quantum chemical calculations were recently published. We have used these new collisional coefficients together with the radiative transfer code RADEX to model the HNCO lines profiles. The observed HNCO line profiles are interpreted to arise from the superposition of three physical components along the line of sight: a dense, warm and compact source associated with the hot corino in IRAS 16293-2422, a more extended component representing the warm part of the envelope and a cold and extended component corresponding to the outer layer of the envelope. A chemical modelling with the gas-grain code Nautilus reveals that younger ages for the protostar are in better agreement with our radiative transfer modelling.

- Cyanide (CN) is also present in IRAS 16293-2422, and the observed line profiles from this molecules present a complex morphology since deep absorptions are observed. On the fly maps of the $J = 1 - 0$ and $J = 2 - 1$ transitions reveal the extension of the warm envelope to be about 50″. Moment 1 maps reveal the velocity field of the $J = 2 - 1$ transition and show a clear velocity gradient in the NE-SW direction, associated with the rotation of the envelope. A radiative model for each of the CN transitions in LTE is needed to reproduce the line profiles. The model consists of three physical components as we had for HNCO with a hot corino, an envelope, and a more extended and cold component. The abundances derived from the Nautilus chemical code are in good agreement with the abundances computed by our radiative transfer model. We found that the $^{12}C/^{13}C$ radio is $\sim$ 55. This value is almost twice larger that the ratio found by Jørgensen et al. (2016) in source B.

By combining all the described observations with our radiative transfer and chemical models for the protostar IRAS 16293-2422, we are able to describe in detail not only

the nature of the sources composing the binary system as seen in the continuum, but also the chemistry of the protostar at several spatial scales from the molecular emission/absorption of nitrogen-bearing species, providing a full picture of the structure of this protostar from a multi-frequency point of view.

Future work

To make further progress on the determination of the dynamics, physics and chemistry in IRAS 16293-2422, additional high spatial resolution continuum observations are necessary to constrain the astrometry and orbital motions of the multiple system, the variability of the recent ejecta from source A and changes in the morphology of this source. In addition, high spectral resolution line observations are required to extract detailed information about the structure of the envelope along the line of sight.

From the analysis of line profiles of HNCO and CN in this thesis, we were able to determine how these molecules are distributed in the envelope of IRAS 16293-2422, and place constraints on the structure of the envelope. In order to constrain further the three-dimensional structure of this source, additional observations of other nitrogen-bearing molecules will be needed to extract more information on their spatial distribution and the velocity field at different radii. The advantage of analyzing nitrogen-bearing molecules is that at the same time we can study the chemistry of nitrogen by comparing the abundance predictions from chemical codes such as Nautilus with the ones derived directly from the observations. This would be relevant to understand nitrogen chemistry in low-mass star-formation environments in general. It is worth mentioning that very recent high spatial resolution observations performed with ALMA toward IRAS 16293–2422 have just recently become available to the public. We expect to analyze these observations to constrain better the chemistry at the scale of the individual sources A and B.

We have begun with the study of the properties of other nitrogen-bearing species such as HCN, HNC, NO, NH_3, etc. Since these molecules trace different parts of the envelope, we can use them to constrain the three-dimensional structure of the envelope of IRAS 16293-2422. The analysis of the deuteration of these molecules will helps us constrain how chemical processes proceed during the protostellar phase.

On the other hand, we are interested in characterizing the spectral energy distribution (SED) of the envelope of IRAS 16293-2422. In order to do so, we have observations with the following instruments:

- Herschel Space observatory: HIFI, PACS and SPIRE.
- Spitzer: MIPS and IRS
- IRAM: NIKA-2
- JCMT: SCUBA

– APEX: LABOCA

Given that these instruments cover a frequency range between 80 GHz and 2 THz, we can build the SED of IRAS 16293–2422 accurately. In addition, since we have built the SED for the individual compact sources A and B, we can substract their contribution to have a pure SED associated with the envelope. From this SED we will be able to derive the continuum level over a wide range of frequencies. This is a fundamental ingredient to correctly model the line profiles of molecules that present absorption features. Because in some cases we cannot recover the continuum directly from observations due to particular observing modes in some radiotelescopes, we could add the predicted continuum emission in these observations to proceed with the right analysis and modelling of the observed spectra of IRAS 16293-2422.

Bibliography

F. C. Adams, S. P. Ruden, and F. H. Shu. Eccentric gravitational instabilities in nearly Keplerian disks. ApJ, 347:959–976, December 1989. doi: 10.1086/168187.

F. O. Alves, W. H. T. Vlemmings, J. M. Girart, and J. M. Torrelles. The magnetic field of IRAS 16293-2422 as traced by shock-induced H_2O masers. A&A, 542:A14, June 2012. doi: 10.1051/0004-6361/201118710.

P. André and T. Montmerle. From T Tauri stars to protostars: Circumstellar material and young stellar objects in the rho Ophiuchi cloud. ApJ, 420:837–862, January 1994. doi: 10.1086/173608.

P. André, D. Ward-Thompson, and M. Barsony. Submillimeter continuum observations of Rho Ophiuchi A - The candidate protostar VLA 1623 and prestellar clumps. ApJ, 406: 122–141, March 1993. doi: 10.1086/172425.

H. G. Arce and A. I. Sargent. The Evolution of Outflow-Envelope Interactions in Low-Mass Protostars. ApJ, 646:1070–1085, August 2006. doi: 10.1086/505104.

A. Bacmann, E. Caux, P. Hily-Blant, B. Parise, L. Pagani, S. Bottinelli, S. Maret, C. Vastel, C. Ceccarelli, J. Cernicharo, T. Henning, A. Castets, A. Coutens, E. A. Bergin, G. A. Blake, N. Crimier, K. Demyk, C. Dominik, M. Gerin, P. Hennebelle, C. Kahane, A. Klotz, G. Melnick, P. Schilke, V. Wakelam, A. Walters, A. Baudry, T. Bell, M. Benedettini, A. Boogert, S. Cabrit, P. Caselli, C. Codella, C. Comito, P. Encrenaz, E. Falgarone, A. Fuente, P. F. Goldsmith, F. Helmich, E. Herbst, T. Jacq, M. Kama, W. Langer, B. Lefloch, D. Lis, S. Lord, A. Lorenzani, D. Neufeld, B. Nisini, S. Pacheco, J. Pearson, T. Phillips, M. Salez, P. Saraceno, K. Schuster, X. Tielens, F. F. S. van der Tak, M. H. D. van der Wiel, S. Viti, F. Wyrowski, H. Yorke, A. Faure, A. Benz, O. Coeur-Joly, A. Cros, R. Güsten, and L. Ravera. First detection of ND in the solar-mass protostar IRAS16293-2422. A&A, 521:L42, October 2010. doi: 10.1051/0004-6361/201015102.

S. E. Bisschop, J. K. Jørgensen, T. L. Bourke, S. Bottinelli, and E. F. van Dishoeck. An interferometric study of the low-mass protostar IRAS 16293-2422: small scale organic chemistry. A&A, 488:959–968, September 2008. doi: 10.1051/0004-6361:200809673.

G. A. Blake, E. F. van Dishoeck, D. J. Jansen, T. D. Groesbeck, and L. G. Mundy. Molecular abundances and low-mass star formation. 1: Si- and S-bearing species toward IRAS 16293-2422. ApJ, 428:680–692, June 1994. doi: 10.1086/174278.

A. P. Boss and P. Bodenheimer. Fragmentation in a rotating protostar - A comparison of two three-dimensional computer codes. ApJ, 234:289–295, November 1979. doi: 10.1086/157497.

S. Bottinelli, C. Ceccarelli, R. Neri, J. P. Williams, E. Caux, S. Cazaux, B. Lefloch, S. Maret, and A. G. G. M. Tielens. Near-Arcsecond Resolution Observations of the Hot Corino of the Solar-Type Protostar IRAS 16293-2422. ApJ, 617:L69–L72, December 2004. doi: 10.1086/426964.

S. Bottinelli, V. Wakelam, E. Caux, C. Vastel, Y. Aikawa, and C. Ceccarelli. CH in absorption in IRAS 16293-2422. MNRAS, 441:1964–1973, July 2014. doi: 10.1093/mnras/stu700.

C. Brinch and M. R. Hogerheijde. LIME - a flexible, non-LTE line excitation and radiation transfer method for millimeter and far-infrared wavelengths. A&A, 523:A25, November 2010. doi: 10.1051/0004-6361/201015333.

S. T. Bromley, T. P. M. Goumans, E. Herbst, A. P. Jones, and B. Slater. Challenges in modelling the reaction chemistry of interstellar dust. *Phys. Chem. Chem. Phys.*, 16: 18623–18643, 2014. doi: 10.1039/C4CP00774C. URL http://dx.doi.org/10.1039/C4CP00774C.

H. M. Butner, S. B. Charnley, C. Ceccarelli, S. D. Rodgers, J. R. Pardo, B. Parise, J. Cernicharo, and G. R. Davis. Discovery of Interstellar Heavy Water. ApJ, 659:L137–L140, April 2007. doi: 10.1086/517883.

A. Castets, C. Ceccarelli, L. Loinard, E. Caux, and B. Lefloch. Multiple shocks around the low-luminosity protostar IRAS 16293-2422. A&A, 375:40–53, August 2001. doi: 10.1051/0004-6361:20010662.

E. Caux, C. Kahane, A. Castets, A. Coutens, C. Ceccarelli, A. Bacmann, S. Bisschop, S. Bottinelli, C. Comito, F. P. Helmich, B. Lefloch, B. Parise, P. Schilke, A. G. G. M. Tielens, E. van Dishoeck, C. Vastel, V. Wakelam, and A. Walters. TIMASSS: the IRAS 16293-2422 millimeter and submillimeter spectral survey. I. Observations, calibration, and analysis of the line kinematics. A&A, 532:A23, August 2011. doi: 10.1051/0004-6361/201015399.

S. Cazaux, A. G. G. M. Tielens, C. Ceccarelli, A. Castets, V. Wakelam, E. Caux, B. Parise, and D. Teyssier. The Hot Core around the Low-mass Protostar IRAS 16293-2422: Scoundrels Rule! ApJ, 593:L51–L55, August 2003. doi: 10.1086/378038.

C. Ceccarelli. The Hot Corinos of Solar Type Protostars. In D. Johnstone, F. C. Adams, D. N. C. Lin, D. A. Neufeld, and E. C. Ostriker, editors, *Star Formation in the Interstellar Medium: In Honor of David Hollenbach*, volume 323 of *Astronomical Society of the Pacific Conference Series*, page 195, December 2004.

C. Ceccarelli, D. J. Hollenbach, and A. G. G. M. Tielens. Far-Infrared Line Emission from Collapsing Protostellar Envelopes. ApJ, 471:400, November 1996. doi: 10.1086/177978.

C. Ceccarelli, A. Castets, L. Loinard, E. Caux, and A. G. G. M. Tielens. Detection of doubly deuterated formaldehyde towards the low-luminosity protostar IRAS 16293-2422. A&A, 338:L43–L46, October 1998.

C. Ceccarelli, A. Castets, E. Caux, D. Hollenbach, L. Loinard, S. Molinari, and A. G. G. M. Tielens. The structure of the collapsing envelope around the low-mass protostar IRAS 16293-2422. A&A, 355:1129–1137, March 2000.

C. Ceccarelli, P. Caselli, E. Herbst, A. G. G. M. Tielens, and E. Caux. Extreme Deuteration and Hot Corinos: The Earliest Chemical Signatures of Low-Mass Star Formation. *Protostars and Planets V*, pages 47–62, 2007.

C. Ceccarelli, A. Bacmann, A. Boogert, E. Caux, C. Dominik, B. Lefloch, D. Lis, P. Schilke, F. van der Tak, P. Caselli, J. Cernicharo, C. Codella, C. Comito, A. Fuente, A. Baudry, T. Bell, M. Benedettini, E. A. Bergin, G. A. Blake, S. Bottinelli, S. Cabrit, A. Castets, A. Coutens, N. Crimier, K. Demyk, P. Encrenaz, E. Falgarone, M. Gerin, P. F. Goldsmith, F. Helmich, P. Hennebelle, T. Henning, E. Herbst, P. Hily-Blant, T. Jacq, C. Kahane, M. Kama, A. Klotz, W. Langer, S. Lord, A. Lorenzani, S. Maret, G. Melnick, D. Neufeld, B. Nisini, S. Pacheco, L. Pagani, B. Parise, J. Pearson, T. Phillips, M. Salez, P. Saraceno, K. Schuster, X. Tielens, M. H. D. van der Wiel, C. Vastel, S. Viti, V. Wakelam, A. Walters, F. Wyrowski, H. Yorke, R. Liseau, M. Olberg, R. Szczerba, A. O. Benz, and M. Melchior. Herschel spectral surveys of star-forming regions. Overview of the 555-636 GHz range. A&A, 521:L22, October 2010. doi: 10.1051/0004-6361/201015081.

C. J. Chandler, C. L. Brogan, Y. L. Shirley, and L. Loinard. IRAS 16293-2422: Proper Motions, Jet Precession, the Hot Core, and the Unambiguous Detection of Infall. ApJ, 632:371–396, October 2005. doi: 10.1086/432828.

X. Chen, H. G. Arce, Q. Zhang, T. L. Bourke, R. Launhardt, J. K. Jørgensen, C.-F. Lee, J. B. Foster, M. M. Dunham, J. E. Pineda, and T. Henning. SMA Observations of Class 0 Protostars: A High Angular Resolution Survey of Protostellar Binary Systems. ApJ, 768: 110, May 2013. doi: 10.1088/0004-637X/768/2/110.

A. Coutens, C. Vastel, E. Caux, C. Ceccarelli, S. Bottinelli, L. Wiesenfeld, A. Faure, Y. Scribano, and C. Kahane. A study of deuterated water in the low-mass protostar IRAS 16293-2422. A&A, 539:A132, March 2012. doi: 10.1051/0004-6361/201117627.

N. Crimier, C. Ceccarelli, S. Maret, S. Bottinelli, E. Caux, C. Kahane, D. C. Lis, and J. Olofsson. The solar type protostar IRAS16293-2422: new constraints on the physical structure. A&A, 519:A65, September 2010. doi: 10.1051/0004-6361/200913112.

G. Duchêne, J. Bouvier, S. Bontemps, P. André, and F. Motte. Multiple protostellar systems. I. A deep near infrared survey of Taurus and Ophiuchus protostellar objects. A&A, 427: 651–665, November 2004. doi: 10.1051/0004-6361:20041209.

G. Duchêne, S. Bontemps, J. Bouvier, P. André, A. A. Djupvik, and A. M. Ghez. Multiple protostellar systems. II. A high resolution near-infrared imaging survey in nearby star-forming regions. A&A, 476:229–242, December 2007. doi: 10.1051/0004-6361:20077270.

C. Favre, J. K. Jørgensen, D. Field, C. Brinch, S. E. Bisschop, T. L. Bourke, M. R. Hogerheijde, and W. W. F. Frieswijk. Dynamical Structure of the Inner 100 AU of the Deeply Embedded Protostar IRAS 16293-2422. ApJ, 790:55, July 2014. doi: 10.1088/0004-637X/790/1/55.

R. S. Furuya, Y. Kitamura, A. Wootten, M. J. Claussen, and R. Kawabe. Water Maser Survey toward Low-Mass Young Stellar Objects in the Northern Sky with the Nobeyama 45 Meter Telescope and the Very Large Array. ApJS, 144:71–134, January 2003. doi: 10.1086/342749.

R. T. Garrod and E. Herbst. Formation of methyl formate and other organic species in the warm-up phase of hot molecular cores. A&A, 457:927–936, October 2006. doi: 10.1051/0004-6361:20065560.

J. M. Girart, R. Estalella, A. Palau, J. M. Torrelles, and R. Rao. On the Origin of the Molecular Outflows in IRAS 16293-2422. ApJ, 780:L11, January 2014. doi: 10.1088/2041-8205/780/1/L11.

T. Greene. Protostars. *American Scientist*, 89:316, August 2001. doi: 10.1511/2001.4.316.

T. P. Greene, B. A. Wilking, P. Andre, E. T. Young, and C. J. Lada. Further mid-infrared study of the rho Ophiuchi cloud young stellar population: Luminosities and masses of pre-main-sequence stars. ApJ, 434:614–626, October 1994. doi: 10.1086/174763.

K. E. Haisch, Jr., T. P. Greene, M. Barsony, and S. W. Stahler. A Near-Infrared Multiplicity Survey of Class I/Flat-Spectrum Systems in Six Nearby Molecular Clouds. AJ, 127:1747–1754, March 2004. doi: 10.1086/381952.

E. Herbst and E. F. van Dishoeck. Complex Organic Interstellar Molecules. ARA&A, 47: 427–480, September 2009. doi: 10.1146/annurev-astro-082708-101654.

N. Hirano, H. Mikami, T. Umemoto, S. Yamamoto, and Y. Taniguchi. SIO Emission in the Multilobe Outflow Associated with IRAS 16293-2422. ApJ, 547:899–906, February 2001. doi: 10.1086/318432.

M. Hogerheijde and F. van der Tak. RATRAN: Radiative Transfer and Molecular Excitation in One and Two Dimensions. Astrophysics Source Code Library, August 2000.

D. Hollenbach, M. J. Kaufman, E. A. Bergin, and G. J. Melnick. Water, O_2, and Ice in Molecular Clouds. ApJ, 690:1497–1521, January 2009. doi: 10.1088/0004-637X/690/2/1497.

H.-C. Huang, Y.-J. Kuan, S. B. Charnley, N. Hirano, S. Takakuwa, and T. L. Bourke. Organic molecules in the hot corinos and circumstellar disks of IRAS 16293-2422. *Advances in Space Research*, 36:146–155, 2005. doi: 10.1016/j.asr.2005.03.115.

H. Imai, T. Iwata, and M. Miyoshi. Rotation-Infall Motion around the Protostar IRAS 16293-2422 Traced by Water Maser Emission. PASJ, 51:473–477, August 1999. doi: 10.1093/pasj/51.4.473.

H. Imai, K. Nakashima, T. Bushimata, Y. K. Choi, T. Hirota, M. Honma, K. Horiai, N. Inomata, K. Iwadate, T. Jike, O. Kameya, R. Kamohara, Y. Kan-Ya, N. Kawaguchi, M. Kijima, H. Kobayashi, S. Kuji, T. Kurayama, S. Manabe, T. Miyaji, T. Nagayama, A. Nakagawa, C. S. Oh, T. Omodaka, T. Oyama, S. Sakai, S. Sakakibara, K. Sato, T. Sasao, K. M. Shibata, R. Shimizu, M. Shintani, Y. Sofue, K. Sora, H. Suda, Y. Tamura, M. Tsushima, Y. Ueno, and K. Yamashita. Astrometry of H_2O Masers in Nearby Star-Forming Regions with VERA I. IRAS 16293-2422 in ρ Oph East. PASJ, 59:1107–1113, December 2007. doi: 10.1093/pasj/59.6.1107.

S. K. Jacobsen, J. K. Jørgensen, M. H. D. van der Wiel, H. Calcutt, T. L. Bourke, C. Brinch, A. Coutens, M. N. Drozdovskaya, L. E. Kristensen, H. S. P. Müller, and S. F. Wampfler. The ALMA-PILS survey: 3D modeling of the envelope, disks and dust filament of IRAS 16293-2422. A&A, 612:A72, April 2018. doi: 10.1051/0004-6361/201731668.

J. K. Jørgensen, F. Lahuis, F. L. Schöier, E. F. van Dishoeck, G. A. Blake, A. C. A. Boogert, C. P. Dullemond, N. J. Evans, II, J. E. Kessler-Silacci, and K. M. Pontoppidan. Protostellar Holes: Spitzer Space Telescope Observations of the Protostellar Binary IRAS 16293-2422. ApJ, 631:L77–L80, September 2005. doi: 10.1086/497003.

J. K. Jørgensen, T. L. Bourke, Q. Nguyen Luong, and S. Takakuwa. Arcsecond resolution images of the chemical structure of the low-mass protostar IRAS 16293-2422. An overview of a large molecular line survey from the Submillimeter Array. A&A, 534:A100, October 2011. doi: 10.1051/0004-6361/201117139.

J. K. Jørgensen, C. Favre, S. E. Bisschop, T. L. Bourke, E. F. van Dishoeck, and M. Schmalzl. Detection of the Simplest Sugar, Glycolaldehyde, in a Solar-type Protostar with ALMA. ApJ, 757:L4, September 2012. doi: 10.1088/2041-8205/757/1/L4.

J. K. Jørgensen, M. H. D. van der Wiel, A. Coutens, J. M. Lykke, H. S. P. Müller, E. F. van Dishoeck, H. Calcutt, P. Bjerkeli, T. L. Bourke, M. N. Drozdovskaya, C. Favre, E. C. Fayolle, R. T. Garrod, S. K. Jacobsen, K. I. Öberg, M. V. Persson, and S. F. Wampfler. The ALMA Protostellar Interferometric Line Survey (PILS). First results from an unbiased submillimeter wavelength line survey of the Class 0 protostellar binary IRAS 16293-2422 with ALMA. A&A, 595:A117, November 2016. doi: 10.1051/0004-6361/201628648.

C. Kahane, C. Ceccarelli, A. Faure, and E. Caux. Detection of Formamide, the Simplest but Crucial Amide, in a Solar-type Protostar. ApJ, 763:L38, February 2013. doi: 10.1088/2041-8205/763/2/L38.

Y.-J. Kuan, H.-C. Huang, S. B. Charnley, N. Hirano, S. Takakuwa, D. J. Wilner, S.-Y. Liu, N. Ohashi, T. L. Bourke, C. Qi, and Q. Zhang. Organic Molecules in Low-Mass Protostellar Hot Cores: Submillimeter Imaging of IRAS 16293-2422. ApJ, 616:L27–L30, November 2004. doi: 10.1086/426315.

S. Kurtz, R. Cesaroni, E. Churchwell, P. Hofner, and C. M. Walmsley. Hot Molecular Cores and the Earliest Phases of High-Mass Star Formation. *Protostars and Planets IV*, pages 299–326, May 2000.

C. J. Lada and B. A. Wilking. The nature of the embedded population in the Rho Ophiuchi dark cloud - Mid-infrared observations. ApJ, 287:610–621, December 1984. doi: 10.1086/162719.

R. B. Larson. Numerical calculations of the dynamics of collapsing proto-star. MNRAS, 145:271, 1969. doi: 10.1093/mnras/145.3.271.

R. B. Larson. The Collapse of a Rotating Cloud. MNRAS, 156:437, 1972. doi: 10.1093/mnras/156.4.437.

R. Le Gal, P. Hily-Blant, A. Faure, G. Pineau des Forêts, C. Rist, and S. Maret. Interstellar chemistry of nitrogen hydrides in dark clouds. A&A, 562:A83, February 2014. doi: 10.1051/0004-6361/201322386.

L. Loinard. Large Proper Motions in the Young Low-Mass Protostellar System IRAS 16293-2422. Rev. Mexicana Astron. Astrofis., 38:61–69, April 2002.

L. Loinard, C. J. Chandler, L. F. Rodríguez, P. D'Alessio, C. L. Brogan, D. J. Wilner, and P. T. P. Ho. New Radio Sources and the Composite Structure of Component B in the Very Young Protostellar System IRAS 16293-2422. ApJ, 670:1353–1360, December 2007. doi: 10.1086/522568.

L. Loinard, R. M. Torres, A. J. Mioduszewski, and L. F. Rodríguez. A Preliminary VLBA Distance to the Core of Ophiuchus, with an Accuracy of 4%. ApJ, 675:L29, March 2008. doi: 10.1086/529548.

L. Loinard, L. A. Zapata, L. F. Rodríguez, G. Pech, C. J. Chandler, C. L. Brogan, D. J. Wilner, P. T. P. Ho, B. Parise, L. W. Hartmann, Z. Zhu, S. Takahashi, and A. Trejo. ALMA and VLA observations of the outflows in IRAS 16293-2422. MNRAS, 430:L10–L14, March 2013. doi: 10.1093/mnrasl/sls038.

M. Lombardi, C. J. Lada, and J. Alves. Hipparcos distance estimates of the Ophiuchus and the Lupus cloud complexes. A&A, 480:785–792, March 2008. doi: 10.1051/0004-6361:20079110.

J. M. Lykke, A. Coutens, J. K. Jørgensen, M. H. D. van der Wiel, R. T. Garrod, H. S. P. Müller, P. Bjerkeli, T. L. Bourke, H. Calcutt, M. N. Drozdovskaya, C. Favre, E. C. Fayolle,

S. K. Jacobsen, K. I. Öberg, M. V. Persson, E. F. van Dishoeck, and S. F. Wampfler. The ALMA-PILS survey: First detections of ethylene oxide, acetone and propanal toward the low-mass protostar IRAS 16293-2422. A&A, 597:A53, January 2017. doi: 10.1051/0004-6361/201629180.

S. Maret, A. Faure, E. Scifoni, and L. Wiesenfeld. On the robustness of the ammonia thermometer. MNRAS, 399:425–431, October 2009. doi: 10.1111/j.1365-2966.2009.15294.x.

R. Martín-Doménech, V. M. Rivilla, I. Jiménez-Serra, D. Quénard, L. Testi, and J. Martín-Pintado. Detection of methyl isocyanate (CH_3NCO) in a solar-type protostar. MNRAS, 469:2230–2234, August 2017. doi: 10.1093/mnras/stx915.

A. Mizuno, Y. Fukui, T. Iwata, S. Nozawa, and T. Takano. A remarkable multilobe molecular outflow - Rho Ophiuchi East, associated with IRAS 16293-2422. ApJ, 356:184–194, June 1990. doi: 10.1086/168829.

L. G. Mundy, A. Wootten, B. A. Wilking, G. A. Blake, and A. I. Sargent. IRAS 16293 - 2422 - A very young binary system? ApJ, 385:306–313, January 1992. doi: 10.1086/170939.

G. Narayanan, C. K. Walker, and H. D. Buckley. The "Blue-Bulge" Infall Signature toward IRAS 16293-2422. ApJ, 496:292–310, March 1998. doi: 10.1086/305363.

G. N. Ortiz-León, L. Loinard, M. A. Kounkel, S. A. Dzib, A. J. Mioduszewski, L. F. Rodríguez, R. M. Torres, R. A. González-Lópezlira, G. Pech, J. L. Rivera, L. Hartmann, A. F. Boden, N. J. Evans, II, C. Briceño, J. J. Tobin, P. A. B. Galli, and D. Gudehus. The Gould's Belt Distances Survey (GOBELINS). I. Trigonometric Parallax Distances and Depth of the Ophiuchus Complex. ApJ, 834:141, January 2017. doi: 10.3847/1538-4357/834/2/141.

Y. Oya, K. Moriwaki, S. Onishi, N. Sakai, A. López-Sepulcre, C. Favre, Y. Watanabe, C. Ceccarelli, B. Lefloch, and S. Yamamoto. Chemical and Physical Picture of IRAS 16293-2422 Source B at a Sub-arcsecond Scale Studied with ALMA. ApJ, 854:96, February 2018. doi: 10.3847/1538-4357/aaa6c7.

L. Pagani, A. Bacmann, S. Cabrit, and C. Vastel. Depletion and low gas temperature in the L183 (=L134N) prestellar core: the N2Hˆ+-N2D$^+$ tool. A&A, 467:179–186, May 2007. doi: 10.1051/0004-6361:20066670.

B. Parise, C. Ceccarelli, A. G. G. M. Tielens, E. Herbst, B. Lefloch, E. Caux, A. Castets, I. Mukhopadhyay, L. Pagani, and L. Loinard. Chemistry as a Diagnostic of Star Formation xi Detection of Deuterated Methanol in the Low-mass Protostar IRAS 16293-2422. In C. L. Curry and M. Fich, editors, *SFChem 2002: Chemistry as a Diagnostic of Star Formation*, page 378, 2003.

B. Parise, F. Du, F.-C. Liu, A. Belloche, H. Wiesemeyer, R. Güsten, K. M. Menten, H.-W. Hübers, and B. Klein. Detection of OD towards the low-mass protostar IRAS 16293-2422. A&A, 542:L5, June 2012. doi: 10.1051/0004-6361/201218784.

G. Pech, L. Loinard, C. J. Chandler, L. F. Rodríguez, P. D'Alessio, C. L. Brogan, D. J. Wilner, and P. T. P. Ho. Confirmation of a Recent Bipolar Ejection in the Very Young Hierarchical Multiple System IRAS 16293-2422. ApJ, 712:1403–1409, April 2010. doi: 10.1088/0004-637X/712/2/1403.

M. V. Persson, J. K. Jørgensen, and E. F. van Dishoeck. Warm water deuterium fractionation in IRAS 16293-2422. The high-resolution ALMA and SMA view. A&A, 549:L3, January 2013. doi: 10.1051/0004-6361/201220638.

J. E. Pineda, A. J. Maury, G. A. Fuller, L. Testi, D. García-Appadoo, A. B. Peck, E. Villard, S. A. Corder, T. A. van Kempen, J. L. Turner, K. Tachihara, and W. Dent. The first ALMA view of IRAS 16293-2422. Direct detection of infall onto source B and high-resolution kinematics of source A. A&A, 544:L7, August 2012. doi: 10.1051/0004-6361/201219589.

D. Quénard, S. Bottinelli, and E. Caux. Modelling the 3D physical structure of astrophysical sources with gass. MNRAS, 468:685–702, June 2017. doi: 10.1093/mnras/stx404.

D. Quénard, S. Bottinelli, E. Caux, and V. Wakelam. 3D modelling of HCO^+ and its isotopologues in the low-mass proto-star IRAS16293-2422. MNRAS, 477:5312–5326, July 2018. doi: 10.1093/mnras/sty1004.

R. Rao, J. M. Girart, D. P. Marrone, S.-P. Lai, and S. Schnee. IRAS 16293: A "Magnetic" Tale of Two Cores. ApJ, 707:921–935, December 2009. doi: 10.1088/0004-637X/707/2/921.

R. Rao, J. M. Girart, S.-P. Lai, and D. P. Marrone. Detection of a Magnetized Disk around a Very Young Protostar. ApJ, 780:L6, January 2014. doi: 10.1088/2041-8205/780/1/L6.

L. F. Rodríguez, L. Loinard, P. D'Alessio, D. J. Wilner, and P. T. P. Ho. IRAS 16293-2422B: A Compact, Possibly Isolated Protoplanetary Disk in a Class 0 Object. ApJ, 621:L133–L136, March 2005. doi: 10.1086/429223.

F. L. Schöier, J. K. Jørgensen, E. F. van Dishoeck, and G. A. Blake. Does IRAS 16293-2422 have a hot core? Chemical inventory and abundance changes in its protostellar environment. A&A, 390:1001–1021, August 2002. doi: 10.1051/0004-6361:20020756.

F. L. Schöier, J. K. Jørgensen, E. F. van Dishoeck, and G. A. Blake. On the origin of H_2CO abundance enhancements in low-mass protostars. A&A, 418:185–202, April 2004. doi: 10.1051/0004-6361:20035769.

F. H. Shu. Self-similar collapse of isothermal spheres and star formation. ApJ, 214:488–497, June 1977. doi: 10.1086/155274.

F. H. Shu, F. C. Adams, and S. Lizano. Star formation in molecular clouds - Observation and theory. ARA&A, 25:23–81, 1987. doi: 10.1146/annurev.aa.25.090187.000323.

BIBLIOGRAPHY

G. Siringo, E. Kreysa, A. Kovács, F. Schuller, A. Weiß, W. Esch, H.-P. Gemünd, N. Jethava, G. Lundershausen, A. Colin, R. Güsten, K. M. Menten, A. Beelen, F. Bertoldi, J. W. Beeman, and E. E. Haller. The Large APEX BOlometer CAmera LABOCA. A&A, 497:945–962, April 2009. doi: 10.1051/0004-6361/200811454.

V. V. Sobolev. *Moving envelopes of stars*. 1960.

R. Stark, G. Sandell, S. C. Beck, M. R. Hogerheijde, E. F. van Dishoeck, P. van der Wal, F. F. S. van der Tak, F. Schäfer, G. J. Melnick, M. L. N. Ashby, and G. de Lange. Probing the Early Stages of Low-Mass Star Formation in LDN 1689N: Dust and Water in IRAS 16293-2422A, B, and E. ApJ, 608:341–364, June 2004. doi: 10.1086/392492.

S. Terebey, S. N. Vogel, and P. C. Myers. Probing the circumstellar environments of very young low-mass stars using water masers. ApJ, 390:181–190, May 1992. doi: 10.1086/171269.

F. F. S. van der Tak, J. H. Black, F. L. Schöier, D. J. Jansen, and E. F. van Dishoeck. A computer program for fast non-LTE analysis of interstellar line spectra. With diagnostic plots to interpret observed line intensity ratios. A&A, 468:627–635, June 2007. doi: 10.1051/0004-6361:20066820.

E. F. van Dishoeck, G. A. Blake, D. J. Jansen, and T. D. Groesbeck. Molecular Abundances and Low-Mass Star Formation. II. Organic and Deuterated Species toward IRAS 16293-2422. ApJ, 447:760, July 1995. doi: 10.1086/175915.

C. Vastel, T. G. Phillips, C. Ceccarelli, and J. Pearson. First Detection of Doubly Deuterated Hydrogen Sulfide. ApJ, 593:L97–L100, August 2003. doi: 10.1086/378261.

C. Vastel, S. Bottinelli, E. Caux, J.-M. Glorian, and M. Boiziot. CASSIS: a tool to visualize and analyse instrumental and synthetic spectra. In F. Martins, S. Boissier, V. Buat, L. Cambrésy, and P. Petit, editors, *SF2A-2015: Proceedings of the Annual meeting of the French Society of Astronomy and Astrophysics*, pages 313–316, December 2015.

C. K. Walker, C. J. Lada, E. T. Young, P. R. Maloney, and B. A. Wilking. Spectroscopic evidence for infall around an extraordinary IRAS source in Ophiuchus. ApJ, 309:L47–L51, October 1986. doi: 10.1086/184758.

C. K. Walker, C. J. Lada, E. T. Young, and M. Margulis. An unusual outflow around IRAS 16293-2422. ApJ, 332:335–345, September 1988. doi: 10.1086/166659.

D. C. B. Whittet and I. G. van Breda. The ratio of total to selective absorption in dark clouds. Ap&SS, 38:L3–L8, November 1975. doi: 10.1007/BF00646110.

B. A. Wilking and M. J. Claussen. Water masers associated with low-mass stars - A survey of the Rho Ophiuchi infrared cluster. ApJ, 320:L133–L137, September 1987. doi: 10.1086/184989.

A. Wootten. The Duplicity of IRAS 16293-2422: A Protobinary Star? ApJ, 337:858, February 1989. doi: 10.1086/167156.

S. C. C. Yeh, N. Hirano, T. L. Bourke, P. T. P. Ho, C.-F. Lee, N. Ohashi, and S. Takakuwa. The CO Molecular Outflows of IRAS 16293-2422 Probed by the Submillimeter Array. ApJ, 675:454–463, March 2008. doi: 10.1086/524648.

L. A. Zapata, L. Loinard, L. F. Rodríguez, V. Hernández-Hernández, S. Takahashi, A. Trejo, and B. Parise. ALMA 690 GHz Observations of IRAS 16293-2422B: Infall in a Highly Optically Thick Disk. ApJ, 764:L14, February 2013. doi: 10.1088/2041-8205/764/1/L14.

Y. Zhou, S.-L. Qin, A. Sanchez-Monge, P. Schilke, T. Liu, L. A. Zapata, D. Li, Y. Wu, Q. Qian, and X. Li. First detection of vibrationally excited Glycolaldehyde in the solar-type protostar IRAS 16293-2422. *ArXiv e-prints*, July 2018.